IN-SITU AND EX-SITU STUDIES ON EARLY-STAGE SCALE ESTABLISHMENT

by

Yihong Kang

BS in Physics, University of Science and Technology of China, 2006

MS in Physics, University of Missouri-Kansas City, 2009

Submitted to the Graduate Faculty of

Swanson School of Engineering in partial fulfillment

of the requirements for the degree of

Doctor of Philosophy

University of Pittsburgh

2016

UNIVERSITY OF PITTSBURGH

THE SWANSON SCHOOL OF ENGINEERING

This dissertation was presented

by

Yihong Kang

It was defended on

April 20, 2016

and approved by

Gerald H. Meier, PhD, Professor,

Department of Mechanical Engineering and Materials Science

Jorg M. Wiezorek, PhD, Professor,

Department of Mechanical Engineering and Materials Science

Lei Li, PhD, Assistant Professor,

Department of Chemical and Petroleum Engineering

Dissertation Director: Brian Gleeson, PhD, Harry S. Tack Chair

Professor, Department of Mechanical Engineering and Materials Science

IN-SITU AND EX-SITU STUDIES ON EARLY-STAGE SCALE ESTABLISHMENT

Yihong Kang, PhD

University of Pittsburgh, 2016

This thesis study is divided into two parts. In the first part, competitive oxidation during the nucleation-and-growth stage was investigated based on studies on Cu-Ni and Ni-Cr alloys. Two competing oxidation mechanisms were proposed to interpret the competitive oxidation behavior of a dilute Cu-Ni alloy during the nucleation-and-growth stage of oxidation under 10^{-4} Torr oxygen pressure at a temperature range from 350℃ to 600℃. NiO was found to be the preferred oxide phase to form initially on the Cu-Ni alloy surface rather than a copper oxide product. Depending on the time of the growth process, an individual NiO island could be limited by oxygen surface diffusion, diffusion of Ni in the Cu-Ni matrix towards the surface, or a combination of these two processes. In the competitive oxidation of dilute Ni-Cr alloys under low oxygen partial pressures (10^{-7} to 10^{-5} Torr) at 600℃, it was found that Cr_2O_3 is the preferred oxide to form on the alloy surface, with the growth of Cr_2O_3 being limited by diffusion of Cr in the alloy towards the surface. Only when the amount of Cr_2O_3 formed initially on the surface was sufficiently high that the oxygen inward diffusion into alloy could be reduced to the extent that establishment of a continuous Cr_2O_3 scale was possible.

The second part of this study investigated the third-element effect on Al_2O_3-scale formation on Ni-based alloys. Two new perspectives of the third-element effect were proposed. The Cr addition to a relatively dilute Ni-Al alloy resulted in the formation of much coarser internal oxides, and

decreased the internal oxidation rate significantly; on the contrary, Mn addition, which has the similar affinity to oxygen as Cr, to a similar Ni-Al alloy led to the formation of much finer rod-like internal oxides, and increased the internal oxidation rate significantly. Based on this experimental observation, it was proposed that the addition of a third element may change the internal oxide phase and morphology, such that the diffusion path of oxygen in the internal oxidation zone could be significantly affected, which in turn could affect the internal-to-external oxidation transition. The Cr addition into a relative dilute Ni-Al alloy was also found to enhance the Al grain-boundary diffusion at lower temperature (below 1000 ℃), which consequently enhanced the Al_2O_3-scale establishment during the heating process. Surface recrystallization, which occurs during the heating of alloys prepared with an abraded surface finish (i.e., 500-grit), could result in the formation of fine sub grains around 1 μm in size near the alloy surface, and provide necessary fast diffusion paths for Al. This Cr effect on the Al grain-boundary diffusion was much more evident during the oxidation of surface-abraded Ni-Al-Cr alloys than on the same alloys with a polished surface finish.

TABLE OF CONTENTS

LIST OF TABLES

LIST OF FIGURES

PREFACE

Firstly, I owe an enormous debt of gratitude to my mentors, Profs. Gerald H. Meier, Jorg M. Wiezorek, Judith C. Yang and Brian Gleeson, from whom I have learned an immeasurable amount about materials science, scientific research, technical writing skill, and what it means to be a professional.

To my mother Ping, my father Jinquan, my uncles Lei and Qiang, and my lovely wife Yuanyuan, I haven't the words to describe what you mean to me. Your love, patience, and support have contributed more to my success than any number of study sessions or late nights in the lab.

1.0   INTRODUCTION

The oxidation behavior of metals and alloys has been studied for many years because of its technological importance as well as scientific interest. Developing oxidation-resistant alloys for harsh environments is one of the most important applications associated with the study of oxidation. The design of oxidation-resistant alloys generally depends on the ability to form a continuous and adherent protective chromia or alumina scale. Specifically, the addition of Cr and/or Al in sufficient quantities can make a given alloy chromia or alumina scale forming, which prevents the further aggressive attack by the harsh service environment. Further alloying additions may also be made to increase mechanical properties or further enhance protective scale-forming behavior [1].

From a thermodynamic point of view, the overall chemical reaction involved in the oxidation of a metal with a single oxidant may be simply written as:

$$A + \frac{1}{2}xO_2 \leftrightarrow AO_x \qquad (2.1)$$

However, even for such a simple reaction, the kinetic process of oxidation, which involves the diffusion of both reactants (i.e., A and O during the oxidation of pure A) and microstructural factors, could be complex. Generally, the more reactive elements and oxide phases involved in a given system, the more complex the overall process will be. Although a multi-component system could be very complex, it still shares some commonalities with simpler systems (like binary and ternary alloys). Therefore, most fundamental studies of oxidation mechanisms are based on metals

1

and/or alloys containing less than three elements. The study of simpler systems could provide basic understanding of oxidation mechanisms, such as selective oxidation (only one or a few components in the alloy would be oxidized) and protective scale forming, which will be helpful for the development of complex multi-component alloys.
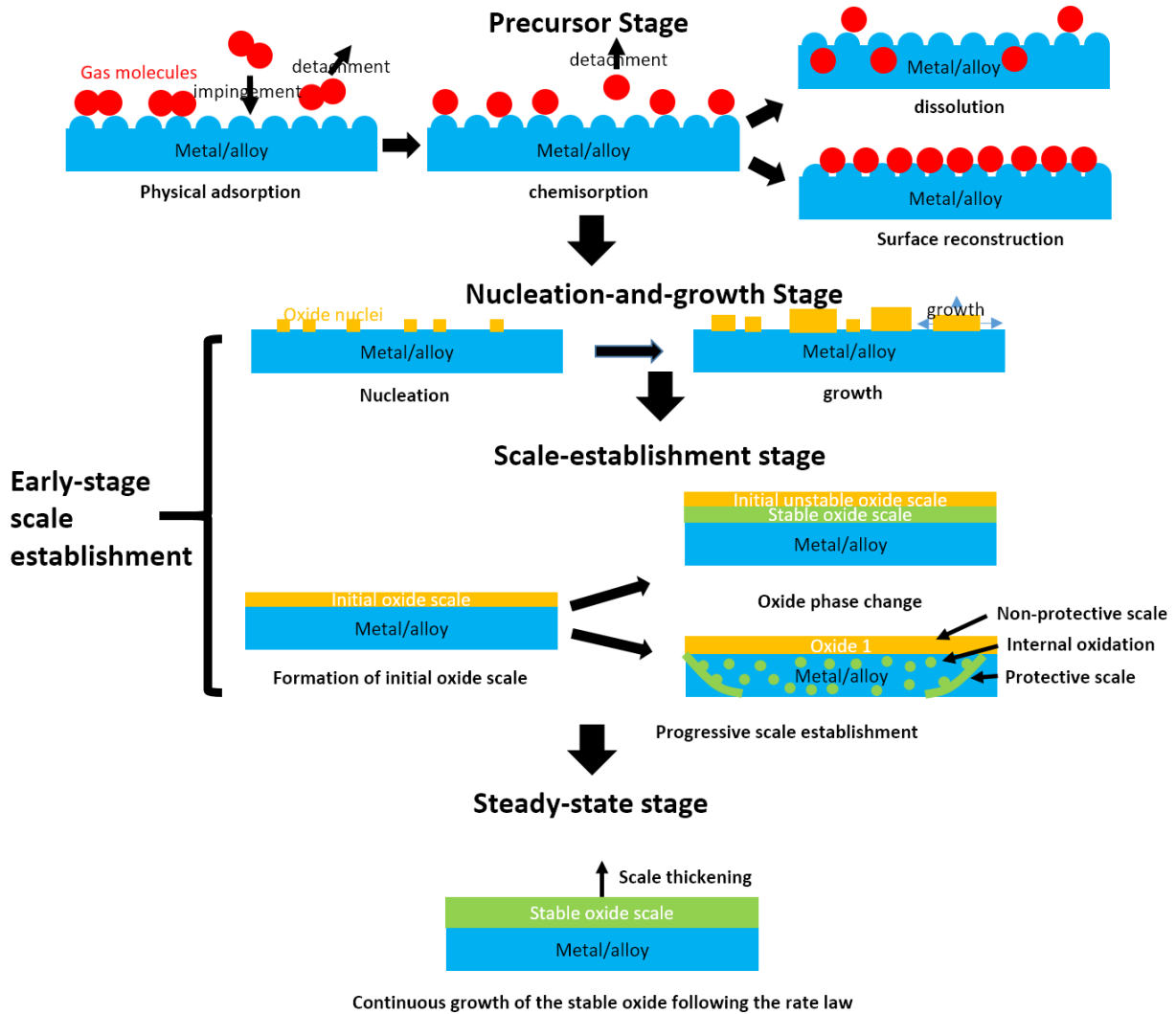
Figure 1.2.1 Schematics of the four stages of oxidation.

Although the complexity of the oxidation mechanisms can be reduced by limiting the components in a system, the whole oxidation process is still quite complex. Hence, several stages

2

have been defined in past studies to isolate the dominant mechanisms during the whole oxidation process [1-3]. There is no strict definition of each stage, so it may vary depending on the particular system and/or oxidizing conditions. In this study, the whole oxidation process will be separated into four stages: the precursor stage, the nucleation-and-growth stage, the scale-establishment stage, and the steady-state stage, as schematically shown in Figure 1.1. Oxidation starts with adsorption of the oxygen on the metal/alloy surface and subsequent dissolution of the oxygen into metal/alloy [4-6]. Depending on the oxidation conditions and materials, adsorption and dissolution of oxygen may lead to a reconstructed surface, which contains metal-oxygen bands, but does not have distinct oxide structures [7-10]. All the oxidation processes, prior to the formation of oxide, are defined as the precursor stage in this study. Once an oxide nucleates, it will grow into a continuous film [2, 11]. This particular process is defined as the nucleation-and-growth stage. The initial oxide film may not have the same phase or structure as the final oxide scale. The oxide scale may undergo structural and even compositional changes, especially for alloys, until the steady state is reached [12, 13]. This period of oxidation is defined as the scale-establishment stage. In most cases, the scale growth kinetics in the steady state will follow a general rate law.

$$x = (kt)^{1/n} \tag{2.2}$$

where

x – scale thickness

k – corrosion rate constant

t – time

n – a constant range from 1 to 3

Once the oxidation process reaches the steady-state stage, the scale assemblage and the growth rate (contains k and n) are time invariant [14-17].

Fundamental studies on the oxidation of metals and alloys date back to the classic works of Tammann et al.[18-20], followed by Wagner [14-18, 20, 21], who established mathematical solutions for limiting cases of oxidation of both metals and alloys. Most of those studies were concerned with development of thick scales (quantum mechanical tunneling effect and/or thermionic emission of electrons can be neglected) and focused on the steady-state growth of that scale layer. However, the design of an alloy resistant to the oxidation requires understanding of the establishment of protective oxide scale, which occurs in the stages prior to steady-state [1, 22].

Another approach to gaining an improved understanding of the oxidation process is utilization of surface science techniques. From a fundamental standpoint, it is advantageous to study the interaction of oxygen with a model system in an ideal environment. Hence, most of such studies were done in ultra-high vacuum (UHV) on atomically clean metal surfaces, using scanning tunneling microscopy (STM), X-ray photoelectron spectroscopy (XPS), as well as computational simulation [4, 10, 23, 24]. Although this approach provides some insight into the precursor stage of oxidation, it works only for highly restricted materials and conditions, such as atomically flat metal/alloy surfaces, a limited temperature range, and ultra-high vacuum. As a result, it gives very limited information regarding the oxidation behavior of alloys under realistic high-temperature gaseous environments.

Noting the huge gap between a model system and real-world applications, some attempts have been made to study the early stages (including nucleation-and-growth stage and the scale-establishment stage) of oxidation [13, 25-32]. Such studies have revealed the mechanisms involved in the nucleation of oxide and establishment of oxide scales. However, this field is fairly new compared to the other approaches described above and existing results are consequently fairly limited. Most previous studies have focused on the pure metal or simple binary alloys (just one

oxidizing component, no competitive oxidation), the nature of selective oxidation and how the alloying elements promote the formation of protective scales is still unclear. The results of this study serve to elucidate the mechanisms for the scale-establishment process and how the oxidation conditions and alloy compositions affect the protective scale establishment, thus guiding oxidation resistant alloy development.

1.1   STEADY-STATE OXIDATION

When a system is in the steady-state regime of oxidation, it should be at local equilibrium from a thermodynamic point of view; meanwhile, from a kinetic point of view, the oxide scale assemblage and its limiting boundary conditions are invariant with time.

In this section, the oxidation behavior of metals and alloys in the steady-state regime will be described from both thermodynamic and kinetic aspects, with emphasis on selective oxidation and scale growth kinetics.

1.1.1   Oxidation of metals

1.1.1.1 **Thermodynamics of oxidation**

From a thermodynamic point of view, as shown in equation (2.1), the oxidation of a metal with single oxidant is just a simple chemical reaction. An equilibrium constant K is associated with this reaction, when the system is in thermodynamic equilibrium,

$$\frac{a_{AO_x}}{a_A P_{O_2}^{x/2}} = K \tag{2.3}$$

where

a_{AO_x} and a_A – chemical activities of the oxide and the metal A.

P_{O_2} – the oxygen partial pressure.

The equilibrium constant K can be determined from by the standard Gibbs free energy ΔG_F^0 associated with the formation of the oxide (also referred as formation energy), the reaction temperature T and ideal gas constant R as shown in equation (2.4).

$$K_e = \exp(-\frac{\Delta G_F^0}{RT})$$

(2.4)

If the metal and the oxide are both solid and immiscible with each other, the chemical activities of both phases will be equal to unity. Equating equations (2.3) and (2.4), an equilibrium oxygen partial pressure $\mathbf{P_{O_2}^{eq}}$ can be obtained,

$$\frac{1}{(P_{O_2}^{eq})^{x/2}} = \exp\left(-\frac{\Delta G_F^0}{RT}\right)$$

(2.5)

$P_{O_2}^{eq}$ is also called dissociation pressure of the oxide, below which the oxide is unstable and the metal stays unoxidized (i.e. $K>K_e$). As shown in equation (2.5), $P_{O_2}^{eq}$ or the stability of an oxide is directly related to the temperature and the Gibbs free energy change for the oxide formation. Under certain reaction temperatures, the larger the absolute value of ΔG_F^0 of an oxide, the more stable is the oxide. Ellingham constructed a diagram to represent the stability of different oxides as a function of temperature, as shown in Figure 1.2 [33]. The lower a curve sits in the diagram, the higher the stability of the oxide is.
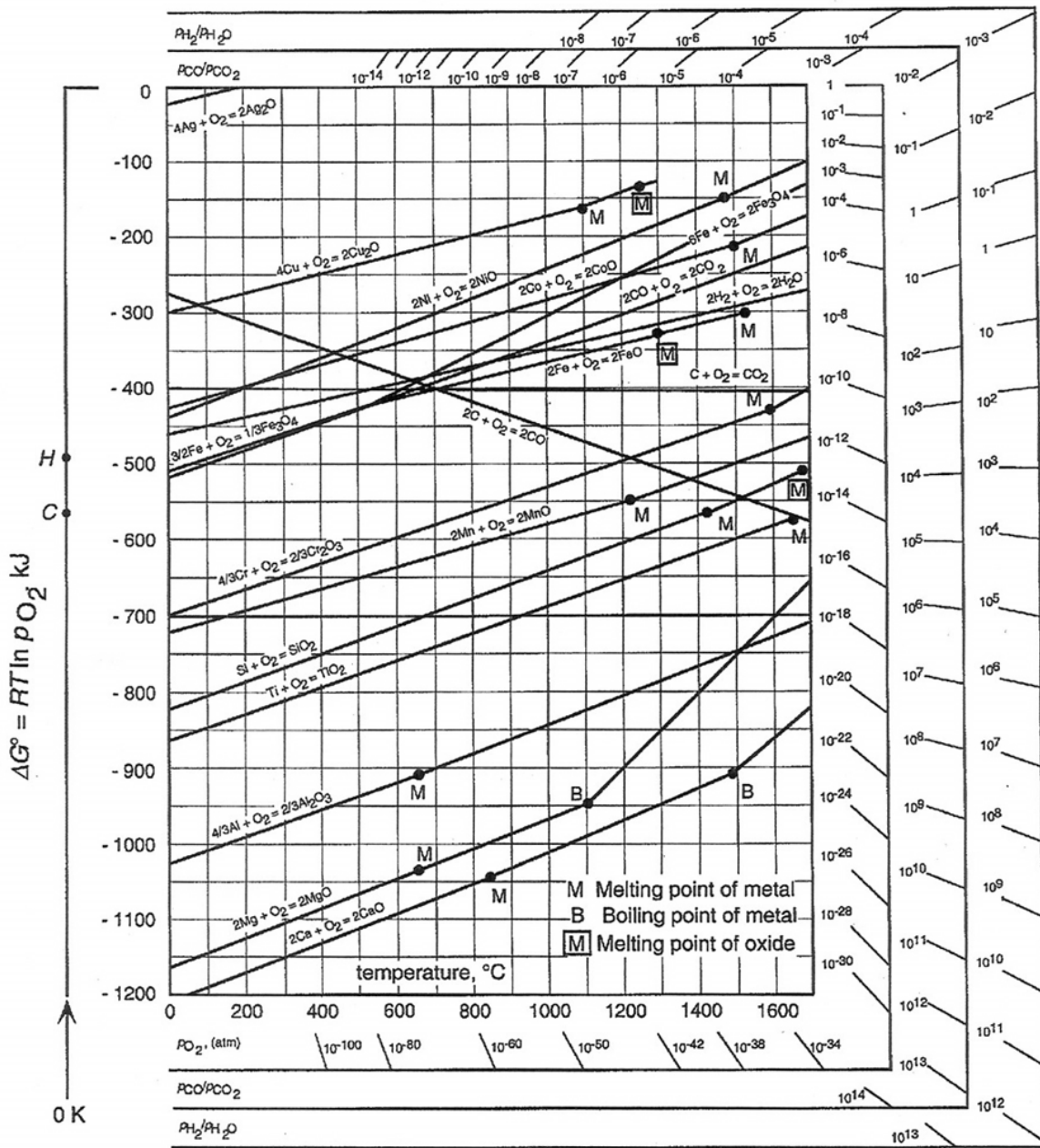
Figure 1.2.2 The Ellingham diagram for selected oxides [33].

1.1.1.2 **Kinetics of scale growth**

A parabolic rate law for scale thickening is generally observed when the oxide growth is diffusion controlled [18, 20]. Following the classic works of Tammann in Germany [18] and

Pilling and Bedworth in the UK [19, 20], Wagner [14] established a basic kinetic model of parabolic oxidation upon which most thick-film models are based. In Wagner's theory for scale thickening, he assumed that the oxide films are thick and compact, so that the rate-determining process in the oxidation is the diffusion of cations, anions and electrons through the oxide via lattice defects under the influence of an electrochemical potential gradient [14].

Based on the assumptions made by Wagner, an expression for the parabolic rate constant can be derived from diffusion equations as shown below. According to the Fick's law, the flux J_i of each spice i across the scale can be described,

$$J_i = -\frac{D_i C_i}{RT} \frac{\partial \eta_i}{\partial x} \tag{2.6}$$

where,

η_i – the electrochemical potential of constituent i, $\eta_i = \mu_i + N_A Z_i e \phi$,

N_A – Avogadro's number,

e – the electronic charge,

ϕ – the electrical potential,

μ_i – the chemical potential of constituent i, $\mu_i = \mu_i^0 + RT \ln a_i$.

D_i, C_i, Z_i – the diffusivity, concentration and valence of constituent i,

Based on the assumption of steady-state conditions, where charge-neutrality and thermodynamic equilibrium for both the alloy and the oxide scale should be reached, and ϕ equals 0. If oxide only forms on the phase boundaries, J_i will be the same cross the scale, and can be further simplified,

$$J_i = \frac{C_i D_i \ln(\frac{a_i''}{a_i'})}{x} \tag{2.7}$$

where,

8

a_i' and a_i'' - the chemical activities of constituent i at the oxide/metal interface and oxide/oxygen interface.

According to the mass conservation, the growth rate of a scale can be obtained,

$$\frac{dn}{dt} = \sum_i J_i = \frac{\sum_i C_i D_i \ln(\frac{a_i''}{a_i'})}{x} = \frac{k_r}{x} \tag{2.8}$$

where,

n – the number of particles in the scale per unit area. $n = x\frac{\rho N_A \sum_i Z_i}{M}$.

M and ρ – mole weight and density of the oxide.

$\sum_i Z_i$ represents the total number of atoms in an oxide molecule, and k_r is called rational rate constant by Wagner with the unit of m/s.

k_r – a constant termed by Wagner as "rational constant".

Let $k_p = \frac{Mk_r}{\rho N_A \sum_i Z_i}$, the rate law of the thickening of a scale can be obtained solving the differential equation,

$$\frac{dx}{dt} = \frac{k_p}{x} \tag{2.9}$$

The solution of this differential equation is the a parabolic rate law,

$$x^2 = 2k_p t \tag{2.10}$$

Wagner's theory for the parabolic oxidation of pure metals has been successfully validated for some important oxides in practice, such as Cu_2O, CoO and FeO [2, 34]. Since, the parabolic oxidation rate law is based on the assumption of electrochemical potential driven diffusion of species via lattice defects; it may not be valid for some oxidation behaviors driven by other rate-limiting mechanisms, where linear, cubic and logarithmic oxidation rates have been also observed [35, 36]. For instance, a linear rate law of scale thickening may occur, when an oxide scale is

9

sufficiently porous that a phase-boundary reaction may become the rate-determining process instead of lattice diffusion [36-38].

1.1.2 Oxidation of alloys

The oxidation of alloys is generally more complex than that of pure metals, due to the non-unity chemical activity of each component in an alloy, possible existence of multiple oxide phases and diffusion of multiple constituents.

Although alloys containing three or more elements present a higher level of complexity, general principles can be learned from oxidation studies of binary systems [1, 15, 16]. Hence, this section will focus on the oxidation of binary alloys.

1.1.2.1 Categorization of binary alloys

The chemical activity of each element in an alloy AB, where B is the less noble element, is related to the mole faction of that element N_X (X can be either A or B), and can be written as,

$$a_X = \gamma_X N_X \tag{2.11}$$

where γ_X is activity coefficient, which account for deviations from ideal behavior in a mixture of chemical substances [39]. For an arbitrary system, γ_X can be complex and dependent on the composition; however, for a dilute system, γ_X is a constant (Henry's Law) [40]. Assuming for simplification that alloys form ideal solutions, γ_X equals to unity. If there is more than one stable oxide phase under a given oxidation condition, the oxide phases are assumed to be immiscible with each other, so that the chemical activity of an oxide XO_z (a_{XO_z}) equals unity, where z is the valence of X in the oxide. Based on these two assumptions, the thermodynamic equilibrium for equation (2.3) can be rewritten as,

$$N_X P_{O_2}^{z/2} = \exp(\frac{\Delta G_{XO_z}}{RT})$$ (2.12)

Depending on the oxidation conditions and the formation energies for the oxides, binary alloys can be separated into three categories: (a) there is only one stable oxide phase; (b) both A and B can form stable oxides AO_x and BO_y, and the formation energies of AO_x and BO_y are not significantly different; (c) both A and B can form stable oxides AO_x and BO_y, and the formation energies of AO_x and BO_y differ significantly. The mathematical solution for the oxidation process of alloys in each category was developed initially by Wagner [15-17, 41], and later complemented by Gesmundo et al. [15-17, 41-45].

The oxidation behavior of the alloys in each category will be discussed separately in the following sections.

1.1.2.2 **Only one stable oxide during the oxidation**

Alloys AB containing a noble metal A (Au, Pt), which are not reacting with oxygen under the given conditions, belong to this category. Additionally, alloys containing two components for which both can form thermodynamic stable oxides, AO_x and BO_y, could fall in this group, in cases where BO_y grows faster than AO_x. In this situation, BO_y will form a continuous layer; as a result, the AO_x formed during the early stage will be overtaken and later covered by BO_y giving the thermodynamic conditions for the AO_x to become unstable. Finally, AO_x will be reduced by B via the displacement reaction $yAO_x + xB = yA + xBO_y$. This type of alloy can be treated in the same way as those alloys containing noble metals during the steady-state regime.

For the alloys in this category, a single-phase scale is expected to form on the surface, and the oxidation behavior is generally similar to what is observed during the oxidation of pure metals, but with additional features and variables. The presence of a secondary element not only changes

11

the chemical activity of the oxidizing element, but may also change the kinetic oxidation behavior, such as the diffusivity of the oxidizing component in the alloy, as well as the morphology of the oxide scale. Considering the change in local concentration at the alloy/oxide interface due to diffusion, Wagner provided a mathematical approach for this case based on the theories for pure metals [15, 17]. The local change in concentration is assumed to be the result of outward diffusion of oxidizing metal ions and inward diffusion of noble metal atoms into the alloy [15]. Based on the assumption of an ideal solid solution, the composition of the oxidizing component B at alloy/oxide interface is the same as its chemical activity at that interface, which is related to the oxidation rate. A lower interdiffusivity (between A and B) and higher initial noble metal A concentration will lead to a smaller local concentration of oxidizing component B at alloy/oxide interface, and thus a slower oxidation rate compared with the oxidation of pure metal B. The growth rate of a single-layer BO_y forming on the alloy AB, can be expressed as:

$$k_c = \left[\frac{1 - (\frac{N_B^e}{N_B^i})^{2/yn}}{1 - (N_B^e)^{2/yn}} \right] k_c^0 \tag{2.13}$$

where

k_c^0 – the parabolic rate constant of oxidation of pure metal B determined form measurements of loss of metallic core thickness, thus called the corrosion constant.

k_c – the corrosion constant of alloy

N_B^i – the local concentration of metal B in alloy at the oxide/alloy interface

N_B^e – the equilibrium concentration of metal B in the alloy, and it may be calculated on the basis of the equation, $N_B^e = (p_{O_2}^r/p_{O_2}^a)^{y/2}$

$p_{O_2}^r$ – the dissociation pressure of BO_y

12

$p_{O_2}^a$ – the oxidant pressure during alloy oxidation for which the above calculation are performed.

n – the dependence of the rate of oxidation of pure metal B (obtained from the measurement of the oxidation of pure metal B).

The only quantity in equation (2.13), which is not readily measured, is N_B^i. Assuming for simplification that the diffusion coefficient of metal B in the alloy is, in the concentration range considered, independent of alloy composition, Wagner provided another equation permitting the calculation of N_B^i.

$$N_B^i = -F\left[\left(\frac{\alpha}{2\gamma}\right)^{\frac{1}{2}}\right]\left(1 - N_B^i\right) + N_B \tag{2.14}$$

where,

N_B – the initial concentration of metal B in the alloy.

γ – the ratio of the interdiffusion coefficient to the corrosion constant of pure metal B ($\gamma = D/k_c^0$)

α – the ratio of the corrosion constants of alloy and metal B ($\alpha = k_c/k_c^0$)

and $F(u) = \pi^{\frac{1}{2}}u[1 - \text{erf}(u)]\exp(u^2)$.

In some cases, multi-layer oxide scales may be expected due to interface wrinkling, which is considered a result of the initial roughness and a much higher diffusivity of metal ions in the oxide scale compared to the diffusivity of metal ions in the alloy [17].
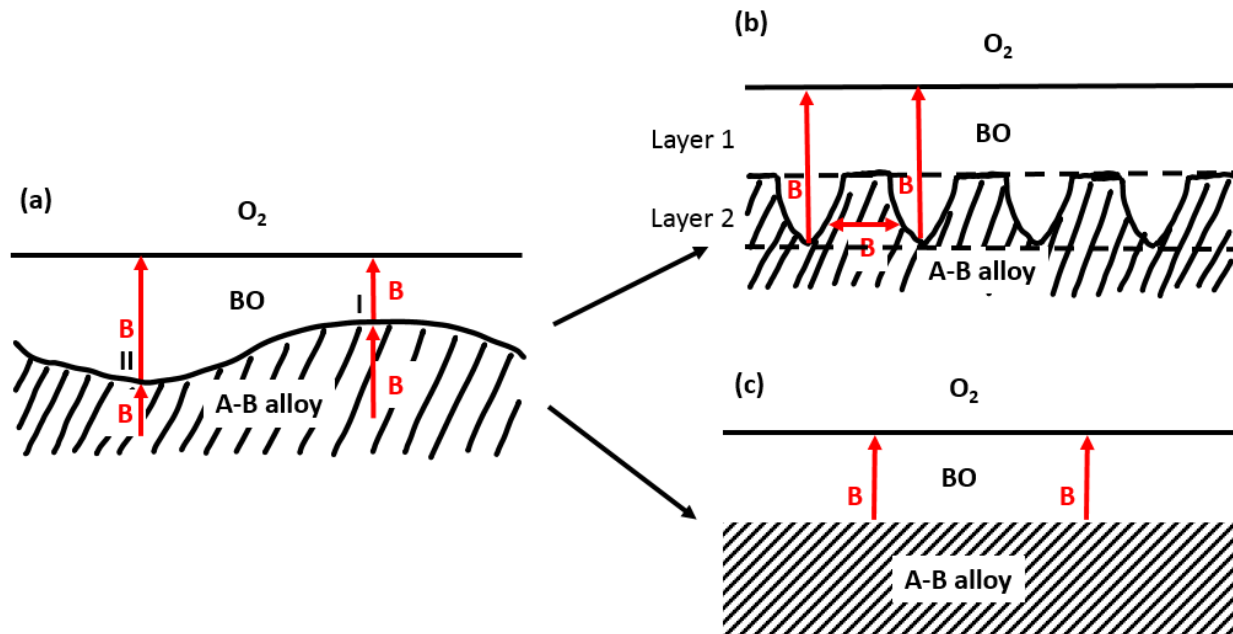
Figure 1.2.3 (a) The initial oxide scale of BO with a slight perturbations on the oxide/metal interface. (b) Double layer scale formed in the system where the diffusion of B in the alloy is the slowest process. (c) Single phase scale with plane interface formed in the system where the diffusion of B in the oxide is the slowest process.

In accordance with Wagner's model for the oxidation of alloys containing only one oxidizing component, slight perturbations always exist on a nearly planar oxide/metal interface during the earlier stages of oxidation, as shown in Figure 1.3 (a), and the initial roughness of oxide/metal interface may be flattened or enlarged depending on the dominant diffusion process. If the diffusion of B through the oxide scale is the slowest process, the consumption of metal at point II will be slower than point I due to the longer diffusion distance of B through the BO scale. Consequently, a single-layer, planar oxide scale will be established at the oxide/alloy interface, as shown in Figure 1.3 (c). On the other hand, if the slowest process is the metal B diffusion in the alloy, the consumption of metal at point I will be slower due to the less supply of B, and finally, a double-layer scale will be formed as shown in Figure 1.3 (b). This model shows quite good

14

agreement with the oxidation experiments on certain alloys, such as the sulfidation of Cu-Au alloys.[46, 47]

1.1.2.3 **Both AO$_x$ and BO$_y$ are thermodynamic stable and their Gibbs free energies are not significantly different**

This category is represented by alloys AB in which both A and B can form thermodynamically stable oxides AO$_x$ and BO$_y$, and the formation energies of AO$_x$ and BO$_y$ are not significantly different (e.g., Ni-Cu systems forming Cu$_2$O and NiO). Due to the existence of multiple oxide phases, a competitive oxidation and/or multi-phase scale formation are typically observed for this group [1].

Based on the oxidation behavior, these type of AB alloys can be separated into two categories: 1) exclusively AO$_x$ or BO$_y$ formation; and 2) formation of a mixture of AO$_x$ and BO$_y$ [15]. Mathematical solutions for both cases, which will be discussed below, were established by Wagner [15, 16].

In both cases, a thermodynamic equilibrium should be reached at the oxide/alloy interface according to the steady-state assumption, so the local equilibrium of the reaction $A + \frac{x}{2}O_2 = AO_x$ and/or $B + \frac{y}{2}O_2 = BO_y$ must be established at the interface. Based on equation (2.12), those two equilibrium conditions can be expressed,

$$(N_A^i)^{2/x} p_{O_2}^i = \exp(\frac{\Delta G_{AO_x}}{RT}) \tag{2.15}$$

and

$$(N_B^i)^{2/y} p_{O_2}^i = \exp(\frac{\Delta G_{BO_y}}{RT}) \tag{2.16}$$

where

N_A^i and N_B^i – location concentrations of metals A and B at oxide/alloy interface.

$p_{O_2}^i$ – oxygen partial pressure at the oxide/alloy interface.

When a critical concentration of B N_B^{i*} in the alloy AB is reached, below which AO_x is more stable than BO_y, both thermodynamic equilibria described above will be established. Since oxygen partial pressure $p_{O_2}^i$ is the same in both equations, it can be eliminated. Based on the fact that the alloy is only composed of A and B, another equation can be obtained, $N_A^i + N_B^i = 1$. With known formation energies of the AO_x and BO_y, an equation containing only a single unknown N_B^{i*} can be derived.

$$\frac{(1 - N_B^{i*})^{2/x}}{(N_B^{i*})^{2/y}} = \exp(\frac{\Delta G_{AO_x} - \Delta G_{BO_y}}{RT}) \qquad (2.17)$$

The calculation of N_B^{i*}, which represents the critical concentration of B at the alloy/oxide interface for the BO_y formation during the oxidation, is permitted by solving the above equation.

Upon substituting N_B^{i*} in equations (2.13) and (2.17), a minimum initial concentration N_B^* of B, above which exclusive BO_y formation should be expected, can be obtained as below,

$$N_B^* = N_B^{i*} + (1 - N_B^{i*})F[(\frac{1 - (N_B^e/N_B^{i*})^{2/yn}}{2\gamma(1 - N_B^{e\frac{2}{yn}})})^{1/2}] \qquad (2.18)$$

The predictions made using this theory find some good agreements with the experimental oxidation results [19]. For instance, the formation of a single-phase NiO scale on a Cu-Ni alloy at 950°C, in air requires at least 75at.%Ni according to the prediction based on above theory. While the oxidation experiments of Cu-Ni alloys under the same oxidation condition show that alloys containing over 80at.% Ni forms a homogeneous compact NiO scale [19].

For the cases when both AO_x and BO_y form on the surface, the mathematical solution is much more complex. For a simplification, it was assumed by Wagner that outward diffusion of a certain metal cation can only be through its own oxide phase (A diffuse through AO_x, B diffuse

through BO_y), as shown in Figure 1.4 [16]. Even with such a simplifying assumption, the formula provided by Wagner, which permits calculation of dependence of the scale chemical composition and the thickness of individual scale layers on the alloy composition, involve a considerable number of varied parameters and are very complicated. Due to the complexity of the mathematical solution and the strict assumption regarding the diffusion paths for cations and anions, Wagner's theory for heterophasic scale formation is only valid for a limited number of systems [34, 44, 46, 48, 49].
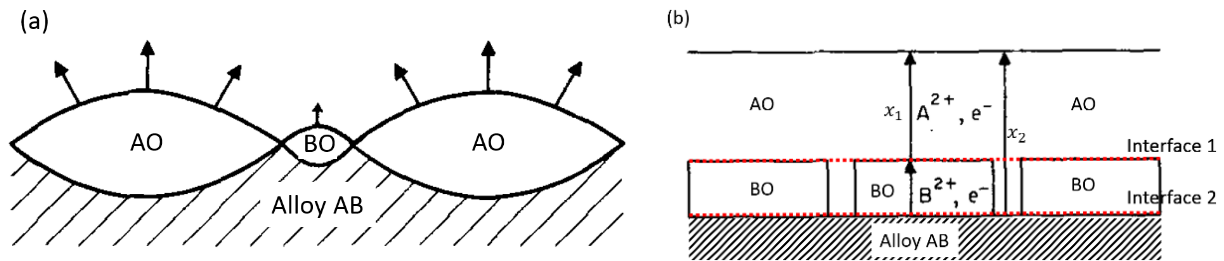
Figure 1.2.4 (a) Initial stage of oxidation of an alloy AB, when both AO and BO nucleated on the surface. (b) Schematic cross-section of the scale of an alloy AB with an outer layer of AO and an inner two-phase layer of AO and BO.

1.1.2.4 Both AO_x and BO_y are thermodynamic stable and their Gibbs free energies differ significantly

Within the last group, both components A and B can react with the oxygen and form their stable oxide AO_x and BO_y (e.g., Ni-Al systems forming NiO and Al_2O_3), and the formation energy of one oxide differs significantly from the other, $\Delta G_{AO_x} >> \Delta G_{BO_y}$. It is further assumed that the more noble metal A reacts with oxygen considerably faster than B. During the oxidation of these type of alloys, either a protective scale or non-protective scale coupled with internal oxidation, during which isolated BO_y particles precipitate in the alloy instead of growing externally, may

form [1]. For the simplification, Wagner assumed that the two oxides AO_x and BO_y do not form a solid solution or react with each other.

Considering the minimum concentration of B in the alloy for the formation of a protective oxide film composed exclusively with BO_y, Wagner provided a criterion based on maintaining the growth of BO_y, using the same diffusion model for the oxidation of binary alloys in other two categories [15, 16, 50].

$$N_{B(min)} = \frac{1}{M_O z_B C} \left(\frac{k''_{p(B)}}{D} \right)^{1/2} \tag{2.19}$$

where

M_O – atomic weight of oxidant.

z_B – valence of metal B in BO oxide.

C – number of metal gram atoms in unit alloy volume.

D – interdiffusion coefficient.

$k''_{p(B)}$ - corrosion constant of pure metal B.

The above criterion only leads to a minimum concentration of B to sustain the growth of a protective scale assuming the exclusive external growth of BO_y film. It is not applicable for the initial establishment of a scale due to the possible internal oxidation.

Knowing the limitation of the first criterion, Wagner developed another theory for internal oxidation and the transition from internal to external oxidation [51]. In this theory, the depth ξ of the internal oxidation zone is assumed to follow a parabolic rate law, which can be expressed as

$$\xi^2 = 4\gamma^2 D_O t \tag{2.20}$$

where

D_O – the diffusion coefficient of oxygen in the alloy.

γ – a dimensionless parameter related to parabolic rate constant for internal oxidation.

Equating the outward diffusion of B cations with the inward diffusion of O anions at internal oxidation front, Wagner obtained an equation, which permits the calculation of γ.

$$\frac{2N_O^s}{z_B N_B^0} = \frac{\exp(\gamma^2)\,\text{erf}(\gamma)}{\varphi^{\frac{1}{2}}\exp(\gamma^2\varphi)\,\text{erfc}(\gamma\varphi^{\frac{1}{2}})} \tag{2.21}$$

where

N_O^s – the mole fraction of O_2 dissolved in the alloy in equilibrium with the partial pressure of oxidant prevailing in the gas.

N_B^0 – initial mole fraction of B in the alloy.

φ – the ration D_O/D_B. D_B is diffusion coefficient of B in the alloy

erf (r) and efrc (r) - effort function and complementary error function.

Wagner also proposed that the transition from internal to external oxidation of B is related to a critical volume fraction of internal BO_y oxide, f_v^*, above which the permeability of oxygen is decreased to certain level that BO_y forms a protective layer and the internal oxidation stop. Based on the above assumptions, an equation can be derived to calculate the minimum concentration of B in the alloy that is needed for the transition from internal to external oxidation of BO_y.

$$N_B^{0*} = \frac{1}{\rho} f_v^* F(\gamma\varphi^{\frac{1}{2}}) \tag{2.22}$$

Equation (2.22) is considered as the second criterion for the external exclusive BO_y formation.

Following the work of Wagner [14], Boehm and Kahlweit [52] introduced the concept of supersaturation, which complemented Wagner's theory regarding the internal oxidation. Gesmundo et al. [42, 45, 52, 53] extended the analysis of alloy oxidation in this category to multi-phase scale formation, including the internal oxidation of B coupled with external oxidation of A.

19

1.2   PRECURSOR STAGE OF OXIDATION

Study of the precursor stage of oxidation typically utilizes surface science techniques and computational simulations, and focuses on the initial reaction between oxygen and bare metals or alloys [4, 10, 23, 24]. In real-world applications, the precursor stage of oxidation are either too complex to characterize or too short to capture. Therefore, studies regarding the precursor stage are typically conducted in ideal conditions (model systems), such as ultra-high vacuum, an atomically clean metal/alloy surface and in a limited temperature range (usually 0°C ~ 200°C).

The precursor stage of oxidation involve several processes before the formation of a three-dimensional oxide, namely, physical adsorption, chemisorption, dissolution (or absorption) and possible surface reconstruction (or formation of sub-oxide). All these processes will be discussed in the following sections.

1.2.1   Physical adsorption and chemisorption

Physical adsorption is a process in which oxidant molecules are attracted to a surface by long-range forces and stick to that surface in a non-activated state [54]. Since there is no change of chemical bonds between atoms, no activation energy is needed for this process. Lower temperature and/or higher pressure usually result in a higher physical adsorption rate [55]. By contrast, chemisorption involves a dissociation of oxidant molecules into constituent species, which usually requires an activation energy. The interaction of a bimolecular molecule, such as O_2, with a metal surface may be illustrated by the potential energy diagram as shown below (Figure 1.5) [54].
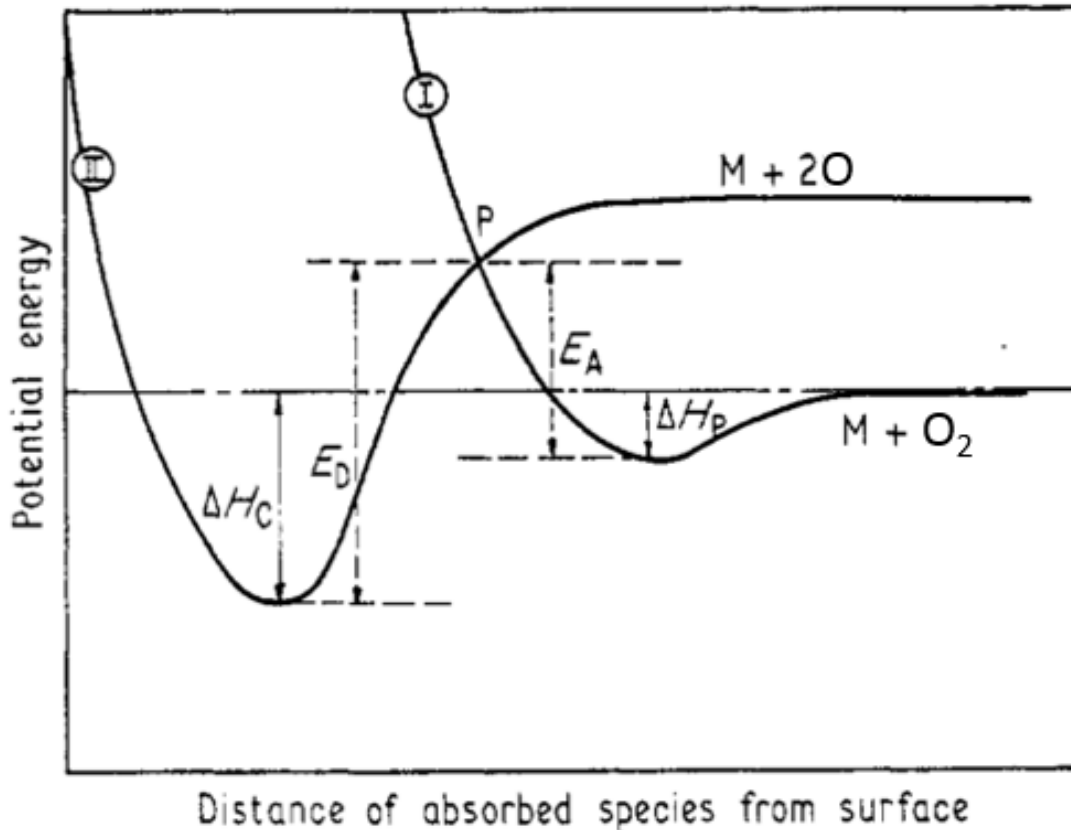
Figure 1.2.5 Schematic potential energy diagram for the interaction of an oxygen molecule with a metal substrate. Curve I and II represent the physical adsorption and chemisorption. E_A and E_D are activation energies for chemisorption and desorption respectively. ΔH_C and ΔH_P are heats of chemisorption and physical adsorption respectively.

Here it is seen that if the point of intersection P is above zero, an activation energy E_A will be required for the molecule to switch from curve I (physical adsorption) to curve II (chemisorption). It is further seen in Figure 1.5 that a higher energy, E_D, is needed for desorption of the chemisorbed oxygen to occur.

1.2.2   Surface reconstruction and dissolution of oxygen

A surface reconstruction or oxygen dissolution may occur following the chemisorption of oxygen [10, 56-58]. Surface reconstruction is a rearrangement of the surface layer of atoms, which consists of both metal and oxygen ions, to minimize the surface energy. It usually occurs at lower temperatures (e.g., room temperature), and is also considered as the formation of "sub-oxide", which has the oxygen-metal bond but not the crystalline structure of the oxide [2]. Dissolution of oxygen, which usually occurs at an elevated temperature, is believed to be critical for the initial nucleation of oxides. It was proposed by Mitchell and Lawless [57] that oxygen will continuously dissolve into the alloy until the oxygen concentration near the surface reaches a critical value, and then oxide nuclei form immediately by a precipitation process due to the supersaturation of oxygen. This dissolution process is experimentally supported by the observation of an induction period, during which oxidation does not occur after the introduction of oxygen into the system [57-59].

1.3   NUCLEATION-AND-GROWTH STAGE OF OXIDATION

A surface reconstruction or oxygen dissolution may occur following the chemisorption of oxygen [10, 56-58]. Surface reconstruction is a rearrangement of the surface layer of atoms, which consists of both metal and oxygen ions, to minimize the surface energy. It usually occurs at lower temperatures (e.g., room temperature), and is also considered as the formation of "sub-oxide", which has the oxygen-metal bond but not the crystalline structure of the oxide [2]. Dissolution of oxygen, which usually occurs at an elevated temperature, is believed to be critical for the initial

nucleation of oxides. It was proposed by Mitchell and Lawless [57] that oxygen will continuously dissolve into the alloy until the oxygen concentration near the surface reaches a critical value, and then oxide nuclei form immediately by a precipitation process due to the supersaturation of oxygen. This dissolution process is experimentally observed by May and Germer [58].

1.3.1 Nucleation-and-growth stage of oxidation for pure metals

1.3.1.1 **Nucleation of oxides**

During a heterogeneous nucleation processes in a solution or solid matrix, there will a nucleation barrier associated with the formation of oxide nuclei, which is determined by the changes in Gibbs free energy ΔG.[60, 61]

$$\Delta G = V\Delta G_V + \sum_i A_i \gamma_i \qquad (2.23)$$

Where

V – the volume of the precipitate. For a hemi-spherical precipitate, $V = \frac{2}{3}\pi r^3$.

ΔG_V – the free energy change per unit volume accompanying the chemical reaction.

A_i and γ_i – the interface area and corresponding interfacial energy of each interface.

At small values of r, surface area term A_i, which is proportional to r^2, is more important than the volume term V, which is proportional to r^3, however, at larger values the reverse is true. The general shape of the ΔG curve is represented schematically in Figure 1.6 based on a negative value for ΔG_V and positive ones for γ_i (a negative ΔG_V corresponds to a volumetric thermodynamic driving force existing for the reaction).
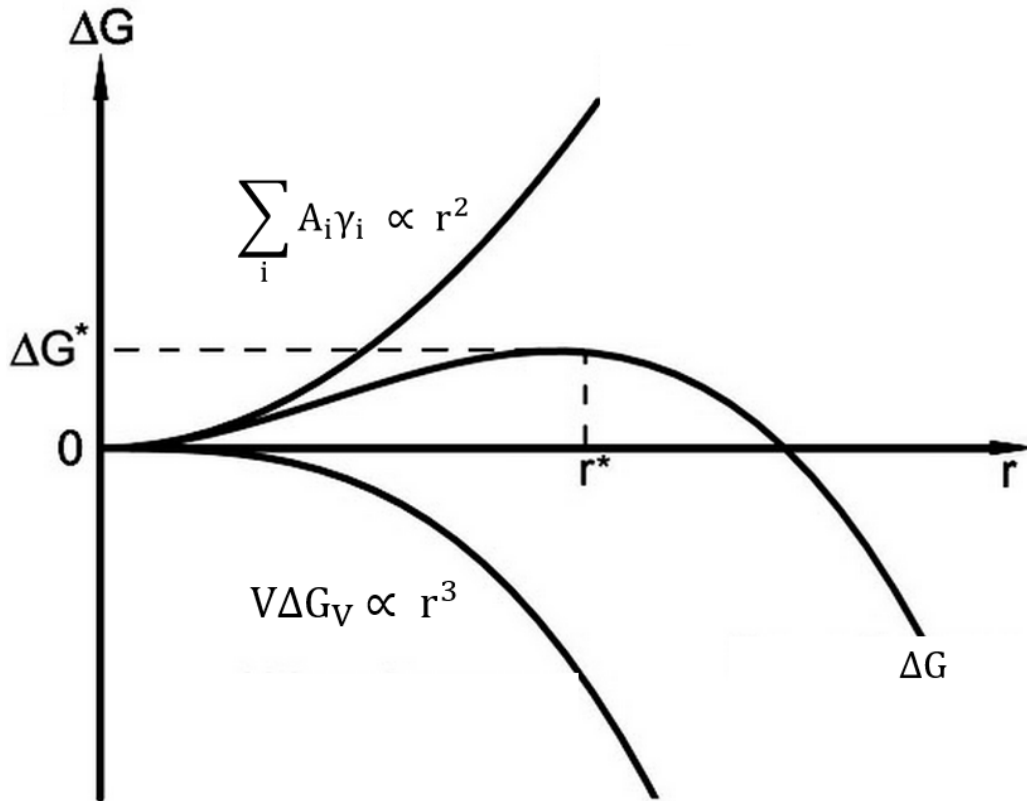
Figure 1.2.6 Free energy of spherical nucleus formation.

As shown in Figure 1.6, for $r < r^*$, a nucleus is unstable due to the increase of free energy during the growth, whereas for $r \geq r^*$, free energy will be reduced by the growth of precipitate. Therefore, r^* is known as the critical nucleus size, and the associated free energy ΔG^*, is the nucleation barrier to overcome for the formation of a stable oxide nucleus.

The nucleation-and-growth stage of oxidation is initiated by the nucleation of oxides on the surface following a supersaturation of oxygen in the metal [57]. Oxidation is slightly different from the general nucleation process that occurs in a solution or a solid matrix. Specially, during oxide formation on a metal surface, the original gas/metal surface is replaced by a gas/oxide surface and an oxide/metal interface. Therefore, the interfacial energy term γ_i in equation (2.23) needs to be replaced with a change of interfacial energy $\Delta\gamma_i = \gamma_{gas/oxide} + \gamma_{oxide/metal} -$

24

$\gamma_{gas/metal}$. In most situations involving the formation of a new oxide on the surface, where $\Delta\gamma_i >$ 0, interfacial energy tends to introduce a barrier to nucleation. However, in some special cases, such as the oxidation of Cu [62] and Fe [63], $\gamma_{gas/metal}$ is higher than $\gamma_{gas/oxide} + \gamma_{oxide/metal}$, hence, $\Delta\gamma_i < 0$; consequently, the surface-energy term contributes to the thermodynamic driving force for the formation of oxide.

Since surface energy depends on the crystal orientation of the surface and local conditions [64], the thermodynamic driving force for nucleation will consequently vary on the surface of multi-orientation systems. Even on a single grain of metal surface, the surface energy can vary due to surface roughness and/or defects [60]. Surface or interfacial defects tend to lower the surface energy, and are generally considered as preferred nucleation sites for an oxide [28, 65, 66], so that surface finish of a metal, which affects the surface defects, could have a great impact on the nucleation of oxides.

Besides the change of thermodynamic driving force resulting from the surface-energy term, many other aspects of nucleation have been investigated. It was shown by Zhou et al. [31, 67] that the nucleation rate and the epitaxial relationship between an oxide and the substrate are controlled by the supersaturation of oxygen. A higher environmental oxygen partial pressure will lead to a higher degree of oxygen supersaturation and, consequently, a higher nucleation rate and more randomly oriented nuclei will be expected to form on the surface.

1.3.1.2 **Growth of oxide nuclei**

Following the nucleation of a stable nucleus, the growth of the oxide should be expected. During this period, the individual nuclei are often called oxide islands before the coalescence. When the supply of oxygen is sufficient, a continuous layer of oxide may quickly develop after

25

the initial formation of dense nuclei, and the oxidation will proceed into the scale-establishment stage without a noticeable growth period. On the other hand, if supply of oxygen is the limiting step for the whole oxidation process, lateral growth of oxide nuclei will be observed [25, 26, 68, 69].

A detailed model regarding the lateral growth of oxide nuclei has been proposed by Orr [27], taking into account such processes as the sticking, surface diffusion and capture of the oxygen atoms. As shown in Figure 1.7, a portion of oxygen molecules impinging on the surface can be adsorbed, while adsorbed oxygen may also undergo a desorption process. Theses adsorption and desorption processes lead to an equilibrium oxygen concentration on the surface away from the reaction zones, where oxide islands are growing. When the supply of oxygen is limited (oxygen partial pressure is low), the growth rate of an oxide island will tend to depend on the surface diffusion of oxygen atoms. During the growth of an oxide island, the diffusion and consumption of nearby oxygen may decrease the degree of oxygen supersturation on the surrounding surface, and thus, lead to a much lower possibility of forming new nuclei in the local area. This can create what is termed an oxygen-capture zone [70]. The average size of oxygen capture zones on a metal surface under a specific oxidation condition can be estimated experimentally from the inverse of saturation nucleation density [71].
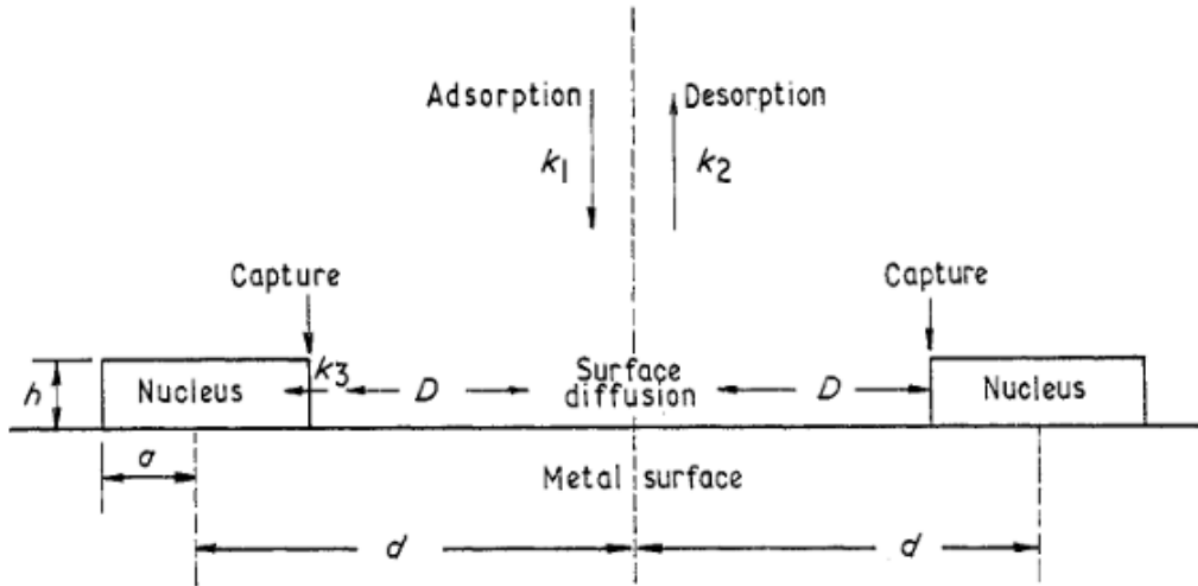
Figure 1.2.7 Model for growth of oxide nuclei on a metal surface. k_1 and k_2 are rate constants for adsorption and desorption, respectively, of oxygen molecules, k_3 is the rate constant for capture of adsorbed oxygen by the oxide island, D is the surface diffusion constant for adsorbed oxygen molecules, a is the radius for the oxide nucleus, h is the height of the nucleus and d is the centerline distance between oxide nuclei [2].

1.3.2   Nucleation-and-growth stage of oxidation for alloys

In order to minimize complexity, most studies of nucleation-and-growth stage of oxidation are based on the alloys containing a single oxidizing component (e.g., Cu-Au alloys), and trying to gain insight into the impact of noble metals on the nucleation barrier and morphology of the oxide islands [30, 72-74].

If an oxide island is coherent with the alloy matrix, then the degree of oxide/alloy lattice mismatch is proportional to the interfacial energy and, hence the nucleation barrier [30, 68]. It was found by Zhou et al. [30] that the addition of Au into Cu decreases the lattice mismatch between the oxide and matrix, and consequently decreases the nucleation barrier. The morphology change of an oxide island due to the addition of a noble metal into the base metal is more complicated. It

27

not only depends on the interfacial energies but also the diffusion of metal atoms surrounding an oxide island as shown in Figure 1.8. An enrichment of Au around an oxide island was observed during the oxidation of Cu-Au alloys, which allows the oxide to grow deeply into the alloy or follow a dendritic-like growth on the surface [72, 73]. On the other hand, an enrichment of Pt beneath an oxide island was observed during the oxidation of Cu-Pt alloys and was found to increase the thickness of a given island easier via protruding above the alloy/oxide interface [73]. The different oxidation behavior between Cu-Au and Cu-Pt alloys is apparently related to the diffusion path of both metal and oxygen atoms (in the Cu-Au system lateral diffusion of Cu seems much faster, while Cu-Pt system follows a primary outward diffusion of Cu), which is still not well understood.
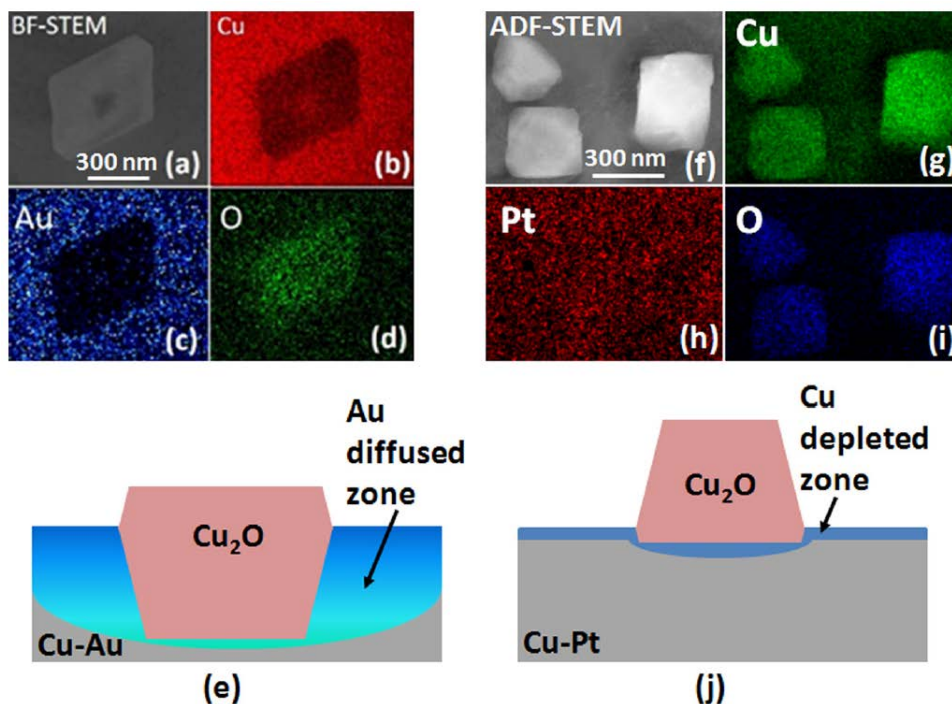
Figure 1.2.8 EDX elemental mapping of oxide islands formed on (a)–(d) Cu-10at.%Au (100) and (f)–(j) Cu-10at.%Pt (100) under the condition of 450°C and $P_{O_2} = 5 \times 10^{-4}$ Torr. (e) and (j) Show schematic of oxide growth model on two alloy, respectively [73].

Although the nucleation-and-growth stage of oxidation for alloys containing more than one oxidizing component presents a high level of complexity, previous studies of those alloys still reveal some fundamental mechanisms regarding the selective oxidation process. For instance, the observation of a nanoscale duplex oxide island (containing both Cu_2O and NiO) during the oxidation of Cu-Ni alloys indicates a local depletion of Ni near the surface and a possible surface diffusion of Cu, as shown in Figure 1.9 [29].
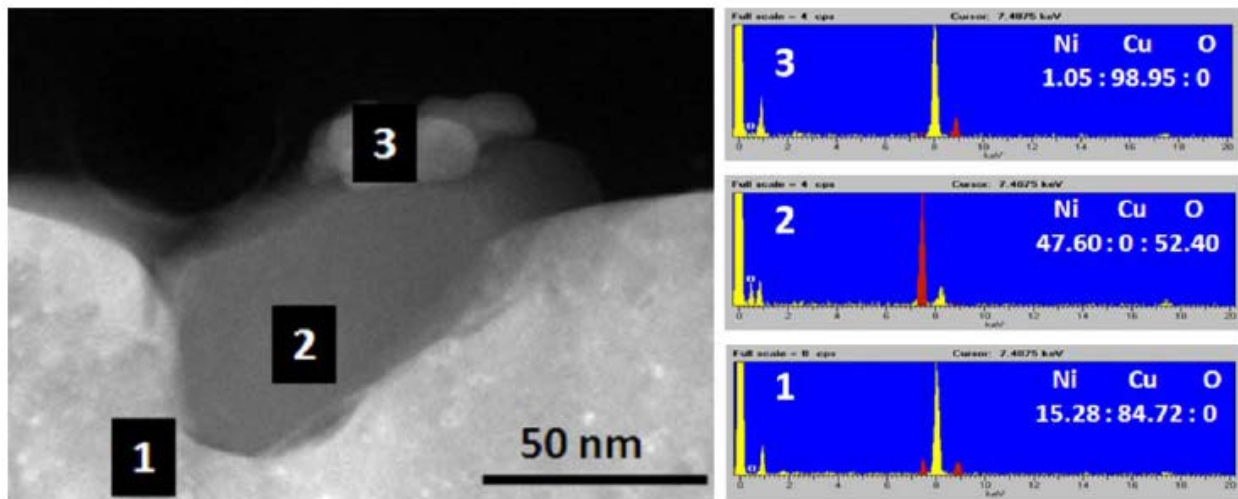
Figure 1.2.9 Elemental analysis of the composition of different regions of the Cu-Ni sample. Quatification of the EDS data indicates that region 1 has a Ni/Cu ratio of ~15.28/84.72 (close to the initial composition), and region 2 has a Ni/O ratio of ~47.6/52.4 (almost pure NiO), and region 3 is almost pure Cu [29].

The formation of such duplex oxide island during nucleation-and-growth stage involves both surface diffusion of oxygen and lattice diffusion of metal cations driven by chemical potential. The combination of Orr's theory regarding the oxide island growth driven by the oxygen surface diffusion and Wagner's theory regarding the selective oxidation is necessary to gain a

comprehensive understanding regarding the formation of duplex oxide islands as well as selective oxidation during the nucleation-and-growth stage.

1.4 SCALE-ESTABLISHMENT STAGE OF OXIDATION

After the initial formation of an oxide scale, it may undergo a scale-establishment stage, during which the oxidation mechanisms and/or the oxide phases may change, prior to a steady-state growth [13, 75-77]. During the scale-establishment stage, many mechanisms other than the lattice diffusion driven by chemical potential gradient, which was proposed to be most important by Wagner [15-17], may have significant impacts on the scale-forming process. These include grain-boundary diffusion, formation of metastable oxide phases and scale-structure evolution [75, 77, 78]. Studies of the scale-establishment stage should lead to a better understanding of the overall oxidation process, especially the formation of protective scales (e.g., Cr_2O_3 and Al_2O_3). This ultimately would lead to a better design of oxidation resistant alloys.

1.4.1 The scale-establishment stage of oxidation for binary alloys

As mentioned earlier, the addition of a certain amount of alloying elements, usually aluminum and/or chromium, to a base metal (e.g., Ni or Fe), can maintain the high melting point and good mechanical properties of that base metal, while at the same time dramatically increase the oxidation resistance. The study of binary alloys containing a base metal and a protective scale-forming element (e.g., NiAl) can provide basic understanding of the structural evolution of the

oxides formed during the oxidation and the transition from internal to external oxidation during the establishment of a protective layer without introducing too much complexity [77, 79-81].

In cases where non-steady-state transient oxidation occurs, the establishment of a protective scale may involve multiple processes, such as oxide phase transformation and scale cracking/healing processes [77, 80]. Since the oxides of base metals have faster growth kinetics, the initial-formed scale tends to be generally composed of these non-protective oxides [76, 79]. Following the formation of the initial oxide scale, oxygen partial pressure at the alloy/oxide interface decreases dramatically, and thus, slow growing but more stable oxides become more favorable for subsequent oxidation.

Scale-establishment processes will tend to vary with different systems. In Cr_2O_3-forming systems, a transient oxidation process usually occurs following the formation of less protective spinels (e.g., $NiCr_2O_4$) resulting from the reaction between existing base-metal oxides and newly formed Cr_2O_3 [81]. In Al_2O_3-forming systems, the scale-establishment process also involves formation of spinels, but may be more complex due to the existence of metastable alumina structures (e.g., γ-Al_2O_3), which is less protective than α-Al_2O_3 [80, 82]. For instance, a $\gamma \rightarrow \alpha$ Al_2O_3 transformation was observed on NiAl at various temperatures (from 900°C to 1100°C); the higher the temperature, the faster the transition occurred [80]. Despite many studies to understand the transition from metastable alumina structures to α-Al_2O_3, there remains some fundamental unanswered questions [83-85]. In particular, the precise conditions that determine the formation of one or another Al_2O_3 structure are still unknown.

In addition to the oxide phase transformation process, the progressive establishment of a protective scale is another possible process involved in the scale-establishment process. When the concentration of the primary protective scale-forming element is close to the critical value, below

which a continuous protective scale cannot form on the surface, a transition from internal to external oxidation may occur [75, 76, 81, 86]. This transition usually follows a progressive establishment of a protective scale, during which a protective scale forms and propagates along the internal oxidation front [75, 77, 86]. Depending on the alloy system, the healing process may follow different mechanisms.

Giggins and Pettit [87] suggested a possible scale-establishment process, which is initiated at the grain boundaries of Ni-Cr alloys, based on the rapid chromium diffusion along the alloy grain boundaries. According to the analysis of these authors, a Cr_2O_3 layer can be locally developed at grain boundaries where rapid chromium transport supplies a sufficient amount of this component to the surface. Grain boundaries intersecting with the surface can also supply chromium to the grain interiors and sustain a lateral growth of a Cr_2O_3 layer across each grain. As described above, grain boundaries act as easy pathways for chromium to diffuse from the bulk alloy to the surface. This mechanism was latter verified and elaborated by Stott et al. [77, 86, 88] from the experimental observation of the "angular-terraced" healing of Cr_2O_3 scales, as shown in Figure 1.10. The progressive scale establishment during the oxidation of Ni-15wt%Cr in 1 atm oxygen at 1025°C started from the grain boundaries, and propagated to the center of grains following a terrace pattern.
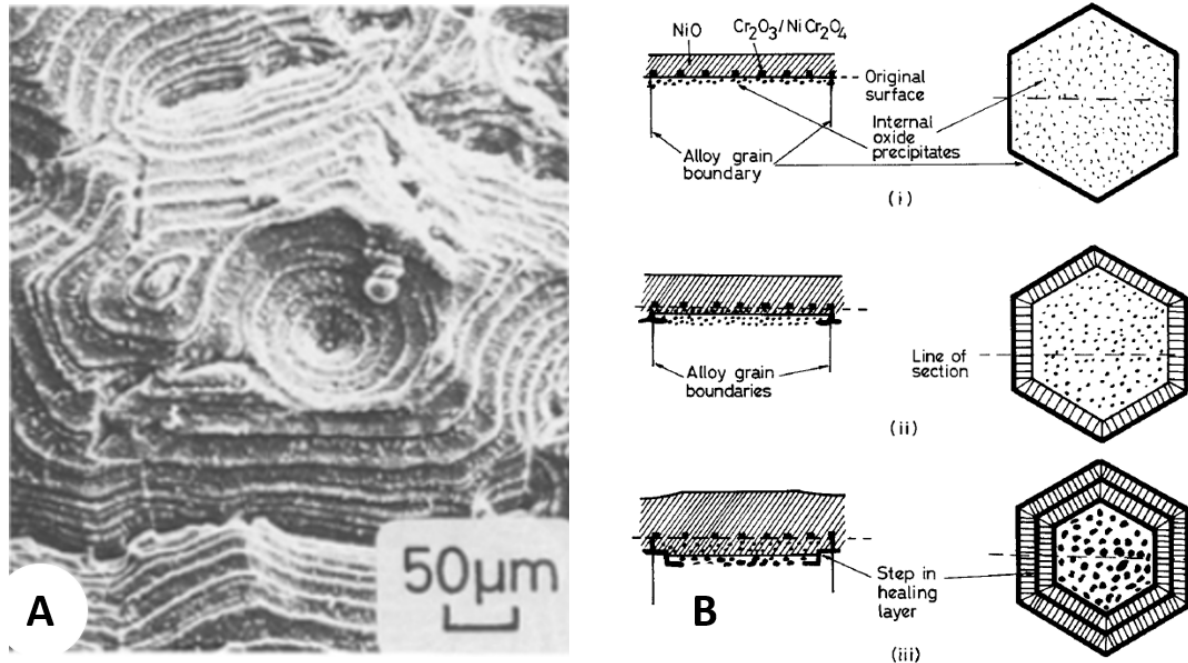
Figure 1.2.10 "angular-terraced" healing of Cr_2O_3 scales. (A) SEM image of underside of scale after 1 hour's oxidation of Ni-15wt%Cr in 1 atm oxygen at 1025°C. (B) Schematic representation of the progressive development of the healing Cr_2O_3 layer. Left side represents the cross-section view, right side represents the plan view [88].

Progressive scale establishment may not always follow a terrace pattern initiated at grain boundaries, as lateral propagation of protective scales at internal oxidation front (also termed self-healing) was also observed after a short time oxidation of Ni-20wt%Cr and a longer time oxidation of Ni-15wt%Cr [88, 89]. This lateral propagation of protective scales occurs when the velocity of penetration of the internal oxide front has slowed sufficiently to prevent nucleation in advance of already precipitated oxide particles, allowing sustained precipitate growth and coalescence [88].

This progressive scale-establishment process was not only observed in chromia forming systems, but also alumina forming systems [75, 76, 81]. Although the general behaviors of this process have been observed and studied, the initiation of such scale-establishment processes is still

not clear. Another issue that concerns the progressive scale-establishment process is how it is affected by the morphology and structure of the internal oxide precipitates.

1.4.2 Third element effect

The addition of certain elements into protective-scale forming binary systems can be beneficial for the establishment of that scale, and ultimately improves the oxidation resistance of those alloys [90-92]. For instance, for the Cu-Zn-Al system containing 29at% Zn, only 4.7at% of Al is needed for the formation of a continuous Al_2O_3 scale, which is much less than the amount of Al required (>10%) in Cu-Al binary system [50]. This third element effect was first proposed by Wagner as a "gettering effect", during which Zn (the third element) acts to "getter" the oxygen and consequently decrease the oxygen permeability into the alloy, which in turn favors the formation of an external Al_2O_3 layer [93]. According to Wagner's theory regarding the "gettering" effect, the thermodynamic stability and growth rate of the third-element's oxide must be intermediate to the base-metal oxide and the protective oxide, so that it quickly form a scale near the surface that block oxygen diffusion and reduce its flux into the alloy, consequently, promote the establishment of the protective scale. This effect was experimentally proven for Ni-15Cr-6Al (in wt%) by Pettit et al. [13, 90]. During the oxidation of this alloy at 1000°C in 0.1 atm of oxygen, NiO and Ni(Cr, Al)O_4 spinels was found to form first, followed by a mixed layer of Cr_2O_3 and Al_2O_3, and eventually a continuous layer of Al_2O_3, as shown schematically in Figure 1.11 Schematic of sequential growth of multi-layer scale on Ni-15Cr-6Al (wt%) alloy. (a) Formation of NiO and spinels. (b) Nucleation of Cr_2O_3 and Al_2O_3, (c) Formation of a continuous layer of Cr_2O_3. (d) Formation of a continuous layer of Al_2O_3.Figure 1.11.
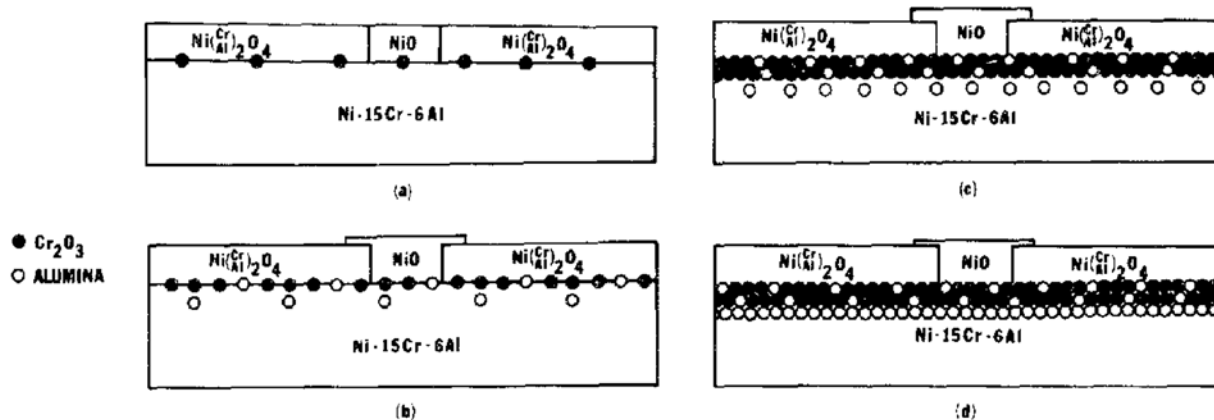
Figure 1.2.11 Schematic of sequential growth of multi-layer scale on Ni-15Cr-6Al (wt%) alloy. (a) Formation of NiO and spinels. (b) Nucleation of Cr_2O_3 and Al_2O_3, (c) Formation of a continuous layer of Cr_2O_3. (d) Formation of a continuous layer of Al_2O_3.

However, this "gettering effect" does not seem to be universal. For instance, the addition of Mn, which has the intermediate affinity between Fe and Al to the oxygen, into Fe-Al alloys may increase the critical amount of Al needed for the establishment of a protective Al_2O_3 scale [94, 95]. Jackson and Wallwork [94] determined an oxidation map for Fe-Mn-Al system at 800°C in pure oxygen at a pressure of 200 Torr, as shown in Figure 1.12. Fe-Mn-Al alloys were separated into four types depending on the oxidation behavior. Scale morphologies of alloys from region I consisted of alumina interspersed with large bulky oxide nodules. Scales formed on alloys from region II were of two types. Bulky manganese rich oxides were found in some area, while alumina scale (may spall) in other area. Region III of the oxide map was characterized by the formation of very adherent protective external scales. Alloys in region IV form alumina scales but with a penetration by small oxide nodules composed of either one or two manganese oxide phases. Generally, alloys in regions III and IV are considered oxidation resistant. It can be noticed that for the alloys containing 7-10wt% Al, the addition of more than 10wt% of Mn may decrease the oxidation resistance, which is counter to the "gettering effect" proposed by Wagner [93].

35
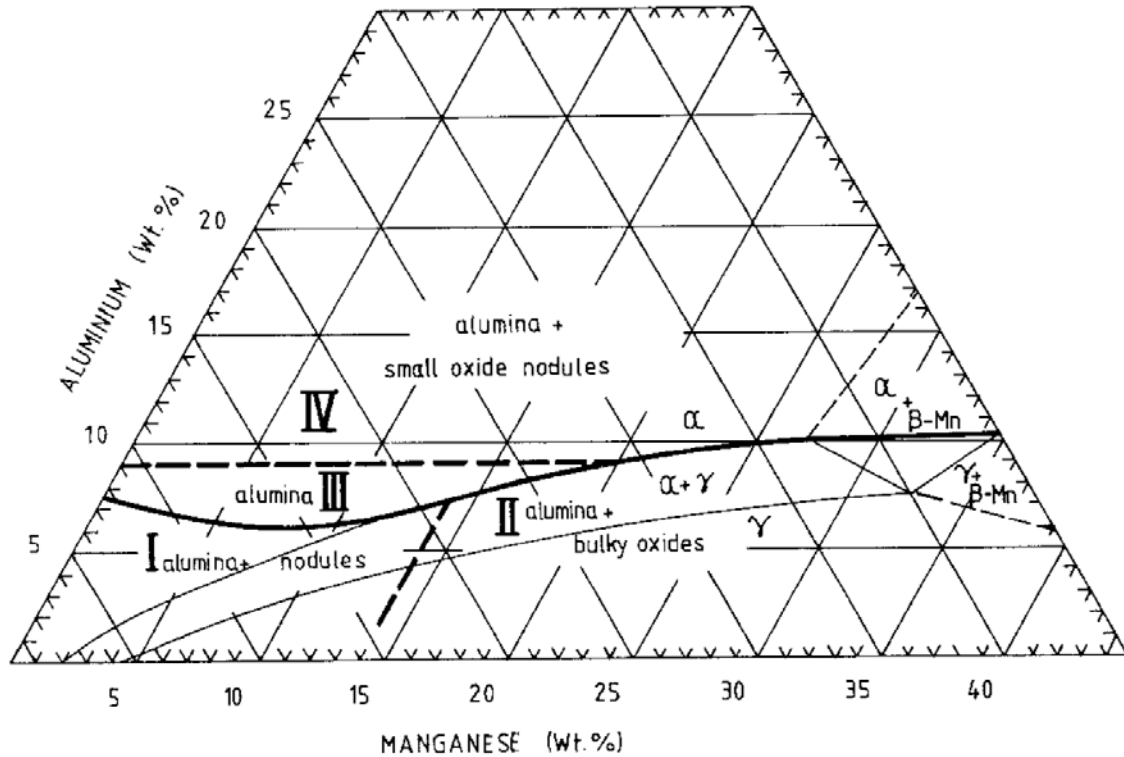
Figure 1.2.12 Oxide map for the Fe-Mn-Al system at 800°C showing the alloy phase present and the composition regions with similar scale morphologies.

This inconsistency indicates other mechanisms beside the impact on the oxygen permeability are involved in the third-element effect. Therefore, other mechanisms were also proposed for the third-element effect.

A "template" effect was proposed by several groups of researchers [96-99]. Although there is some disagreement regarding detailed process of "template" effect, it is generally believed that the formation of $\alpha-Cr_2O_3$ promoted the formation $\alpha-Al_2O_3$, which improve oxidation protection in contrast to the other transient alumina phases, due to the similar crystal structure. A "cross-turn" or "booster" effect, by which the addition of Cr increases the diffusivity of Al, was also associated with this Cr beneficial effect [91, 100, 101].

2.0   THESIS OBJECTIVES

This thesis study will consist of two parts. In the first part, competitive oxidation in nucleation-and-growth stage will be investigated. In order to focus on the fundamental mechanism of competitive oxidation without introducing too much complexity, this part of the study will be limited to single-crystal Cu-Ni thin films and low oxygen partial pressure conditions. Cu and Ni alloy to form a substitutional solid solution with complete miscibility, however, their oxides Cu_2O and NiO, which will form under relatively low oxygen partial pressure conditions, are immiscible. Moreover, the thermodynamic stabilities of Cu_2O and NiO are close to each other [33], so that, a competitive oxidation process is expected.

In the second part, the scale-establishment process of binary and ternary alloys will be studied. In particularly, the beneficial effect of Cr in promoting Al_2O_3-scale establishment during the oxidation of Ni-Cr-Al alloys will be investigated in comparison with the impact of Mn on the Al_2O_3-scale establishment during the oxidation of Ni-Mn-Al alloys. A detailed study of the effect of Cr on the meta-stable vs. stable Al_2O_3 formation and its impact on the oxygen permeability in the alloy will be presented and compared to the effect of Mn addition. The impact of kinetic factors on the scale establishment will also be assessed.

2.1 THE STUDY OF COMPETITIVE OXIDATION DURING NUCLEATION-AND-GROWTH STAGE

Competitive oxidation was studied extensively by many researchers, however, most of those results are based on steady-state studies involving a uniform layer of oxide growth on the surface under thermodynamic equilibrium conditions [1, 15, 17, 22]. The oxidation theories developed based on those studies focused on the thermodynamic stability of different oxide phases and transport kinetics of different constituents through the oxide scale or alloy. These oxidation theories cannot be applied directly to the nucleation-and-growth stage oxidation, where the thermodynamic equilibrium is not yet reach and individual oxide islands form on the surface instead of a uniform layer of oxide. Cabrera and Mott [102] tried to characterize the initial stage of oxidation by introducing other driving forces, such as electron tunneling and thermal emission, other than the electrochemical potential introduced by Wagner [14, 15, 34, 103, 104]. However, they still followed the basic assumption that the oxide grows uniformly as a layered structure, which is not always the case for early-stage oxidation. Many metals and alloys, such as Cu, Ni, Cu-Au and Cu-Ni, initially form isolated oxides on the surface. These isolated oxides are usually termed as oxide islands. Depending on the oxidation condition, the nucleation-and-growth process may last a very long time and significantly affect the microstructure of the resulting oxide scale [25, 26, 29, 31, 69, 70, 72, 105-107]. Orr [27] provided an oxidation theory to characterize the growth of individual oxide islands forming on the surface of metals based on oxygen surface diffusion. This model was adapted by many other researchers and successfully interpreted the oxidation behavior of some metals and alloys [25, 26, 29, 68]. However, most of those studies regarding the nucleation-and-growth stage are based on the oxidation of metals or alloys containing only one oxidizing component [27, 30, 69]. Therefore, a comprehensive oxidation

theory regarding the nucleation-and-growth stage of competitive oxidation, which considers both the oxygen surface diffusion and competition of different elements to the oxygen, is needed. Based on the review presented, the scientific objectives for the first part of this study can be formulated as follows:

- Assess the impact of temperature on the competitive oxidation during nucleation-and-growth stage of Cu-Ni alloy exposed to low oxygen partial pressure condition.
- Assess the competitive oxidation dependencies on temperature, oxygen partial pressure and surface condition.

2.2 THIRD ELEMENT EFFECT ON ALUMINA PROTECTIVE SCALE ESTABLISHMENT DURING ALLOY OXIDATION

The beneficial effect of Cr on alumina protective scale establishment during alloy oxidation is a special case of the so-called "third-element" effect, which was first introduced by Wagner as a "gettering" effect [93]. Generally, the addition of a third element, which has an intermediate affinity to oxygen in comparison to the other two elements in the alloy, should reduce the oxygen solubility at the oxide/alloy interface due to the formation of the stable oxide of that third element. According to Wagner's theory [51] regarding the internal-to-external oxidation transition, decreased oxygen solubility at oxide/alloy interface should be able to enhance the external scale establishment due to this "gettering" effect. However, this "gettering" effect is on the basis of two assumptions. Firstly, the diffusion of oxygen in the alloy will not change due to the addition of the third element; and secondly, the scale establishment is controlled by the second criterion of

Wagner's theory [51] not the first criterion[15, 16]. The latter criterion is for sustaining the growth of the protective oxide scale.

Those two basic assumptions in the "gettering" effect were questioned by many researchers due to inconsistency in oxidation behavior after the addition of different third elements, as discussed in the previous chapter. Additional mechanisms were proposed for the Cr beneficial effect on the alumina scale establishment, however, none of them are comprehensive [96-98, 100, 101]. Detailed kinetic understanding and experimental support for these mechanisms are still lacking, such that debate regarding the Cr beneficial effect or general third-element effect is still going on.

Based on the reviews presented, the scientific objectives for the second part of this study can be formulated as follows:

- Assess the third-element effect on Al_2O_3 phase transition based on the study of internal oxidation of Ni-Al-Cr and Ni-Al-Mn alloys.

- Illustrate the possible changes of internal oxide morphology and oxygen effective diffusivity due to the addition of a third element.

- Assess the structural and kinetic factors affect scale establishment on Ni-Al and Ni-Al-Cr alloys.

- Establish a better understanding of the "gettering" effect.

3.0   EXPERIMENTAL PROCEDURES

3.1   COMPETITIVE OXIDATION IN NUCLEATION-AND-GROWTH STAGE

In order to focus on the fundamental mechanism of competitive oxidation without introducing too much complexity, this part of the study was limited to binary alloys (Cu-Ni and Ni-Cr) and low oxygen partial pressure conditions. Both thin films and bulk alloys sample were prepared as shown in Table 3.1.

Table 3.1 Nominal composition, thickness, crystalline of binary alloys used for the study of competitive oxidation in nucleation-and-growth stage

	Composition (at%)	Thickness	Crystalline
#1	Cu-5Ni	80 nm	Single crystal
#2	Cu-5Ni	500 nm	Single crystal
#3	Ni-8Cr	500 nm	Single crystal
#4	Ni-16Cr	500 nm	Poly crystal
#5	Ni-8Cr	0.5 cm	Poly crystal
#6	Ni-16Cr	0.5 cm	Poly crystal

Thin films with various compositions were prepared by simultaneous evaporation of 99.999% pure Ni and Cu (or Cr) onto NaCl (001) substrates heated to 380°C at a rate around $4\text{Å}/s$ using Pascal dual-gun UHV e-beam evaporator. The final thickness of the thin films varies from

50 – 500nm. The films can be removed from the substrates by dissolving the NaCl in de-ionized water, and then transferred into fresh deionized water several times to remove the residual NaCl.

Bulk Ni-Cr alloys were manufactured as a dropcast bar approximately 10mm in diameter and homogenized at 1000°C for 24 hours in Ar, at Materials Preparation Center at Ames Laboratory, Ames, IA. Sample specimens, which are approximately 0.5 cm thick for the oxidation experiments, were cut from the dropcast bar. Specimens surfaces were ground (using a series of silicon carbide abrasive papers down to a 600-grit finish) and then polished to a 1μm finish. A final polishing using either colloidal-silica suspension or 600 SiC paper was conducted prior to the oxidation experiments.

In-situ (or quasi in-situ) techniques were utilized in this study to gain detailed understanding of kinetic processes in the competitive oxidation in nucleation-and-growth stage. In order to explore how environmental conditions and alloy composition affected the nucleation-and-growth stage of oxidation, experiments were carried out under a variety of temperature and oxygen partial pressure combinations using alloys with different compositions, as shown in Table 3.2.

Table 3.2 Oxidation environment for each alloy

Equipment	Alloy	Temperature (°C)	Oxygen partial pressure (Torr)
In-situ TEM	#1	350, 550, 700	5×10^{-4}
Quasi in-situ XPS	#2 - #6	600	5×10^{-7}, 5×10^{-6}, 5×10^{-5}, 5×10^{-3}

The in-situ oxidation experiments were carried out in the modified JEOL 200CX. As shown in Figure 3.1, this modified JEOL 200CX utilizes a top-entry TEM holder, which can be resistively heated to 1000°C [108]. Gas can be admitted into the column of the microscope through a leak valve from 1×10^{-5} to 760 Torr. In order to minimize contamination, a UHV chamber is attached to the middle of the column, where the base pressure is less than 10^{-8} Torr without the use

of a cryoshroud. The cryoshroud inside the microscope column can reduce the base pressure to approximately 10^{-9} Torr when filled with liquid helium. The sample holder as shown in Figure 3.1 (c), is a modified top-entry design for the in-situ heating experiments. Two metal posts were electrically insolated and used to support the special grid, which was held by clips. A given sample was heated by passing a current through the Si base of the grid, which was insulated from the metal or alloy thin films by the Si_3N_4 film in the middle.
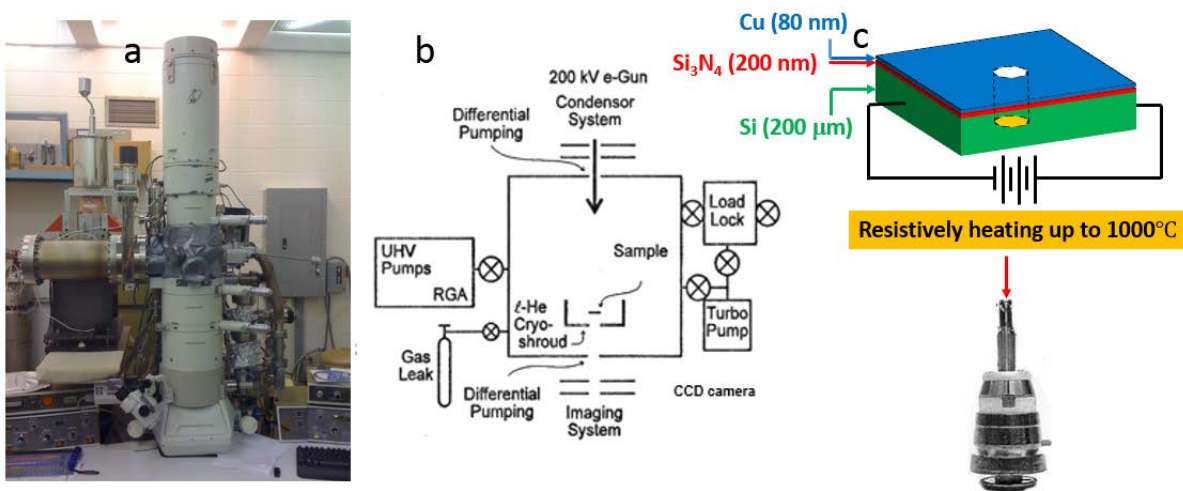
Figure 3.1 (a) The modified in-situ UHV-TEM. (b) Schematic drawing of the main elements of the system. (c) The top-entry sample holder and schematic of a thin-film sample on a grid.

There was no thermocouple attachment to measure the sample temperature in the sample holder, so it was necessary to rely on a calibration curve converting the power (P=IV) passing through the heating piece (the Si base of the grid) to actual temperature. The dissipation of heat was assumed to not significantly change with the varying size of the alloy thin films loaded on the Si_3N_4 membrane for the temperature calibration. The temperature-power relationship was obtained in two ways. One was performing a heating test inside a vacuum chamber with a thermocouple attached to the sample. The other was performing several in-situ heating or oxidation experiments

using known phase transformation or specific oxide morphology to relate some specific temperatures to the heating power, such as the Cu-Au phase transition from ordered to disordered during heating and the Cu oxide morphology change during oxidation at 5×10^{-4} Torr oxygen partial pressure at different temperatures [69]. A smooth curve connecting calibrated points on a temperature-power graph was used as the calibration curve to covert arbitrary heating power into experimental temperature.

An alloy (either bulk or as a thin film) usually forms a native oxide layer on the surface due to air exposure. Before the oxidation, the native oxide of Cu-Ni (001) film was reduced inside the TEM by annealing the film at 750°C within an Ar plus 2% H_2 gas mixture at a pressure of 5×10^{-4} Torr, as shown in Figure 3.2. To oxidize the thin films, scientific grade oxygen gas (99.999% purity) was introduced into the TEM chamber at a partial pressure of $1 \times 10^{-5} \sim 5 \times 10^{-5}$ Torr and temperature between 350°C and 700°C. A Gatan SC 1000 OriusTM CCD camera was used to capture the oxidation process in-situ.
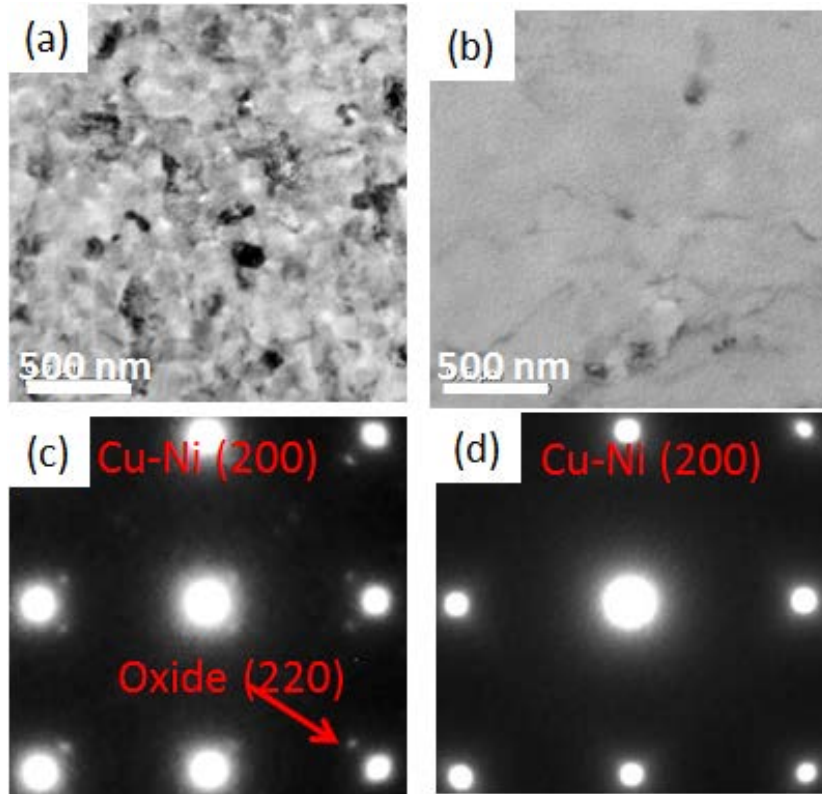
Figure 3.2 (a) is the bright field TEM image of the Cu-5at.%Ni(001) before H2 exposure where the contrast could be due to strain from the native oxide. Fig. 1(c) is the corresponding select area electron diffraction (SAED) pattern revealing the oxide formation where additional weak diffraction spots are due to the native oxide that formed during air exposure during the transport from the e-beam evaporator to the in-situ UHV-TEM. After H2 annealing in-situ, the metal alloy film is smoother and the native oxide is removed (Fig. 1b and d).

Unlike the in-situ TEM, which captures the real-time evolution of the oxide islands' morphology, the XPS system utilizes a quasi in-situ technique. During a quasi in-situ experiment, the sample position does not change during the entire experimental process (e.g., oxidation and characterization), but, in contrast to typical in-situ experiments, the experimental data is collected after an oxidation process instead of in real time.

The XPS system used in this study contains a UHV chamber equipped with an X-ray photoelectron spectrometer PECS phoibos 100 MCD analyzer and an Ar^+ ion sputtering gun. The chamber typically had a base pressure of 2×10^{-10} Torr. A non-monochromatized Al-Kα X-ray source (hν = 1486.6 eV) was used for the XPS studies. The samples were heated via a Si button heater and their temperatures were monitored with a type-K thermocouple. Either a bulk sample or an alloy thin film was mounted on Ta substrates, which were place directly on the button heater.

Similar to the in-situ TEM experiments, the Cu-Ni (001) samples were annealed in the XPS chamber at 750°C in H_2 gas to remove the native oxide. The Ni 2p peak was used to identify the formation of NiO due to the distinctive changes of the XPS spectrum (see Figure 3.3a) [109]. Since Cu_2O and Cu have similar 2p XPS spectra, Cu LMM Auger peak was used to identify Cu_2O, which has a 2eV shift from metallic Cu (see Figure 3.3b) [110, 111]. Figure 3.3 (a) and (b) show a clear shift of Ni 2p and Cu LMM peaks obtained from the XPS system after hydrogen annealing, which also demonstrates the reduction of the native oxide to its metallic state.
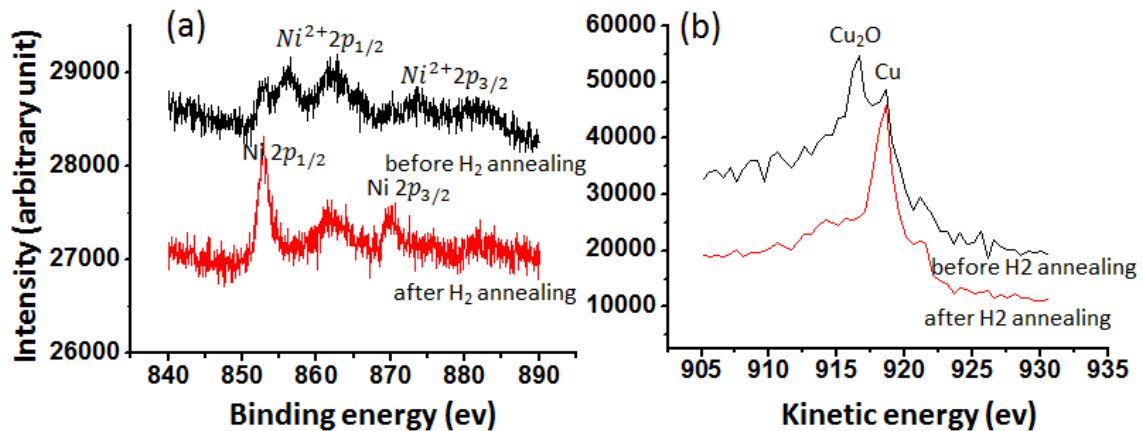
Figure 3.3 XPS data of the Cu-5at.%Ni(001) before and after H2 annealing for 1 hour at 550°C (a) The changes of Ni 2p peak after annealing indicating Ni oxides are reduced to Ni metal. (b) The shift of Cu LMM peak suggests reduction of the copper oxides to copper.

The stability of Cr_2O_3 is too high to use hydrogen annealing to remove the native oxides. Therefore, ion sputtering was used to remove the native oxides on Ni-Cr samples. Ion sputtering was carried out at room temperature, but samples were annealed at 600°C for 5 minutes after sputtering to remove the residual gas molecules. The Cr 2p peak was used to identify the formation of Cr_2O_3, which has a 2.5ev shift from metallic Cr (see Figure 3.4) [109].

Oxidation process was carried out in the XPS chamber. After obtaining clean and oxide free surface, pure oxygen gas (99.999%) was introduced to the system through a variable pressure leak valve and the samples were oxidized under a controlled P_{O_2} range from 10^{-7} to 10^{-3} Torr for a certain amount of time. After the oxygen exposure, the system was quickly pumped back to 10^{-10} to 10^{-9} in just a few seconds, and the XPS spectra was collected. A sequential oxygen exposure could be carried out to investigate the temporal evolution of the oxide scale on the surface. During the entire quasi in-situ oxidation process, samples remained at the desired operating temperature.
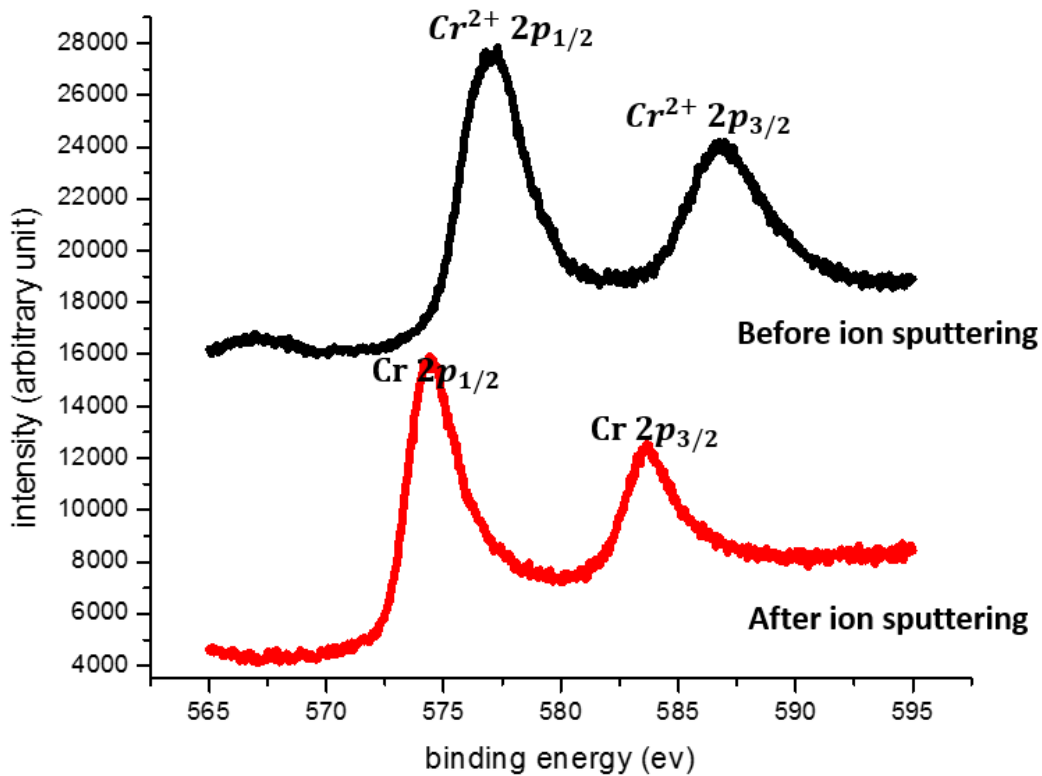
Figure 3.4 XPS data of the Ni-8at.%Cr before and after ion sputtering for 10 minutes. The shift of Cr 2p peak after annealing indicating Cr2O3 is reduced to Cr metal.

Besides the in-situ and quasi in-situ characterization, ex-situ analytic studies were also carried out using high-resolution TEM (HR-TEM) and AFM. Cross-section samples were prepaid using dual beam-focused ion beam (DB-FIB) to provide additional structure and oxide phase information.

Ex-situ analytic TEM experiments were carried out mainly using the JOEL 2100F with energy-dispersive X-ray spectroscopy (EDS), Z contrast imaging and high-resolution imaging capability. The AFM used in this study is a Veeco Manifold Dimension V with tapping mode.

Preparation of sample cross-sections was carried out using a Seiko Instruments SMI3050SE FIB-SEM in the Nanoscale Fabrication and Characterization Facility (NFCF) at

University of Pittsburgh or a Nova NanoLab 200 FEG-SEM/FIB in the Department of Materials Science and Engineering at Case Western Reserve University. A typical DB-FIB sample preparation is described as follows. After initial deposition of a 1 µm Pt protective layer onto the sample top surface, a cross-section sample was sliced out of the sample by Ga^+ ion milling. An Omniprobe was used for the sample lifting out and transferring to an Omnigrid. A final DB-FIB thinning was performed to obtain a 150~50 nm thick cross-sectional TEM sample.

3.2 THIRD ELEMENT EFFECT ON ALUMINA SCALE ESTABLISHMENT DURING ALLOY OXIDATION

As discussed in previous sections, the beneficial Cr effect is still the subject of debate. In order to provide improved understanding of this effect and the third-element effect in general, the Ni-Al-Cr, Ni-Al and Ni-Al-Mn systems were investigated. Due to the complexity of oxide phases, and the extended oxidation period, in-situ or quasi in-situ techniques were not used for this part of the study.

All the alloys investigated in this part of study were prepared the same way as Ni-Cr bulk alloys described in previous section.

The nominal compositions (at%) of those alloys are shown in Table 3.3. The positions of the Ni-Al and Ni-Al-Cr alloys on the oxidation map [90] are shown on Figure 3.5. All the alloys are single phase γ-Ni(Cr, Al, Mn) according to Ni-Al-Cr and Ni-Al-Mn phase diagram [112, 113].

Table 3.3 Nominal composition of model alloys

Alloy	Ni	Al	Cr	Mn
#1	Bal	8	3	0
#2	Bal	8	4	0
#3	Bal	8	6	0
#4	Bal	8	8	0
#5	Bal	8	0	3
#6	Bal	8	0	6
#7	Bal	8	0	8
#8	Bal	8	0	0
#9	Bal	10	0	0
#10	Bal	12	0	0
#11	Bal	14	0	0

Most ex-situ oxidation experiments were carried out in a horizontal tube furnace. The procedure consisted of placing the given specimen in the cold zone of the furnace, admitting a stream of air (working gas), waiting 15 minutes for the stabilization of the stream, and then transferring the specimen from the cold zone to the hot zone of the furnace. The time of oxidation was taken as the time the specimen entered in the hot zone of the furnace. Since some time is required for the specimen to achieve thermal equilibrium in the hot zone, a calibration of the actual sample temperature was carried out by attaching a thermo couple to a sample surface as shown in Figure 4.33. 20-second, 1-minute, 3-minute, 5-minute, 4-hour and 20-hour oxidation experiments of alloy samples of various compositions and different surface finishes were carried out. The Rhines pack method [114] was used in some heating experiments to provide a vacuum condition, under which the sample did not oxidize. In the Rhines pack method, samples were separated from Ti shavings by a neck in the silica container, which was evacuated and filled with about 0.1 atm Ar and finally sealed.
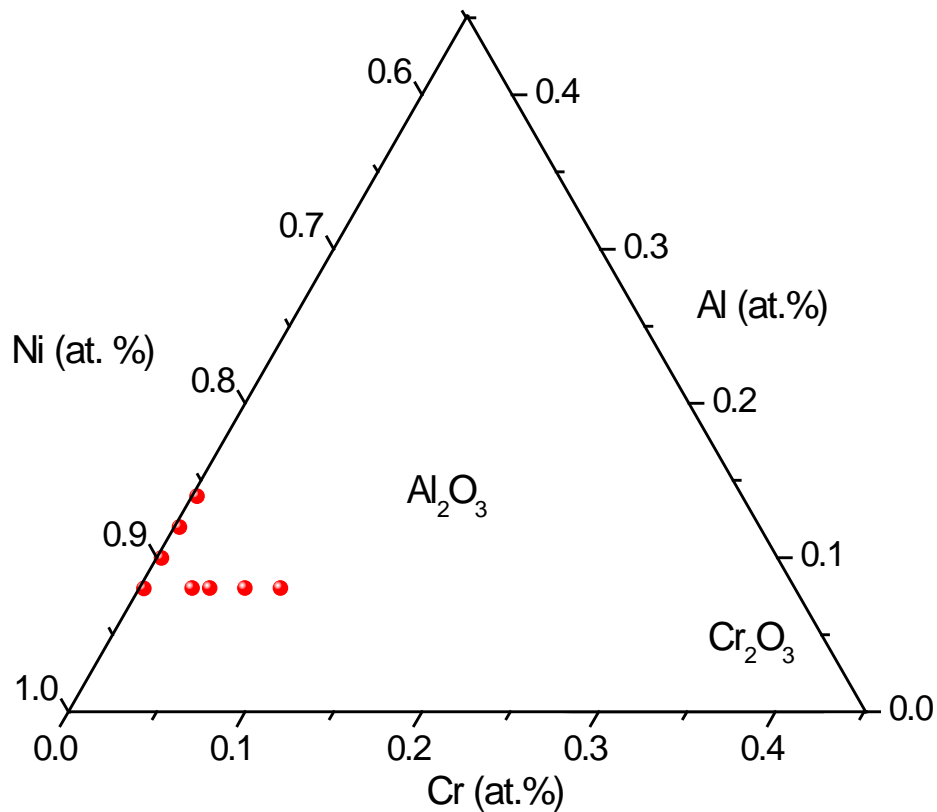
Figure 3.5 Oxidation map for Ni-Al-Cr alloys oxidized in 0.1 atm dry oxygen at 1100°C for 20h [90].

Cross-sectional samples were prepared using both DB-FIB and metallographic methods. Preparation using metallographic methods started by using a low-speed, diamond-wafer blade to cut the sample. Samples were mounted in pairs, using a low-viscosity, cold-setting epoxy, with the oxidized surfaces facing each other to avoid edge rounding during polishing. The mounted samples were wet grounded using a series of silicon-carbide abrasive papers down to a 1200-grit finish. In order to reveal the microstructure, the samples were mechanochemically polished with a commercial colloidal silica suspension (MasterMet2, Buehler, USA). Finally, the samples were ultrasonically cleaned in methanol and deionized water for 20 min and then dried with nitrogen

gas. Electropolishing was conducted for some samples to remove the alloy and reveal the 3D morphology of internal oxides.

In addition to the SEM and TEM characterization methods described in previous section, orientation and phase mapping of cross-section samples were done by using ASTAR[tm] system in the 2100F TEM. Detailed descriptions of the ASTAR[tm] system are given in a series of publications [115-117]. In brief, this system allows the scan of a chosen field of view by a nanosized electron beam, which generates an electron diffraction pattern (EDP) at each scanned spot. All the EDPs were recorded and matched against a set of pre-calculated templates, which enabled the reconstruction of virtual bright field images as well as phase maps of the chosen field of view. Morphology of internal oxidation precipitates, the progressive establishment of the protective scale, and the oxide phases in accordance with oxidation conditions and alloy compositions were investigated.

Raman spectroscopy and X-ray diffraction (XRD) were also be used to determine the oxide phases. Raman spectra and photo-stimulated luminescence spectra (PSLS) measurements of oxidized Ni-Cr and Ni-Al bulk alloy samples were performed using a micro-Raman mapping spectrometer, which was connected to a Leica microscope equipped with a 633 nm line-focus laser. The microscope stage was fitted with an automated xyz-motorized stage. Wavelength and laser intensity were internally calibrated using a silicon standard using the peak at 520 cm^{-1}. A 5X microscope objective was used to focus the spot-sized laser beam and to collect the scattered light. The laser power at the sample was 5 mW, and the acquisition time for each spectrum was in the 10-20 s and 0.5–2.0 s range for the Raman and PSLS, respectively. For some specimens a Raman and/or PSLS spectra was obtained by mapping the sample surface over a 1 mm^2 area with a pitch size of 1 μm.

The glancing angle (GA) mode of an XRD with Co-Ka radiation was used for the characterization of the crystal structure of oxide phases on the Ni-Cr and Ni-Al bulk alloy samples after oxidation. The optics included mirror parallel beam geometry, a divergence slit of ¼ mm, a soller slit of 0.5° in the incident beam side, a 0.27° parallel plate collimator, and a proportional detector photon counting solid-state pixel detector. All the GA-XRD spectra were performed at 0.5° for the incident beam.

4.0   RESULTS AND DISCUSSIONS

4.1   THE STUDY OF COMPETITIVE OXIDATION DURING NUCLEATION-AND-GROWTH STAGE

4.1.1   Temperature effect on the competitive oxidation of Cu-Ni alloys during nucleation-and-growth stage

4.1.1.1 In-situ observation of oxide islands growth

Wagner's kinetic model of parabolic oxidation [14] and multi-layer scale formation on alloys [17], as well as complementary theories developed by other researchers [44, 118, 119] reached some significant achievement in predicting the oxidation behavior of metals and alloys. However, those theories regarding the oxidation behavior of metals and alloys are only applicable for the steady-stage oxidation and miss how initial surface conditions and early stages of oxidation lead to the final oxide scale composition and microstructure; although, it is well-known that oxidation environment, surface conditions and alloy compositions dramatically impact the oxide phase and structure. Visualizing the oxidation process at the nanometer scale with in-situ

experiments provides essential insights into the complex kinetics and energetics of the early stages of oxidation.

Cu-Ni alloys were used as model alloys and expected to show less complex behavior, where Cu and Ni are complete solid-soluble down to ~300°C as shown in Figure 4.1, but Cu_2O and NiO show very limited miscibility.

Figure 4.1 Phase diagram of Cu-Ni [120].

NiO, which has the cubic NaCl crystal structure with a =4.195 Å, is thermodynamically more stable than Cu_2O, which is simple cubic with a =4.269 Å. Both oxides are thermodynamically stable in air, so depending on pO_2, temperature, surface condition and composition, either one or both components of the alloy will oxidize, thus enabling systematic determination of the effects of compositional and phase development during oxidation. Such insights into selective oxidation

55

behavior of alloys are of significant importance since multiple elements are added to materials to provide optimal performance in an oxidizing environment.

Figure 4.2 compares the morphologies of oxide islands that formed during the oxidation of Cu(001) and Cu-5at.%Ni(001) in 10^{-4} Torr pure oxygen at various temperatures for 30 minutes (Cu-5Ni oxidized at 700℃ only for 3 minutes). Since Cu_2O has a simple cubic structure whereas NiO is face-centered cubic (fcc), the appearance of (110) diffraction spots indicates Cu_2O formation. At 350℃, epitaxial Cu_2O islands with cube-on-cube orientation formed on the Cu-5at.%Ni(001) surface similar to Cu(001), but the morphology of the islands is different. Oxides with triangular morphology were formed during the oxidation of pure Cu(001), as shown in Figure 4.2a, while polyhedral oxides were observed on Cu-5Ni(001), as shown in Figure 4.2b. At 550℃, the appearance of the (220) diffraction spots without (110) diffraction spots indicate that the primary oxide phase formed on Cu-5Ni(001) under such oxidation condition is f.c.c. NiO not simple cubic Cu_2O (see the inset of Figure 4.1d). Moreover, an epitaxial relationship between oxide and the film substrate was observed to be NiO (111)//CuNi (001) and NiO (220)//CuNi (220), not cube-on-cube.
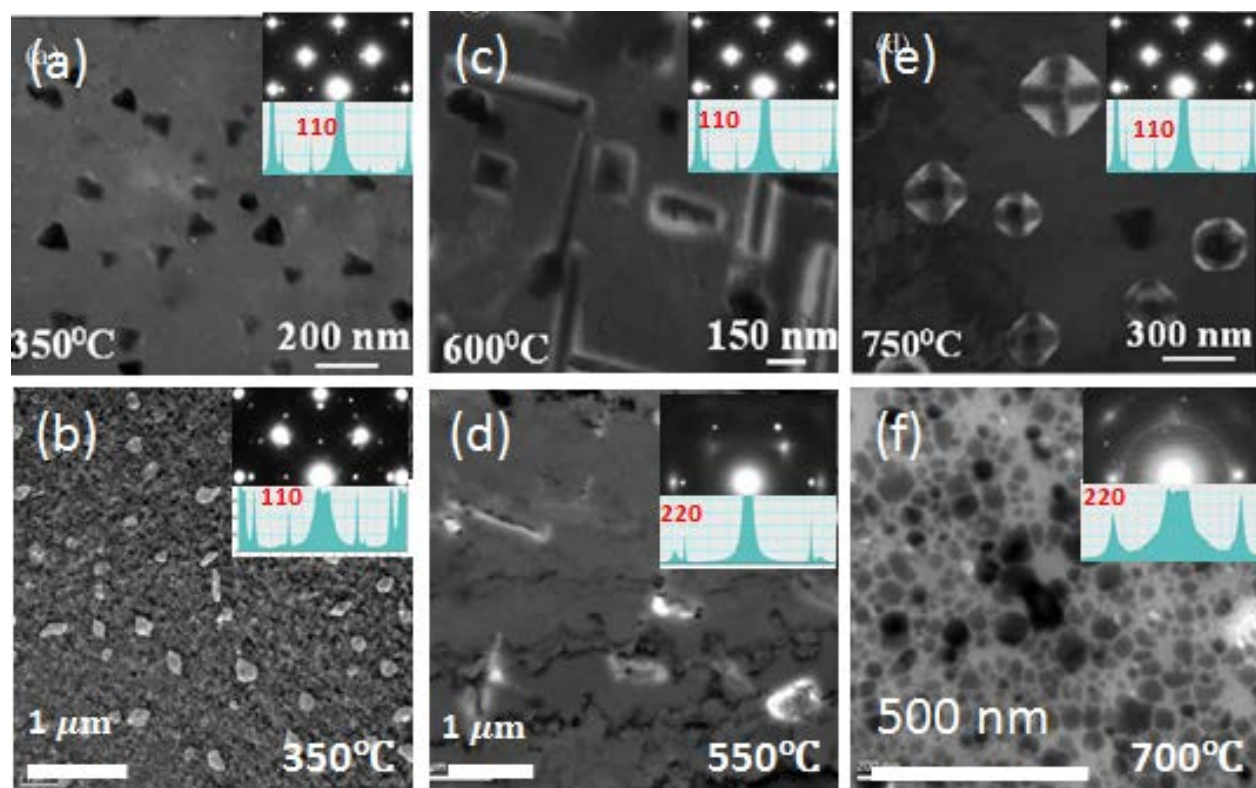
Figure 4.2 Comparison of the oxide islands formed on Cu(001) and Cu-5at.%Ni(001) film under various temperatures and pO2=5×10-4 Torr. The insets are the corresponding SAED pattern. The presence of (110) diffraction spots indicates the formation of Cu2O, otherwise, NiO formed on the surface. (a) Triangular Cu2O oxide islands formed on the Cu(001) surface at 350℃. (b) Polyhedral oxide islands formed on the Cu-5at.%Ni(001) surface at 350℃. (c) Rectangular and rod-like Cu2O islands formed on the Cu(001) surface at 600℃. (d) Polyhedral and rod-like NiO islands formed on the Cu-5at.%Ni(001) surface at 550℃. (e) Cross-hatched Cu2O islands formed on the Cu(001) surface at 750℃. (f) Dense and round NiO islands formed on the Cu-5at.%Ni(001) surface at 700℃.

At 700℃, the ring pattern of SAED identifies the predominant oxide phase as NiO, but the islands are no longer epitaxial with respect to the Cu-5at.%Ni(001) film. Langli et al. [31] reported a change of epitaxy of Cu₂O islands formed on pure Cu(001) thin films as a function of oxidizing pressure. As suggested by those authors, epitaxy is favored at low oxidizing pressures when the energy barrier to oxide nucleation is high and supply of oxygen is low; whereas, high oxygen

pressure enhances rapid nucleation and the probability for randomly oriented oxide nuclei. Comparing Figure 4.2d and f, it is evident that higher temperature can also result higher nucleation rate and density, and this rapid nucleation results in non-epitaxial NiO formation.

Since Cu_2O and NiO have similar lattice parameters, one can only rely on the absence of weak (110) diffraction of f.c.c. NiO to distinguish it from simple cubic Cu_2O using electron diffraction. This technique is not accurate enough to detect the presence of a small amount of NiO or Cu_2O. Therefore, ex-situ analytical TEM was used to detect the minor oxide phase formed on the surface. Figure 4.3a is a bright field TEM image of a Cu_2O island formed on Cu-5Ni oxidized at 350℃ in 10^{-4} Torr pure oxygen for 30 minutes, in which some small particles with dark contrasts were observed. An EDS line scan was conducted across a particle with darker contrast, as indicated by a dotted line marked in Figure 4.3a. According to the EDS data shown in Figure 4.3b, there is an increase in Ni concentration at the small particle, suggesting that it is either Ni or NiO. Due to the low sensitivity of EDS for light elements such as oxygen, and the existence of Cu_2O, it is difficult to separate Ni and NiO particles. To counter this limitation of EDS, additional quasi in-situ XPS characterization was carried out. Ni 2p XPS spectrum was taken after 3 and 120-minute oxygen exposure at 10^{-4} Torr and 350°C, where a significant NiO peak was noted after only 3 minutes, and no metallic Ni was detected by XPS after 120 minutes. XPS confirmed the formation of NiO at 350°C after short-time exposure to the oxygen, consequently, the small particles containing Ni, which were observed on the Cu-5Ni alloy oxidized for 30 minutes, are inferred to be NiO. The combination of the XPS and TEM results indicate that NiO can co-exist with Cu_2O forming a duplex oxide structure on the surface of Cu-5Ni alloy when oxidized in 10^{-4} Torr oxygen at 350°C. A similar duplex oxide structure has also been reported for Cu-12.5Ni alloy oxidized at

500°C under various oxygen partial pressure range from 10^{-5} to 5×10^{-4} Torr, but with Cu on the top of NiO [29].
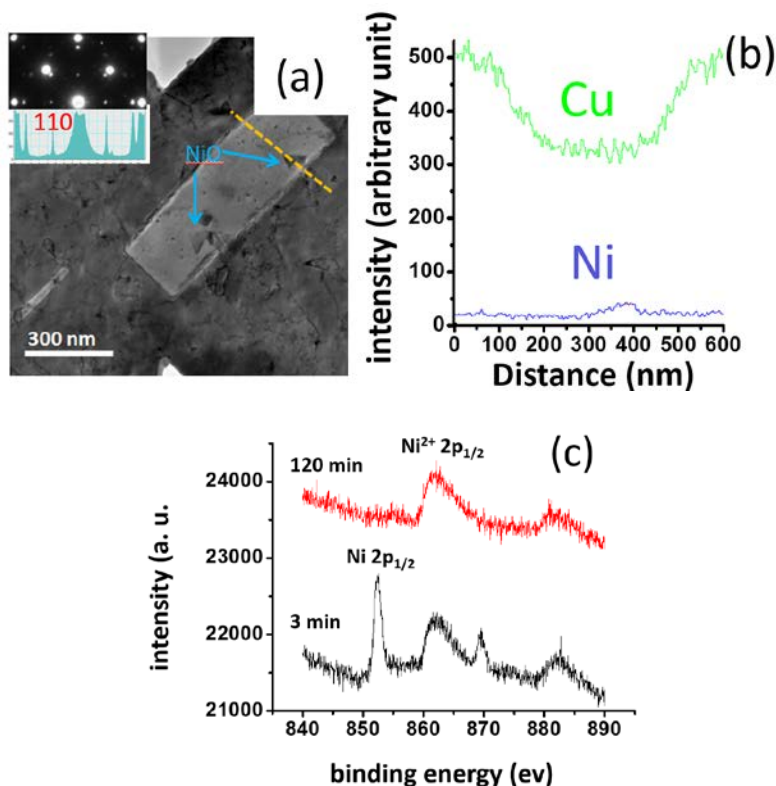
Figure 4.3 (a) TEM bright field image of small NiO islands on a large Cu_2O island and corresponding electron diffraction pattern (inset). (b) Energy-dispersive X-ray spectroscopy (EDS) line-scan across a Cu_2O island where Ni is detected. (c) Ni 2p XPS data taken at 350°C and $pO_2 = 10^{-4}$ Torr as 3 and 120 minutes.

To further understand the sequential oxidation of NiO and Cu_2O, the oxidation behavior of Cu-5Ni(001) alloys at 550°C was investigated by quasi in-situ XPS and in-situ UHV-TEM. Figure 4.4(a) shows the temporal evolution of Ni 2p XPS spectrum of a Cu-5Ni alloy thin film exposed in pure oxygen atmosphere with a pressure of 10^{-4} Torr. Before oxidation, it shows the metallic Ni 2p pattern. After 3-minute oxygen exposure, the Ni 2p peak shifted to the higher energy and between doublets, which indicates the formation NiO. On the other hand, Cu LMM peak remained

the same (Figure 4.4(b)) after 3-minute oxidation, and after 30 minutes of oxidation, Cu LMM peak started to show a small hump at the Cu^{1+} position, revealing the formation of a small amount of Cu_2O on the surface.
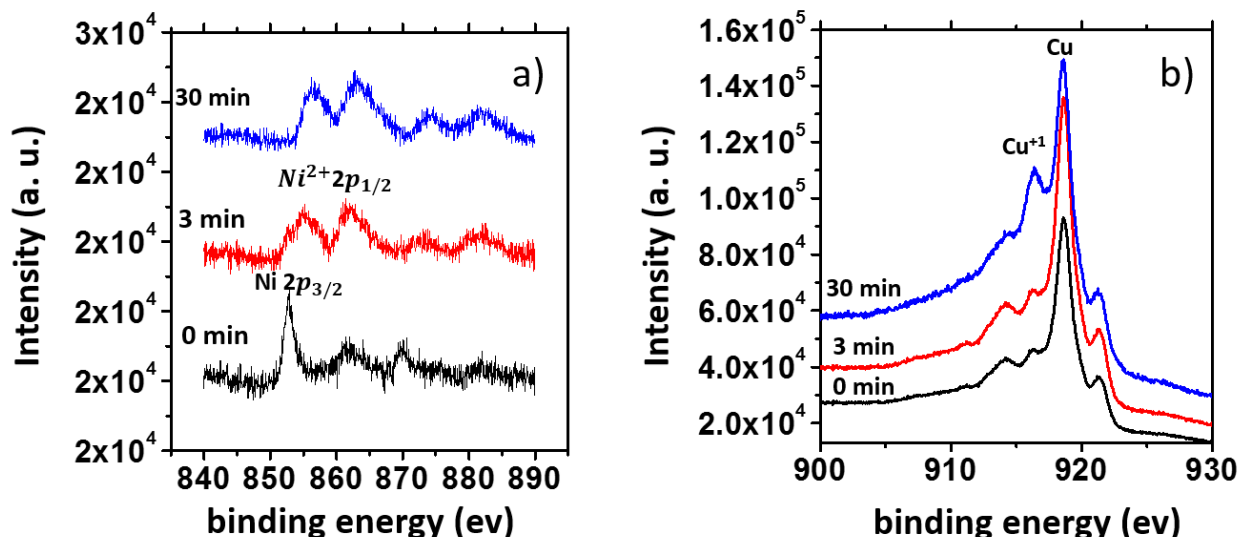
Figure 4.4 Oxidation in XPS system under 550°C and pO2=10^{-4} Torr. (a) The change of Ni 2p peak after oxidation. (b) The change of Cu LMM peak after oxidation.

The same experiment was conducted in the in-situ UHV TEM. Figure 4.5 shows sequential in-situ bright field TEM images of nucleation and growth of an NiO island. In comparison to Cu(001) oxidation under similar conditions [68], the growth rate of oxide islands on Cu-5Ni(001) film was significantly faster. The nucleation density of oxide islands on the Cu-5Ni(001) surface, which can be obtained by counting the number of oxide islands per unit area from a TEM image, was about two orders of magnitude lower than that on the Cu(001) surface. Specifically, the nucleation density of oxide islands on Cu(001) surface was approximately 40/μm^2 after 30-minute oxidation [68], while the density of oxide islands on Cu-5Ni(001) measure from Figure 4.2d was only approximately 0.5/μm^2 under the same condition.
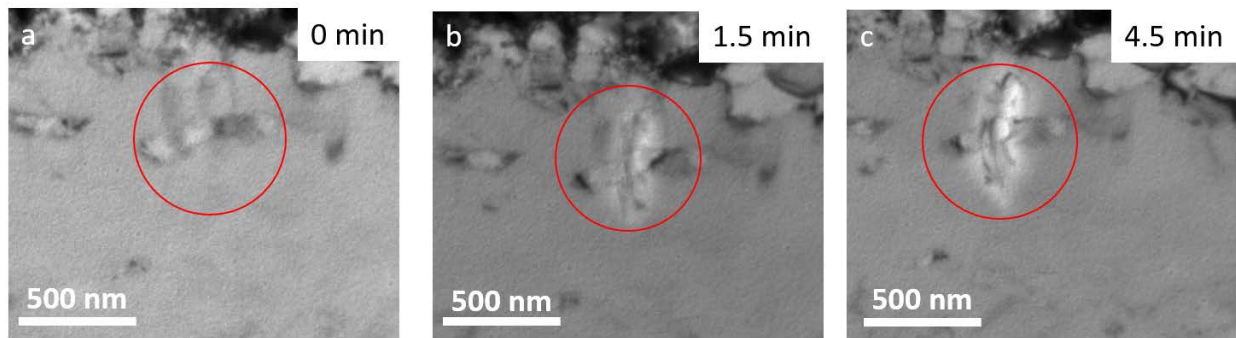
Figure 4.5 In-situ TEM observation of NiO island growth under 550°C and pO$_2$=1 × 10^{-4} Torr. (a) Before oxidation. (b) After 1.5-minute oxidation. (c) After 4.5-minute oxidation.

Figure 4.6 compares the temporal evolution of the plan-view area of an individual NiO island formed on the Cu-5Ni(001), which was measured from the in-situ TEM observation as indicated in Figure 4.5, to Cu$_2$O island formed on Cu(001). Previous studies by Zhou et al. [68] showed that the growth of the Cu$_2$O island on Cu(001) is primarily controlled by oxygen surface diffusion and strain energy introduced by the epitaxial growth of Cu$_2$O on Cu substrate. Cu$_2$O formed on Cu(001) under such oxidation condition initially has a square shape and binomial growth rate, but after about 2 minutes its shape starts to change to an elongated rod-like morphology to lower the strain energy, and the growth rate also changes to an exponential dependence. By contrast, the growth rate of rod-like NiO islands formed on Cu-5Ni(001) did not follow the similar exponential growth rate as found for Cu$_2$O on Cu(001), but instead follows a parabolic growth rate, indicating a diffusion limited process for the oxide growth. It is know that Cu$^+$ is the principal diffusor in Cu$_2$O [15].
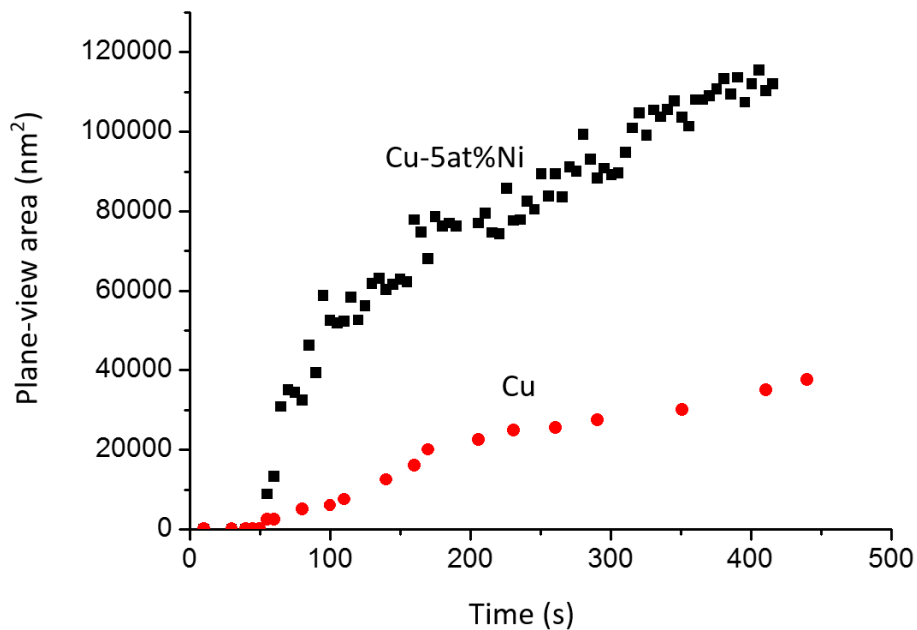
Figure 4.6 The temporal evolution of the area of a NiO island formed on Cu-5at.%Ni (001) at 550°C and $pO_2 = 10^{-4}$ Torr, and comparison with a Cu_2O island formed on Cu (001) when the film was oxidized at 600°C and $pO_2 = 10^{-4}$ Torr [68].

In order to quantify the volume growth rate of an individual oxide island, AFM was utilized to provide 3-dimentional morphology information. Most oxides formed on the surface of Cu-5Ni thin films after 1-5-minute oxidation at 500-600°C were elongated nanorod-like wedged shape with different lengths but keeping a similar height, as indicated in Figure 4.7. This elongated shape is similar to the oxide islands formed on the pure Cu thin film under similar conditions [68]. The contact angle, $\theta \approx 36°$, and height, $h \approx 35$ nm, were measured in the AFM images.
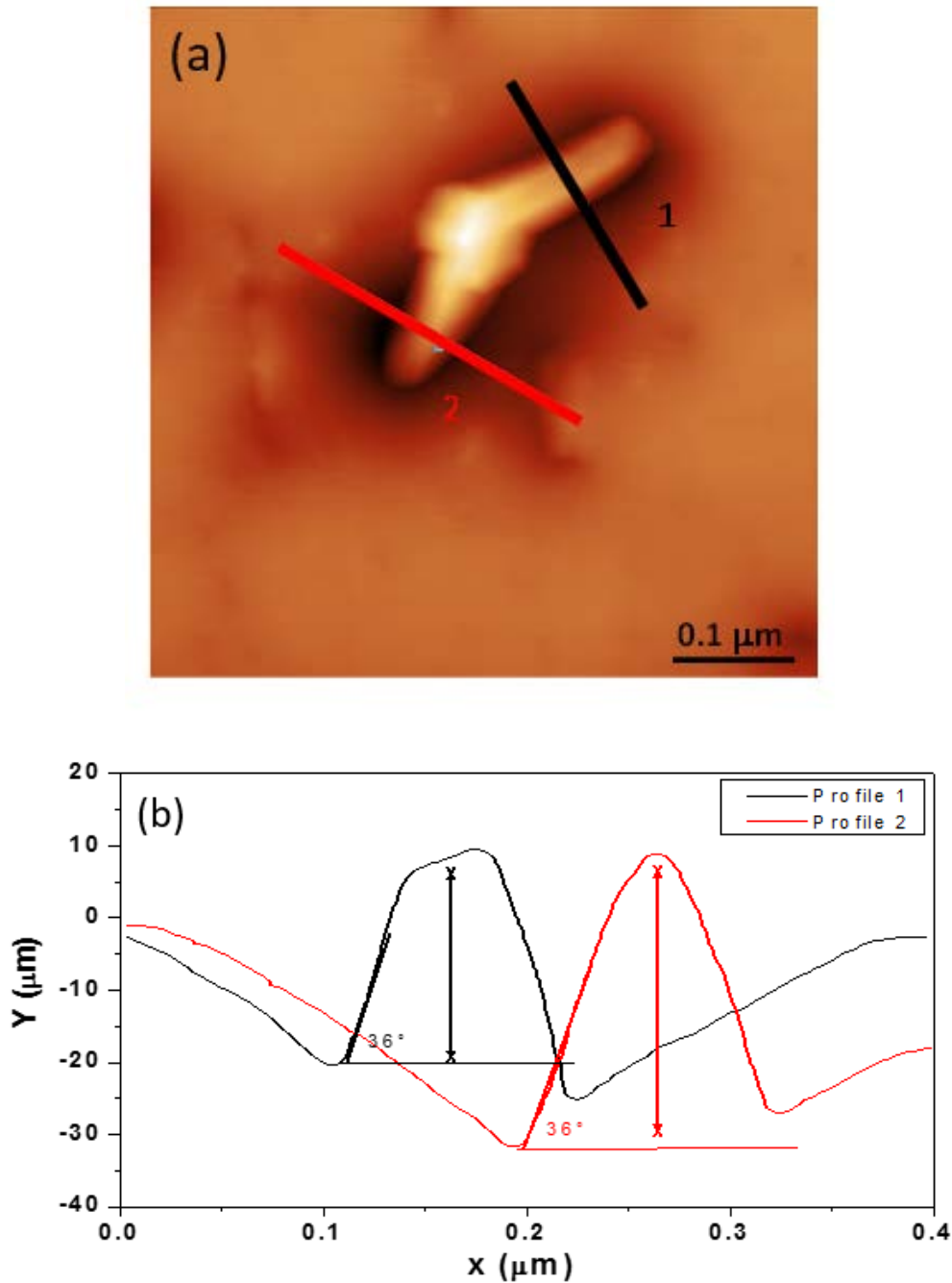
Figure 4.7 Morphology of an oxide island: (a) AFM image and (b) the corresponding line profiles marked in (a).

For simplicity and also based on previous studies [68], it will be assumed that the height of individual oxide islands are constant (36nm) during the entire growth period. Thus, the volume of an oxide island can be calculated using the length and width measured from TEM images. Figure

63

4.8a shows the temporal volumetric evolution of a typical island formed on Cu-5Ni thin film at 550°C under a $pO_2 = 1 \times 10^{-4}$ Torr. The island volume growth rate decreases as the oxidation duration increases. A second oxidation experiment was conducted at 600°C under a $pO_2 = 1 \times 10^{-4}$ Torr. This time the evolution of the NiO island volume as a function of the oxidation time clearly shows at least two different oxidation stages (Figure 4.8b).
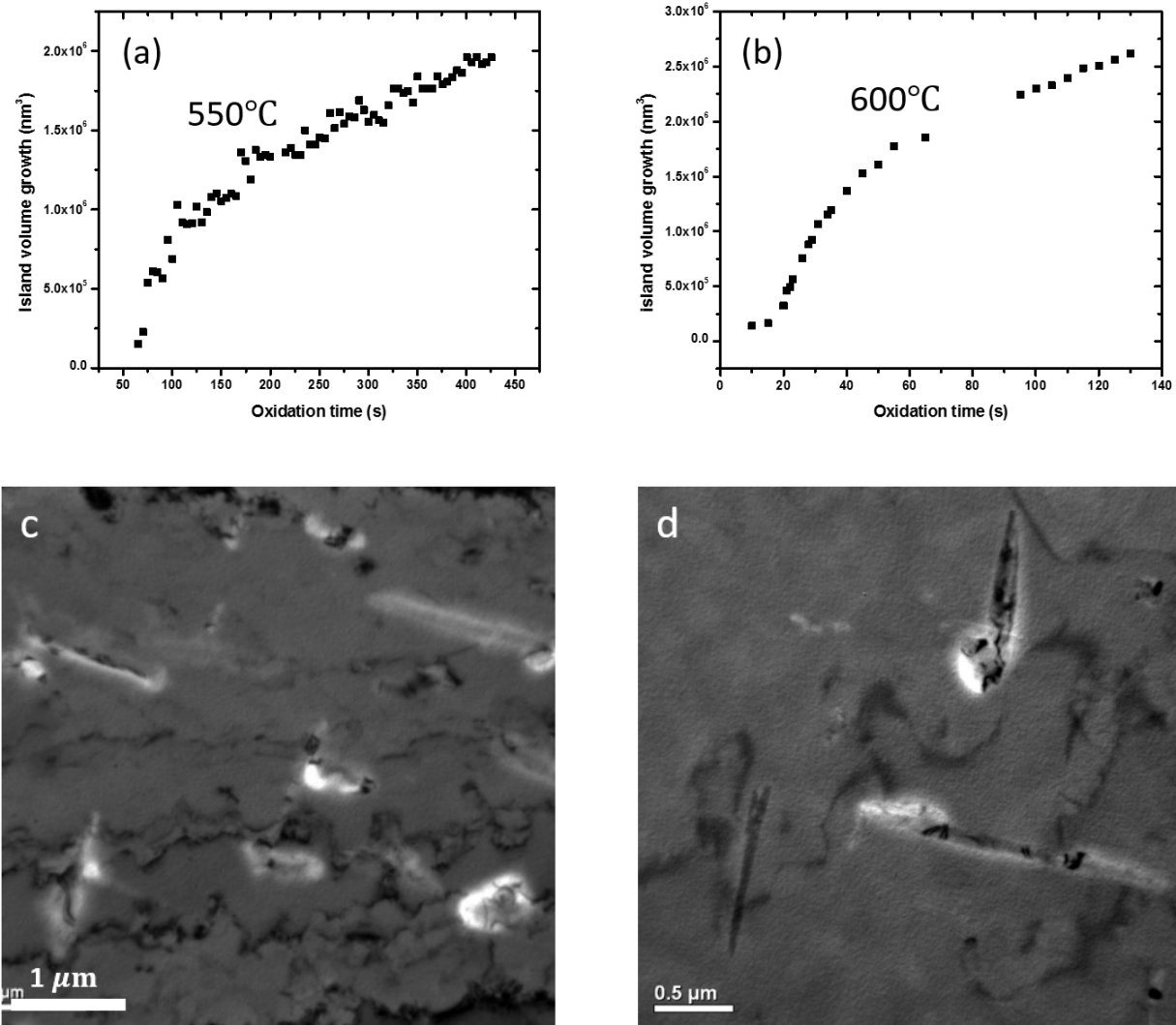
Figure 4.8 Evolution of the island volume (based on a constant-height model) as a function of the oxidation time: (a) growth rate of an oxide island formed on the Cu-5Ni thin film oxidized under 10^{-4} Torr, 550°C (b) growth rate of an oxide island formed on the Cu-5at%Ni thin film oxidized under 10^{-4} Torr, 600°C. (c) TEM bring field image of oxide

64

islands formed on the Cu-5Ni thin film oxidized under 10^{-4} Torr, 550°C. (d) TEM bring field image of oxide islands formed on the Cu-5Ni thin film oxidized under 10^{-4} Torr, 600°C.

4.1.1.2 Discussion

Based on the theory for the nucleation of oxide on the metal or alloy surface developed by Orr [27], the formation of oxide is the result of reaction between metal atom and chemi-adsorbed oxygen atoms. The reactions occur on the surface of Cu-Ni alloy during the nucleation-and-growth stage can be expressed by the following reactions:

$$Ni + O = NiO \tag{4.1}$$

$$2Cu + O = Cu_2O \tag{4.2}$$

The activity coefficient of Ni, γ_{Ni}^0, in dilute Cu-Ni alloy was reported by Oishi et al. [121] as a function of temperature to be:

$$\ln \gamma_{Ni}^0 = \frac{604}{T} + 0.691 \tag{4.3}$$

According to the equation (4.3), for Cu-5Ni alloy oxidized at 550°C, $\gamma_{Ni}^0 = 4.16$. Consequently, the activity of Ni in the Cu-5Ni alloy can be calculated using equation (2.11) to give $a_{Ni} = 4.16 N_{Ni}$. Based on the activity measurement and calculation done at 700°C and 1000°C [122], assuming the same trend at 550°C, γ_{Cu}^0 can be approximated to unity for Cu-5at%Ni, so that $a_{Cu} \approx N_{Cu}$. Since both NiO and Cu$_2$O are not soluble in the alloy, the activity of both these phases taken to be unity. Therefore, the formation energy of NiO and Cu$_2$O can be expressed as follows

$$\Delta G_{NiO}^0 = G_{NiO}^0 - G_O = -RT\ln\left(\frac{1}{a_{Ni}a_O}\right) \tag{4.4}$$

$$\Delta G_{Cu_2O}^0 = G_{Cu_2O}^0 - G_O = -RT\ln\left(\frac{1}{a_{Cu}^2 a_O}\right) \tag{4.5}$$

where

ΔG_{NiO}^0 and $\Delta G_{Cu_2O}^0$ are the changes of Gibbs free energy for the Ni oxidation and Cu oxidation, respectively.

G_{NiO}^0 and $G_{Cu_2O}^0$ is the standard Gibbs free energy of NiO and Cu₂O respectively.

G_O is the Gibbs free energy for oxygen dissociation and chemi-adsorption on Cu-Ni alloy surface.

Subtracting equation (4.5) from (4.4), the thermodynamic equilibrium between NiO and Cu₂O can be obtained.

$$\Delta G_{NiO}^0 - \Delta G_{Cu_2O}^0 = -RT\ln\left(\frac{a_{Ni}}{a_{Cu}^2}\right) \tag{4.6}$$

Since $a_{Cu} \approx N_{Cu}$ and the sum of N_{Ni} and N_{Cu} equals to unity, equation (4.6) can be rewritten as

$$\Delta G_{NiO}^0 - \Delta G_{Cu_2O}^0 = -RT\ln\left(\frac{4.16 N_{Ni}}{(1-N_{Ni})^2}\right) \tag{4.7}$$

The standard molar Gibbs energy of formation for Cu₂O and NiO can be obtained from the CRC handbook [120]. At 550°C, $\Delta G_{NiO}^0 - \Delta G_{Cu_2O}^0 = 52 kJ/mole$, therefore, from thermodynamic point of view, based on equation (4.7), if $N_{Ni} > 10^{-4}$, NiO is stable on the Cu-5Ni alloy surface instead of Cu₂O.

Taking the nucleation process into account, thermodynamic stability of the oxide is just one contributing factor for the oxide formation on the surface. In the classic nucleation theory, the standard free energy change per critical nucleus to form is defined by $\Delta G = \Delta G_v + \Delta G_s$, where ΔG_v is the volume free energy and ΔG_s is the interfacial energy. In the case of oxidation, the ΔG_v is comprised of oxide formation energy and strain energy introduced by the epitaxial growth, whereas the interfacial energy is mainly controlled by the energetics of the oxide-alloy interface.

The above calculation for the thermodynamic stability of different oxide phase is based on the molar Gibbs energy of formation ΔG^0, but in the nucleation theory volumetric Gibbs free energy ΔG_v^0 is used. ΔG_v^0 can be obtained by dividing ΔG^0 of an oxide phase by its molar volume

$\overline{V}$. The larger molar volume of an oxide phase, the lower the ΔG_v^0. The molar volume of Cu_2O is 24cm^3/mole, which is much larger than that of NiO 11.2cm^3/mole. Therefore, at 550℃ the ΔG_v^{NiO}=-14.7KJ/cm^3 is much lower than that of Cu_2O, $\Delta G_v^{Cu_2O}$=-4.4KJ/cm^3. Both NiO and Cu-Ni alloy have a face-centered cubic (f.c.c.) crystal structure and lattice constants are 0.421 and 0.36 nm, respectively, while Cu_2O has a simple cubic crystal structure and a lattice constant of 0.427 nm. NiO and Cu_2O have similar lattice constants, as a result, the epitaxial growth of NiO on Cu-Ni is expected to have a similar strain energy resulted by the lattice miss match as Cu_2O epitaxial growth on Cu-Ni. In summary, the nucleation of NiO on the surface will likely to have much lower volume free energy, therefore, the volumetric energy change resulted by the formation of NiO is much smaller.

It is hard to estimate the other critical term, interfacial energy, in the nucleation theory. The interfacial energy depends on the interface composition (alloy composition, oxygen pressure, oxide phase), the initial oxide structure (surface reconstruction was reported during the initial stage of oxidation for pure Cu [10, 56]), as well as the epitaxial relationship between the oxide and substrate. Due to the complexity of interface between the oxide and alloy substrate, it is hard to make a direct comparison between NiO and Cu_2O. According to the nucleation theory, the importance of interfacial energy decreases as an oxide grows, therefore, a rough estimation for the critical radius of a particle formed on Cu-Ni alloy, above which the particle is stable, indicates when the change of volumetric energy is the predominant driving force to determine the stability of an oxide phase on the Cu-Ni surface.

The change of interfacial energy due to the formation of Cu_2O on Cu at 927℃ was reported to has a value around 600mJ/m^2 by McLean and Hondros [62]. Based on the temperature dependent of interfacial energies summarized by Lippmann et al. [123], an interfacial energy of

500mJ/m^2 at 550℃ can be estimated between Cu$_2$O and a dilute Cu-Ni alloy substrate which is mainly Cu. Assuming a hemi-sphere particle nucleated on the surface of Cu-Ni alloy, the critical volume can be estimated by solving the equation

$$0 = \frac{2}{3}\pi r^3 \Delta G_v + \pi r^2 \gamma \tag{4.8}$$

For Cu$_2$O, whose $\Delta G_v = -4.4$kJ/cm^3, the critical radius is about 0.17 nm. If the interfacial energy between NiO and alloy substrate is in the same order as that between Cu$_2$O and Cu, the critical radius for the NiO is less than 0.1 nm, which is about the size of NiO lattice parameter. If the interfacial energy estimated is close to the real situation, the nucleation barrier for both NiO and Cu$_2$O formation at 550℃ on Cu-Ni oxide formation are quite small. Consequently, for oxide island with a radius larger than 10 nm, which is about the lower limit for the in-situ TEM to detect, volumetric energy is the predominant term to determining the stability of an oxide island, and NiO is the preferred oxide phase. The XPS results shown in Figure 4.4 also confirm this prediction that nickel on the surface was oxidized rapidly at 550℃, since no metallic Ni signal was observed after only 3-minute oxidation. This analysis is also consistent with previous studies on the oxidation of pure Ni and Cu [25, 26, 124]. Based on the studies of Yang and Yeadon [124], it takes more than 15 minutes for the Cu$_2$O to cover a pure Cu surface at 350℃ in 10^{-4} Torr oxygen; whereas, Holloway and Hudson [25, 26] predicted that it only takes less than 3 seconds for NiO to cover a pure Ni surface under the same oxidation condition.

Therefore, for the oxidation conditions used in the present study (350℃ -700℃, 10^{-4} Torr oxygen partial pressure), NiO is the preferred oxide to form on the Cu-5Ni alloy surface from both thermodynamic and kinetic points of view.

Previous study concerning with the oxidation behavior of pure Cu thin films proposed an oxygen-surface-diffusion model to predict the binomial growth rate of the nanorod structure at

initial stage and exponential growth after 5-minute oxidation [68]. Unlike the oxidation of pure Cu, NiO forms on the surface at the onset of oxidation, as analyzed above, so that bulk diffusion of Ni through Cu solid solution towards the alloy/gas interface must play a role during the nucleation-and-growth oxidation stage.

In the following discussion two different quantitative growth models are used to assess the oxidation behavior in the context of the experimental data obtained from the in-situ TEM measurement.

Based on our assumption of Ni bulk diffusion limited oxidation, a 1-D model, which is similar to the treatment utilized by Wagner for the oxygen of binary alloys involving noble metals [17], is used to calculate the growth of NiO islands during the Ni limited stage. Assuming the Ni concentration on the surface to be close to nil, as indicated by the XPS results, then it can be modeled using an error function according with the Fick´s second law

$$C(x) = C_0 \text{Erf} \left(\frac{x}{2\sqrt{Dt}} \right) \text{ (e.g. Ni atoms/nm}^3) \tag{4.9}$$

where C_0 is the initial concentration of Ni, D is the diffusivity of Ni in Cu, and x is the distance from the surface. Applying the Fick's first law, we can obtain the flux of Ni towards the surface as

$$J_{Ni}(x) = D \frac{\partial C(x)}{\partial x} = \frac{DC_0 e^{-\frac{x^2}{4Dt}}}{\sqrt{\pi} \sqrt{Dt}} \quad \text{(Ni atoms/nm}^2\text{s)} \tag{4.10}$$

On the surface, where x=0, the flux of Ni is $J_{Ni}^s = \frac{C_0\sqrt{D}}{\sqrt{\pi} \sqrt{t}}$, which leads to the following oxide growth rate, in terms of Ni atoms added to a given oxide island

$$\frac{dN_{Ni}}{dt} = J_{Ni}^s * A \quad \text{(Ni atoms/NiO island} * \text{s)} \tag{4.11}$$

where A is the inverse of the nucleation density, N_{Ni} is the total number of Ni atoms in the oxide islands. In others words, A is the Ni capture zone, in which the Ni atoms diffused to the surface is attached to an existing island instead of forming new islands [124].

Integrating the equation (4.11) (detail in Appendix A), gives the temporal evolution of volume of the oxide island with a parabolic growth:

$$V_{NiO}^{Ni\,limited}(t) = \frac{2\,\Omega\,AC_0\sqrt{D}}{\sqrt{\pi}}\left(\sqrt{t-t_0}\right) + V_0 \quad (nm^3) \tag{4.12}$$

where Ω is the geometrical volume occupied by an atom in a unit cell assuming that all the atoms in the lattice are the same (in NiO, Ni:O=1:1, so $\Omega = \Omega_{Ni} = \Omega_O$) and V_0 is island volume at time t_0.

The growth rate of NiO limited by the Ni diffusion towards the surface can be obtained from the derivative of equation (4.12) with respect to time:

$$\frac{dV_{NiO}^{Ni\,limited}(t)}{dt} = \frac{\Omega\,\alpha AC_0\sqrt{D}}{\sqrt{\pi(t-t_0)}} \quad (nm^3/s) \tag{4.13}$$

Based on the equation (4.13), this growth mechanism is rapid at the onset of the oxidation, but as oxidation duration increases, the growth rate will continuously decrease.

Alternatively, following the derivation by Orr [27], the oxygen surface diffusion process is proportional to the island perimeter [27],

$$\frac{dN_O}{dt} = PK_OJ_O^s \quad (O\ atoms/NiO\ island * s) \tag{4.14}$$

Where N_O is the total number of oxygen atoms in the oxide island, P is the perimeter of an island at three-phase (gas-alloy-oxide) boundary, K_o is sticking coefficient of the oxygen to the oxide island, J_O^s is the diffusive flux of oxygen [124].

Based on the 3D morphology of oxide islands obtained by the AFM, as shown in Figure 4.7, a wedged nanorod model can be used to calculate the volume of the NiO islands, V=hwl/2,

where h is the height of the island, w is island width, l is island length. The perimeter around island can be calculated as P=2w+2l. Based on this, equation (4.14) can be solved as (detail in Appendix A)

$$V_{NiO}^{O\ limited}(t) = \left(\frac{hw^2}{2} + V_0\right) e^{\frac{4}{hw}\Omega_O K_O J_O^s(t-t_0)} - \frac{hw^2}{2} \ (nm^3) \qquad (4.15)$$

This shows the same exponential dependence of time as the Cu_2O growth on pure Cu film [68]. A value of $\Omega = 0.0185 \ nm^3$ per atom /NiO unit cell can be obtained from the handbook [120] and w and $V_0(t_o)$) can be approximated based on TEM analysis.

The growth rate of NiO limited by the oxygen surface diffusion can be obtained from the derivative of equation (4.15),

$$\frac{dV_{NiO}^{O\ limited}(t)}{dt} = \left(2w + \frac{4V_0}{hw}\right)\Omega_O K_O J_O^s e^{\frac{4}{hw}\Omega_O K_O J_O^s(t-t_0)} \ (nm^3/s) \qquad (4.16)$$

Based on equation (4.16), this growth mechanism is slow at the onset of oxidation, but as oxidation duration increases, the growth rate will exponentially increase.

Comparing NiO growth rate calculated using equations (4.12) and (4.15), the island growth is initially controlled by oxygen supply and follow an exponential law when $\frac{dV_{NiO}^{Ni\ limited}}{dt} \gg \frac{dV_{NiO}^{O\ limited}}{dt}$; whereas that a Ni bulk diffusion control is establish when $\frac{dV_{NiO}^{O\ limited}}{dt} \gg \frac{dV_{NiO}^{Ni\ limited}}{dt}$ following a parabolic behavior. Finally, when $\frac{dV_{NiO}^{Ni\ limited}}{dt} = \frac{dV_{NiO}^{O\ limited}}{dt}$, the transition from one dominant mechanism to the other will occur. Solving this equation, the transition time can be estimated from

$$4\Omega\alpha A C_0 \sqrt{\frac{D}{\pi t}} - \left(\frac{4K_0 J_0^s \Omega}{wh}\right)\left(\frac{w^2 h}{2} + V_0\right) e^{\frac{4K_0 J_0^s \Omega(t-t_0)}{wh}} = 0 \qquad (4.17)$$

Therefore, the NiO island growth on Cu-5Ni thin films can be defined by 2 stages as schematically shown in Figure 4.9. A first stage controlled by the oxygen surface diffusion, in which the Ni supply is still sufficient to be oxidized on the surface of Cu-Ni alloy, followed by a transition period, in which the dominance mechanism starts to shift to Ni bulk diffusion controlled, and finally proceed to second stage where the diffusion of nickel is controlling the oxidation behavior. The length of three stages is dependent of the oxidation conditions.
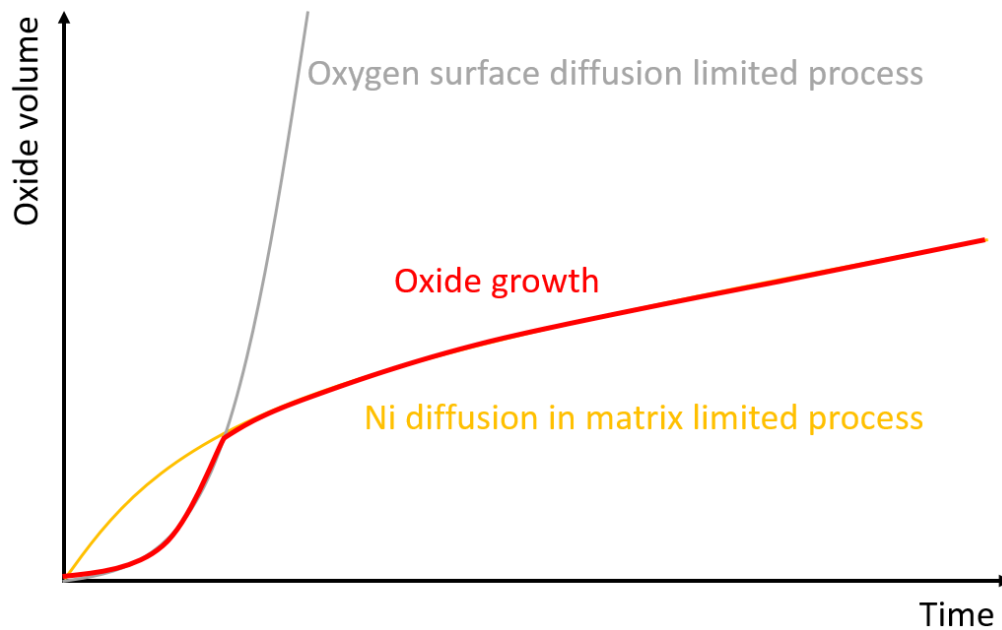
Figure 4.9 Schematic of the oxide growth controlled by two competing oxidation mechanisms.

For the sample oxidized at 550°C under $pO_2 = 1 \times 10^{-4}$ Torr, the exponential growth was not apparent in our experimental measurements and just a parabolic behavior was observed after 65s of oxidation based on TEM analysis (Figure 4.8a). The lattice constant for Cu-5Ni was measured as a=0.36nm from the SAED, as indicated by the inset of Figure 4.2b. Since Cu-5Ni has an f.c.c. structure, each unit cell contains 4 atoms, divided it by the size of unit cell a^3 gives the atomic density n=85.7atoms/nm^3. The concentration of Ni, C_0 can be calculated

$$C_0 = N_{Ni} * n = 0.05 * 85.7 = 4.3 \left(\frac{atom}{nm^3}\right) \tag{4.18}$$

At the same time, the inverse of the nucleation density was determined using TEM image analysis

(Figure 4.8c) to be A=5.05 μm^2/island. Finally, by fitting the experimental data in Figure 4.8a with

the kinetic model described by equation (4.12), as shown in Figure 4.10, the diffusivity of Ni in

Cu, D, is calculated to be 4×10^{-16} cm^2/s, which is in good agreement the value, 2.23×10^{-16}

cm^2/s, reported by Dijk and Mittemeijer for Cu-Ni bimetallic film [125].

The equation (4.15) can be used to fit the experimental data at 600°C from 10s<t<23s. The

parabolic growth of NiO island from t=31s to 130s can be fitted by the Ni bulk diffusion limited

kinetic models (equation (4.12)) similar to oxidation carried out at 550°C, using the experimental

data measure from in-situ TEM as indicated in Figure 4.8b and d, A=2.5 μm^2/island and a V_0=7.9

x 10^{6}nm^3 at t_0= 31s. By fitting of experimental data, as shown in Figure 4.10, the diffusivity of

Ni was determined to be D = 7×10^{-15} cm^2/s. This value is in very good agreement with

extrapolation from the interdiffusion coefficients measured by Dijk and Mittemeijer [125].
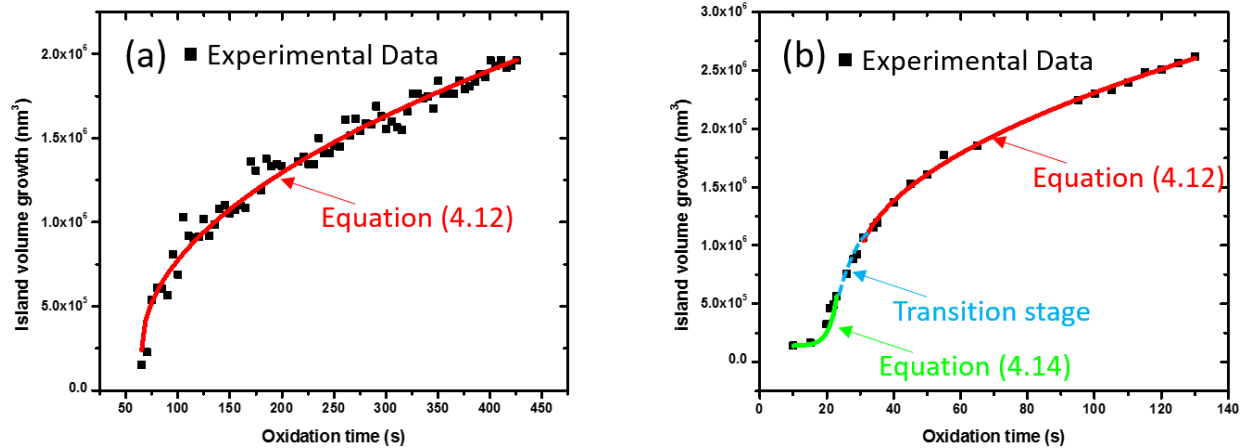
Figure 4.10 Fitting of growth rate limited by oxygen surface diffusion and growth rate limited by Ni diffusion on

oxidation experiments of Cu-5Ni thin films (a) carried out at 550°C, in 10^{-4} Torr oxygen, (b) carried out at 600°C, in

10^{-4} Torr oxygen.

Previous diffusion studies can give an estimation of J_o^s [126, 127], which should be proportional to $e^{-\frac{Q_o^s}{kT}}$. While K_o can be given by $\alpha[1 + \frac{\upsilon_d}{\upsilon_a}\exp\left(-\frac{E_d-E_a}{kT}\right)]^{-1}$ [128], where α is the probability for trapping into the precursor state, υ_d/υ_a is the ratio between the pre-exponential factors for desorption and dissociation, and $E_d - E_a$ is the difference in activation energy for desorption and dissociation. Based on previous studies on the oxidation of Cu(001) thin film [68, 124], the activation energy for $K_o J_o^s$ or oxygen surface diffusion on pure Cu surface is about 50kJ/mol. As a result, the oxide growth rate only increases by a factor of two when the temperature is increased from 350°C to 600°C, as shown in Figure 4.11.
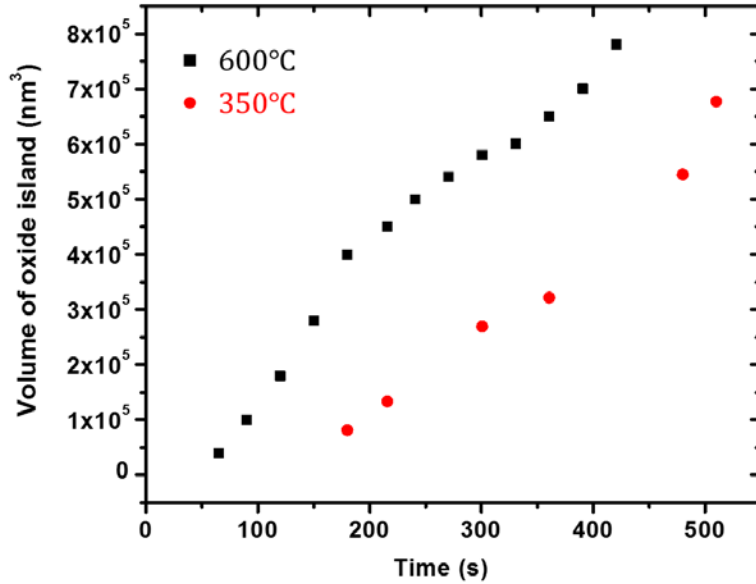
Figure 4.11 The growth rate of oxide islands on Cu thin film at 350°C and 600°C.

Although no report regarding the temperature dependence of K_o for NiO was found, NiO has a similar crystal structure as Cu_2O, one can expect the K_o for the formation of NiO to be in the same order as that for Cu_2O. Cu-5Ni was used in the present study, and Ni on the surface is

consumed rapidly, as shown by based on the XPS analysis, Figure 4.4. Therefore, the oxygen surface diffusion on Cu-5Ni alloy is similar to that on pure Cu, as a result, the value of J_O^s on Cu-5Ni should be close to that on pure Cu. Since both K_O and J_O^s for the oxidation of Cu-5Ni are similar to the case of pure Cu oxidation, $K_O J_O^s$ also doesn't change significantly with the increase of temperature. Therefore, the growth rate of NiO limited by oxygen surface diffusion $\frac{dV_{NiO}^{O\,limited}}{dt}$ doesn't change significantly when the oxidation temperature increases.

On the other hand, according to equation (4.15), $V_{NiO}^{Ni\,limited}(t) \propto \sqrt{D}$. Based on both previously reported Ni diffusivity in Cu [125] and experimental results in the present study, the activation energy for lattice diffusion of Ni in Cu is estimated to be about 230 kJ/mol, which is much higher than the activation energy for oxygen surface diffusion. The growth rate of NiO limited by Ni lattice diffusion will increase three orders of magnitude when the temperature is increased from 350°C to 600°C. Therefore, the growth rate limited by Ni diffusion $\frac{dV_{NiO}^{Ni\,limited}}{dt}$ will increase rapidly when the oxidation temperature increases.

Considering the temperature dependence of $\frac{dV_{NiO}^{O\,limited}}{dt}$ and $\frac{dV_{NiO}^{Ni\,limited}}{dt}$, based on equation (4.17), the lower the temperature used for oxidation the faster transition of NiO growth mechanism occurs. This prediction reaches good agreement with the experimental observation obtain from in-situ TEM. At 550°C, the exponential growth was not apparent in our experimental measurements, as shown in Figure 4.10a, and this could be the result of fast transition not being captured by in-situ TEM. At higher temperature, 600°C, which elongates the transition time, and thus, oxygen surface diffusion limited stage was observed at the onset of oxidation as shown in Figure 4.10b.

As mention earlier, metallic Ni was oxidized rapidly leaving a Cu rich surface, as a result, the Cu$_2$O growth rate on pure Cu thin film measured by previous studies [68, 124] can be used to

estimate the Cu_2O growth rate on Cu-5Ni. Comparing NiO growth rate calculated using equations (4.12) and (4.15), the competitive oxidation on the Cu-5Ni alloy surface can be further predicted depending on the oxidation conditions, as shown in Figure 4.12.
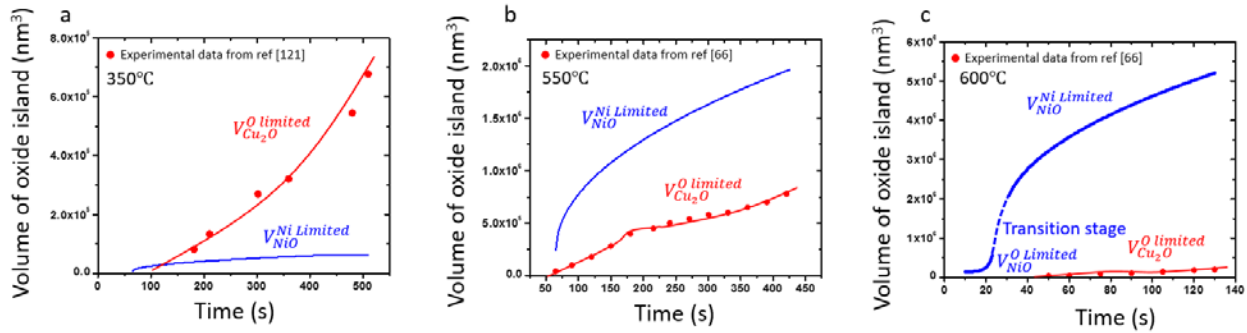
Figure 4.12The growth rate of Cu_2O island and NiO island on Cu-5Ni thin films in 10^{-4} Torr pure oxygen under different temperature. (a) 350℃, (b) 550℃, (c) 600℃.

When the Cu-5Ni alloy is oxidized at lower temperature (~350℃) in 10^{-4} Torr pure oxygen, the growth rate of NiO, which is limited by the lattice diffusion of Ni, is much slower than the growth rate of Cu_2O (Figure 4.12a). Consequently, the primary oxide formed on the surface was Cu_2O. At an intermediate temperature, which is about 550℃ under the oxidation condition used in the present study, the growth rate of NiO is still limited by the lattice diffusion of Ni, but it is much faster than the growth rate of Cu_2O (Figure 4.12b). As a result, the predominant oxide phase detected on the surface was NiO. At temperature higher than 600℃, the lattice diffusion of Ni becomes so fast that oxygen supply to the oxide island is not sufficient at the onset of the oxidation process. Under such a condition, only NiO islands will form on the surface of Cu-5Ni alloy during the early-stage oxidation, and will show a three-stage growth as indicated in Figure 4.12c. This trend is in very good agreement with the experimental results as shown in Figure 4.2.

4.1.2   The impact of oxygen partial pressure, grain structure and surface condition on the competitive oxidation of Ni-Cr alloys during nucleation-and-growth stage

4.1.2.1 Quasi in-situ oxidation of Ni-Cr

Expanding from the fundamental understanding of competitive oxidation of Cu-Ni alloys during the nucleation-and-growth stage, they next step was to study a more complex and more widely used base system, Ni-Cr, was investigated. The dissociation oxygen pressure of Cr_2O_3 is much lower than those of NiO and Cu_2O. Consequently, it is hard to prevent Cr from oxidizing during the heating process in in-situ TEM due to the presence of residual water vapor in the chamber. Therefore, quasi in-situ XPS was used to investigate the competitive oxidation process on Ni-Cr alloys during the nucleation-and-growth stage.

Since Cr_2O_3 has much higher thermodynamical stability and a much smaller scale-growth rate, it is possible to form a protective scale on a Cr-containing alloy the surface that prevents the oxidation of Ni and significantly decreases the degradation rate of the alloy. The formation of such a protective Cr_2O_3 scale depends on oxidation conditions (such as temperature and oxygen partial pressure), as well as the alloy composition and microstructure [87, 129].

The atomic percent of Ni, Ni^{2+}, Cr, and Cr^{3+} presented at the surface was obtained from XPS. Atomic percent or mole fraction of Cr^{3+} was used to present the amount for chromia on the surface of alloys. Although $CrO_{1.5}$ should be a more precise expression for chromia in the following XPS data, Cr_2O_3 is used instead for convenience. Figure 4.13 shows the temporal evolution of the scale composition on the surface of Ni-8Cr and Ni-16Cr alloys with a 600-grit surface finish oxidized in10^{-5} Torr pure oxygen at 600℃. After only one minute of oxidation, no metallic Cr was detected on the surface and the amount of metallic Ni was also very small on both samples. The rapid consumption of metallic phase on the surface indicated a fast nucleation

process for both Cr_2O_3 and NiO under such an oxidation condition. A small amount of Cr_2O_3 was detected on the surface of Ni-8Cr during the very early stage of oxidation, but was quickly overgrown by NiO. On the other hand, Ni-16Cr formed a significant amount of Cr_2O_3, which remained constant after 5-minute oxidation. As indicated by the composition of oxide on the surface, Ni-8Cr could not form an external protective Cr_2O_3 under the given oxidation condition. Although Ni-16Cr oxidized under the same condition also did not form a continuous Cr_2O_3 layer, the molar fraction of Cr_2O_3 formed on the surface increased significantly to about 60% and remained almost constant for 15 minutes.
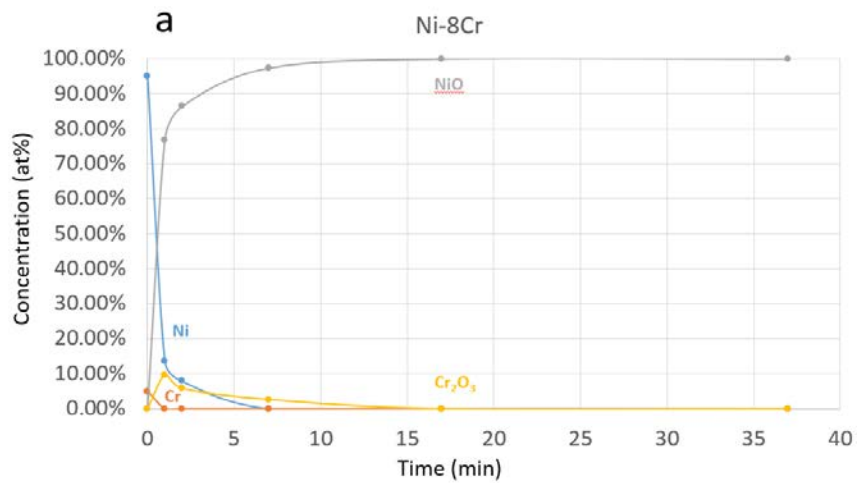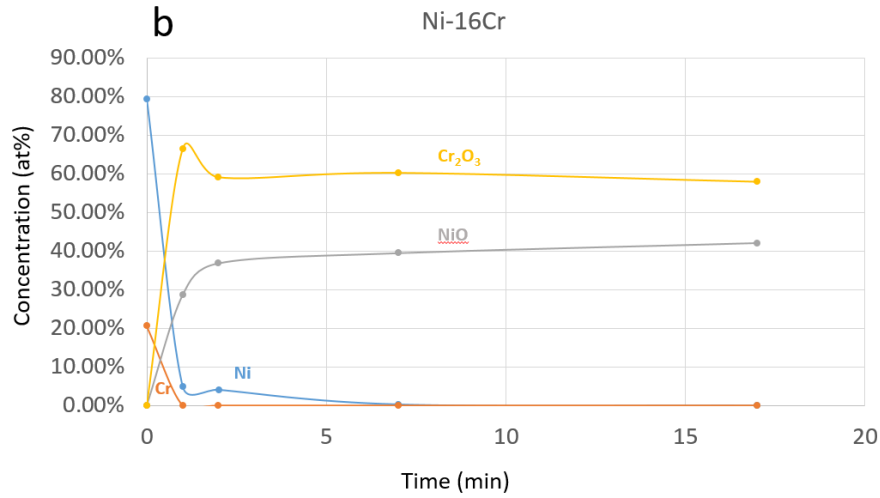
Figure 4.13 Oxide scale formation on the surface of Ni-8at%Cr and Ni-16at%Cr bulk alloy samples with 600-grit finish exposed in pure oxygen with a pressure of 10^{-5} Torr at 600℃. (a) Ni-8at%Cr, (b) Ni-16at%Cr.

The impact of surface finish and alloy grain structure on the oxide scale formation was also investigated, as shown in Figure 4.14. Three Ni-8at%Cr alloy samples with different surface finishes or microstructures were prepared. One of them was thin film with a thickness of 500nm prepared by e-beam deposition. The other two samples were bulk cast alloys but with different surface finishes: colloidal-silica or 600-grit, respectively. These three samples were oxidized under an oxygen partial pressure of 10^{-6} Torr at 600℃. After only one minute, the mole fraction of Cr_2O_3 formed on the surface of thin film sample was about 70%, and remained almost constant within the entire oxidation duration, as shown in Figure 4.14a. Alternatively, the maximum mole fraction of Cr_2O_3 detected on the sample surface prepared using colloidal-silica finish was only 20%, and kept decreasing as the oxidation duration increased. A competition process between the formation of Cr_2O_3 and NiO was observed on Ni-8Cr alloy with 600-grit SiC finish. The mole fraction of Cr_2O_3 initially went up to 60% during the first 2-minutes oxidation, but then decreased to below

40% as the oxidation increased to 17 minutes. As the oxidation time continued to increase, the

mole fraction of Cr_2O_3 increased again back to 50%.

a Thin film

b 600-grit SiC
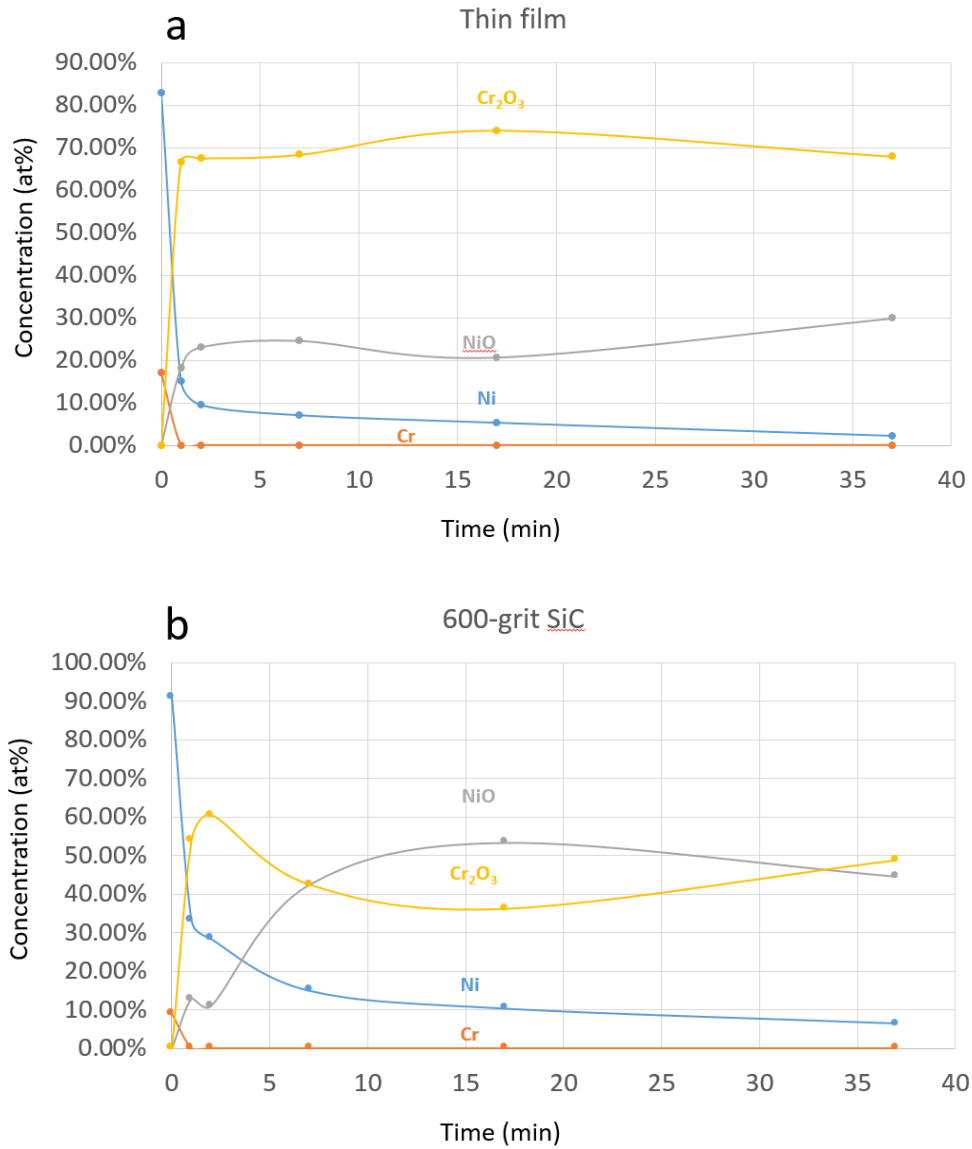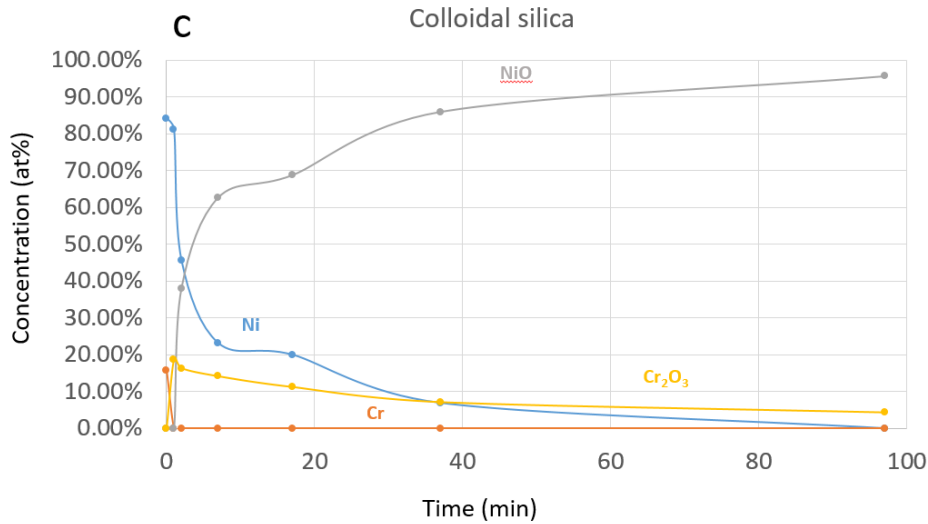
Figure 4.14 Oxide scale formation on the surface of Ni-8at%Cr alloys with different grain structure and surface finish exposed in pure oxygen with a pressure of 10^{-6} Torr at 600°C. (a) Thin film sample, (b) bulk alloy with 600-grit finish, (c) bulk alloy with colloidal-silica finish.

Similar to the oxidation experiments carried in 10^{-5} Torr pure oxygen, no metallic Cr was detected after only one minute of oxidation in 10^{-6} Torr oxygen. However, the amount of metallic Ni left on the surface is different for each sample. The thin-film sample had the lowest mole fraction of metallic Ni (less than 20%) on the surface, while the sample prepared with colloidal silica had the highest mole fraction of metallic Ni (about 80%).

Additionally, oxygen partial pressure was found to affect the scale formation on the surface, as shown in Figure 4.13a and Figure 4.14b. The scale formed on the Ni-8at%Cr alloy with 600-grit finish oxidized at 600°C in 10^{-6} Torr pure oxygen was composed of both NiO and Cr_2O_3 with a ratio close to unity (Figure 4.14b). When the same alloy oxidized at the same temperature but a higher oxygen pressure (10^{-5} Torr), almost no Cr_2O_3 was found except in the very early stage of oxidation, as shown in Figure 4.13a.

4.1.2.2 Discussion

It was reported by Giggins and Pettit [129] that the critical mole fraction of Cr for the formation of an exclusive Cr_2O_3 scale on Ni-Cr alloys is higher than 30wt%, when oxidized in 0.1 atm oxygen between 800℃ and 1200℃. The lower the temperature, the more Cr is needed to form an exclusive Cr_2O_3 scale. However, with as low as 10wt% of Cr, a progressive Cr_2O_3 scale can result along the internal oxidation front, and the lower the temperature the less Cr is needed to initiate such a process scale establishment [87]. The results in this study indicate the existence of two kinetic boundaries for the protective Cr_2O_3 scale formation. The first one is the formation of protective Cr_2O_3 at a grain boundary which can initiate a progressive Cr_2O_3 scale formation along the internal oxidation front. The second is the external formation of Cr_2O_3 layer.

These two kinetic boundaries were also reported by Zhao et al. [130]for Ni-Al alloys oxidized in air at 1200℃. The authors referred to a partial Al_2O_3 layer formed in localized areas on the surface as a "node". When the Al content in the alloy is higher than a critical value (less than 10at% for Ni-Al alloys oxidized in air at 1200℃), those "nodes" will start to form on the surface, and may propagate to eventually establish a continuous Al_2O_3 layer along the internal oxidation front. If the node density is sufficiently high, a continuous scale can develop, as indicated in Figure 4.15. This represents the generally perceived transition from internal to external oxidation, and also can be defined as the first kinetic boundary for the establishment of a protective scale. An increase of Al content in the alloy will increase the number density of nodes on the surface and decrease the time to form a continuous layer of protective scale through progressive propagation along the internal oxidation front. Once the Al content in the alloy reaches another critical value, when the number density of nodes forming on the surface during the early-stage oxidation is so high that they connect to each other, the second kinetic boundary for the

82

establishment of protective scale is reached, as shown in Figure 4.15e and f. This second kinetic

boundary can be also referred as the formation of exclusive external protective scale formation.
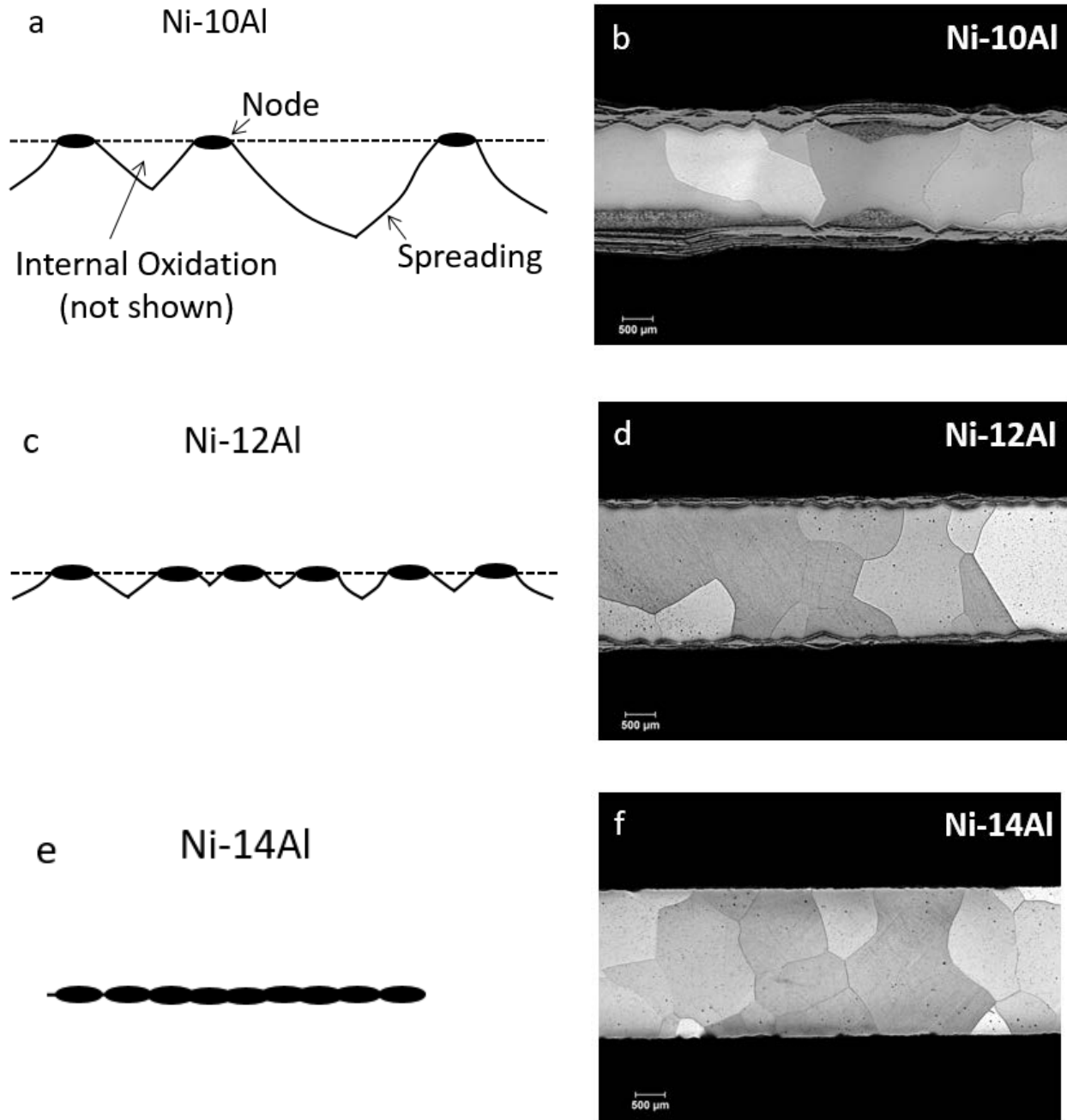
Figure 4.15 schematics and micrographs of protective scale formation on Ni-Al alloys. (a) Schematic of progressive

protective scale formation on Ni-10Al alloy, (b) cross-section image of Ni-10Al alloy oxidized in dry air at 1200℃

for 24 hours, (c) schematic of progressive protective scale formation on Ni-12Al alloy oxidized in dry air at 1200℃ for 24 hours, (d) cross-section image of Ni-12Al alloy, (e) schematic of external protective scale formation on Ni-14Al alloy, (f) cross-section image of Ni-14Al alloy oxidized in dry air at 1200℃ for 24 hours.

XPS experiments of Ni-Cr early-stage oxidation in the present study also agrees with this initial nodes formation proposed by Zhao et al. [131], as indicated by the profile result in Figure 4.13. Even on Ni-8Cr (Figure 4.13a), where the amount of Cr was not sufficient to form a protective scale, an increase in Cr concentration in the form of Cr_2O_3 on the surface of the Ni-Cr alloy was observed after 1 minute of oxidation at 600℃ in 10^{-5} Torr oxygen. This surface enrichment of Cr indicated the formation of initial nodes on the surface. However, the number density of the nodes formed was so small that a progressive scale formation cannot be attained. As a consequently, the rapid forming NiO overgrew the Cr_2O_3 and covered the entire surface (concentration of NiO on the surface approaches 100% after 17 minutes of oxidation), as shown schematically in Figure 4.16.
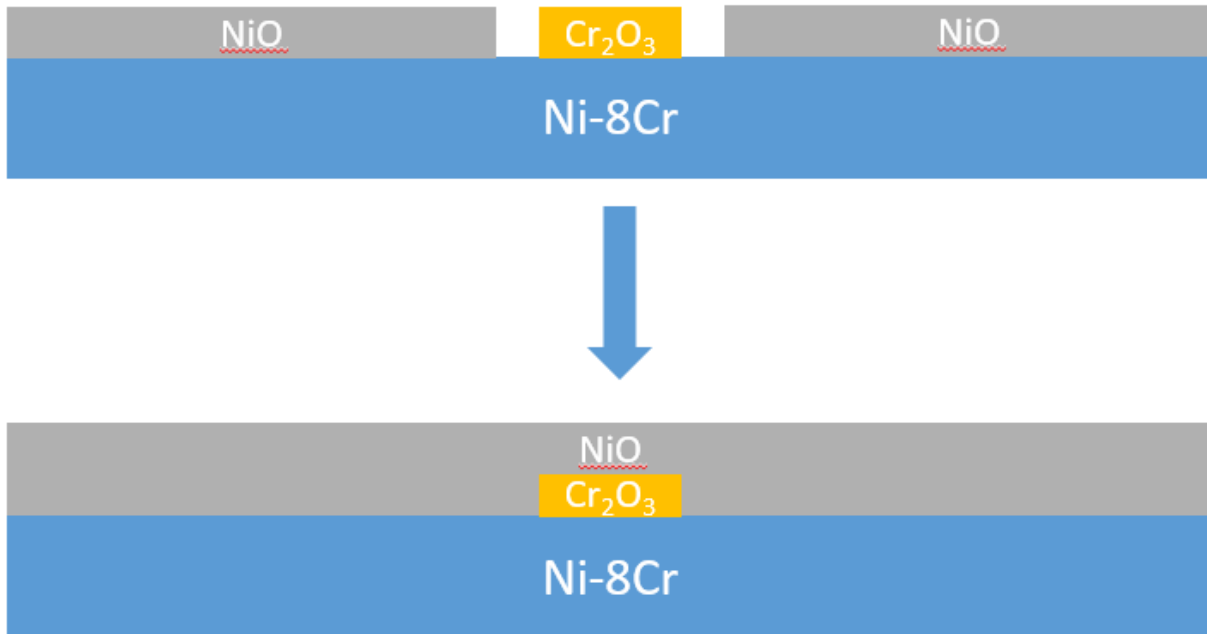
Figure 4.16 Schematic representation of the scale formation on Ni-8Cr alloy with 600-grit finish oxidized in 10^{-5} Torr oxygen at 600℃

When the concentration of Cr in the Ni-Cr alloy increased to 16at% (Figure 4.13b), a significant enrichment of Cr_2O_3 (60%) was observed. The concentration of Cr_2O_3 and NiO on the surface remained almost constant from 2 minutes to 17 minutes. This indicated the formation of protective Cr_2O_3 layer in localized areas on the surface, which could be correlated to the formation of nodes. The slight decrease of Cr concentration on the surface after 17-minute oxidation compared to what was obtained after 7 minutes could be a resulted of the overgrowth of NiO at some NiO/Cr_2O_3 interfaces as shown schematically in Figure 4.17.
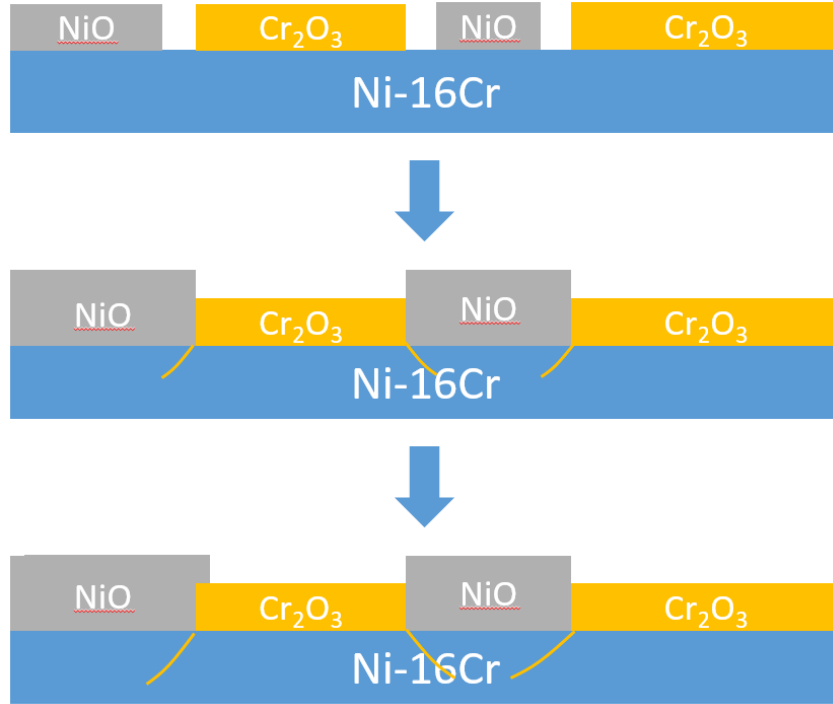
Figure 4.17 Schematic representation of the scale formation on Ni-16Cr alloy with 600-grit finish oxidized in 10^{-5} Torr oxygen at 600℃

Based on the nucleation theory, and as discussed in last section, $\Delta G = \Delta G_v + \Delta G_s$. The change of Gibbs free energy due to the oxidation process is the main driving force for the nucleation. The change of Gibbs free energy change for the oxidation process on the alloy surface of alloy is directly related to the oxygen activity. During the precursor stage of oxidation, oxygen molecules will dissociate and then adsorb on the alloy surface or dissolve into alloy process on the surface [54], i.e.,

$$O_2 = 2O \tag{4.19}$$

Since the Gibbs free energy change of this process will not alter significantly with oxygen partial pressure [4-6, 9, 25, 26, 132], the oxygen activity at the surface primarily depends on the local P_{O_2}.

Therefore, the decrease of oxygen partial pressure will result in decrease in oxygen activity on the alloy surface, and thus decreasing the driving force for the nucleation of oxides on the surface.

At 600°C, the dissociation oxygen partial pressure for Cr_2O_3 and NiO is 10^{-27} Torr and 10^{-16} Torr, respectively [120]. Although both values are much lower than the oxygen partial pressure used in the present study, the kinetic process of oxidation on Ni-8Cr alloys with 600-grit finish was changed significantly when the oxygen partial pressure dropped from 10^{-5} Torr (Figure 4.13a) to 10^{-6} Torr (Figure 4.14b). Since no metallic Cr was observed after just one minute of oxidation in both cases, the growth of Cr_2O_3 should be Cr lattice diffusion limited, as discussed in previous section. This should be the result of rapid nucleation and growth of Cr_2O_3 islands due to the huge driving force generated by the change of Gibbs free energy related to formation of Cr_2O_3, as well as the fast oxygen surface diffusion and high attachment rate. On the other hand, the formation of NiO was greatly slowed by decreasing the oxygen partial pressure, which indicates the oxygen surface diffusion limited growth process for NiO, as discussed in the previous section. The sticking coefficient of oxygen, K_O, to the NiO island should not change significantly with oxygen partial pressure [128], but the oxygen surface diffusion, J_O, is directly related to oxygen chemical potential on the surface, and thus, oxygen partial pressure [25, 26]. Therefore, for the Ni-8Cr oxidized at 600°C, the growth of Cr_2O_3 should follow the same parabolic rate in both oxygen partial pressures, but the growth of NiO, which follows an exponential rate law, highly depends on the oxygen partial pressure, as shown schematically in Figure 4.18. Assuming the total amount of oxide (NiO+Cr_2O_3) required to cover the entire alloy surface is a constant, the lower the oxygen partial pressure, the higher will be the Cr_2O_3 concentration on the surface when the alloy surface is covered by the oxide. Higher Cr_2O_3 concentration on the surface will result in a greater number of protective

nodes formation on the surface, so that low oxygen partial pressure tends to accelerate the protective scale formation.

One should note that the trends presented in Figure 4.18 are based on the oxidation model developed in the previous section, which can only apply to the oxide island growth during the nucleation-and-growth stage in which the growth of oxide is mainly lateral. Once the coverage of oxide on the surface is high enough, coalescence of oxide islands will occur [106], and this model will be no longer valid.
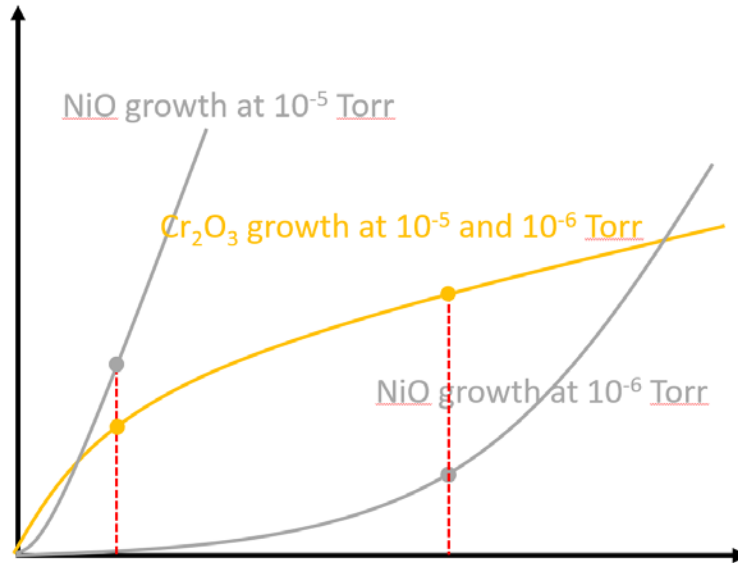
Figure 4.18 Schematics of the competitive oxidation between Cr_2O_3 and NiO on Ni-8Cr alloy with 600-grit finish at 600°C, in 10^{-5} Torr and 10^{-6} Torr oxygen. Red dash lines indicate the time when the alloy surface is covered by the oxide.

Besides the composition and oxygen partial pressure effect, surface finish also played an important role on the initial scale establishment, as indicated by the results in Figure 4.14. This surface effect was also reported by Stott et al. [77] for the oxidation of Ni-Cr alloys oxidized at

1025°C in 1 atm pure oxygen. Laser-treatment conducted on the Ni-Cr samples was found to result additional microstructure and solidification artifacts (such as ripples) [77]. This surface treatment led to additional node formation inside the grain (Figure 4.19), which was absent during the oxidation of Ni-Cr alloys without surface treatment (Figure 2.10). Consequently, faster progressive scale formation was observed on Ni-Cr alloys with surface treatment [77].
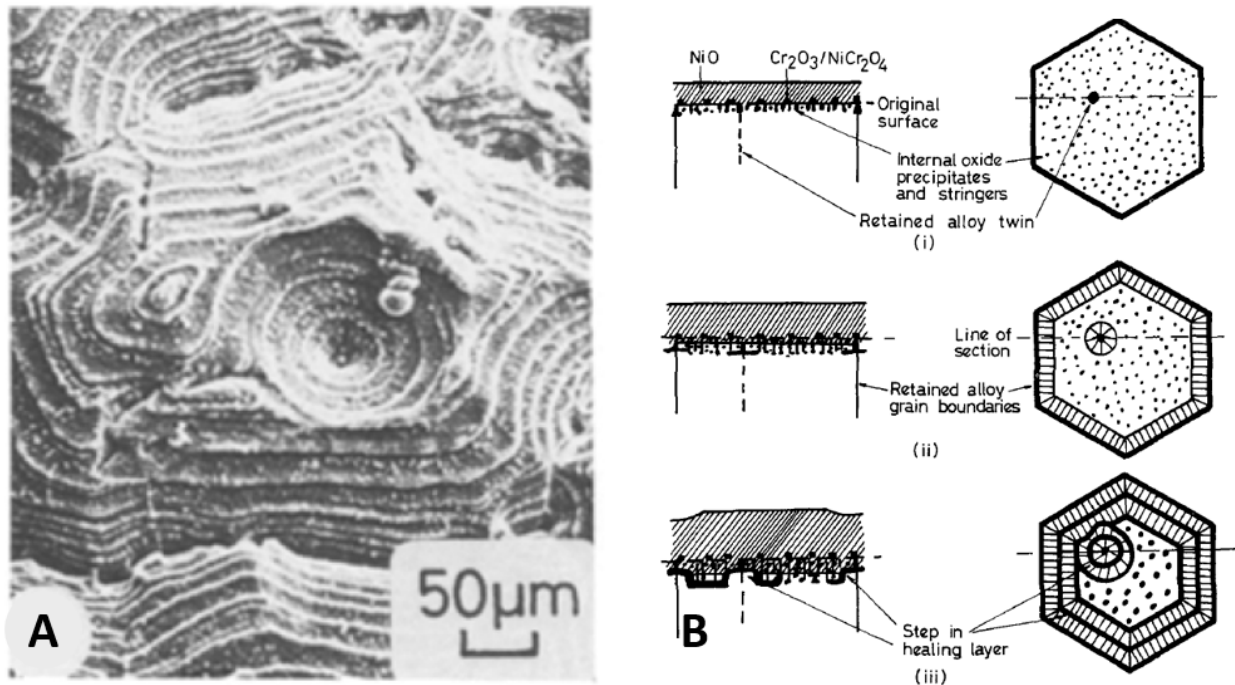
Figure 4.19 (A) SEM micrograph of the underside of scale formed on Ni-15Cr with laser surface treatment after oxidation in 1 atm oxygen at 1025°C for 1 hour, (B) Schematic representation of the progressive development of the Cr_2O_3 layer on laser treated Ni-15Cr oxidized in 1 atm oxygen at 1025°C [77].

When oxidized at 600°C, in 10^{-6} Torr oxygen, the Ni-8Cr alloy with colloidal-silica finish has a smooth surface. As a result, nodes may only form on the grain boundaries as suggested by Stott et al. [77]. The portion of grain boundaries are small compared to the entire surface so that the amount of Cr_2O_3 formed on the surface is very small, as shown in Figure 4.14c. 600-grit SiC

finish introduced more surface defect and stress into the Ni-8Cr, which led to surface recrystallization upon heating (will be discussed in detail in the following chapters). As a result, Cr_2O_3 concentration on the surface increased significantly and remained almost constant for a certain amount of time, as shown in Figure 4.14b, which indicates the formation of more protective nodes on the surface. Ni-8Cr thin film oxidized under the same condition presented the highest Cr_2O_3 concentration on the surface, as shown in Figure 4.14a. In order to understand the microstructure of Ni-Cr thin film, AFM was used to provide a 3D morphology of the alloy surface, as shown in Figure 4.20. The surface roughness of the thin film was very small (~5 nm) and little surface deformation was observed, but very fine grain structure was observed (~50nm) on the surface. This fine-grain structure provided many possible nucleation sites for the protective nodes, and led to a very high concentration of Cr_2O_3 on the surface, as predicted by Stott [77], as well as Giggins and Pettit [87].
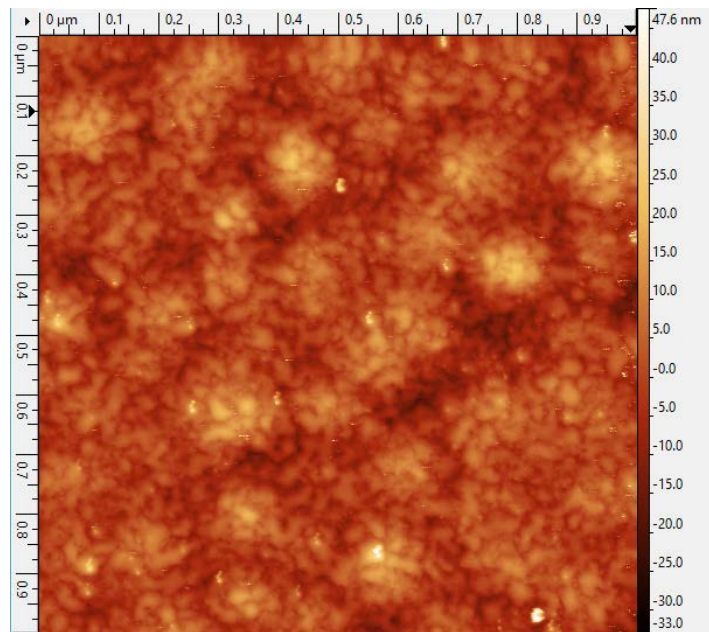
Figure 4.20 AFM image of a Ni-8Cr thin film with 500 nm thickness deposited by ebeam evaporation onto a NaCl substrate at 400℃.

Despite the relatively low concentration of Cr in the bulk Ni-8Cr alloy, a protective scale may still form during the early-stage oxidation of the thin-film sample, which had a fine-grain structure. Therefore, the surface condition and microstructure of an alloy are extremely important for the initial protective scale formation.

4.2   THIRD ELEMENT EFFECT ON THE ALUMINA SCALE ESTABLISHMENT

4.2.1   Third element effect on Al_2O_3 internal oxide formation and oxygen permeability

As introduced in section 1.4.2, the third element effect, especially the beneficial effect of Cr on Al_2O_3-scale establishment, is still not fully understood. The most cited theory is that proposed by Wagner [93], and it pertains to the so-called "gettering" effect. However, this effect is not universal. Limitations of reported "gettering" effect mechanisms proposal will be discussed in the following sections and new perspectives regarding the Cr beneficial effect will be presented.

4.2.1.1 Experimental Results

Experimental observations of internal oxidation penetration depth

Figure 4.21 shows cross-sectional samples of internally oxidized Ni-Al, Ni-8Al-XCr and Ni-8Al-XMn alloys given a 1200-grit finish prior to testing and after 4h exposure in dry air at 1100°C. The depths of the internal oxidation zone were measured and are marked on the images. The outer scale layer formed on all the alloys was inferred by EDS analysis to be NiO (not shown in Figure 4.21a, d and e due to spallation), except for Ni-8Al-8Cr, on which an exclusive Cr_2O_3/Al_2O_3 scale formed (Figure 4.21c). During the oxidation of Ni-8Al, Ni-8Al-3Cr, Ni-8Al-3Mn, and Ni-8Al-8Mn, no external or progressive protective scale formation was observed. Among the alloys that merely experienced internal oxidation, Ni-8Al-8Mn exhibited the largest penetration depth, which is 150% larger than the penetration depth measured in Ni-8Al. By contrast, the addition of 3 at% Cr into Ni-8Al significantly decreased the penetration depth (50%),

92

and the addition of 8 at% Cr generated an Al_2O_3-rich scale after 4 h. The internal oxides present in the alloys containing Cr appeared to be coarser than those in the Ni-Al binary alloy and the alloys containing Mn.
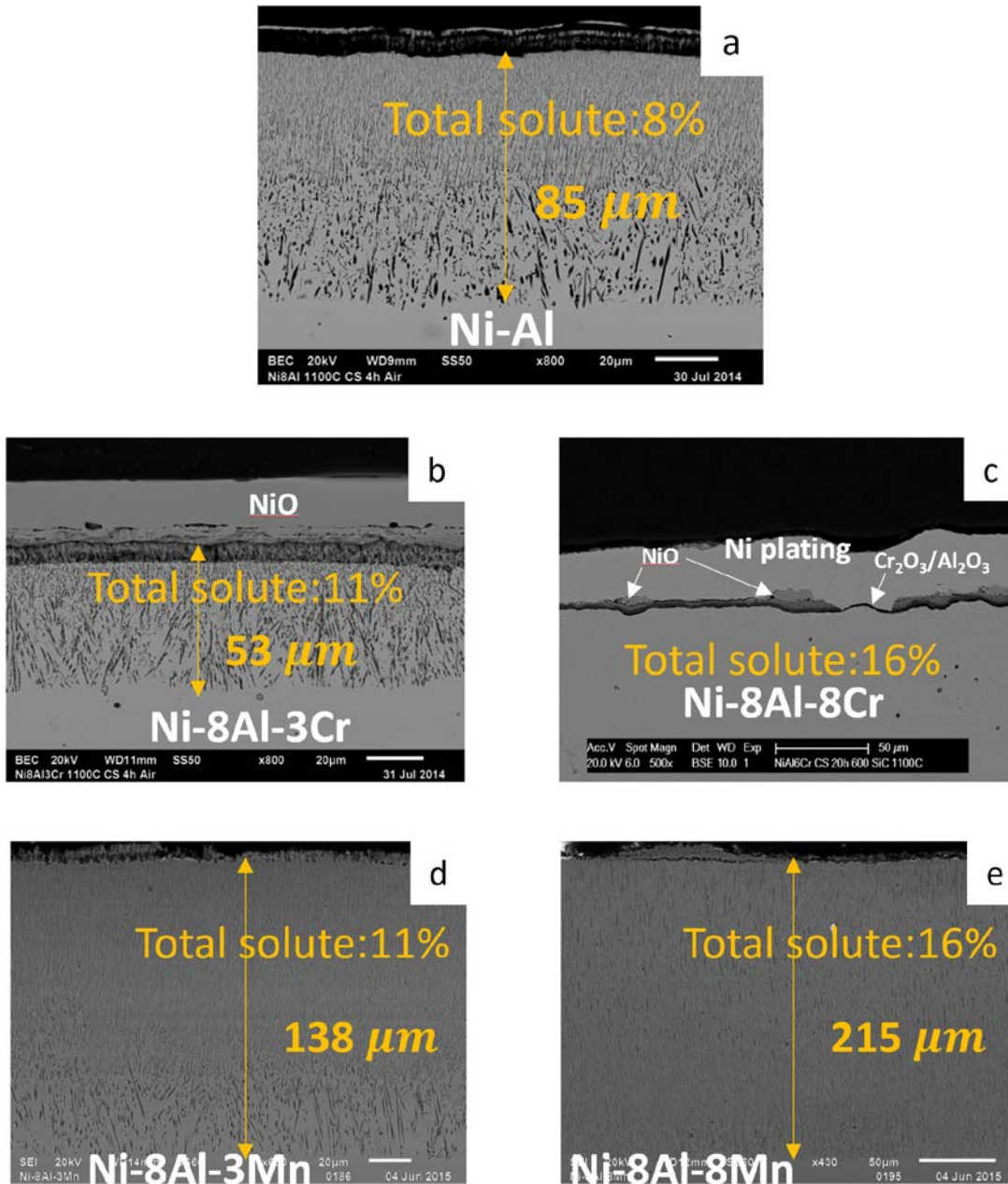
Figure 4.21 Micrographs (SEM) of cross-section samples of Ni-8Al, Ni-8Al-3Cr, Ni-8Al-8Cr, Ni-8Al-3Mn and Ni-8Al-8Mn oxidized for 4 hours in dry air at 1100°C.

The scale that formed on Ni-8Al-8Cr consisted of a layered structure. The outer layer was measured by EDS to be a Cr rich oxide, suggesting the possible existence of a Cr_2O_3 layer at the interface. The darker inner layer at the scale/alloy interface was deduced by EDS analysis to be Al_2O_3.

To better understand the third-element effect on the transition from internal to external oxidation, oxygen permeability in a given alloy calculated from the measured internal oxidation penetration depth. From the classical internal oxidation model [45, 51], the progression rate of the internal oxidation front into the alloy is governed by the inward diffusion of dissolved oxygen with negligible counter-diffusion of Al, Cr or Mn[133]. This gives internal oxidation kinetics as:

$$\frac{\xi^2}{t} = \frac{2N_O^S D_O}{\nu N_B} \tag{4.20}$$

where ξ is the penetration depth of internal oxidation, t is the exposure time, D_O is the diffusivity of oxygen, N_O^S is the atomic fraction of oxygen at the alloy surface, ν is the ratio of oxygen to Al, Cr or Mn in the internal oxide, N_B is the atomic fraction of solute ($N_B = N_{Mn} + N_{Al}$ in Ni-Al-Mn alloys, $N_B = N_{Cr} + N_{Al}$ in Ni-Al-Cr alloys) in the Ni matrix.

Due to the possible formation of spinels, there is an uncertainty in the stoichiometric coefficient, ν. However, this uncertainty in ν is small (3/2 for Al_2O_3, 2 for $NiAl_2O_4$) compared to the variation of oxygen permeability, which can be as large as an order of magnitude. Therefore, the error in the estimations (as well be discussed in detail below) on the effective stoichiometric coefficient, ν_{eff}, will not reverse the general trends of the dependency of oxygen permeability on the concentration of third elements.

In Ni-Al alloys, internal formation of $NiAl_2O_4$ was reported[78]. Based on Meijering's analysis of the kinetics of internal oxidation when two oxides form [134], and assuming $NiAl_2O_4$ to form up to the center of the internal oxidation zone, an effective stoichiometric coefficient, ν_{eff} = 1.8, can be obtained. Following similar analysis, ν_{eff} for Ni-8Al-XMn and Ni-8Al-XCr alloys

can also be estimated. Since $MnAl_2O_4$ is the only additional stable spinel phase in Ni-8Al-XMn alloys, which starts to form very rapidly close to the oxidation front (to be discussed in the following section), the internal oxides formed in Ni-8Al-XMn are expected to be Al_2O_3, $NiAl_2O_4$ and $MnAl_2O_4$ (ν=1.33, since $N_B=N_{Mn}+N_{Al}$) when X<4, and $MnAl_2O_4$ and MnO (ν=1) when X>4. Therefore, assuming all the Al and Mn were oxidized internally, $NiAl_2O_4$ forms up to the center of the internal oxidation zone, $\nu_{eff}^{Ni-Al-Mn}$ for Ni-8Al-3Mn, Ni-8Al-6Mn and Ni-8Al-8Mn is estimated to be 1.44, 1.28 and 1.25, respectively. In the Ni-Al-Cr alloys, $NiAl_2O_4$ is the only stable spinel phase, assuming $NiAl_2O_4$ to form up to the center of the internal oxidation zone (similar to Ni-Al system), which leads to $\nu_{eff}^{Ni-Al-Cr}$ = 1.71, 1.67 and 1.65 for Ni-8Al-3Cr, Ni-8Al-6Cr and Ni-8Al-8Cr, respectively.

Based on the measurements in Figure 4.21, the analysis above and equation (4.20), the oxygen permeability can be plotted as a function of the third-element concentration in an alloy, as shown in Figure 4.22, to illustrate the impact of third element on the internal oxidation. It is seen that the addition of Cr lowered the oxygen permeability, as predicated by (4.20). By contrast, the addition of Mn, which like Cr has an intermediate affinity to oxygen between Ni and Al increased the oxygen permeability in Ni.
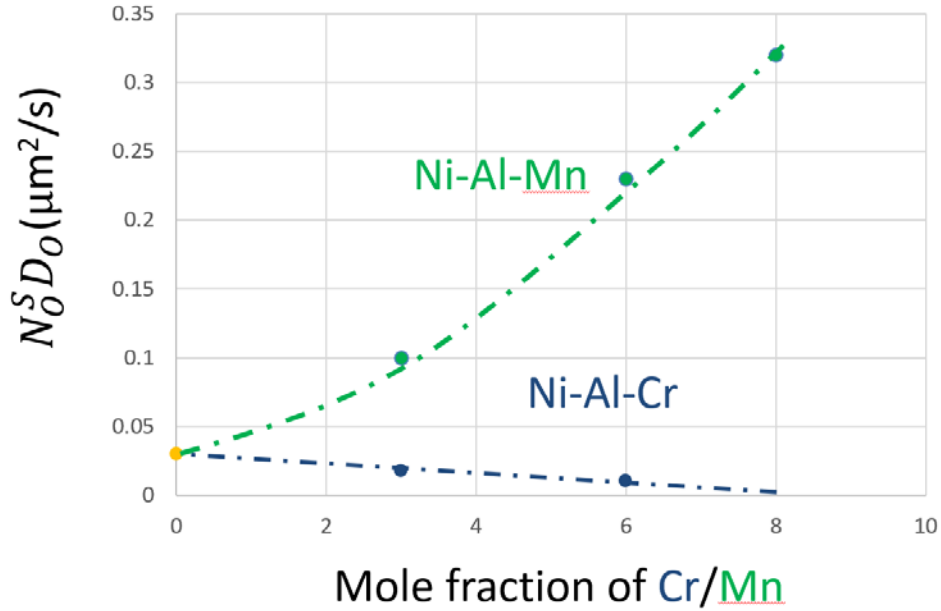
Figure 4.22 Calculated oxygen permeability in Ni-Al, Ni-Al-Cr, and Ni-Al-Mn alloy when oxidized in air at 1100℃.

Internal Al₂O₃ phase transformation and consequent morphology change

The cross-sectional samples of Ni-8Al, Ni-8Al-6Cr and Ni-8Al-6Mn were prepared by DB-FIB after 3 min of exposure in dry-air at 1100°C. The chemical composition and crystal structure of internal oxides were characterized by TEM.

The chemical composition of the internal oxides in Ni-8Al, Ni-8Al-6Cr and Ni-8Al-6Mn were indicated by EDS maps, as shown in Figure 4.23. Figure 4.23a and b show that the Ni content in the internal precipitates in Ni-8Al alloy is negligible, which indicates the primary oxide formed during the early-stage internal oxidation of Ni-8Al alloy is pure Al_2O_3. Figure 4.23c and d show Cr enrichment at the interface between initially-formed Al_2O_3 precipitates and Ni matrix, which suggests the sequential oxidation of Al followed by Cr. Figure 4.23e and f show the uniform distribution of Al and Mn in the internal precipitates in Ni-8Al-6Mn alloy.

Ni-8Al   a

Al Ni

500 nm

Ni-8Al   b

Al Ni

200 nm

Ni-8Al-6Cr   c

Cr Al Ni

1 μm

Ni-8Al-6Cr   d

Cr Al

200 nm
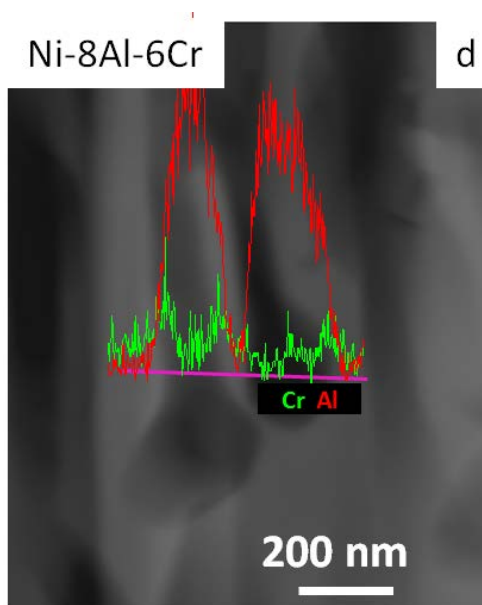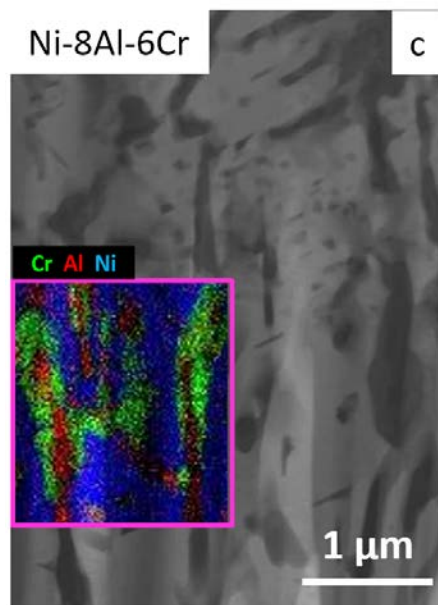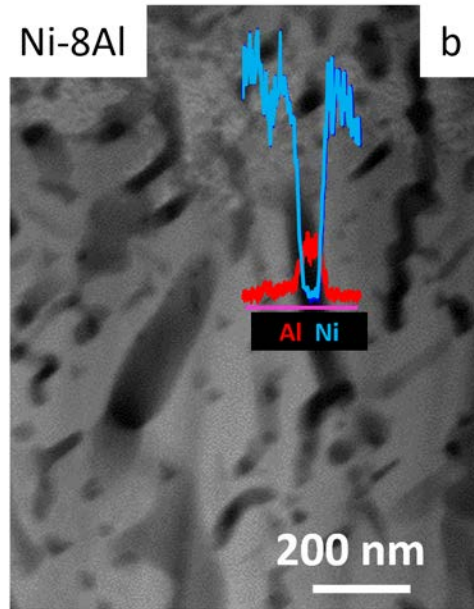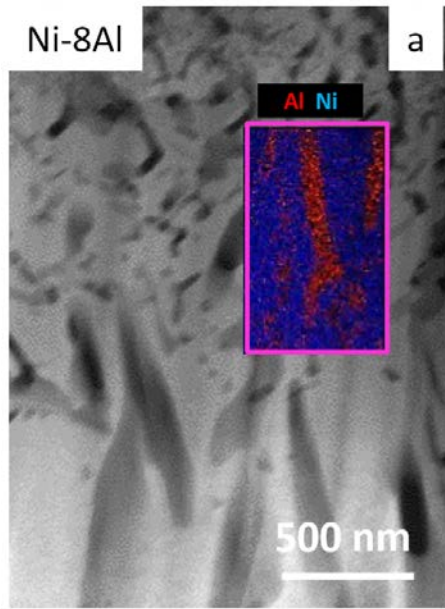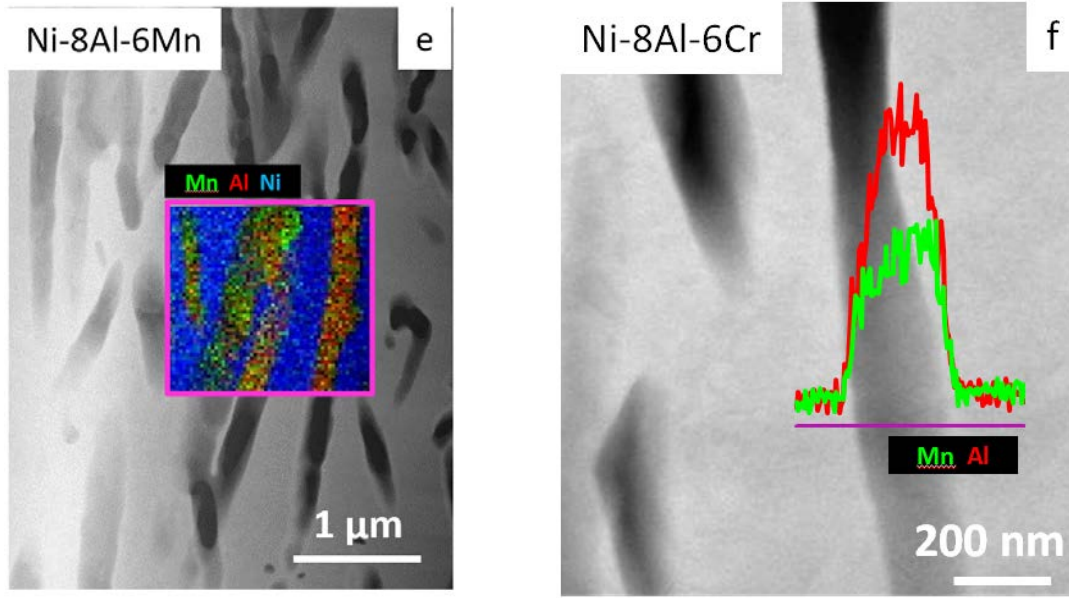
Figure 4.23 Chemical composition the internal precipitates in Ni-8Al, Ni-8Al-6Cr and Ni-8Al-6Mn after 3 min of exposure in dry-air at 1100°C. (a) EDS map of the internal precipitates in Ni-8Al alloy. (b) EDS line scan across an internal precipitate in Ni-8Al alloy. (c) EDS map of the internal precipitates in Ni-8Al-6Cr alloy. (d) EDS line scan across an internal precipitate in Ni-8Al-6Cr alloy. (e) EDS map of the internal precipitates in the Ni-8Al-6Cr alloy. (f) EDS line scan across an internal precipitate in Ni-8Al-6Mn alloy.

Due to the polymorphic nature of Al_2O_3, electron diffraction patterns were used to reveal the crystal structures and identity of internal oxides, as shown in Figure 4.24. Figure 4.24b shows a cube-on-cube orientation relationship $(001)[110]_{\gamma-Al_2O_3}$ // $(001)[110]_{Ni}$ between the internal precipitates, with a measured lattice constant of about 0.79nm, in Ni-8Al and the alloy matrix [135]. The internal precipitates were revealed as pure Al_2O_3 by the EDS, while comparison with structural data [136] leads to the deduction that the internal oxide phase formed in Ni-8Al is γ-Al_2O_3 [135, 137].

Internal oxides with corundum structure, which match the crystal structure of α-Al_2O_3 and α-Cr_2O_3 [138, 139], were primarily observed in the Ni-8Al-6Cr sample, as indicated in Figure

98

4.24d. The following crystallographic orientation relationship was observed between α-Al$_2$O$_3$/α-Cr$_2$O$_3$ and Ni matrix

$$(0001)_{\alpha\text{-}Al_2O_3/\alpha\text{-}Cr_2O_3} // (111)_{Ni} \text{ and } (\bar{1}\bar{1}20)_{\alpha\text{-}Al_2O_3/\alpha\text{-}Cr_2O_3} // (110)_{Ni}$$

The diffraction pattern obtained from Ni-8Al-6Mn showed a similar epitaxial relationship between the internal oxide and Ni matrix as the one observed in Ni-8Al binary alloy, therefore, γ-Al$_2$O$_3$ and similar structured MnAl$_2$O$_4$ spinel [140] should be expected to be presented in this alloy. The epitaxial relation between internal oxide and Ni matrix in Ni-8Al-6Cr can be expressed as

$$(001)_{\gamma\text{-}Al_2O_3/MnAl_2O_4} // (001)_{Ni} \text{ and } (110)_{\gamma\text{-}Al_2O_3/MnAl_2O_4} // (110)_{Ni}$$
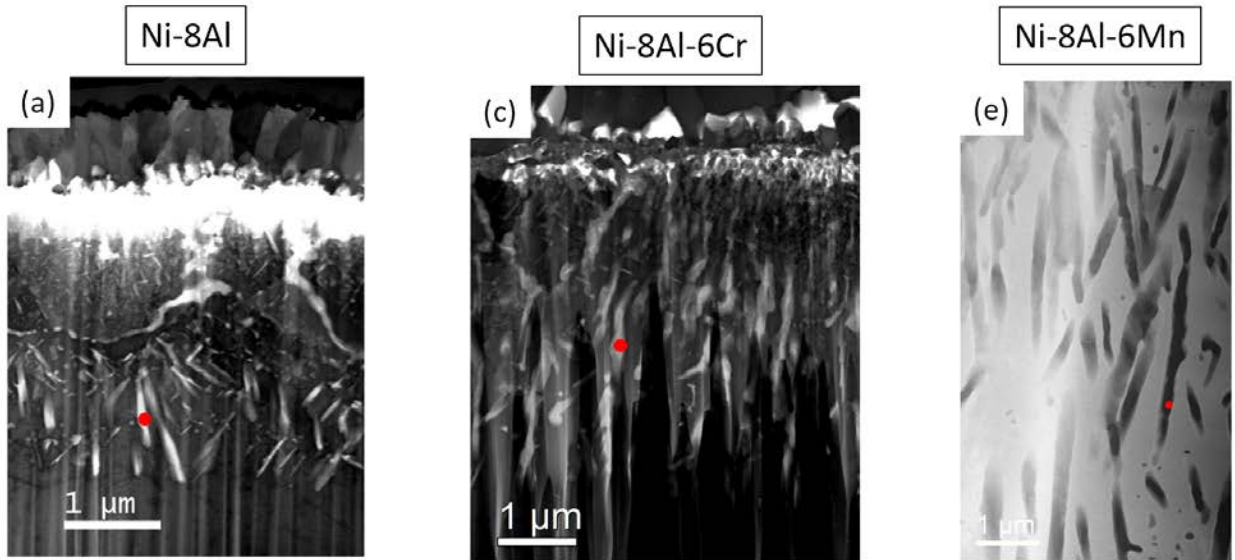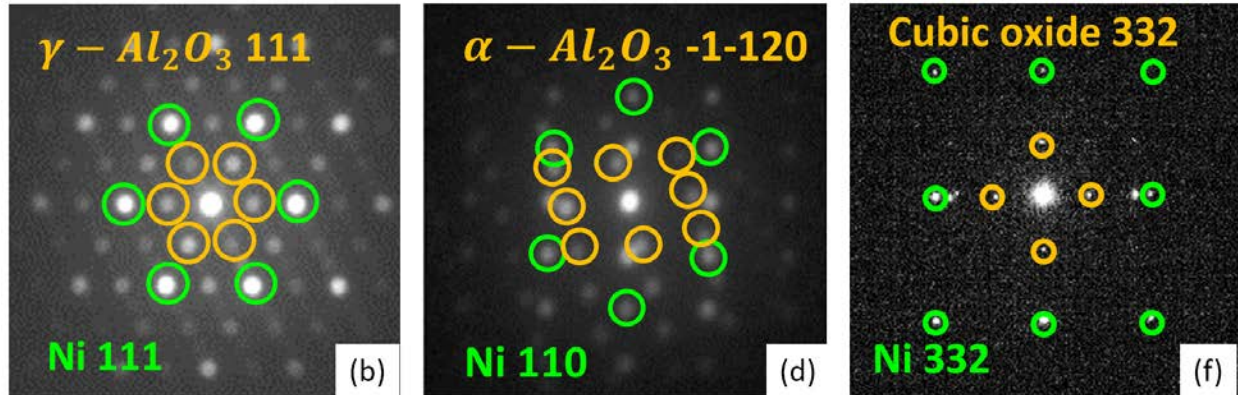
Figure 4.24 (a) STEM bright field image of Ni-8Al after 1 minute of exposure in dry-air at 1100°C, and (b) corresponding electron diffraction. (c) STEM bright field image of Ni-8Al-6Cr after 3 minutes of exposure in dry-air at 1100°C, and (d) corresponding electron diffraction. (e) STEM dark field image of Ni-8Al-6Mn after 3 minutes of exposure in dry-air at 1100°C, and (f) corresponding electron diffraction.

4.2.1.2 Discussion

Aluminum oxide can exist in a variety of crystallographic forms depending on its reaction pathway [141]. Among all the alumina polymorphic phases, α-Al_2O_3 is thermodynamically the most stable. However, the activation energy for the formation is significantly higher than other for alumina phases. Hence, the transformation to α-Al_2O_3 is generally observed at higher temperatures in comparison with the metastable phases, typically at above 1000°C) [135, 142, 143]. Several studies concerning the polymorphic phase transformations of alumina from the metastable alumina phases (e.g., κ-, γ-, θ-Al_2O_3) to the stable α-Al_2O_3 have been conducted [85, 97-99, 144-146]. In general, it is believed that being in contact with a crystal, which has the same or a similar structure as α-Al_2O_3, will accelerate the transformation process. This crystal, which promotes the phase transformation, is usually referred as a "seed" or "template". On the other hand, if the substrate has a similar structure as a given metastable alumina (e. g. γ-Al_2O_3), the α-Al_2O_3 transformation could also be slowed [147, 148].

At lower temperatures and/or the early stage of oxidation metastable alumina phases form due to their rapid growth kinetics[80]. Although alumina has multiple structures which can form, γ-Al_2O_3 was the predominant metastable phase observed in the internal oxidation zone of Ni-Al alloys [135]. This may be due to the lower interfacial energy between γ-Al_2O_3 and Ni matrix, which are of the same crystal structure [135]. Both (111) planes and (100) planes of γ-Al_2O_3 (111) can be Al-terminated, as indicated in Figure 4.25.
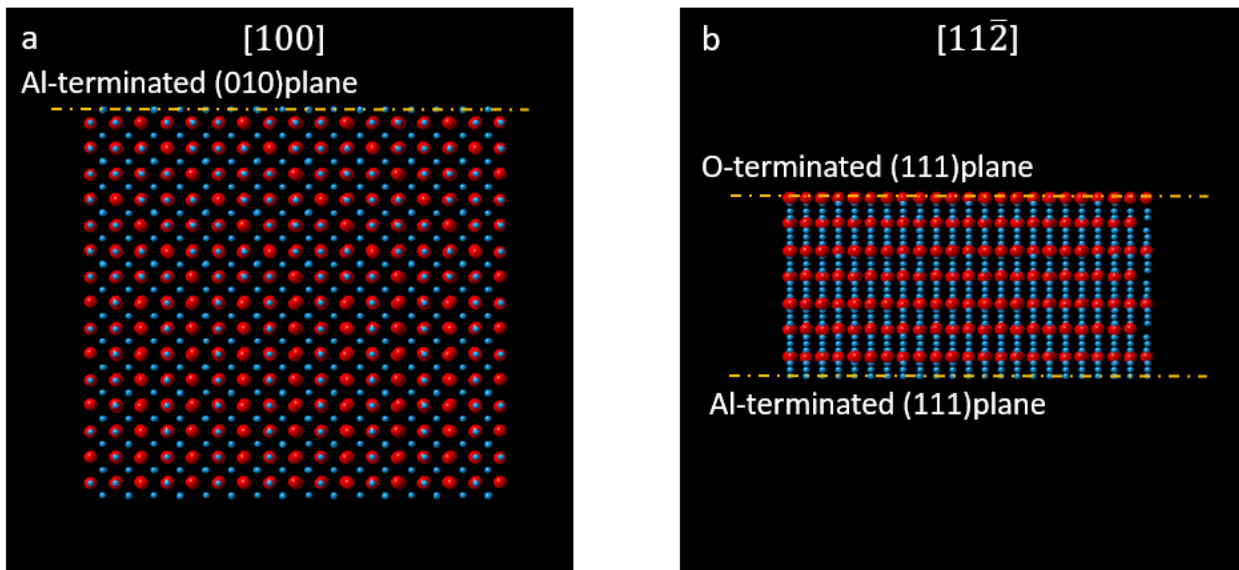
Figure 4.25. (a) γ-Al_2O_3 crystal structure viewed in [100] direction. (b) γ-Al_2O_3 crystal structure viewed in [11$\bar{2}$] direction.

The lattice mismatch between the Ni matrix and γ-Al_2O_3 is about 10%, with the γ-Al_2O_3 typically defined as a defective spinel structure with 6% Al vacancies ($Al_{21+1/3}\square_{2+2/3}O_{32}$). Replacing Al atoms with vacancies at high-energy configuration sites can significantly decrease the interfacial energy between the Ni matrix and γ-Al_2O_3 that is surface terminated by Al [149]. Due to the four-fold symmetry of the f.c.c. structure, the internal γ-Al_2O_3 precipitates in the Ni

matrix could have a square cross-section with each interface corresponding to a low energy configuration, thus resulting in a very low overall interfacial energy.

On the other hand, α-Al$_2$O$_3$ has a stable and compact corundum structure, which is quite different from the crystal structure of Ni (f.c.c.). Indeed, only one interface configuration (0001)$_{\alpha\text{-Al}_2\text{O}_3}$ // (111)$_{Ni}$ has a relatively small lattice mismatch (4.4%) [150], as indicated in Figure 4.26. This small-lattice-mismatch interface configuration is expected to be the lowest energy configuration [151]. Since α-Al$_2$O$_3$ and Ni do not have the same crystal structure, only a two-fold symmetry is common.
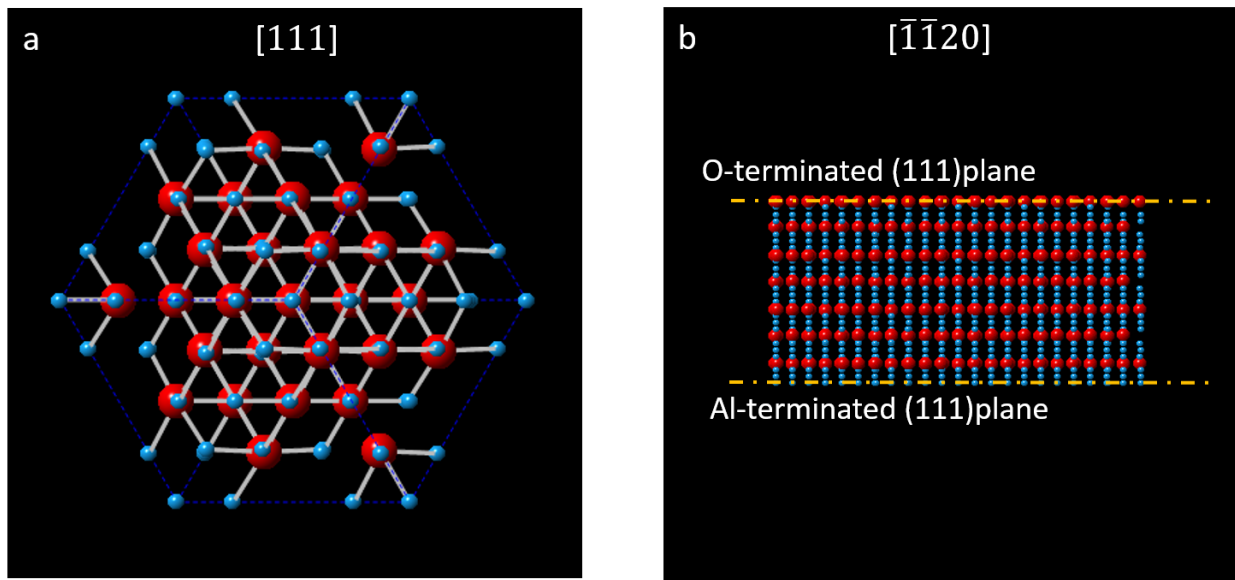
Figure 4.26 (a) α-Al$_2$O$_3$ crystal structure viewed in [111] direction. (b) α-Al$_2$O$_3$ crystal structure viewed in [$\bar{1}\bar{1}20$] direction.

However, for an internal precipitate with a given volume, a platelet morphology (rectangular cross-section) will have a higher total interfacial area compared to a rod-like morphology with square cross-section, as schematically shown in Figure 4.27. γ_γ^{low} and γ_α^{low} are

the lowest interfacial energies that can be achieved by γ-Al₂O₃ and α-Al₂O₃, respectively, when precipitated in Ni matrix; γ_α^{high} represents the interfacial energy between a plane perpendicular to the (111) of α-Al₂O₃ and the Ni matrix, which would be higher than γ_γ^{low}. Due to the symmetry, as discussed above, all the interfaces between γ-Al₂O₃ and Ni should be γ_γ^{low}, then, the total surface energy for γ-Al₂O₃ can be calculated to be

$$\gamma_\gamma = \gamma_\gamma^{low}(1*2 + l*4) = \gamma_\gamma^{low}(2+4l) \tag{4.21}$$

Similarly, the total surface energy for α-Al₂O₃ can be calculated to be

$$\gamma_\alpha = \gamma_\alpha^{high}(2+2wl) + \gamma_\alpha^{low}*2l/w \tag{4.22}$$

where w is the width of the platelet (Figure 4.27b).
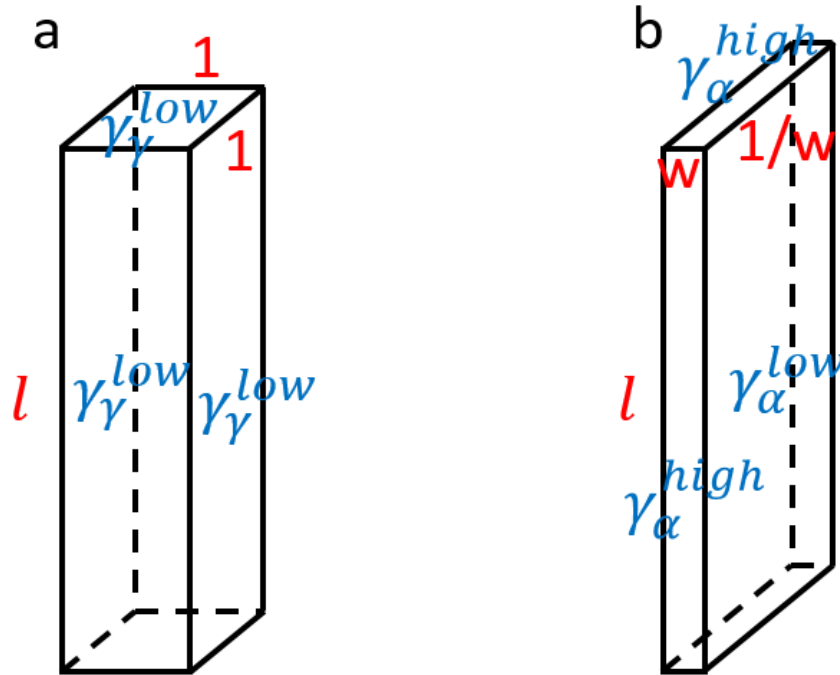
Figure 4.27 (a) A square with unit area. (b) A triangle with unit are.

103

To minimize interfacial energy, an optimized platelet width can be obtained by differentiating equation (4.22)

$$2l\gamma_\alpha^{high} - \gamma_\alpha^{low} * \frac{2l}{w^2} = 0 \tag{4.23}$$

$$w = \sqrt{\frac{\gamma_\alpha^{low}}{\gamma_\alpha^{high}}} \tag{4.24}$$

By inserting equation (4.24) into (4.22), γ_α can be rewritten as

$$\gamma_\alpha = 4l\sqrt{\gamma_\alpha^{high}\gamma_\alpha^{low}} + 2\gamma_\alpha^{high} \tag{4.25}$$

Depending on the values of γ_α^{high}, γ_α^{low} and γ_γ^{low}, the difference between γ_α and γ_γ could be significant. For example, setting the $\gamma_\alpha^{high} = 2\gamma_\alpha^{low} = 2\gamma_\gamma^{low}$, the difference between γ_α of a platelet-shaped internal α-Al₂O₃ with optimized width and γ_γ of a rod-like internal γ-Al₂O₃ is more than 40%.

Indeed, based on nucleation theories, $\Delta G = V\Delta G_V + \sum_i A_i\gamma_i$ [60, 61]. During the nucleation and initial growth stages of the internal precipitates, when the particles are very small, interfacial energy is extremely important. Moreover, γ-Al₂O₃, which has a much faster growth rate, such that it is kinetically favored at lower temperature [80]. Consequently, γ-Al₂O₃ is the preferred phase during the early-stage internal oxidation of Ni-Al alloys.

Even if the γ-Al₂O₃ is the preferred phase during the early-stage oxidation, the transformation to α-Al₂O₃ will eventually occur, due to the more stable structure of α-Al₂O₃. Bobeth et al. [152] developed the following estimation for compression stress associated with the volume expansion introduced by internal oxidation.

$$\Delta G_v^{stress} = \Delta\sigma \cdot V = \frac{3N_{Al}\gamma^2 kT}{\Omega_{Ni}^2 D_{Ni}}\Delta V \tag{4.26}$$

There are two contributing factors that can be changed due to the γ to α phase transformation: interfacial energy (γ_i) and volume expansion (ΔV). Since the molar volume of α-Al_2O_3 is about 14% smaller than γ-Al_2O_3 [153], and the penalty from the interfacial energy γ_i will also decrease as the internal oxide transitions from γ to α due to the formation of coarser internal oxides (as will be discussed in detail in the following analysis). Consequently, the compressive stress will accelerate the γ-Al_2O_3 to α-Al_2O_3 transformation. The higher the Al content in the alloy, the larger the volume expansion due to oxidation, and thus, the higher the compressive stress will be.

With the addition of a third element, the interface between internal oxides and matrix will be altered, and as a result, the interfacial energy may change significantly, which can impact the γ to α Al_2O_3 phase transformation. In the case of Cr, the transformation is significantly accelerated, as shown in Figure 4.24, where α-Al_2O_3 was formed in Ni-8Al-6Cr alloy after the oxygen exposure at 1100°C for only 3 minutes. Since conventional selected area electron diffraction pattern cannot provide precise structural information for every individual internal oxide, PED-TEM phase map was used to visualized the internal oxide structures formed in Ni-8Al and Ni-8Al-6Cr after 3-minute air exposure at 1100°C, as shown in Figure 4.28. Each color in the phase map below represents a crystal structure. By comparing the crystal structures with a preset data base, different phases were identified, where blue represents the Ni matrix, yellow represents γ-Al_2O_3, and red represents α-Al_2O_3.
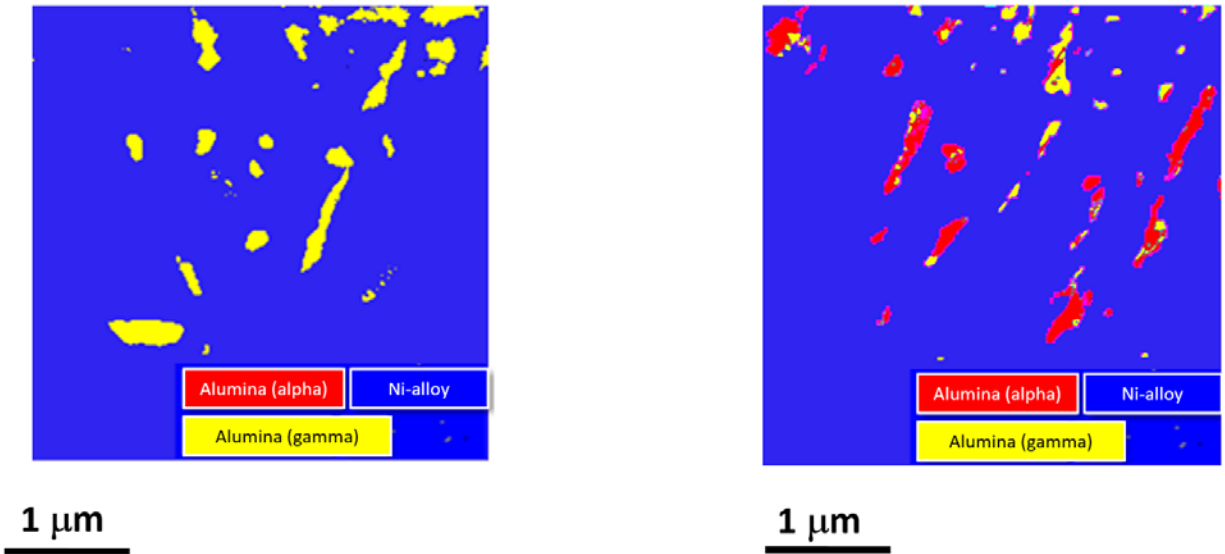
Figure 4.28 PED-TEM phase map of internal oxide of (a) Ni-8Al alloy oxidized in air at 1100℃ for 3 minutes. (b) Ni-8Al-6Cr alloy oxidized in air at 1100℃ for 3 minutes.

Without Cr addition, only γ-Al_2O_3 was detected in the internal oxidation zone of Ni-8Al alloy. Adding just 6 atomic percent of Cr into the binary alloy, α-Al_2O_3 becomes the primary oxide structure after oxidation under the same oxidation condition. This dramatic change of oxide structure, could be attributed to the change of interface structure between the internal oxide and the Ni matrix. The presence of Cr changes the γ-Al_2O_3/Ni interface to an enveloped structure of α-Al_2O_3/Cr_2O_3/Ni due to the segregation of Cr to the initially-formed Al_2O_3, as shown in Figure 4.23 (c) and (d). This is supported by the observation of isolated internal γ-Al_2O_3 particles without surrounding Cr-containing envelop in Ni-Al-Cr alloys, as shown in Figure 4.29. The yellow circles in this figure highlight an individual internal oxide with an enveloped structure, which was identified by PED-TEM phase mapping as α-Al_2O_3, while the blue circles highlight an internal oxide without the presence of a Cr-containing envelop. This internal oxide was identified to be γ-Al_2O_3. There is also a Cr depleted zone (CDZ) near the internal oxidation front (IOF), in which the Cr concentration is too low to be detected by EDS map. In this zone, most Al_2O_3 internal oxides

106

were detected by the EDS map, but not detected by the PED-TEM. This may have been caused by the perfect epitaxial relationship between Al_2O_3 and Ni-matrix and/or lattice expansion/compression due to the stress, which make it difficult for PED-TEM to distinguish the crystal structure of internal oxide and the Ni matrix. This discrepancy in phase maps provided by PED-TEM and EDS indicates the cubic crystal structure of Al_2O_3 internal oxides in CDZ, which corresponds to γ-Al_2O_3.
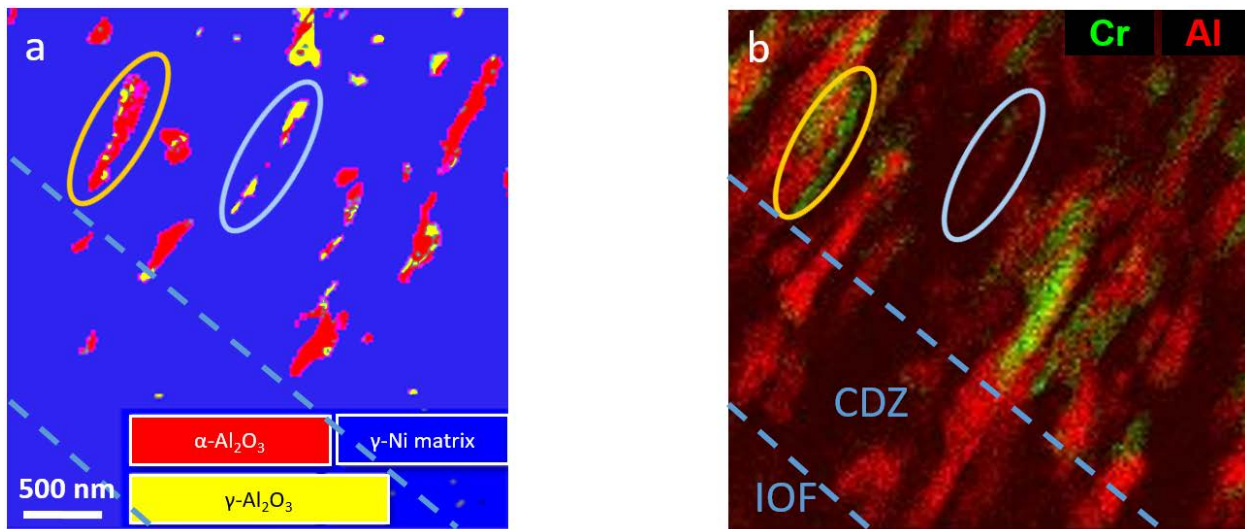
Figure 4.29 Phase mapping and elemental mapping of Ni-8Al-6Cr alloy oxidized in air for 3 minutes at 1100°C. (a) PED-TEM phase mapping, (b) EDS elemental mapping of the same sample area.

Since the dissociation oxygen pressure of Cr_2O_3 is much higher than that of Al_2O_3, only at the locations, where Al concentration is low enough due to the initial internal oxidation, the replacement reaction (4.27) may occur, and Cr_2O_3 nuclei can be stable, i.e.,

$$Cr + Al_2O_3 \rightarrow Cr_2O_3 + Al \tag{4.27}$$

Based on the internal oxidation theories [52], at Al_2O_3/Ni interface, the concentration of Al is the lowest, which can result in the highest possibility for the replacement reaction (4.27) to

occur. Additionally, there will be more dislocations and defects at Al_2O_3/Ni interface due to the lattice mismatch, which can lower the nucleation barrier for Cr_2O_3. As a result, Al_2O_3/Ni interface is the preferred location for the Cr_2O_3 nucleation, and this leads to the formation of Al_2O_3/Cr_2O_3/Ni enveloped structure, as shown in Figure 4.23c and d. Near the internal oxidation front, where the nucleation and growth of Al_2O_3 are taking place, Al concentration in the matrix may remain high enough to prevent the Cr_2O_3 formation, and the initially-formed Al_2O_3 provide fast short-circuit diffusion path for Cr towards the alloy surface. Consequently, a CDZ would form near the internal oxidation front as indicated by the EDS map (Figure 4.29b).

Chromium has only one stable oxide phase, α-Cr_2O_3, under the present oxidation condition, which has a corundum structure similar to α-Al_2O_3 [154, 155]. The formation of Cr_2O_3 can change the Al_2O_3/γ-Ni interface, which favors γ-Al_2O_3 formation, to Al_2O_3/α-Cr_2O_3 interface, which tends to have a lower interfacial energy if Al_2O_3 is the α-corundum structure. As a result of this "template" effect, the transformation from γ-Al_2O_3 to α-Al_2O_3 can be accelerated by the interfacial formation of Cr_2O_3. The entire kinetic process for the formation of internal oxide, including nucleation of Al_2O_3, formation of Cr_2O_3 and phase transformation of alumina, as deduced from this study, is schematically summarized in Figure 4.30. There is no study concerning the transformation speed from γ-Al_2O_3 $\rightarrow$ α-Al_2O_3 accelerated by the presence α-Cr_2O_3, but a rough estimation can be conducted based on the transformation speed measurement of γ-Al_2O_3 on sapphire (α-Al_2O_3) substrate [85, 144]. Depending on the crystallographic orientation, the transformation velocity varies from v_t =0.5 nm/s (c – plane) to 5 nm/s (R – plane) at 1100°C. A typical rod-like internal oxide has a radius, r, of about 50 nm, as shown in Figure 4.24b. If only the lateral transformation is considered, the time required to complete the γ-Al_2O_3 $\rightarrow$ α-Al_2O_3 transformation can be estimated by r/v_t, which gives a very short time (10 – 100 seconds).

Therefore, the primary alumina phase in the internal oxidation region tends to be α-Al$_2$O$_3$, even if the initial nuclei could be γ-Al$_2$O$_3$, as indicated by the PED-TEM (Figure 4.29). Besides the lateral transformation, a vertical transformation should also be expected due to the contact between transformed α-Al$_2$O$_3$ and untransformed γ-Al$_2$O$_3$ in a single internal oxide particle. If the growth rate of the internal oxide, which is approximately the same as the internal oxidation speed, v_i, assuming vertical rod-like internal oxide formation, is slower than the transformation velocity v_t, there may not be any detectable γ-Al$_2$O$_3$ phase even near the oxidation front, where Cr is absent.
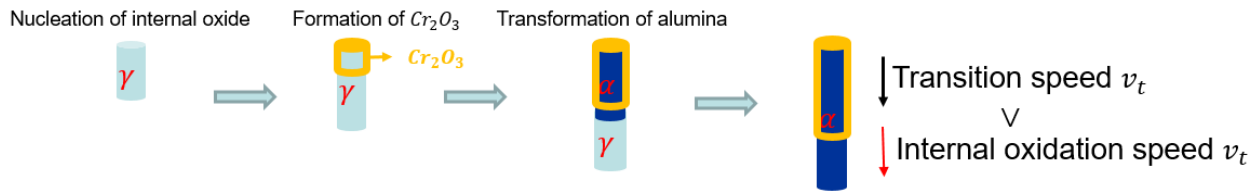
Figure 4.30 Schematics for the internal oxide formation.

Due to the crystal structure change of the internal precipitates, and the epitaxial relationship between the internal precipitates and Ni matrix, the preferred morphology of internal oxides is also changed. As discussed earlier, γ-Al$_2$O$_3$ prefers a rod-like morphology with a square cross-section; while, α-Al$_2$O$_3$ prefers platelet morphology. Consequently, the phase transformation of internal oxides resulted in them having a coarser and more dendritic morphology in Ni-Cr-Al alloys, as shown in Figure 4.31b.

The same analysis regarding the third-element effect on the internal polymorphic alumina particles can also be applied to the Mn-containing alloys. During the internal oxidation of Ni-Al-Mn alloys, Mn will be oxidized after the depletion of Al. However, no significant enrichment of Mn was observed surrounding the internal oxides (Figure 4.23e). This is a consequence of the rapid formation of MnAl$_2$O$_4$, due in part to the extremely low solubility of MnO in Al$_2$O$_3$ [156].

The spinel MnAl$_2$O$_4$ is thermodynamically more stable than MnO. So separate MnO phase may not readily form [157]. Instead of forming an enveloped structure similar to what was found in the in Ni-Cr-Al system, continuous Mn oxidation and dissolution into $\gamma - Al_2O_3$ occurred in Ni-Mn-Al alloys. The formation of MnAl$_2$O$_4$ eliminated the possibility of the γ→α phase transformation by stabilizing the cubic crystal structure of the internal oxides. Due to the same four-fold symmetry, rod-like morphology with square cross-section should remain the preferred shape for the internal oxides. This is consistent with the experimental results, as shown in Figure 4.31c. The morphology of internal oxides formed in Ni-Al-Mn alloys was very similar to that in Ni-Al alloys, as shown in Figure 4.31a and c. However, the addition of Mn changed the growth direction, the size of the internal oxides, and the oxide/matrix interface (from γ-Al$_2$O$_3$/Ni to MnAl$_2$O$_4$/Ni). These aspects will be discussed in the following.
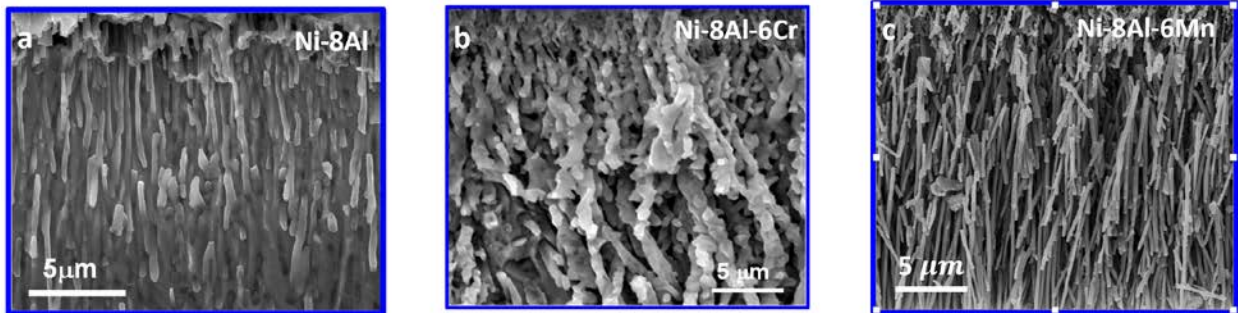
Figure 4.31 Morphology of internal oxides in (a) Ni-8Al, (b) Ni-8Al-6Cr and (c) Ni-8Al-6Mn after oxidization for 4 hours in dry air at 1100°C.

According to Wagner's theory regarding the transition from internal to external oxidation [45, 51], the critical concentration depends on the oxygen permeability $N_O^s D_O$, which is the product of oxygen surface concentration N_O^s and oxygen diffusivity D_O. The classic "gettering" effect [93] only takes into account the impact of third element on N_O^s, but not D_O. It is evident that D_O is highly

dependent on the morphology of internal oxides, which is in accordance with previous studies on the internal oxidation of Ni-Al and Ni-Cr systems [133, 158, 159]. The addition of a third element can also change the internal oxide morphology dramatically as shown in Figure 4.31. Therefore, an investigation regarding the impact of a given third element on the internal oxide morphology and the effective oxygen diffusivity in the internal oxidation zone is crucial for the improved understanding of internal to external oxidation transition.

The presence of internal oxide precipitates in the matrix can either act as fast-diffusion paths for oxygen inward diffusion through oxide/matrix interface or have a blocking effect due to the extremely low diffusivity of oxygen in the oxide phase. According to a study by Stott et al. [133], the effective diffusion coefficient for oxygen in the internal oxidation zone can be given by:

$$D_O^{eff} = D_O^l(1 - A_{ox}) + D_O^i A_i \qquad (4.28)$$

where D_O^l and D_O^i are the lattice and interfacial diffusion coefficient of oxygen, A_{ox} and A_i are the area fractions of oxide and oxide/matrix interface respectively.

This effective diffusion coefficient for oxygen highly depends on the internal oxide morphology, and may significantly deviate from the lattice diffusion coefficient of oxygen in the matrix [133, 158, 159]. Following the method presented by Martinez-Villafane et al. [158], Stott et al. [133] and Whittle et al. [159], the effective diffusivity of oxygen in the internal oxidation zone is given by

$$D_O^{eff} = D_O^l \left(1 - \frac{N_{BO_v} V_{BO_v}}{V_A} cos\theta\right) + \frac{2D_O^i \delta N_{BO_v} V_{BO_v}}{V_A r} cos\theta \qquad (4.29)$$

where N_{BO_v} and V_{BO_v} are the mole fraction and molar volume of the internal oxides, v is the ratio of oxygen to metal atoms in the oxide, V_A is the molar volume of the alloy, δ is the width of the interface, r is the radius of internal oxides, and θ is the inclination angle as shown in Figure 4.32

111

(the angle between an internal oxide platelet and the direction perpendicular to the surface). N_{BO_v} is identical to the original fraction of B in the alloy (N_B).
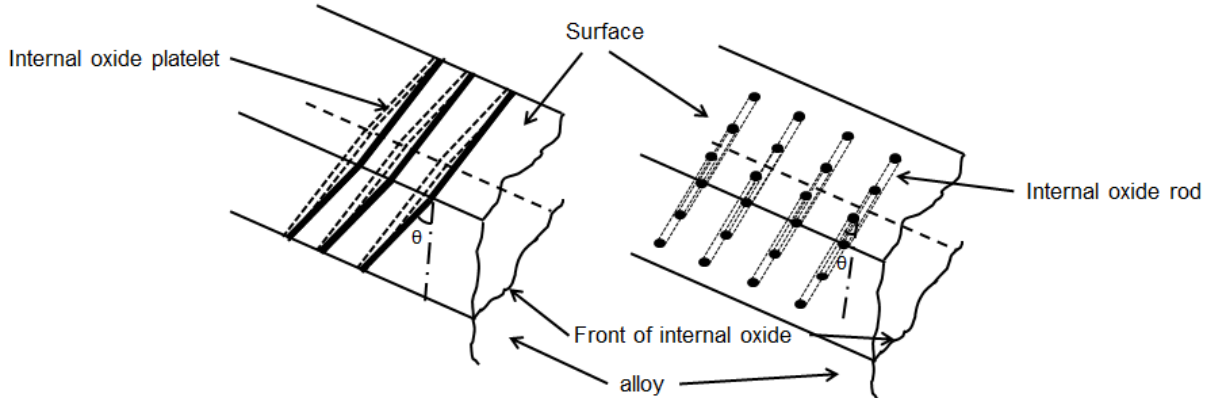
Figure 4.32 Schematic representation of two limiting cases for the internal oxide morphology: platelet-like internal oxides and rod-like internal oxides.

It is generally accepted that the solubility of oxygen at the external oxide/alloy interface, N_O^S, is independent of the initial solute concentration in the alloy since the alloy matrix is virtually pure Ni and the solubility of oxygen is determined by the equilibrium between NiO and Ni [133, 158, 159]. Hence, the permeability of oxygen in the internal oxide zone can be estimated by multiplying the N_O^S measured in pure Ni by the diffusion coefficient of oxygen as indicated by equation (4.29).

According to equation (4.29), if the morphology and size of internal oxides does not change with the continuous addition of third element, then the permeability of oxygen should increase linearly with the addition of the third element (due to the increase of N_B). This is consistent with the experimental results obtained from the addition of Mn in to Ni-Al system (Figure 4.22 green curve from 3at% Mn to 8at%Mn). However, the linear dependence cannot be extrapolated to 0

at% Mn. This can be interpreted as the change of internal oxide phase due to the addition of Mn (i.e., the formation of $MnAl_2O_4$), and thus, the oxide/matrix interface ($D_O^i \delta$) and internal oxide morphology ($\frac{cos\theta}{r}$).

The addition of Cr accelerates the corundum α-Al_2O_3 formation and, as a result, it disrupts the rod-like internal oxide morphology and leads to a much coarser and more dendritic-like internal oxide structure (r increases from 0.4-0.7μm in Ni-8Al to 1-1.4μm with the addition of 6at% Cr). Such a change serves to decrease the effective oxygen diffusivity in the internal oxidation zone.

In summary, the addition of Cr to the Ni-Al system can decrease both the N_O^s and D_O, and hence the oxygen permeability. Although Mn has similar affinity to the oxygen as Cr, and the addition into the same alloy system may decrease the N_O^s, it does dramatically increases the D_O^{eff}. Thus, the oxygen permeability still increases despite the decrease of N_O^s. Therefore, even though the addition of either Cr or Mn can decrease the oxygen solubility in the Ni-Al alloy as suggested by classical "gettering" effect, only the addition of Cr is found to be beneficial to the alumina scale establishment independent of the concentration.

4.2.2   Temperature and surface finish effects on the short-circuit diffusion and protective scale establishment

As mentioned in previous sections, the oxidation conditions and alloy structure will have an impact on the scale establishment. In this section, the temperature effect and surface finish effect will be discussed.

4.2.2.1 Temperature and heating rate in the furnace

Oxidation experiments were carried out in a horizontal tube furnace with a preset temperature ranging from 800˚C to 1150˚C and a steady stream of dry air (working gas at 1 atm). Samples were pushed into and pulled out of the hot zone very rapidly.

The oxidation time used in present study is the time for how long the sample stays in the hot zone. Therefore, the heating process, during which the sample's temperature steadily increases until it reaches a given preset temperature, is included in this oxidation time. The temperature profiles for different preset temperature were measured by a thermo-couple attached to a sample surface (Figure 4.33). It is seen in Figure 4.33 that the time to reach the preset temperature and maximum heating rate, $(dT/dt)_{max}$ vary from 60s and 48℃/s for 1150℃ to 250s and 10℃/s for 600℃. Higher preset temperature will result in faster heating rate.
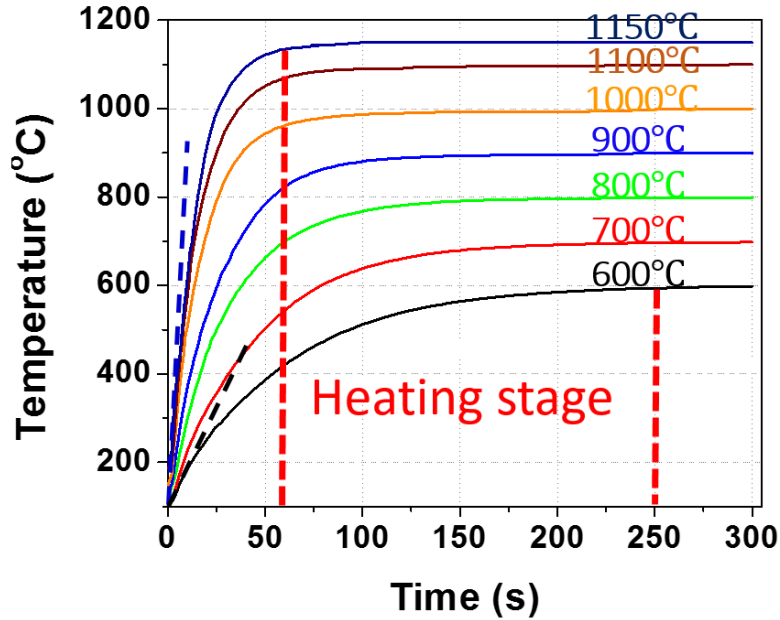
Figure 4.33 Temperature profile of samples' surface when pushed into the hot zone of the horizontal furnace under different preset temperature.

4.2.2.2 Surface recrystallization introduced by the polishing

Surface polishing was previously reported to introduce deformation to the alloy surface, which will lead to a surface recrystallization upon subsequent annealing [87]. The amount of deformation produced by polishing depends on a number of variables (e.g., grit size, force, grit sequence etc.), but the recrystallized grain structures were revealed in this study by the cross-section of polished alloys annealed in vacuum. By contrast, the samples prepared with a final polishing using colloidal-silica suspension (after the polishing using a series of SiC paper and then diamond suspension), presented virtually no surface recrystallization after annealing in vacuum at 1100 ˚C for 3 minutes, as shown in Figure 4.34.
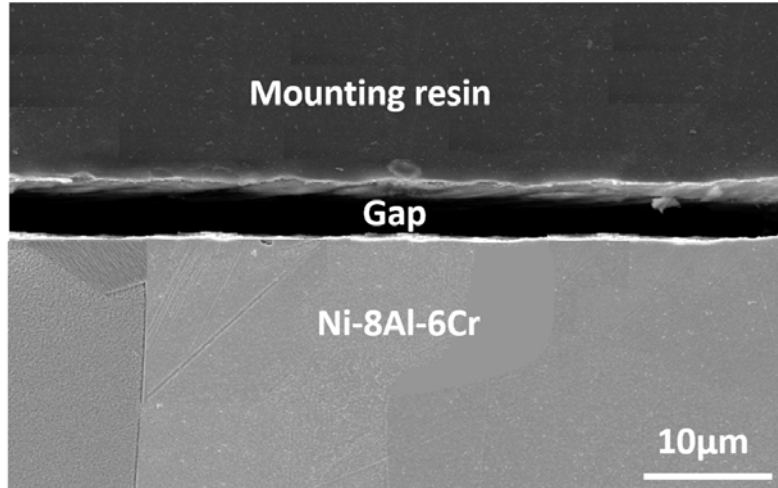
Figure 4.34 Ni-8Al-6Cr with colloidal-silica finish annealed at 1100°C in vacuum for 3 minutes.

A rougher polishing, such as 500-grit SiC paper, introduced a significant amount of surface deformation and surface recrystallization upon the annealing, as shown in Figure 4.35a. However, due to the no-uniform force applied during the polishing, the amount of surface deformation was not uniform. As a consequence, the surface-recrystallization behavior was not uniform. Figure 4.35 shows a cross-section of the Ni-8Al-6Cr specimen polished to a 500-grit SiC paper and then annealed in vacuum at 1100˚C for 3 minutes. The average grain diameter of this alloy was ranging from 50-500μm, but the grain size at the specimen surface, where surface recrystallization occurred (Figure 4.35a), was reduced to an average diameter of about 1μm. There were also regions in which there was no evidence of surface recrystallization (Figure 4.35b). In summary, the gentler the polishing the less the surface recrystallization would occur under the same annealing condition.

116
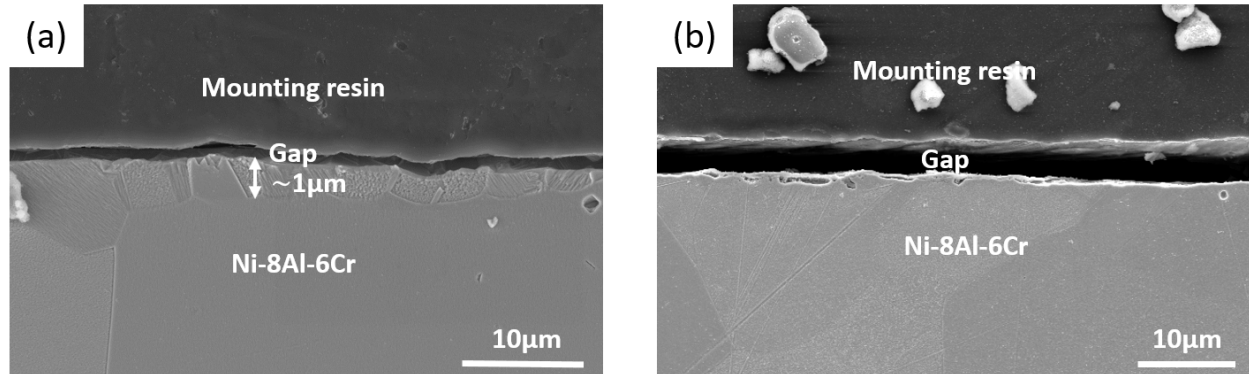
Figure 4.35 Micrographs (SEM) of cross-section sample of Ni-8Al-6Cr specimen polished by 500-grit SiC paper and annealed in vacuum at 1100˚C for 3 minutes. (a) Regions with significant amount of surface recrystallization. (b) Regions without evident surface recrystallization.

This non-uniform surface recrystallization was found to be correlated with non-uniform scaling behavior during the early-stage oxidation, as shown in Figure 4.36. After 3-minute oxidized in air at 1000°C, a portion of Ni-8Al-4Cr specimen surface, which was polished to a 500-grit SiC finish, was covered by the fast growing NiO, while the rest of the sample surface was covered by a mixture of Cr_2O_3 and Al_2O_3 (Figure 4.36a and c). Careful removal of the scale (gentle polishing using colloidal-silica suspension) revealed the alloy surface (Figure 4.36b). The regions with more residual scratches, where the deformation of the alloy surface was more significant, had much more surface recrystallization as indicated by a finer grain structure. Grain structure and orientation mapping (Figure 4.36d) indicated that the scale composed of Cr_2O_3 and Al_2O_3 formed in the regions with finer grain structure. In summary, the polishing process induced surface deformation which enhanced the ability of Ni-8Al-4Cr alloy to form Al_2O_3 externally.
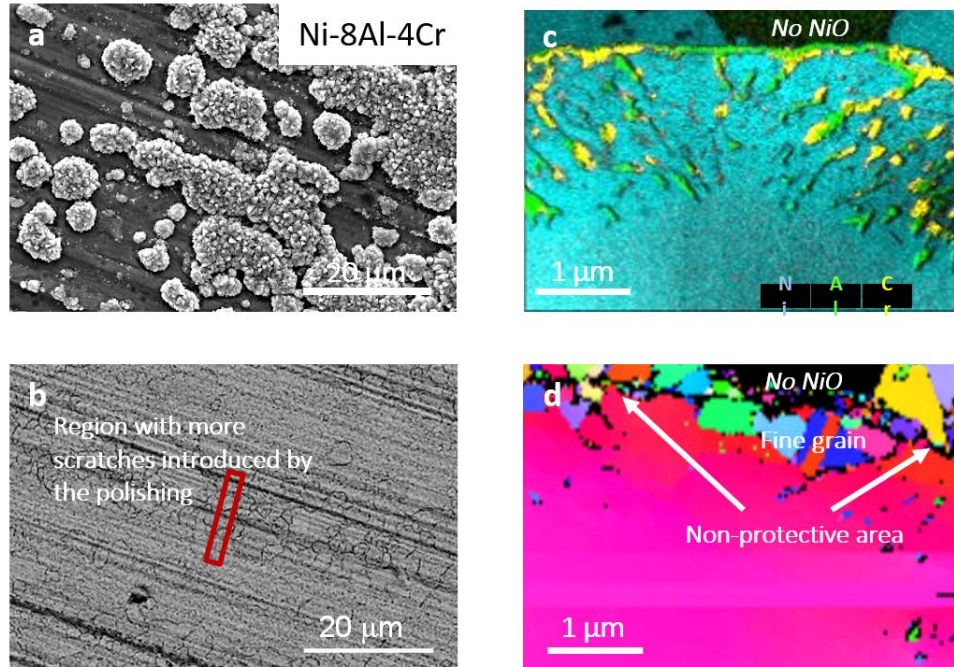
Figure 4.36 Micrographs of a Ni-8Al-4Cr specimen polished by 500-grit SiC paper, oxidized in air at 1000°C for 3 minutes. (a) The plan view (SEM) of sample surface after oxidation. (b) The plan view (SEM) of alloy surface grain structure after the removal of scale (polished by colloidal-silica suspension). (c) The cross-section elemental mapping (EDS) of the same specimen prepared by FIB (a region very similar to the one marked in red in (b)), where cyan represents Ni, green represents Al and yellow represents Cr. (d) grain structure and orientation mapping (TKD) of the same FIB sample.

A test on the recrystallization temperature was conducted. Ni-8Al-6Cr and Ni-14Al with 500-grit finish were prepared and annealed in an oxygen partial pressure controlled by a Ti-rich Ti/TiO mix (Rhines Pack) for 5 minutes at 600°C and 1100°C. As shown in Figure 4.37, surface recrystallization was not observed on both alloys after annealing at 600°C for 5 minutes. At 1100°C, significant surface recrystallization was found in both alloys after annealing for 5 minutes. Although internal oxidation occurred in Ni-14Al during the annealing, the recrystallized grain structure in Ni-14Al and Ni-8Al-6Cr alloys are similar, with an average diameter of 1μm.
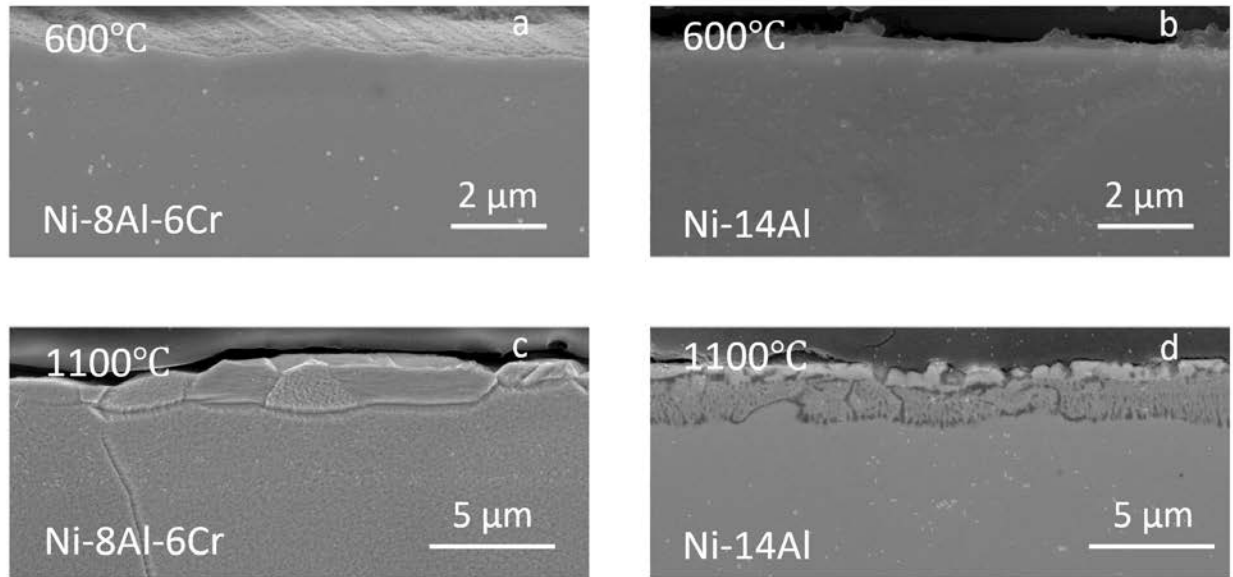
Figure 4.37 Cross-section of alloys annealed in vacuum. (a) Ni-8Al-6Cr annealed at 600℃ for 5 minutes. (b) Ni-14Al annealed at annealed at 600℃ for 5 minutes. (c) Ni-8Al-6Cr annealed at 1100℃ for 5 minutes. (d) Ni-14Al annealed at 1100℃ for 5 minutes.

Microhardness tests were also conducted to reveal the impact of surface finish on the alloy structure and surface recrystallization process. Two loads of 5gf and 300gf were used for the microhardness test. Generally, light load (5gf) limits analysis to surface layer of alloy; whereas, heavy load (300gf) reveals bulk microhardness of the alloy. The microhardness results for Ni-8Al-6Cr and Ni-14Al with different surface finishes under different loads are summarized in Figure 4.38. Regardless the alloy composition and surface finish, the microhardness measured with 5gf load is higher than the microhardness measured with 300gf load. When tested with 5gf, a given alloy (Ni-14Al or Ni-8Al-6Cr) with 500-grit surface finish show a higher microhardness than the same alloy with colloidal silica finish. After annealing at 600℃ in vacuum for 5 minutes, the microhardness of Ni-8Al-6Cr with 500-grit finish increased, whereas the microhardness of Ni-14Al with 500-grit finish decreased. By contrast, surface finish and annealing process do not have

119

significant impact on the microhardness of either Ni-14Al or Ni-8Al-6Cr measured with 300gf load. Alloy grain structure can be deducted from the microhardness measurements, which will be discussed in the following sections.
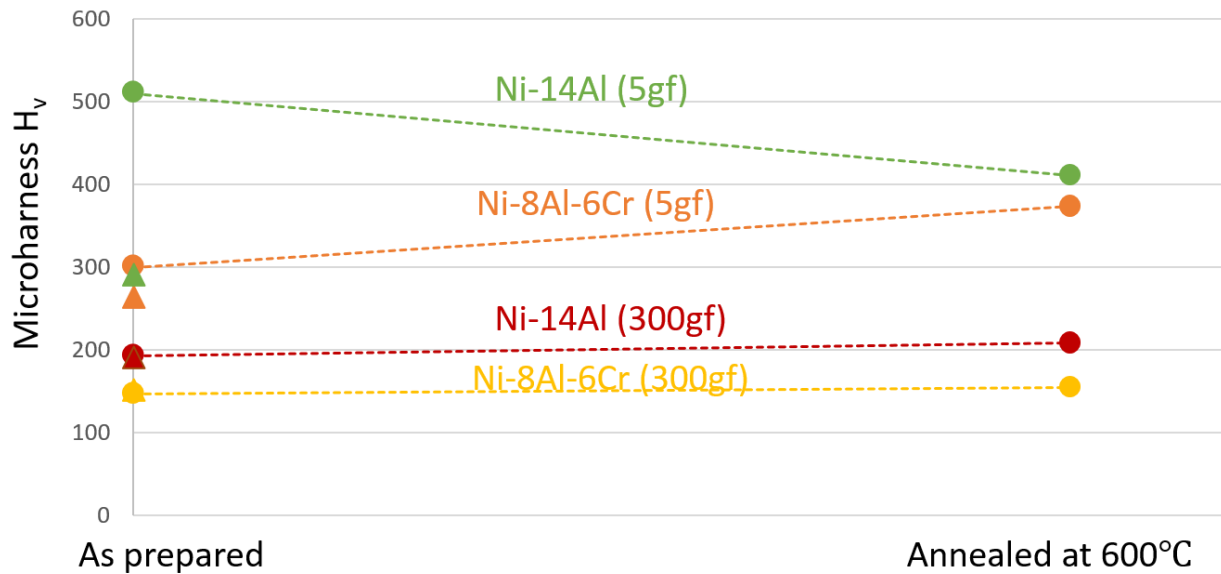
Figure 4.38 Microhardness of Ni-14Al-6Cr and Ni-14Al alloys. The annealing was done in an oxygen partial pressure controlled by a Ti-rich Ti/TiO mixture (Rhines pack) at 600°C for 5 minutes. Two loads of 5gf and 300gf were used. Filled circles represent alloys with 500-grit finish, filled triangles represent alloys with colloidal silica finish.

4.2.2.3 The impact of surface finish on Cr effect

Three specimens of composition, Ni-8Al, Ni-8Al-6Cr and Ni-14Al, were prepared with different finish on each side. One side was polished to a 500-grit SiC finish, while the other side was polished using a series of SiC paper and finally a colloidal-silica suspension. After 4-hours oxidation in air at 1100°C, the three samples exhibited different oxidation behavior, as indicated in Figure 4.39.
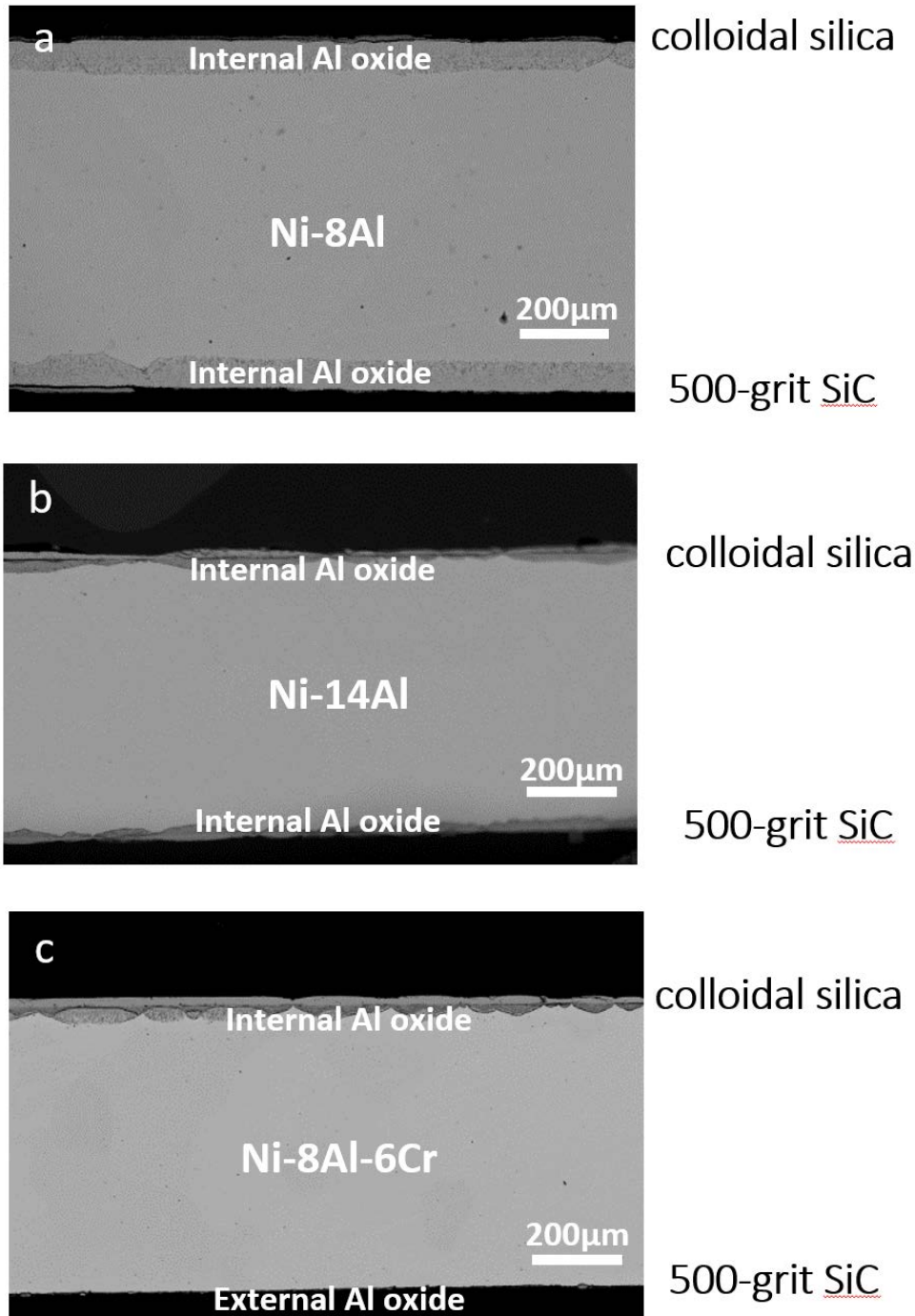
Figure 4.39 Micrographs of cross-section samples of three alloys with different surface finish on each side of the specimen oxidized in air at 1100°C for 4 hours. The top of the samples shown in this figure was polished by a series of SiC paper and finally a colloidal-silica suspension, the bottom of the samples was polished by a 500-grit SiC paper. (a) Ni-8Al (b) Ni-14Al (c) Ni-8Al-6Cr

Ni-8Al showed significant internal oxidation on both sides, and the penetration depth of internal oxidation is similar on both side (Figure 4.39a). Ni-14Al also experienced internal oxidation during early-stage oxidation on both sides, but nodes rich in Al oxide formed on the surface with a 500-grit finish [77], and propagated along the internal oxidation front, resulting in an overall reduction in internal oxidation (Figure 4.39b). However, there was no clear correlation between the surface finish and maximum internal oxidation penetration depth for this alloy. Two different surface finishes for the Ni-8Al-6Cr sample led to two completely different oxidation behaviors, Figure 4.39c. An exclusive Al_2O_3-rich scale formed on the surface with a 500-grit finish, whereas, formation of a significant amount of external NiO coupled with internal oxidation was observed on the side with a colloidal-silica finish. Although the progressive Al_2O_3 layer formation was also present in the Ni-8Al-6Cr sample with a colloidal-silica finish, the maximum internal oxidation penetration depth was much larger (still much less than the internal oxidation penetration observed in Ni-8Al sample). The addition of 6 percent of Cr into the Ni-8Al alloy clearly improved its oxidation resistance compared to Ni-8Al regardless of surface finish. However, only when the Ni-8Al-6Cr had a rough surface finish and hence surface recrystallization, it did exhibit better oxidation resistance than Ni-14Al, which had the same amount of solute, i.e. 14at%.

4.2.2.4 The impact of temperature and heating rate on the scale establishment on Ni-Al-Cr alloys

To examine the impact of temperature on the scale establishment on Ni-Al-Cr alloys, three Ni-8Al-6Cr samples (cut from the sample rod) with a 500-grit finish were oxidized in air during 1-minute heating to 1000°C, 1100°C and 1150°C. Cross-sectional images of these three samples revealed different oxidation behaviors, as shown in Figure 4.40. No internal oxidation was

observed in the Ni-8Al-6Cr sample after 1-minute heating to 1000°C and $(dT/dt)_{max} = 42$°C/s. Rather, a thin scale formed on the surface. When the preset temperature was increase to 1100°C and $(dT/dt)_{max} = 45$°C/s, a portion of the alloy surface was still covered by a layer of thin scale, but the formation of NiO scale coupled with internal Al oxidation was observed on the remaining surface. When heating to 1150°C and $(dT/dt)_{max} = 42$°C/s, no initially protective scale (defined as the scale which can prevent internal oxidation of Al during early-stage oxidation, but not necessarily adherent) was observed when pulled at 1 minute, and the entire alloy surface showed internal oxidation.
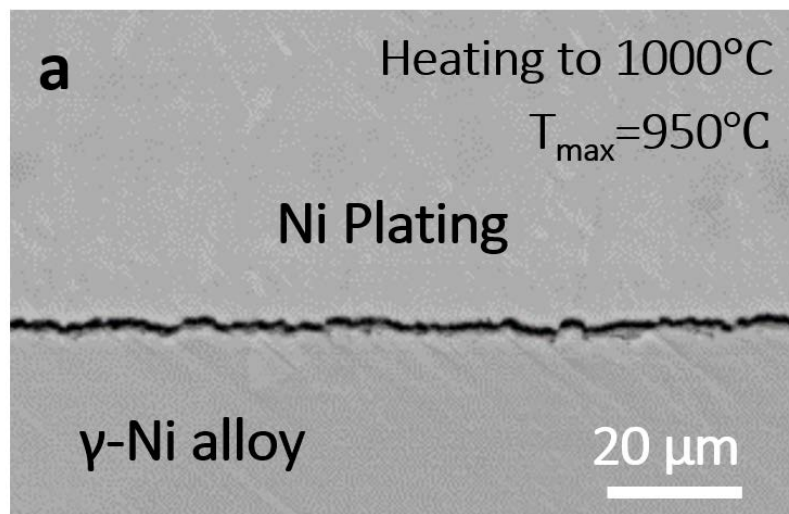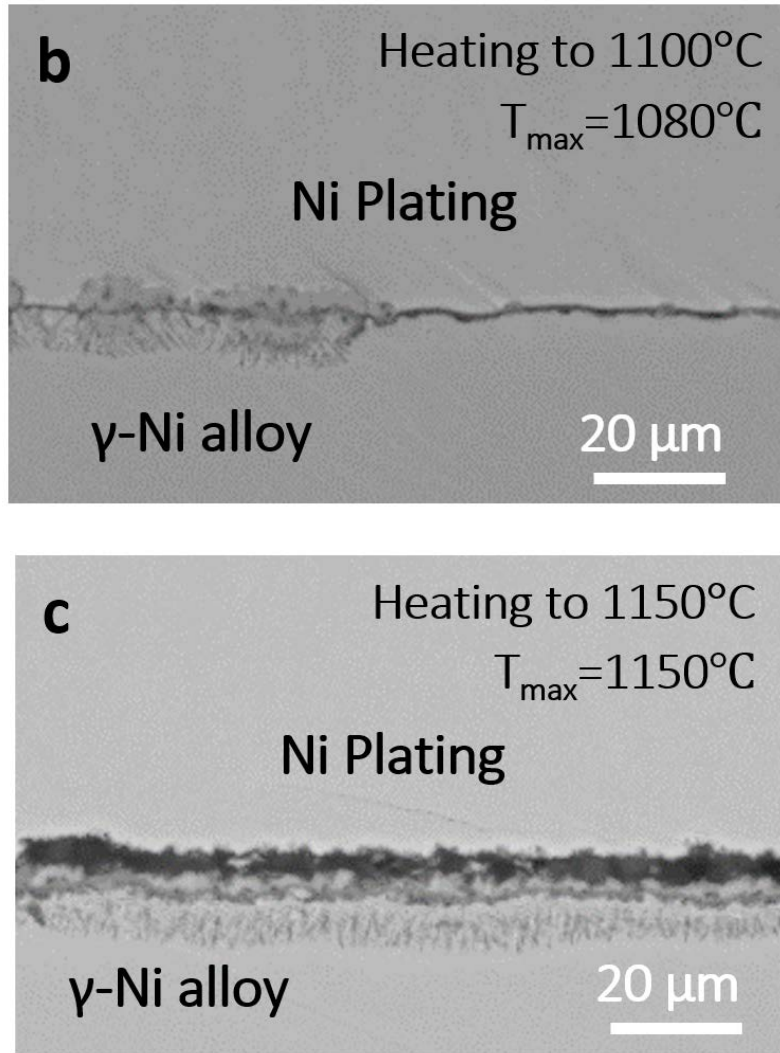
Figure 4.40 Cross-section view of Ni-8Al-6Cr alloys with 500-grit finish oxidized in air for 1minute (a) at 1000°C with an effective heating rate of 16°C/s, (b) at 1100°C with an effective heating rate of 18°C/s, (c) at 1150°C with an effective heating rate of 19°C/s.

Slow heating rate was also found to be detrimental to Al_2O_3-scale establishment on Ni-Cr-Al alloys, as indicated in Figure 4.41. Ni-8Al-6Cr with a 500-grit SiC finish was oxidized in air for a total of 20 hours either in the tube furnace with a maximum heating rate of 2700°C/min or in the TGA with a heating rate of 10°C/min. The preset temperature was 1100°C. The slower heating rate in the TGA resulted in extensive internal oxidation, and almost no exclusive scale formation.

124

By contrast, the alloys oxidized in the tube furnace, which had a more rapid heating rate, only showed very limited internal oxidation during the early stage, and a large portion of the surface was covered by a thin layer rich in Cr_2O_3 and Al_2O_3.
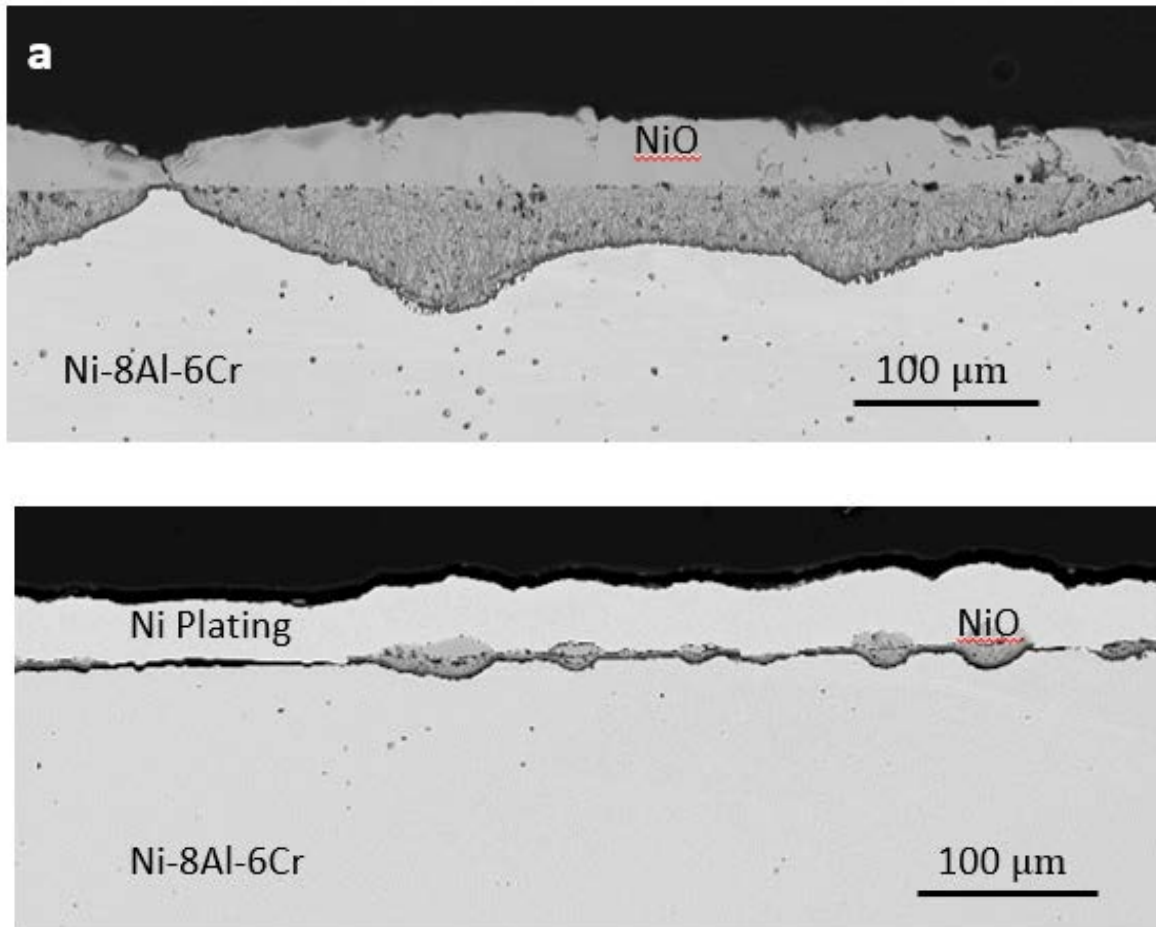
Figure 4.41 Cross-section view of Ni-8Al-6Cr alloys with a 500-grit finish oxidized in air at 1100°C for 20 hours (a) in the TGA with a heating rate of 10°C/min, (b) in tube furnace with a heating rate indicated in Figure 4.33.

Taking the surface finish and heating rate effect into account, three different zones can be introduced into the oxidation map of Ni-Cr-Al alloys established by Giggins and Pettit [90]. Since only the initial establishment of continuous Al_2O_3 was considered in the present study, the

oxidation map is slightly different from the original oxidation map. Alloys in zone 1 cannot establish a continuous Al_2O_3 scale regardless the surface finish and heating rate. Alloys in zone 2 may or may not establish an Al_2O_3 scale initially depending on the surface finish and heating rate. Alloys in zone 3 can establish an Al_2O_3 scale initially regardless the surface finish and heating rate.
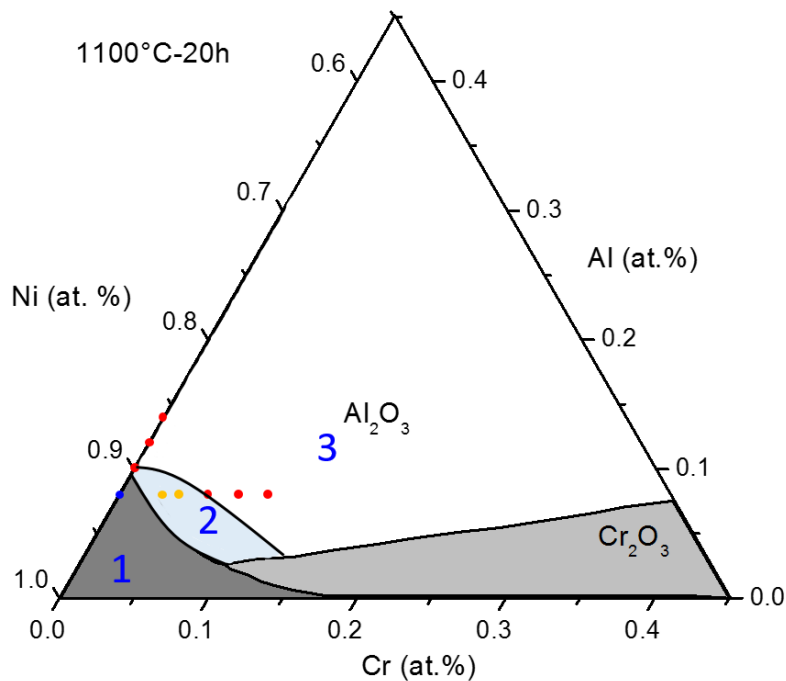
Figure 4.42 Modified Ni-Al-Cr oxidation map at 1100℃ with 3 additional zones. Zone 1 contains blue dots which represent samples experiencing internal oxidation regardless the surface finish and heating rate. Yellow dots in Zone 2 represent samples that may or may not establish a continuous Al_2O_3 scale initially depending on the surface finish and heating rate. Red dots in Zone 3 represent samples which will establish a continuous Al_2O_3 scale initially regardless the surface finish and heating rate.

Ni-8Al-6Cr and Ni-14Al with a 500-grit finish were oxidized at 600℃ in air for 5 minutes. Depth profiles from the oxidized sample were obtained by XPS, and the results are summarized in

126

Figure 4.43 and Figure 4.45. O 1s, Ni 2p, Cr 2p, Al 2p peaks were used for the quantitative analysis of the chemical composition. Since the relative sensitivity factor (R.S.F.) of XPS for Al peak is small [109], when the Al concentration on the surface is less than 10% the intensity of Al peak will be extreme low, which negatively impacts the accuracy for Al content quantification in present study (e.g. XPS may report 3% of Al to be 0). Due to surface contamination, the O content may be higher than the stoichiometry of possible oxide phase in this system (NiO, Cr_2O_3, Al_2O_3, $NiAl_2O_4$). The etching rate used for the depth profiling was 1.5nm/s (based on the etching rate of Ta_2O_5). Since different materials have a different etching rate under the same ion beam condition [160], the etching time cannot be confidently converted into distance from the surface when the etching is conducted on a sample with multiple phases. However, a rough estimation of scale thickness can still be made based on the etching rate of primary material on the surface. If the etching rate of Ta_2O_3 is set to 1, the etching rate of Ni is 0.88, NiO is 0.83, and α-Al_2O_3 is 0.14 [160]. After 5- minute oxidation, significant Al enrichment was found on the surface of the Ni-8Al-6Cr sample. Assuming the etching rate of Al_2O_3 scale observed on the surface is similar to that of α-Al_2O_3, the scale thickness on the Ni-8Al-6Cr sample can be estimated by the product of etching rate and etching time

$$x = 0.14 * 1.46 * 40 \approx 8\ nm \tag{4.30}$$
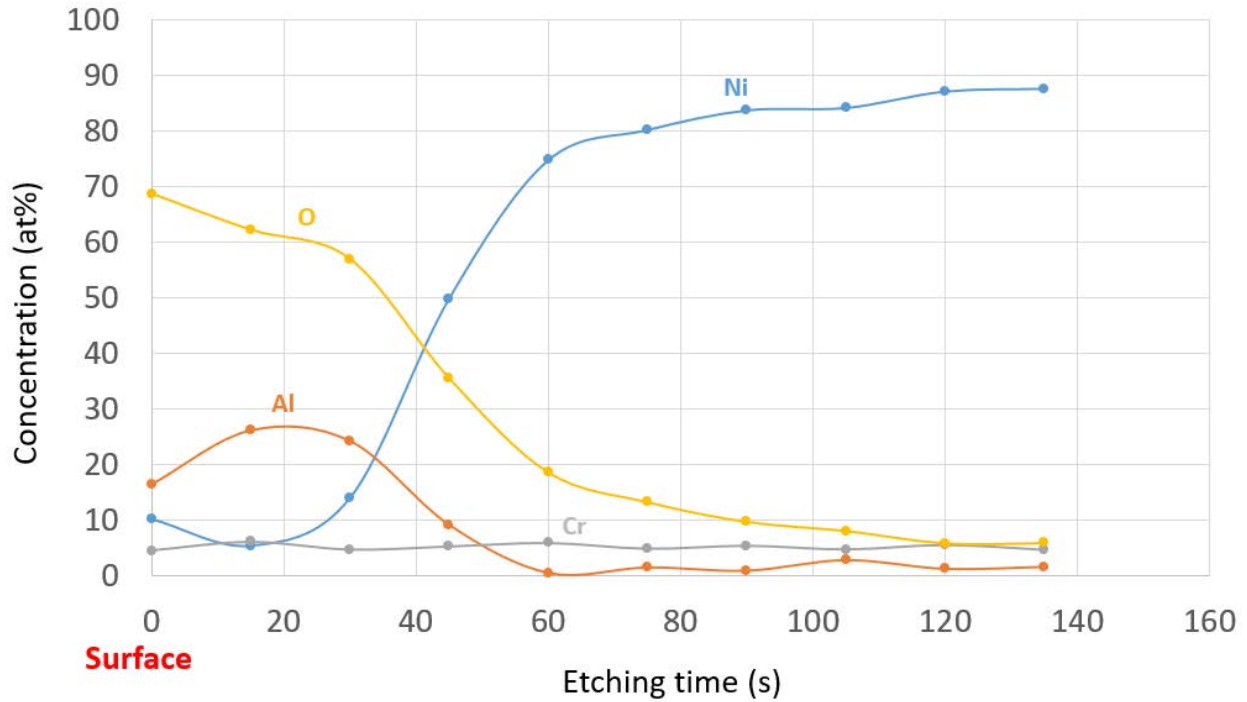
Figure 4.43. Depth profile of the chemical composition of Ni-8Al-6Cr alloy with 500-grit finish oxidized in air at 600℃.

Another Ni-8Al-6Cr sample with 500-grit finish was heated to 1100℃ in air for 1 minute (temperature profile is shown in Figure 4.33). The maximum heating rate was about 45℃/s, and the temperature reached at last was 1080℃. After this oxidation, sample cross-sections were prepared using DB-FIB. A thin oxide layer with a thickness around 13nm was measured on the sample surface, as shown in the Figure 4.44. An EDS line scan across the oxide layer (Figure 4.44c), as marked in Figure 4.44a (yellow line), identified the oxide layer to be Al_2O_3 in composition. No clear crystal structure information was revealed by the FFT of this Al_2O_3 layer (see inset of Figure 4.44b). A lack of crystal structure for the Al_2O_3 formed during the oxidation at lower temperatures (500-600℃) was also reported by other researchers [161-163]. It was defined

as amorphous Al_2O_3 by Venezia and Loxton [162]. Thus, the Al_2O_3 layer shown in Figure 4.44b is inferred to be amorphous.
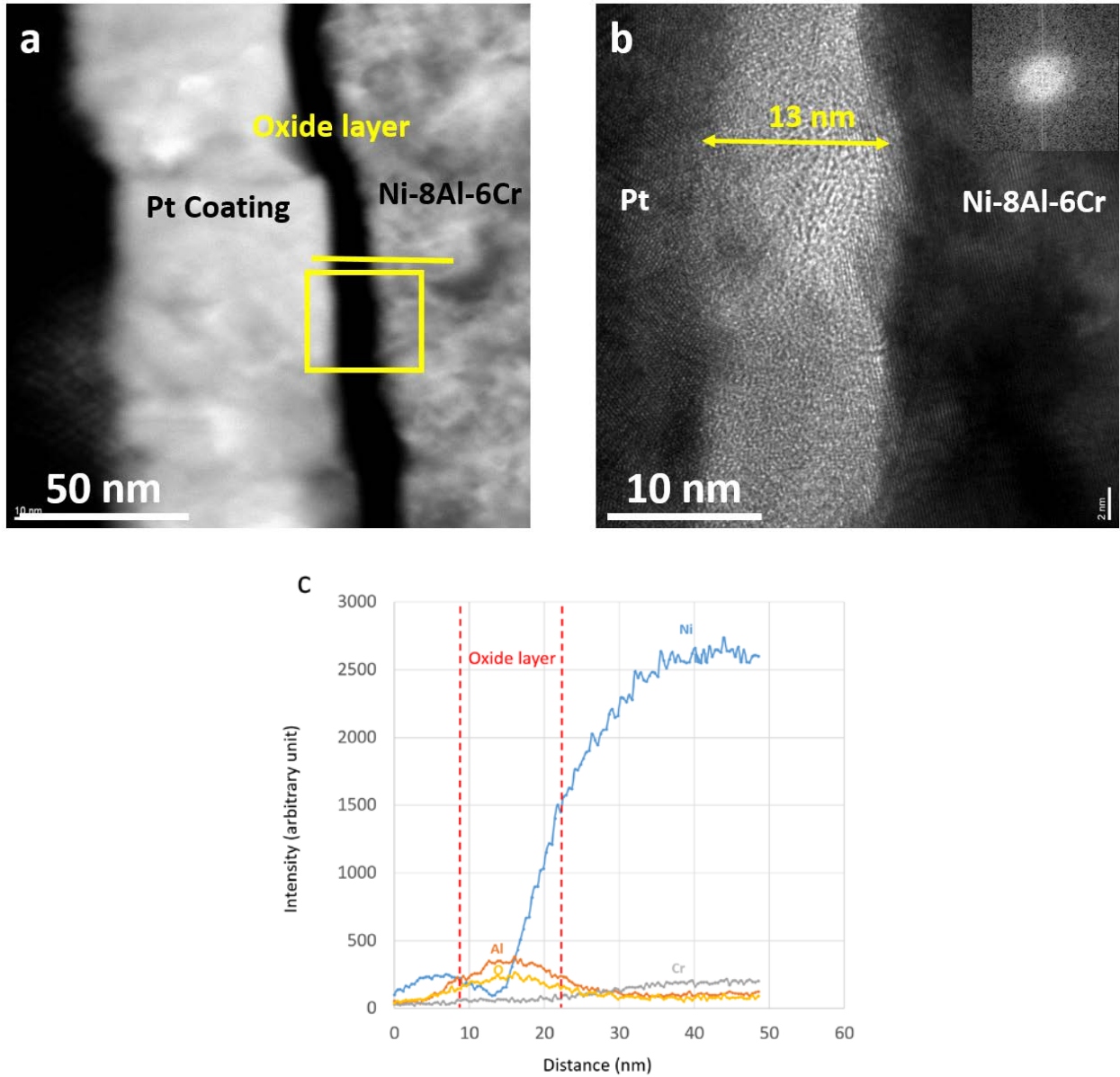
Figure 4.44. (a) STEM dark field image of the cross-section sample of Ni-8Al-6Cr with 500-grit finish heated to 1100°C in air for 1 minutes. (b) High resolution TEM image of the marked area in (a), and the inset is FFT of the Al_2O_3 layer. (c) EDS line scan across the thin oxide layer.

By contrast, after 5-minute oxidation at 600℃, only NiO was found on the Ni-14Al surface, as shown in Figure 4.45. Since NiO is the primary product detected on the surface through the entire depth profile, the minimum thickness of the scale can be estimated

$$x = 0.83 * 1.46 * 130 \approx 158 \ nm \tag{4.31}$$
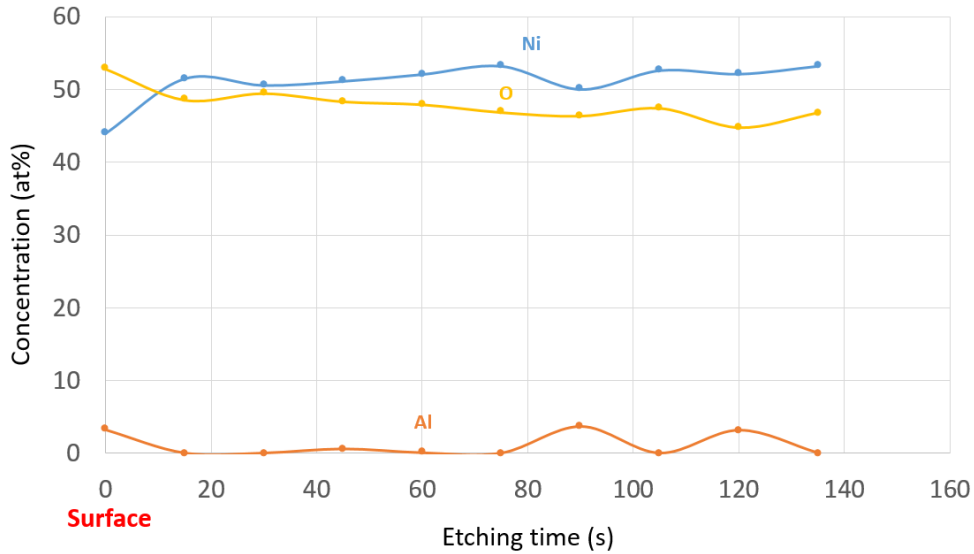
Figure 4.45 Depth profile of the chemical composition of Ni-14Al alloy with 500-grit finish oxidized in air at 600℃.

4.2.2.5 Discussion

The results obtained from the oxidation of Ni-8Al, Ni-8Al-6Cr and Ni-14Al specimens with a colloidal-silica finish and a 500-grit finish on either side of the specimen indicate that the Cr effect on external Al_2O_3 formation depends on both the surface finish and heating rate. There are several possible mechanisms to rationalize the Cr effect, and each will be analyzed in the following in the context of the experimental results obtained.

The most widely considered mechanism is the "gettering" effect proposed Wagner [93]. It suggests that the addition of Cr, or more generally a third element, with intermediate stability between Ni and Al can form a "gettering" layer on the surface, that will act to significantly decrease

130

the oxygen solubility at the scale/alloy interface. Based on Wagner's theory regarding the transition from internal to external oxidation [45, 51], this decrease in solubility will promote alumina scale formation. The formation of a Cr-rich "gettering" layer was observed during the oxidation of Ni-Al-Cr alloys containing a relatively high Cr content [13, 90]. However, during oxidation of Ni-8Al-6Cr when heated to 1100°C in air, Al_2O_3 formation was detected without the formation of a Cr-rich "gettering" layer (Figure 4.44). Moreover, a continuous Cr_2O_3 external scale forms only on binary Ni-Cr alloys with more than 20% Cr [164]. Therefore, one should reconsider the role of Cr as a secondary getter in Ni-Cr-Al alloy with a low Cr content.

A second possible mechanism is a "decrease in the oxygen solubility" by the third-element addition, as proposed by Guan and Smeltzer [165]. These authors suggested that addition of Cr into Ni-Al alloy will decrease the oxygen solubility without formation of a "gettering" layer. Since surface finish will not change the oxygen solubility in the alloy matrix, even if this mechanism contributes to the Cr effect on Al_2O_3 formation, it will not be relevant to surface finish effect found in the present study. As shown in Figure 4.39, Figure 4.43 and Figure 4.45, an Al_2O_3 scale formed on Ni-8Al-6Cr with 500-grit finish but a progressive scale establishment occurred on Ni-14Al, regardless the surface finish.

A third proposed mechanism is the "cross-term" effect proposed by Nesbitt et al. [166, 167]. The diffusion of one alloy element in the matrix will not only depend on its own concentration gradients, but also depend on the concentration gradients of the other alloy elements in the matrix. In the case of Ni-Al-Cr alloys, the flux of Al and Cr towards the surface can be expressed as

$$J_{Al} = -D_{AlAl}^{Ni} \frac{\partial C_{Al}}{\partial X} - D_{AlCr}^{Ni} \frac{\partial C_{Cr}}{\partial X} \tag{4.32}$$

$$J_{Cr} = -D_{CrCr}^{Ni} \frac{\partial C_{Cr}}{\partial X} - D_{CrAl}^{Ni} \frac{\partial C_{Al}}{\partial X} \qquad (4.33)$$

Diffusivities in Ni-Al-Cr alloys with different compositions have been measured at 1100°C and 1200 °C [167]. It was found that D_{AlCr}^{Ni} is positive regardless of the temperature and composition in the γ-Ni phase field. The impact of Cr addition on the D_{AlAl}^{Ni} was found to be limited. Therefore, the addition of Cr into Ni-Al alloys will introduce an additional driving force for the Al diffusion due to the positive value of D_{AlCr}^{Ni} and, as a result, the flux of Al towards the surface can be increased if $\frac{\partial C_{Cr}}{\partial X}$ is negative. For most Al concentrations in the γ phase, $D_{CrCr}^{Ni} \approx D_{CrAl}^{Ni} \approx D_{AlCr}^{Ni} \approx 0.2 - 0.4\ D_{AlAl}^{Ni}$, as listed in Table 4.1. According to the XPS experimental results (Figure 4.43), $\frac{\partial C_{Cr}}{\partial X}$ is very small during the Al₂O₃ establishment process. Therefore, the product $D_{AlCr}^{Ni} \frac{\partial C_{Cr}}{\partial X}$ will have limited impact on J_{Al}, and will therefore not be the primary mechanism controlling the surface finish effect.

Table 4.1 Ternary interdiffusion coefficients - 1200℃ [167]

Intersection. At. Pct.		Diffusion coefficients (cm²/s *10⁻¹⁰)			
Cr	Al	D_{AlAl}	D_{AlCr}	D_{CrAl}	D_{CrCr}
15.4	5.99	9.6	2.77	4.31	3.86
14.14	6.11	9.55	2.86	3.86	3.71
13.94	6.13	11.2	3	4.58	3.74
13.39	6.17	8.97	2.78	4.4	3.6
2.1	6.18	11.66	3.34	1.88	3.94
12.33	6.22	9.79	3.05	2.49	3.4
4.41	6.74	9.16	2.89	1.86	3.8
3.85	6.86	15.94	4.28	5.44	3.05
16.35	6.89	11.31	3.45	5.47	5.43
16.11	7.01	11.15	3.25	4.52	4.55
2.88	7.06	12.72	3.66	3.49	2.18
15.96	7.1	11.15	3.25	5.17	4.91
27.4	8.08	10.93	1.31	-1.2	1.23
17.21	8.1	13.14	4.22	4.95	5.13
17.15	8.12	14.61	4.88	6.76	5.95

Table 4.1 continued

14.1	8.12	14.62	5.14	4.91	4.91
13.86	8.24	12.75	4.1	4.4	4.62
31.44	8.32	15.98	3.83	10.31	7.67
13.72	8.33	11.6	3.49	6.43	5.82
16.54	8.4	13.89	4.6	5.97	5.65
14.34	9.42	17.68	6.62	5.2	5.55
10.89	9.66	15.72	3.15	2.69	4.3
19.72	9.75	20.01	4.31	5.89	6.05
13.63	9.76	16.1	5.97	4.99	5.52
19.7	9.77	21.73	5.84	7.42	7.41
11.31	9.78	12.43	4.27	3.24	4.22

A forth widely accepted mechanism is the "template" effect, as described in the previous section. This effect was reported by Hayashi et al. on both Fe-Al alloys and Ni-Al alloys [97-99, 168]. Based on this "template" effect, the presence of Cr accelerates the transformation from metastable Al_2O_3 to α-Al_2O_3, as shown in Figure 4.28. Since the parabolic rate constant of α-Al_2O_3 is about two orders of magnitude lower than that of metastable alumina [80], as shown in Figure 4.46, the amount of Al required to sustain the growth of α-Al_2O_3 is two orders of magnitude lower than that needed to sustain the growth of metastable alumina [51]. By accelerating the metastable to α-Al_2O_3 transformation, Cr can enhance the maintenance of Al_2O_3 scale that forms initially, which is proven to breakdown if mainly metastable Al_2O_3 is present. This effect is particularly pronounced at lower temperatures [169]. The inferred kinetic effect of Cr is summarized schematically in Figure 4.47.
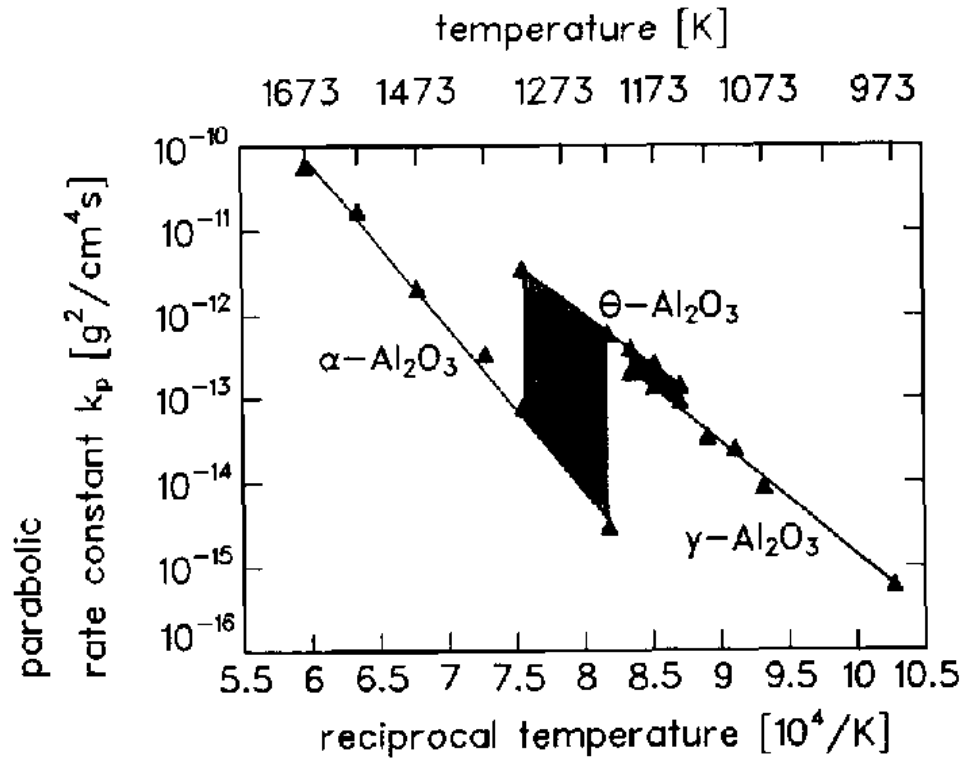
Figure 4.46 Arrhenius plot of the parabolic rate constants of NiAl oxidation [80].
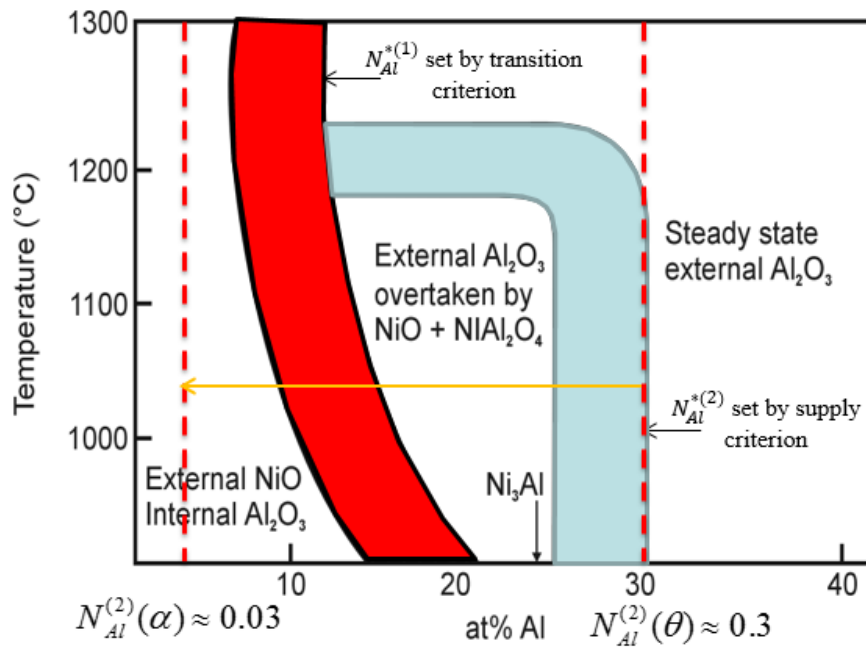
Figure 4.47 Schematics to show the "template" effect on the Al_2O_3 formation [169].

However, the originally proposed "template" [97-99, 168] only targets the second criterion proposed by Wagner [51] for protective scale formation, which is set by the supply of Al to sustain the growth of existing Al_2O_3 scale. Although the analysis done in the previous section showed that the "template" effect can also slow the oxygen inward diffusion, and therefore facilitate the transition from internal to external oxidation, the surface effect shown in Figure 4.39 cannot be rationalized based on such an effect. Moreover, this "template" effect relies on the formation of α-Al_2O_3, but an amorphous Al_2O_3 layer was found to form on the surface of Ni-8Al-6Cr with a 500-grit finish during the heating in air to 1100℃, as shown in Figure 4.44, and this amorphous Al_2O_3 layer also prevented the internal oxidation. The formation of amorphous Al_2O_3 was also observed by Hayashi [163]. In Hayashi's study [163], A Ni-14Al-20Cr sample with 1μm-diamond surface finish was heated to 1000℃ in an in-situ synchrotron system with a heating rate of 50℃/min. X-ray diffraction intensities of NiO, Cr_2O_3 and Al_2O_3 were recorded in real-time, as shown in Figure 4.48a. Initially, only Cr_2O_3 was detected by the X-ray diffraction, and the intensity kept increasing until the temperature reached 890℃. NiO started to form around 890℃ when the Cr_2O_3 intensity started to decrease. The only Al_2O_3 phase detected by the X-ray diffraction was α-Al_2O_3, which was not visible until the temperature reached 1000℃. A cross-sectional sample was made during the heating process at 890℃ (Figure 4.48b). Elemental mapping of this cross-sectional sample (Figure 4.48c) indicated the formation of an Al_2O_3 layer beneath the Cr_2O_3 layer. Since no crystal structure of this Al_2O_3 layer was revealed by X-ray diffraction and high-resolution TEM image, it is inferred to be amorphous.
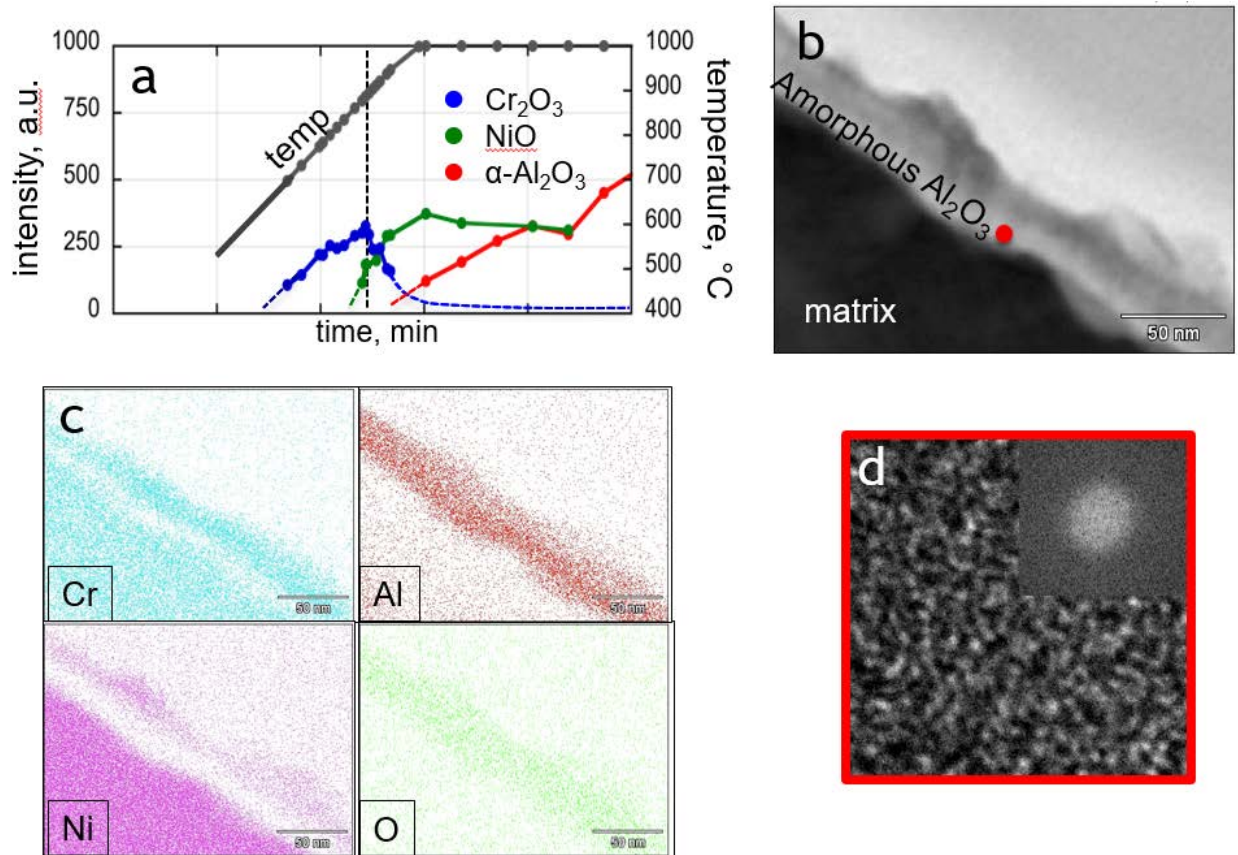
Figure 4.48 (a) In-situ high-temperature X-ray diffraction measurement of a Ni-14Al-20Cr sample heated to 1000℃. (b) Cross-sectional sample of the Ni-14Al-20Cr sample during the heating process at 890℃ as marked in dash line in (a). (c) Elemental mapping of the cross-sectional sample present in (b). (d) High-resolution TEM image of the Al_2O_3 layer as marked by the red dot in (b), and the inset is FFT of this TEM image [163].

In summary, none of the existing theories or models can fully explain and rationalize the Cr effect during the oxidation of Ni-Al-Cr alloys. A new perspective regarding the Cr effect is therefore needed. By carefully examining the experimental results obtained in this study, it was found that only Ni-Cr-Al alloys with a rough surface finish (500-grit finish in present study) heated to 1100℃ with an optimized heating rate can display the best oxidation resistance. The impact of surface finish and heating rate on the Cr effect will be discussed in the following analysis.

A rough surface finish can introduce two possible mechanisms which may impact the oxidation behavior. One is increasing the surface defects and nucleation rate, while the other is formation of a surface-deformed zone that provides short-circuit diffusion paths via dislocations and grain boundaries [87, 170-174]. It is conceivable that both of these mechanisms are operating.

An increase in surface defects may decrease the nucleation barrier for the oxide formation [67]. However, this will not only affect the oxidation of Al, but also other elements on the surface (Ni and Cr). According the nucleation theory, $\Delta G = V \Delta G_V + \sum_i A_i \gamma_i$, the larger the absolute value of ΔG_V, the smaller the impact of surface energy change on the nucleation barrier. Since Al_2O_3 has a much higher thermodynamic stability than that of NiO and Cr_2O_3, the absolute value of ΔG_V for Al_2O_3 may be the lowest, and thus, surface defects may have a small impact on the Al_2O_3 nucleation. Therefore, an increase in the amount of surface defects may not be the primary impact introduced by a rough surface finish.

Indeed, the impact of surface deformation and grain size on the oxide scale formation on Ni-Cr alloys was reported by Giggins and Pettit [87]. It was suggested by these authors that smaller grains can provide rapid diffusion paths along the grain boundaries, and thus, the smaller the grain size the easier the establishment of the Cr_2O_3 scale. Hence, surface recrystallization, which results in a very fine grain structure at the alloy surface, could play an important role on the initial establishment of Al_2O_3 on Ni-Cr-Al alloys. Recrystallization of Ni-based alloys usually occurs above 600℃ with an activation energy of about 160kJ/mole [175-177]. This is consistent with the experimental observation in the present study, as shown in Figure 4.37. Overlaying the time-dependent surface recrystallization curve, above which 50% of recrystallization is achieved [175], and the heating rate curve obtained in present study, an estimation for the recrystallization behavior during heating process can be obtained (Figure 4.49).

137
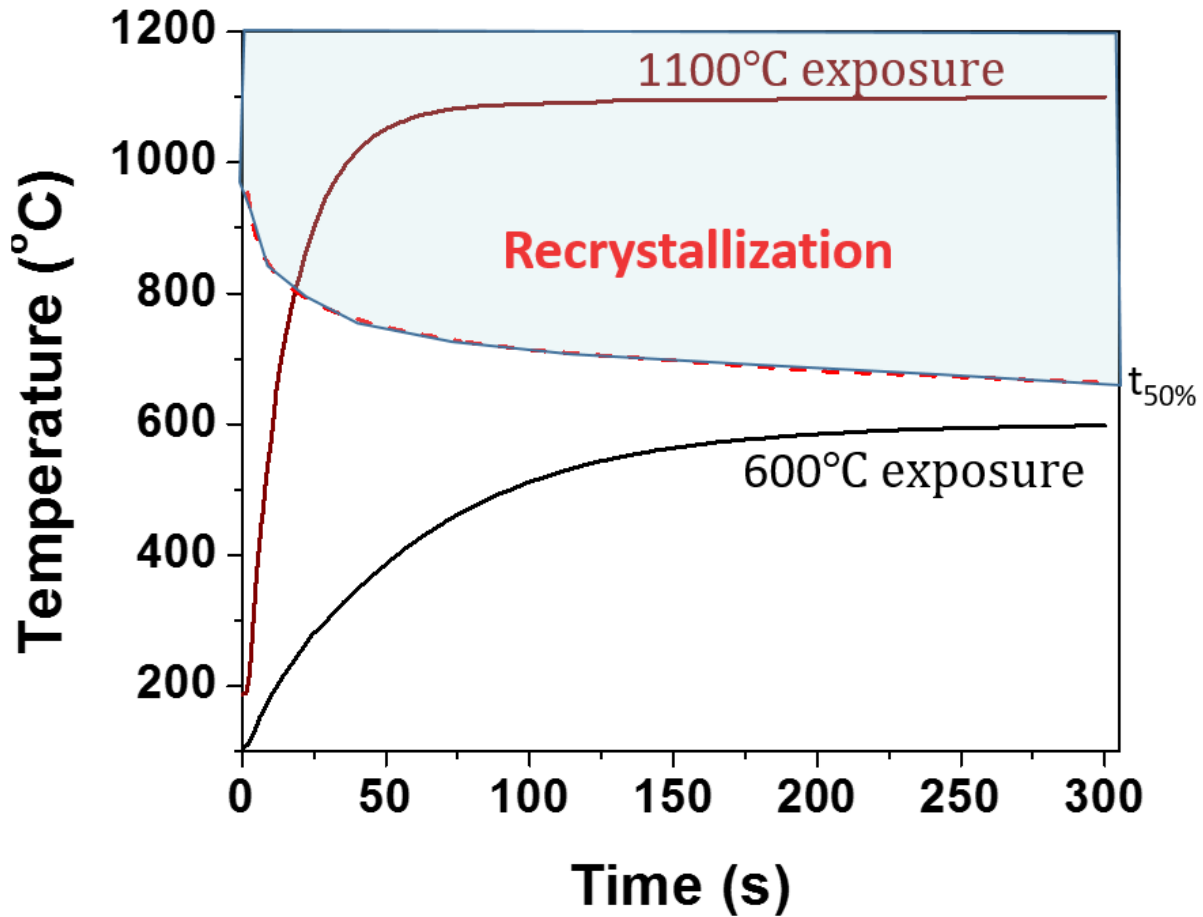
Figure 4.49 Surface recrystallization behavior of Ni-based alloys during the heating process.

Although surface recrystallization only occurs above 600℃, dislocations resulting from the surface deformation can also provide short-circuit diffusion paths [170, 174], and thus, enhance the scale formation. This achieves a good agreement with the observation of a thin alumina layer formed on the surface of Ni-8Al-6Cr alloy with 500-grit surface finish oxidized at 600℃ for 5 minutes (Figure 4.43).

However, this surface-deformation enhanced scale formation was not evident during the oxidation of the Ni-Al binary alloy (Figure 4.39 and Figure 4.45). Thus, it is inferred that the presence of Cr is critical for the enhanced scale establishment from short-circuit diffusion.

Unfortunately, short-circuit diffusivities, including grain-boundary diffusivities D_g and pipe diffusion along dislocations D_d, for Cr and Al in the Ni-Cr-Al alloys are not readily available, and the reported values in Ni-based alloys or Ni-Al intermetallic differ significantly [170, 178-180]. Therefore, an estimation of D_g is made in the following based on the Wagner's theory for internal to external oxidation transition[43, 45, 51, 165, 181] and oxidation experiments of Ni-Cr and Ni-Al alloys [87, 131].

As discussed in the introduction, Wagner [51] derived two equations (2.21) and (2.22) to present a criterion for the internal to external oxidation transition based on the establishment of initial protective scale.

$$\frac{2N_O^s}{z_B N_B^0} = \frac{\exp(\gamma^2)\,\text{erf}(\gamma)}{\varphi^{\frac{1}{2}} \exp(\gamma^2 \varphi)\, erfc(\gamma\varphi^{\frac{1}{2}})} \tag{2.21}$$

$$N_B^{0*} = \frac{1}{\rho} f_v^* F(\gamma\varphi^{\frac{1}{2}}) \tag{2.22}$$

Although oxygen solubility in Ni-Cr-Al alloys depends on the concentration of Al and Cr [165], both Al and Cr on the surface can be oxidized extremely fast, as discussed in a previous section, leaving an alloy matrix of virtually pure Ni near the surface. In the following estimation of grain-boundary diffusivities, N_O^s for the pure Ni in equilibrium with NiO was used for simplification [133, 182]. As discussed in previous sections, the protective scale usually established first at grain boundaries. The critical mole fraction of solute B (Al or Cr), at which the slow-growing BO_v scale starts to form at grain boundaries, shall be defined as N_B^{*GB}. The experimental determination for N_B^{*GB} is based on the observation of formation of protective nodes and initiation of progressive protective scale formation. An example of N_{Al}^{*GB} for the Ni-Al system is shown in Figure 4.50, and was determined by Zhao et al. [131].
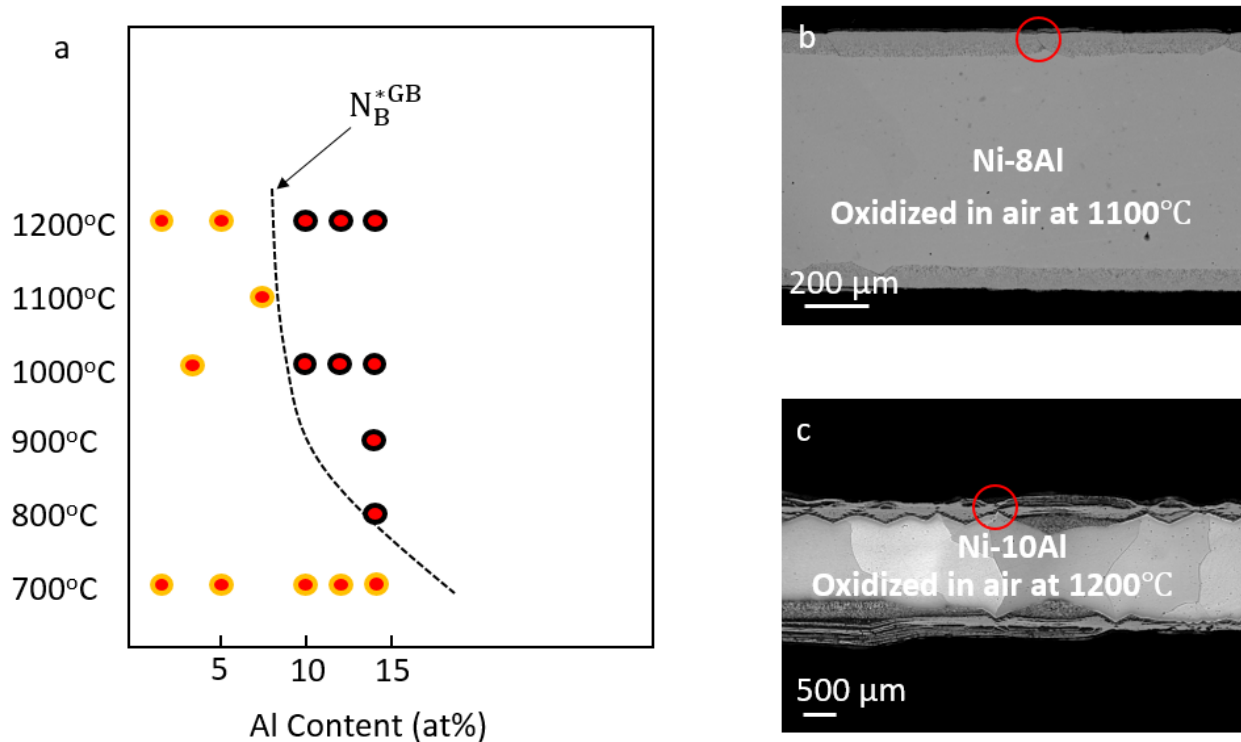
Figure 4.50 (a) The determination of N_B^{*GB} for Ni-Al alloys for different temperatures depending on the oxidation behavior. Red circles with orange outline present the alloys without nodes formation and progressive scale establishment; red circles with black outline present the alloys showing nodes formation and progressive scale establishment. (b) Ni-8Al alloy with 600-grit finish oxidized in air at 1100℃ for 4 hours. Red circle indicates a grain boundary without node formation on the surface. (c) Ni-10Al alloy with 600-grit finish oxidized in air at 1200℃ for 24 hours. Red circle indicates a node formation at grain boundary and progressive scale establishment initiated at this point.

Similarly, N_{Cr}^{*GB} for Ni-Cr alloys at different temperatures was indirectly reported by Giggins and Pettit [129], Figure 4.51. Although these authors didn't define the term N_{Cr}^{*GB}, the virtual line that separated Ni-Cr alloys in group one (internal oxidation) and group two (Cr_2O_3 scale formation at grain boundaries) is in accordance to N_{Cr}^{*GB} used in present study.

140
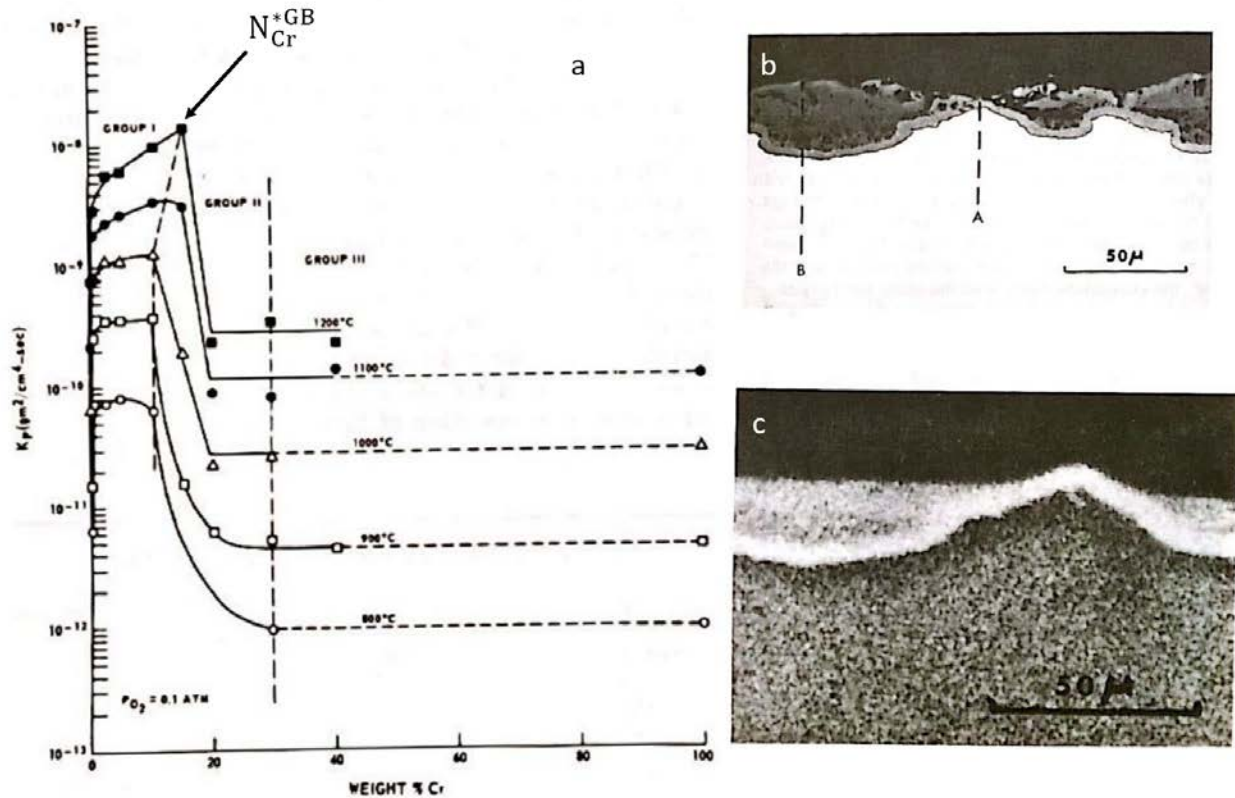
Figure 4.51 (a) Oxidation behavior of Ni-Cr alloys under various temperature. Group II alloys presented nodes formation and progressive scale establishment as shown in (b) and (c). (b) Microstructural photo of electropolished Ni-20Cr alloy oxidized for 66 hours in 0.1 atm of oxygen at 900℃. (c) X-ray image of the chromium radiation of electropolished Ni-20Cr alloy oxidized for 66 hours in 0.1 atm of oxygen at 900℃.

All the data used for the calculation of the grain-boundary diffusion coefficients of Al and Cr are listed in Table 4.2. f^* and v used in present study are based on the analysis by Zhao et al. [181]. Upon substituting N_B^0 with N_B^{0*} in equation (2.21), there are only two unknowns, γ and φ, remaining in equations(2.21) and (2.22). It is recalled the φ is D_O/D_B, at the grain boundaries, φ^{GB}, and can be estimated by solving the equations. These values are given in Table 4.2.

Table 4.2 N_B^{*GB} values and estimation of φ for Ni-Al and Ni-Cr alloys

Temperature(°C)	N_{Al}^{*GB} for Ni-Al alloys[a]	N_{Cr}^{*GB} for Ni-Cr alloys[b]	N_O^{s} [c]	γ [d]	φ_{Ni-Al}^{GB}	φ_{Ni-Cr}^{GB}
1200	0.07	0.17	9.1×10^{-4}	0.012-0.018	91	348
1100	0.09	0.14	6.6×10^{-4}	0.011-0.014	117	342
1000	0.1	0.11	4.6×10^{-4}	0.009-0.010	300	299
900	0.12	0.07	2.9×10^{-4}	0.007-0.009	609	289

[a] From ref. [131, 169].

[b] From ref. [87, 129].

[c] From ref. [182].

[d] Calculated value for γ in Ni-Al alloys and Ni-Cr alloys are slightly different, as a result a range of possible value

is given in the table.

The ratio between grain-boundary diffusion coefficients of Al and Cr can be obtained as

$$\frac{D_{g_{Al}}^{Ni}}{D_{g_{Cr}}^{Ni}} = \frac{\varphi_{Ni-Cr}^{GB}}{\varphi_{Ni-Al}^{GB}} \tag{4.34}$$

The ratio between the lattice diffusivities of Al and Cr ($\frac{D_{Al}^{Ni}}{D_{Cr}^{Ni}}$) can be estimated from reported values

of Al and Cr diffusion coefficients [159]. The temperature dependence of these two ratios is plotted

in Figure 4.52. Although $\frac{D_{Al}^{Ni}}{D_{Cr}^{Ni}}$ is larger than unity at all temperatures considered, as shown in Figure

4.52, the grain boundaries show a different trend. Specifically, Cr can diffuse significantly faster

in Ni-Cr alloys along the grain boundaries than Al in Ni-Al alloys at lower temperatures.

Based on this analysis, when a Ni-8Al-6Cr alloy with a rough surface finish is oxidized at

lower temperature, Cr should enrich on the surface due to the faster diffusion along the

recrystallized grain boundaries. However, this is at variance with the experimental observations,

as shown in Figure 4.44, where an Al_2O_3 layer formed on the surface during heating through

relatively low temperatures.
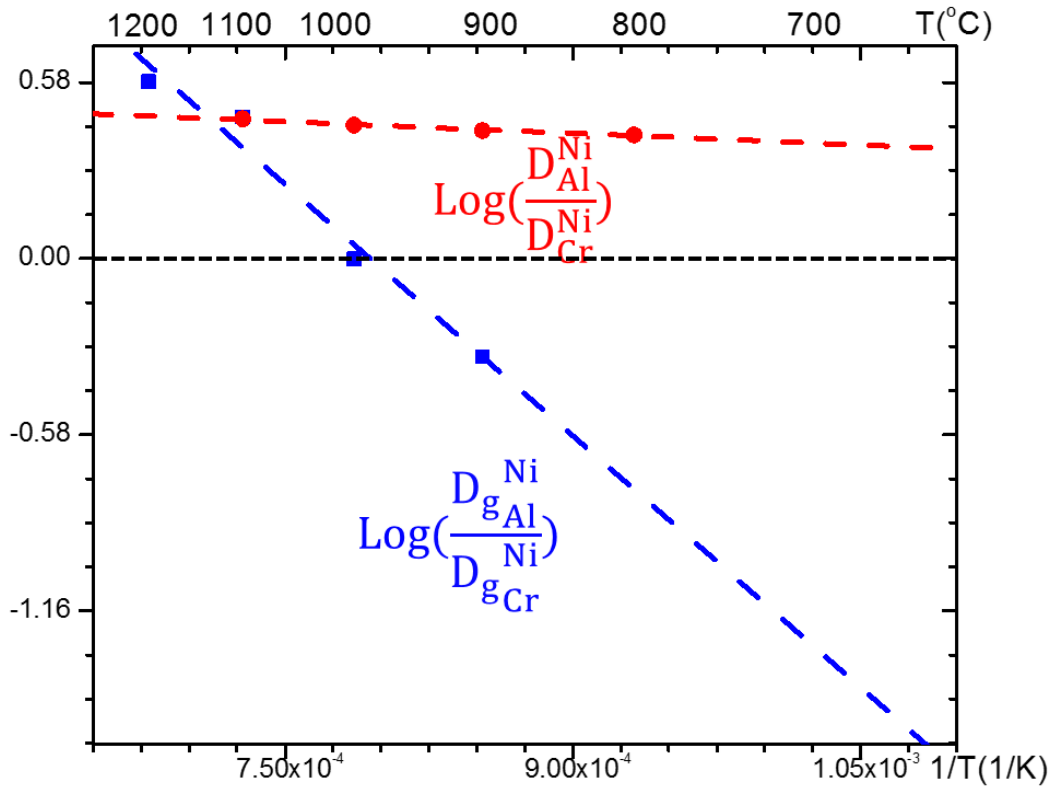
Figure 4.52 Temperature dependence of the ratios between diffusion coefficient of Al and Cr at grain boundaries and in lattice, respectively.

This discrepancy could be the result of oversimplification in the above analysis. The calculations of $D_{g_{Al}}^{Ni}$ and $D_{g_{Cr}}^{Ni}$ were based on the oxidation behavior and diffusion in binary alloys. However, the presence of Cr in the alloy could affect the Al grain-boundary diffusion. There are two possible mechanisms, one is the change of surface recrystallization behavior due to the presence of Cr, the other is a change of grain boundary or dislocation structures.

Although Ni of extremely high purity has a very low recrystallization temperature of about 300 ℃ [183]; Ni with a purity of 99.4%, Ni-30%Cu and Ni-20Cr have higher yet similar recrystallization temperatures, of about 600℃ [176, 183]. Since no surface recrystallization was

observed in both Ni-14Al and Ni-8Al-6Cr with 500-grit finish after annealing at 600℃ for 5 minutes (Figure 4.37a and b), it is deducted that the presence of Cr does not alter the surface recrystallization temperature significantly. Additionally, similar recrystallization structures were observed in Ni-14Al and Ni-8Al-6Cr with 500-grit finish after annealing at 1100℃ for 5 minutes (Figure 4.37c and d). Hence, the surface recrystallized grain structure is not affected by the presence of Cr.

As shown in Figure 4.38, the microhardness of alloys tested with a relatively light load (5gf), which is limits analysis to the surface layer, is much larger than the microhardness of alloys tested with heavy load (300gf), which is close to the bulk value. The increases of microhardness at the alloy surface indicates the formation of dislocation in the surface-deformed zone. Surface microhardness measured on the alloys with rough surface finish (500-grit finish) is much higher than bulk microhardness of that alloy. This indicates the formation of a surface-deformed zone with a high density of dislocations resulting from the rough surface finish. By contrast, the microhardness measured on the alloys with a smooth surface finish (colloidal silica finish) showed limited increase of microhardness, suggesting limited surface deformation and dislocations near the surface. Interestingly, an alumina scale formed on the surface of Ni-8Al-6Cr with 500-grit finish after oxidation at 600℃ for 5 minutes (Figure 4.43) and without the formation of surface recrystallization zone (Figure 4.37); whereas, NiO formed on the surface of Ni-14Al with 500-grit finish oxidized under the same condition (Figure 4.45). Consequently, the presence of Cr enhanced Al diffusion, presumably via the dislocation pipes, in the surface-deformed zone of Ni-8Al-6Cr.

The reason for this Cr effect on the short-circuit diffusivity of Al is still not known. Cermak et al. [179] observed a change in grain-boundary structure by doping of different elements into Ni_3Al, and consequent grain-boundary diffusivity changed. Divinski et al. [173] also suggested

that the impurities in Ni can segregate to the grain boundaries and change the grain-boundary diffusivity significantly. It is possible that the structure of short-circuit diffusion paths in Ni-Al-Cr alloys is similar to that in Ni-Cr alloys, but different from Ni-Al alloys. In such a case, both Al and Cr in Ni-Al-Cr can diffuse along the short-circuit paths in the same manner of Cr short-circuit diffusion in Ni-Cr alloys. As a result, the Al short-circuit diffusion can be enhanced significantly at lower temperatures (Figure 4.52).

As discussed above, this Cr effect on Al diffusion relies on both the presence of a high density of short-circuit diffusion paths in the surface-deformed region and oxidation at lower temperature. A rough surface finish, which can result in significant surface deformation, provides the necessary short-circuit diffusion paths, and thus, promotes the Al_2O_3 formation, as shown in Figure 4.39. But the optimized heating rate to exploit fast Al short-circuit diffusion at lower temperature, is also necessary to establish a protective scale, as shown in Figure 4.40 and Figure 4.41. The optimized oxidation conditions for Ni-Al-Cr alloys to achieve best oxidation resistance will be discussed in the following.

Although the preset temperature of the furnace is much higher than the temperature, at which Al short-circuit diffusion is significantly enhanced, an Al_2O_3 scale can be established during the heating process. Depending on the preset temperature, heating rate can vary significantly, as shown in Figure 4.33. The higher the heating rate, the shorter the exposure time at lower temperatures, and, hence, the less the contribution of the faster short-circuit diffusion to establish a protective scale. As a consequence, it is more difficult to develop an Al_2O_3 scale on the alloys oxidized in a furnace with higher heating rate, as shown in Figure 4.40.

Slowing down the heating rate can enhance the Cr effect on short-circuit diffusion, however, it will not necessarily result in the eventual formation of an Al_2O_3 scale. Since the

surface-deformed region has a limited thickness of about 1μm, as shown in Figure 4.35, the Cr effect on fast short-circuit diffusion will only exist for a finite amount of time. As soon as the surface-deformed region is depleted in Al or Cr due to the scale growth, this Cr effect will vanish. If the heating rate is so slow that the alloy cannot reach the required temperature to sustain the growth of initially protective scale by lattice diffusion before the depletion of Al and Cr from the surface-deformed zone, then breakdown of the initially protective scale may occur and result in internal oxidation, as shown in Figure 4.41.

Since only Al_2O_3 was observed during the lower-temperature oxidation of low Cr-content Ni-Al-Cr alloys, as shown in Figure 4.43 and Figure 4.44, an estimation can be made based on the depletion rate of Al in the surface-deformed zone, of the maximum length of time the Cr effect persists on short-circuit diffusion in association with surface deformation. Since the diffusion of Al in the surface-deformed zone is much faster than that in the lattice, the Al concentration profile in the alloy during the heating process can be schematically shown as Figure 4.53.
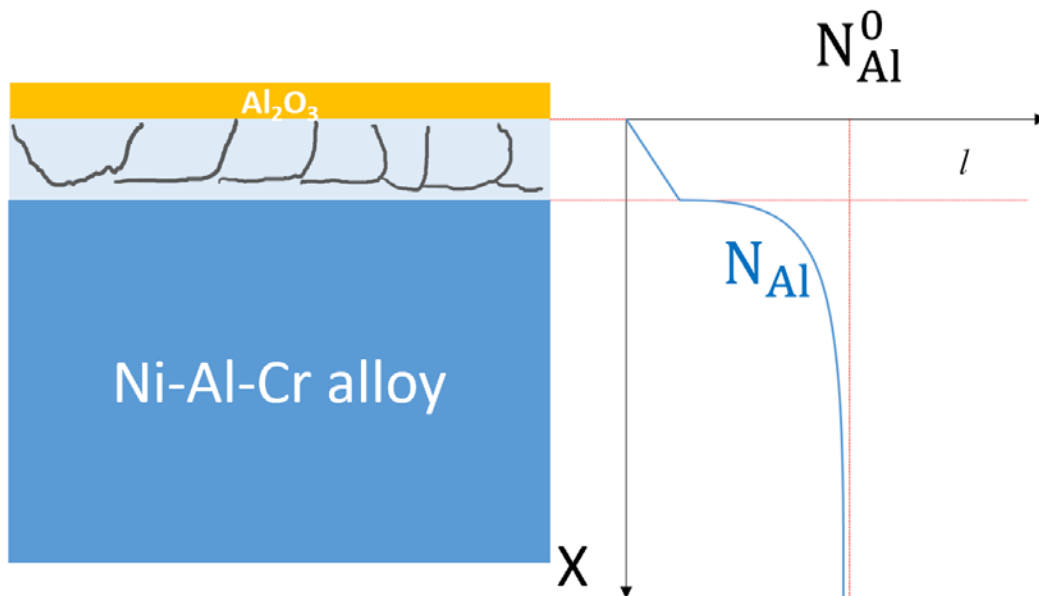
Figure 4.53 Schematics of Al concentration profile during the heating process.

Assuming a fast Al short-circuit diffusion in the surface-deformed zone such that all the Al in this zone can diffuse to the surface to sustain the Al_2O_3-scale growth, the amount of Al initially in the surface-deformed zone will equal to the amount of Al going into Al_2O_3 scale at the time t_{max}, when the Al is depleted in this region.

$$l\rho_{alloy}C_{Al} = (\frac{\Delta m_{Al}}{A})_{max} \tag{4.35}$$

where l is the thickness of the surface recrystallization zone.

ρ_{alloy} is the density of the Ni-Al-Cr alloy.

C_{Al} is the initial weight percent of Al in the surface-deformed zone.

$(\frac{\Delta m_{Al}}{A})_{max}$ is the maximum weight change of Al per unit area in the alloy, before the depletion of Al in surface-deformed zone.

$$\Delta m_{Al} = \frac{2M_{Al}}{2M_{Al} + 3M_O}\Delta m_{Al_2O_3} \tag{4.36}$$

where $\Delta m_{Al_2O_3}$ is the weight change of Al_2O_3 formed on alloy surface.

By inserting equation (4.36) into (4.35), and dividing by the oxide density, ρ_{oxide}, the maximum scale thickness, for which the surface-deformed zone can sustain the growth, can be given

$$x_{max} = \frac{2M_{Al}l\rho_{alloy}C_{Al}}{(2M_{Al} + 3M_O)\rho_{oxide}} \tag{4.37}$$

For Ni-8Al-6Cr, the density of the alloy is measured to be similar to pure Ni, which is 8.9 g/cm^3, M_{Al} and M_O are 27g/mole and 16g/mole, respectively, and the weight percentage of Al in the alloy is 0.029. The thickness of surface-deformed zone was measured to be as about 1µm (Figure 4.35). Assuming the density of this amorphous Al_2O_3 is 3.5 g/cm^3, which is just slightly smaller than γ-Al_2O_3's density of 3.67 g/cm^3 [161], the x_{max} is estimated to be 3.9×10^{-6}cm or 39 nm.

Since k_p depends on the temperature, it will constantly change during the heating process. Following the similar approach used by Markworth[184] for anisothermal oxidation, assuming linear heating rate α, k_p during the heating process can be expressed as

$$k_p = k_p^0 Exp(\frac{-Q}{R(T_0 + \alpha t)}) \tag{4.38}$$

where Q is the activation energy and T_0 is the room temperature.

Thus, the scale thickness (equation (2.8)) can be rewritten as

$$dx = \frac{k_p^0 Exp(\frac{-Q}{R(T_0 + \alpha t)})}{2x\rho_{oxide}{}^2} dt \tag{4.39}$$

Integrating equation (4.39), the scale thickness with the respect of time can be obtained

$$x =$$

$$\sqrt{\frac{k_p^0}{\rho_{oxide}{}^2 R\alpha}[Exp\left(-\frac{Q}{RT_0 + R\alpha t}\right)R(T_0 + R\alpha t) + QExpIntegralEi\left(-\frac{Q}{RT_0 + R\alpha t}\right)]} \tag{4.40}$$

Although Speck et al. [161] suggested that the parabolic constant of this initially-formed amorphous Al_2O_3 is at least as fast as γ-Al_2O_3, the exact values were not given. Therefore, the k_p for this amorphous layer of Al_2O_3 is estimated based on the measured oxide layer thickness. The parabolic rate law for the oxide growth can be expressed as

$$(\frac{\Delta m_{Al_2O_3} - \Delta m_{Al}}{A})^2 = k_p t \tag{4.41}$$

By inserting equation (4.36) into (4.41), and dividing by the oxide density, the parabolic rate law can be rewritten as

$$(\frac{3M_O x\rho_{oxide}}{2M_{Al} + 3M_O})^2 = k_p t \tag{4.42}$$

After 5-minute oxidation in air at 600°C, the oxide layer formed on the Ni-8Al-6Cr alloy is about 10nm thick (Figure 4.44). The k_p for the amorphous Al_2O_3 formed on the Ni-8Al-6Cr alloy at

600°C is calculated from equation (4.42) to be $k_p = 1.5 \times 10^{-14}$ g^2/(cm^4*s). This k_p value is significantly higher than the k_p value for γ-Al$_2$O$_3$ predicted by extrapolating measured values at higher temperatures [80], which is about 10^{-17} g^2/(cm^4*s). Assuming the activation energies of the growth of the amorphous Al$_2$O$_3$ layer is similar to that of γ-Al$_2$O$_3$ (260 kJ/mole) [80], k_p for α-Al$_2$O$_3$, γ-Al$_2$O$_3$, and amorphous Al$_2$O$_3$ can be summarized in an Arrhenius plot (Figure 4.54).
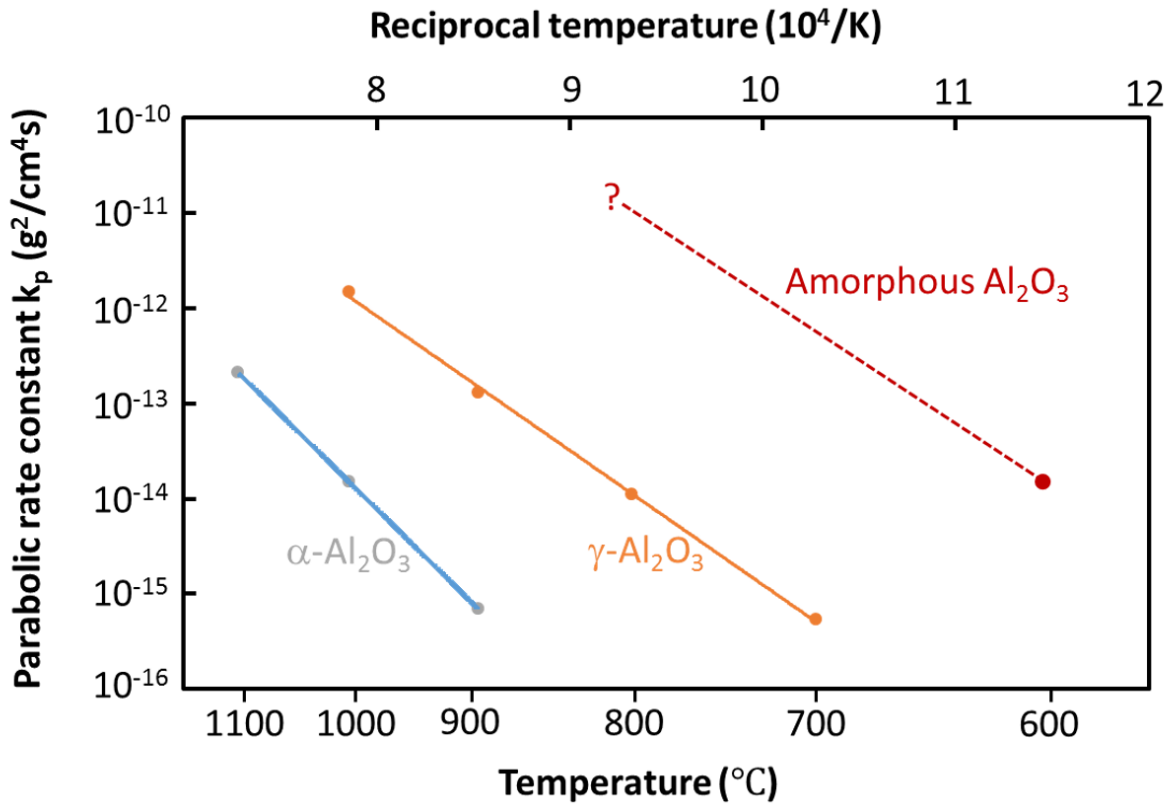
Figure 4.54 Arrhenius plot of the parabolic rate constants k_p of Ni-Al-Cr alloys with alumina scale formation. k_p for α-Al$_2$O$_3$ and γ-Al$_2$O$_3$ are obtained from previous studies [80], k_p for amorphous Al$_2$O$_3$ is calculated from oxidation experiment conducted in present study.

Since amorphous Al$_2$O$_3 \rightarrow$ γ-Al$_2$O$_3$ transformation starts around 700°C, and γ-Al$_2$O$_3$ to α-Al$_2$O$_3$ starts around 1000°C [144], the scale growth will have three stages, as schematically shown

149

in Figure 4.55. Since the lattice flux of Al in dilute Ni-Al-Cr alloys is so slow that it cannot sustain

the growth of Al_2O_3 unless it is α-Al_2O_3 [169], there are two critical points during the formation

of protective Al_2O_3 scale. The first one is related to the amorphous Al_2O_3 $\rightarrow$ γ-Al_2O_3

transformation and the second is related to the γ-Al_2O_3 $\rightarrow$ α-Al_2O_3. At each critical point, the

transformation has to finish before the Al depletion in the surface-deformed zone, otherwise, the

initially protective Al_2O_3 will breakdown.
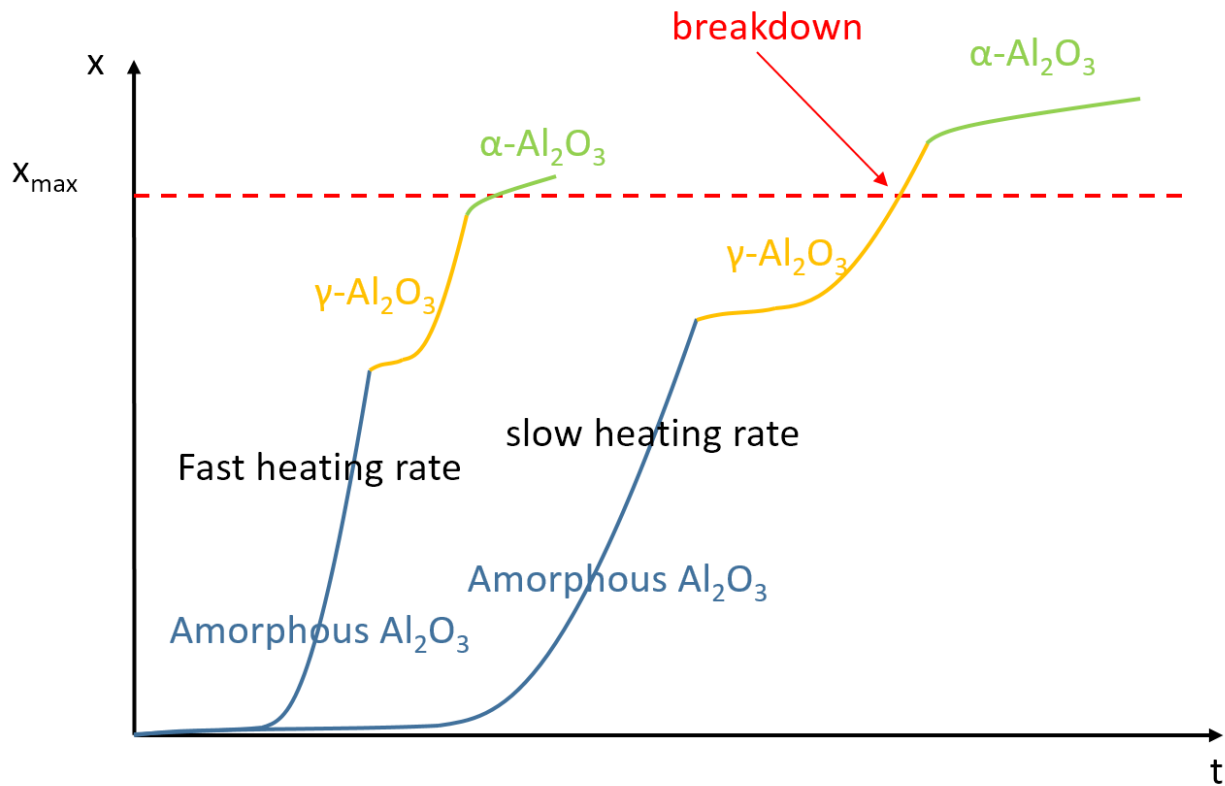
Figure 4.55 Schematics of scale growth during the heating process.

The phase transformation rate, δ, of Al_2O_3 was measured by Simpson et al. on sapphire

[144], and it was found by the authors that δ depends on the crystallographic orientation. The

average value of three reported crystallographic orientations are used in the present study, as

shown in the Table 4.3. One should note that the value listed in the Table 4.3 may be different from the phase transformation rate of Al_2O_3 formed on Ni alloys due to various factors [99], but the general trend should be the same.

Table 4.3 The average phase transformation rate of Al_2O_3 under various temperature [144].

Temperature (℃)	$\delta^{A-\gamma}$ (nm/s)	$\delta^{\gamma-\alpha}$ (nm/s)
700	3×10^{-3}	-
800	0.5	-
900	32	2×10^{-3}
1000	1×10^3	0.1
1100	2×10^4	3

Since the amorphous→γ-Al_2O_3 and γ→α-Al_2O_3 transformations are rapid at 800℃ and 1100 ℃, respectively, for simplicity, the phase transformations were assumed to occur instantaneously at 800℃ and 1100℃. Thus, the scale thickness formed during the heating to 1100℃ at different heating rates can be calculated using equation (4.40), as listed in Table 4.4.

Table 4.4 Calculated scale thickness at two critical points during the heating process.

Heating rate (℃/s)	$x_{armorphous}$ (10^{-6}cm) at 800℃	x_γ (10^{-6}cm) at 1100℃
40	4.4	5.6
20	6.2	8.0
0.17 (equals 10℃/min)	84	101

Although there are errors in the estimations of $x_{armorphous}$, x_γ and x_{max}, e.g., oversimplification of heating profile or inaccuracy in estimating k_p, it is not possible to sustain the growth of initial protective scale if the calculated x_γ is significantly larger than x_{max}. Comparing the calculated scale thickness with the x_{max} (3.9×10^{-6} cm), it is clear that the Al in surface-

151

deformed zone cannot sustain the growth of amorphous Al_2O_3 when the heating rate is 0.17 ℃/s, which was the heating rate used in oxidation experiment in TGA. This is in good agreement with the experimental results (Figure 4.41a). The heating rate in the tube furnace (Figure 4.33) was about 20℃/s and resulted in a scale growth rate that could be sustained by the Al in surface-deformed zone until α-Al_2O_3 formed, thus leading to the formation of continuous α-Al_2O_3 layer (Figure 4.41b).

The Cr effect resulting from the surface deformation is summarized schematically in Figure 4.56. Ni-Al-Cr alloys with a smooth surface finish do not benefit from the fast short-circuit diffusion and, as a result, an initial protective layer cannot be established. By contrast, Ni-Al-Cr alloys with a rough surface finish will experience surface recrystallization upon heating. The formation of this surface-recrystallization zone provides rapid diffusion paths for Al and Cr along the grain boundaries. If the heating rate is not extremely fast, a layer of amorphous alumina will develop on the alloy surface and act as initial protective scale preventing the oxidation of Ni and internal oxidation of Al. However, only the Al in the surface-deformed zone can diffuse fast enough to sustain the growth of this metastable Al_2O_3 layer. If the heating rate is not sufficiently fast to pass two critical temperatures and establish α-Al_2O_3 layer on the surface before the depletion of Al in surface-depletion zone, the initially protective scale will eventually breakdown.
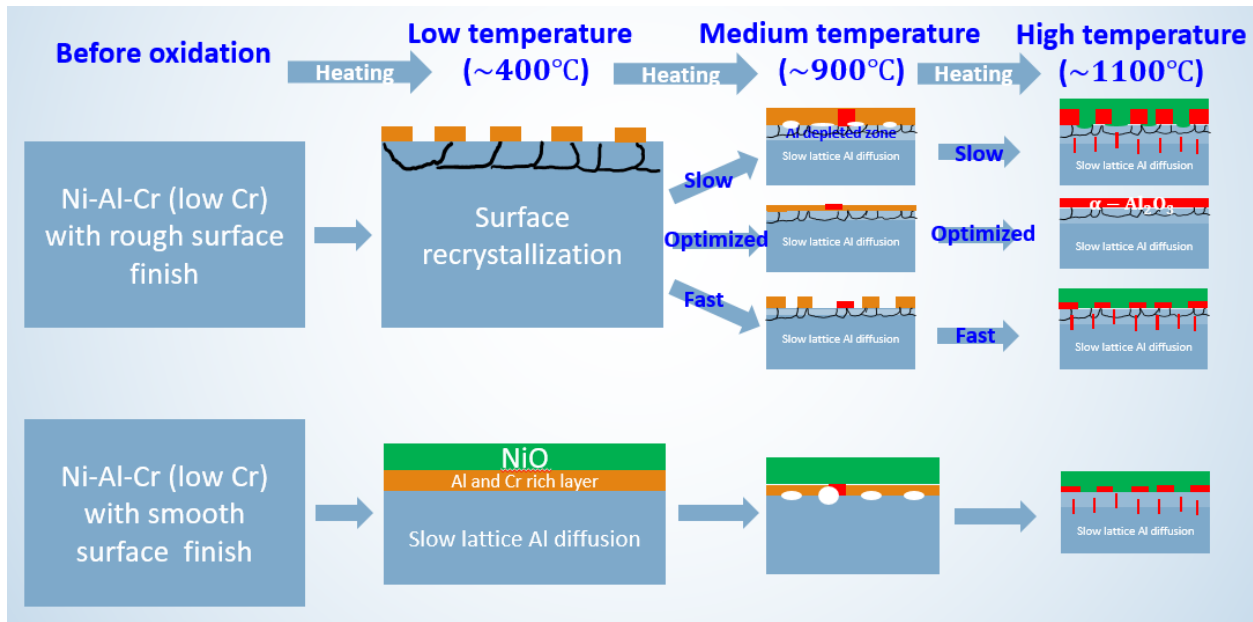
Figure 4.56 Schematics of Cr effect resulted by the surface recrystallization.

In summary, to fully exploit the Cr effect on establishing a continuous Al_2O_3 scale on Ni-Al-Cr alloys with a relatively low Cr content, a rough surface finish and an optimized heating rate to the desired operating temperature were found to be highly beneficial. Since controlling the heating rate without altering operating temperature is difficult, a low-temperature treatment can be introduced prior to the iso-thermal oxidation to achieve a similar result as using an optimized heating rate.

A low-temperature treatment of 800℃ for 5 minutes was conducted in the present study was carried out at 800°C for 5 minutes. At this temperature, the transformation from amorphous Al_2O_3 to γ-Al_2O_3 is fast (Table 4.3); meanwhile, the k_p values for both amorphous and γ-Al_2O_3 are small enough not to consume the Al in the surface-deformed region during this low-temperature treatment. Two Ni-8Al-3Cr alloy samples with a 500-grit finish were prepared and oxidized in air for 1 minute in the furnace with a preset temperature of 1150°C. One of the two samples was given the low-temperature treatment and the other one was not. The measured temperature profile for

153

each of these two samples during the entire oxidation process is shown in Figure 4.57. A comparison between these two samples after oxidation is shown in Figure 4.58. In accordance with the present analysis, the entire surface of the sample without a low-temperature treatment was covered by fast-growing NiO coupled with internal oxidation despite the formation of significant amount of recrystallized grains. By contrast, the sample that was given a low-temperature treatment had a large portion of surface covered by protective scale without any internal oxidation.
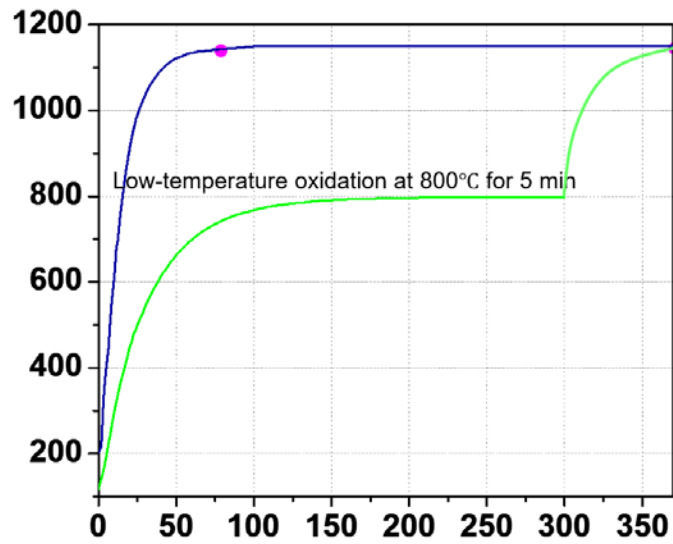
Figure 4.57 Temperature profile of two Ni-8Al-3Cr samples oxidized in air for 1 minute in the furnace with a preset temperature of 1150°C during the entire oxidation process. Purple dots indicate the time when the samples were taken out of the hot zone.
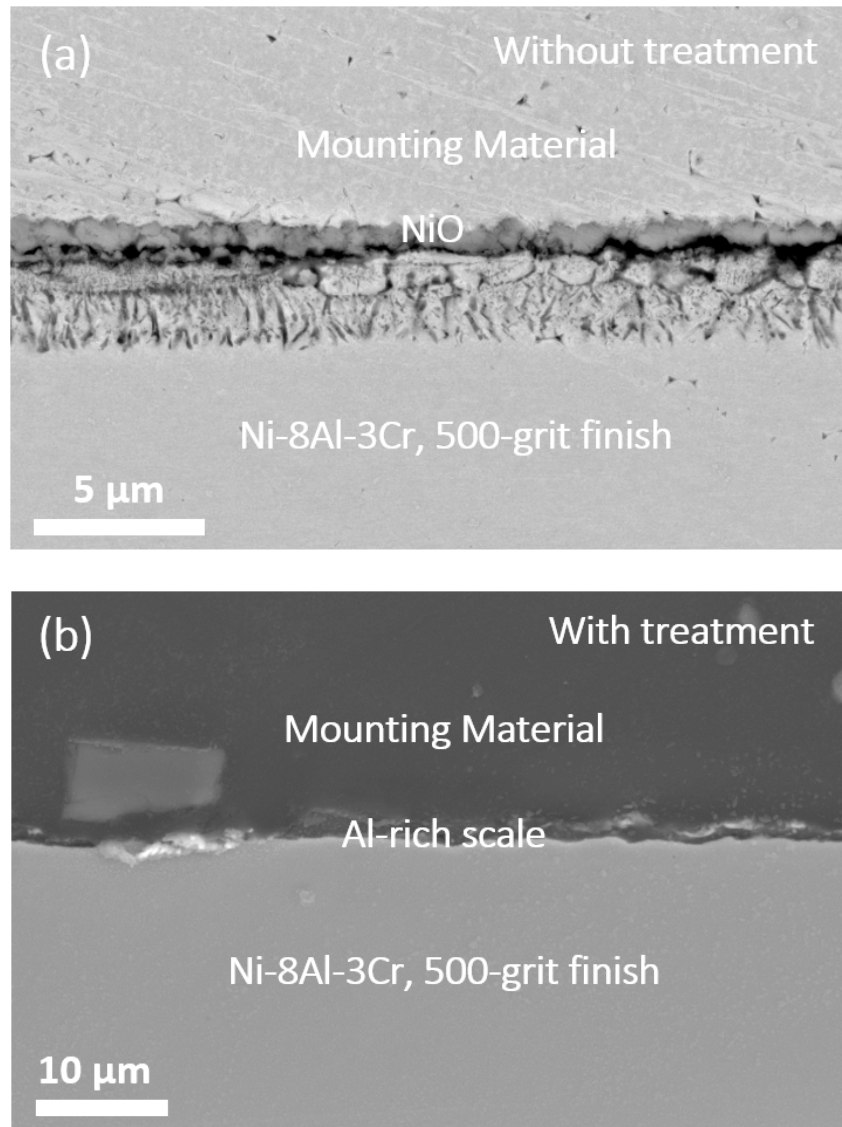
Figure 4.58 The effect of low-temperature treatment. (a) Cross-section micrograph (SEM) of Ni-8Al-3Cr alloy with 500-grit finish oxidized in air at 1150°C for 1 minute without low-temperature treatment. (b) Cross-section micrograph (SEM) of Ni-8Al-3Cr alloy with 500-grit finish oxidized in air at 1150°C for 1 minute with low-temperature treatment.

Additionally, commercial alloys (Haynes 214, Haynes 224 and Rene N5) with either a 500-grit or colloidal-silica finish were also oxidized under the same conditions as the Ni-8Al-3Cr alloy. Depending on the alloy microstructure and composition, the oxidation behavior of a given alloy under a given oxidation condition may vary but the combination of a rough surface finish and low-

temperature treatment repeatedly resulted in the best oxidation resistance (Figure 4.59d, Figure 4.60d, and Figure 4.61d). No internal oxidation or NiO formation was observed on any sample with the combination of 500-grit finish and low-temperature treatment after oxygen exposure; only a thin layer of Cr- and Al-rich scale formed. By contrast, all the other samples experienced much more severe oxidation attack. NiO formed on the surface of these alloys and Al was oxidized internally in the alloy matrix.
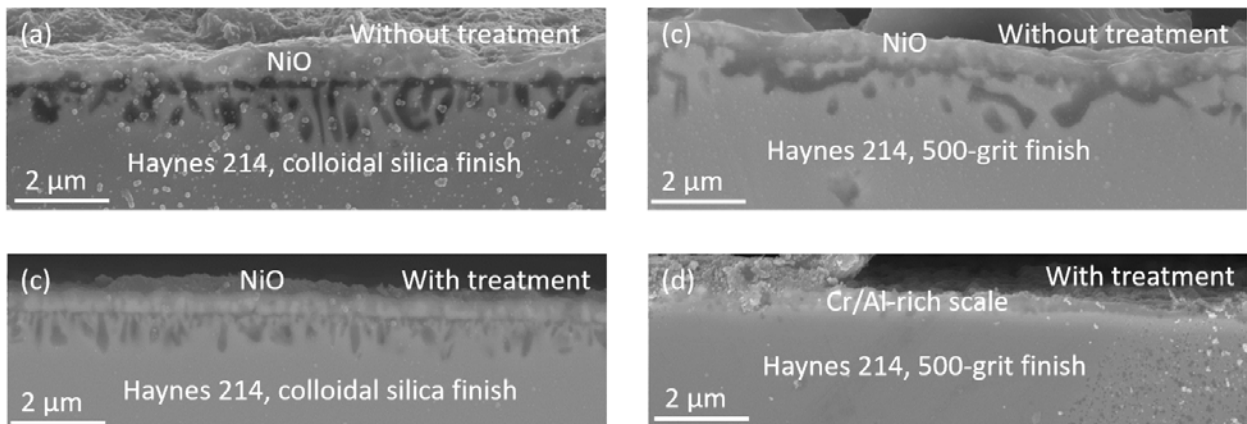
Figure 4.59 The effect of surface finish and low-temperature treatment on Haynes 214 alloy. (a) Cross-section micrograph (SEM) of Haynes 214 alloy with 500-grit finish oxidized in air for 1 minute without low-temperature treatment. (b) Cross-section micrograph (SEM) of Haynes 214 alloy with 500-grit finish oxidized in air for 1 minute with low-temperature treatment. (c) Cross-section micrograph (SEM) of Haynes 214 alloy with 500-grit finish oxidized in air for 1 minute without low-temperature treatment. (d) Cross-section micrograph (SEM) of Haynes 214 alloy with 500-grit finish oxidized in air for 1 minute with low-temperature treatment.
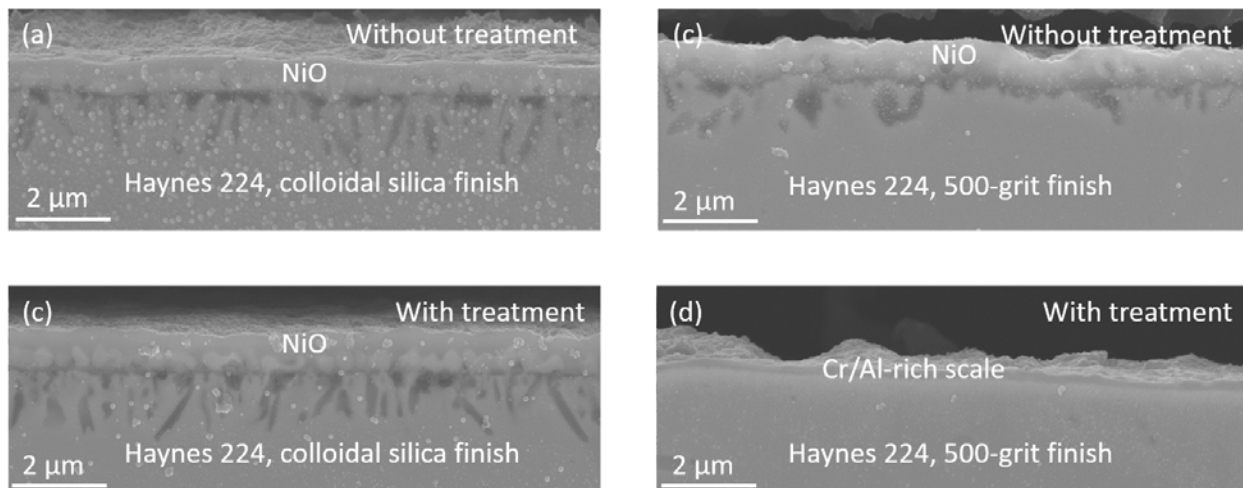
Figure 4.60 The effect of surface finish and low-temperature treatment on Haynes 224 alloy. (a) Cross-section micrograph (SEM) of Haynes 224 alloy with 500-grit finish oxidized in air for 1 minute without low-temperature treatment. (b) Cross-section micrograph (SEM) of Haynes 224 alloy with 500-grit finish oxidized in air for 1 minute with low-temperature treatment. (c) Cross-section micrograph (SEM) of Haynes 224 alloy with 500-grit finish oxidized in air for 1 minute without low-temperature treatment. (d) Cross-section micrograph (SEM) of Haynes 224 alloy with 500-grit finish oxidized in air for 1 minute with low-temperature treatment.
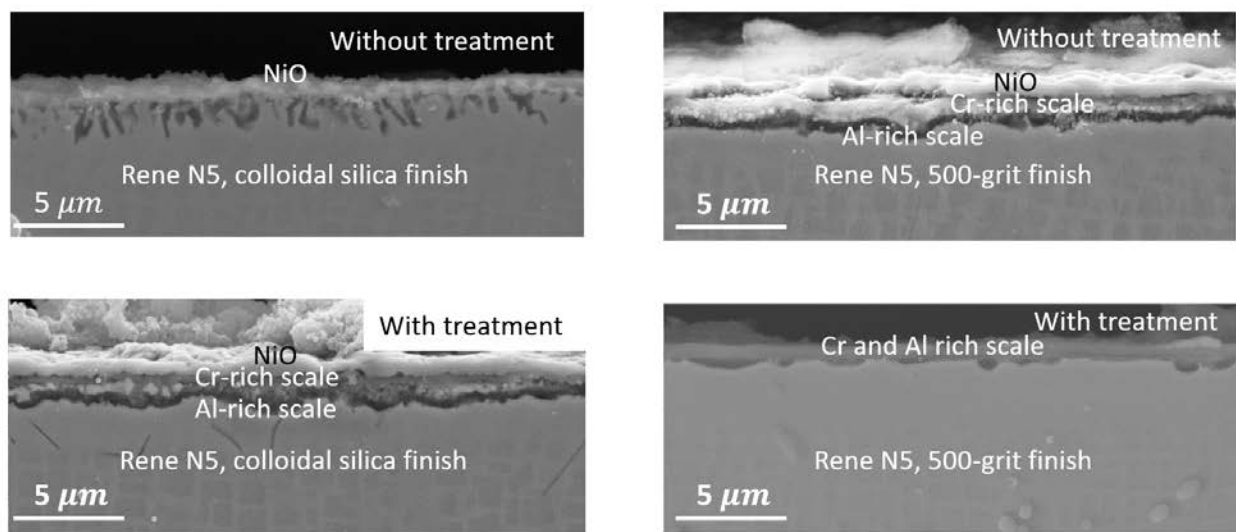
Figure 4.61 The effect of surface finish and low-temperature treatment on Rene N5 alloy. (a) Cross-section micrograph (SEM) of Rene N5 alloy with 500-grit finish oxidized in air for 1 minute without low-temperature treatment. (b) Cross-section micrograph (SEM) of Rene N5 alloy with 500-grit finish oxidized in air for 1 minute with low-

157

temperature treatment. (c) Cross-section micrograph (SEM) of Rene N5 alloy with 500-grit finish oxidized in air for 1 minute without low-temperature treatment. (d) Cross-section micrograph (SEM) of Rene N5 alloy with 500-grit finish oxidized in air for 1 minute with low-temperature treatment.

5.0   CONCLUSIONS

5.1   COMPETITIVE OXIDATION DURING NUCLEATION-AND-GROWTH STAGE

The nucleation-and-growth stage of oxidation of Cu-5at.%Ni(001) was investigated by complementary in-situ and ex-situ TEM and XPS tools to identify the oxide formation and to characterize their morphologies as a function of oxidation time and temperature. Significant differences were noted between earlier studies of Cu(001) [69]and the present study of Cu-5at.%Ni (001). Addition of a small amount of Ni into Cu led to the formation of duplex NiO and Cu_2O islands.   The selection of either NiO or Cu_2O to form initially depended on the oxidation temperature. The oxide island growth was inferred to be governed initially by the oxygen surface diffusion, which follows an exponential rate law; as the oxidation duration increased, the growth became limited by the Ni diffusion towards alloy surface, which follows a parabolic rate law. Experimental measurements from in-situ oxidation and observation were in excellent agreement with the proposed diffusion model. Oxidation temperature could also change the epitaxy between oxide islands and alloy surface from cube-on-cube to polycrystalline. The results here showed the importance of temperature in controlling the microstructure of oxide during the oxidation. These observations of sequential and duplex oxide nucleation and growth may also apply to other alloys containing several oxidizing components owning to the interplay between the thermodynamic stabilities of various oxides and diffusivities of alloying elements.

The oxygen pressure and alloy structure were also found to have a significant impact on the nucleation-and-growth stage of selective oxidation based on the study of Ni-Cr alloys. Lower oxygen pressure and finer grain structure could enhance the formation of Cr_2O_3 on the alloy surface to a greater extent, which will eventually result in a faster internal to external oxidation transition through progressive scale establishment if the initial Cr concentration in the alloy is high enough.

5.2   Cr BENEFICIAL EFFECT ON THE ALUMINA SCALE ESTABLISHMENT

Addition of Cr to the Ni-Al system can accelerate the α-Al_2O_3 formation and consequently lead to a much coarser internal oxide morphology causing a significant decrease in the effective diffusivity of oxygen and promotes the transition from internal to external oxidation of Al. By contrast, the addition of Mn, which has the similar affinity to the oxygen as Cr, to the Ni-Al system does not result in a faster establishment of Al_2O_3 scale, as predicted by the "gettering" effect, but instead increases the internal oxidation penetration. This detrimental Mn effect for Al_2O_3-scale formation was linked to the rapid formation of $MnAl_2O_4$, which has a cubic structure and stabilizes rod-like internal oxide morphology. This rod-like morphology provides fast diffusion paths for the inward oxygen diffusion in the internal oxidation zone, and thus, results in a faster penetration of internal oxidation.

Surface finish and heating rate were found to be important for the Cr beneficial effect on Al_2O_3-scale establishment of dilute Ni-Al-Cr alloys. Deformation introduced by a rough surface finish will result in a surface-deformed region, which provides short-circuit diffusion paths for Cr and Al along the grain boundaries and dislocations. At lower temperatures, Cr short-circuit diffusion in Ni-Cr alloys is found to be extremely fast, and it was inferred that the presence of Cr

in Al_2O_3 forming Ni-based alloys can also significantly increase Al short-circuit diffusion. As a result, an Al-rich scale is much easier to establish on a relatively dilute Cr containing Ni-based alloys prepared with rough surface finish during the oxygen exposure at lower temperatures. Since heating process always exists before a sample reaches the isothermal condition, the slower the heating rate, the higher the possibility that a continuous Al-rich scale may develop on the alloy surface. However, the surface-deformed zone has a limited thickness and the initially-formed Al-rich scale at low temperature consist of amorphous Al_2O_3, which has a very high k_p, can result in the depletion of Al in surface-deformed region. If full depletion occurs before the formation of an α-Al_2O_3 scale, then eventual breakdown of this initially-formed scale may occur. A low-temperature treatment can be introduced prior to fast heating to the desired temperature to leverage the Cr effect and promote the Al_2O_3-scale formation.

In summary, the criterion that the third element must have an intermediate affinity to oxygen between two base metals in order to promote the protective scale formation, as suggested by Wagner's "gettering effect", is not sufficient. The impact of the third element on the diffusivities of scale-forming elements in the matrix must be taken into account.

APPENDIX A

GROWTH RATE OF NIO

Calculation of the growth rate of an individual NiO island.

A.1   OXYGEN SURFACE DIFFUSION LIMITED GROWTH RATE OF NiO

The growth rate of an individual NiO in terms of the attaching rate of O to this island can be given as

$$\frac{dN_O}{dt} = PK_O J_O^s \tag{1}$$

where N_O is the total number of oxygen atoms in the oxide island, P is the perimeter of an island at three-phase (gas-alloy-oxide) boundary, K_o is sticking coefficient of the oxygen to the oxide island, J_o^s is the diffusive flux of oxygen.

Modeling as wedged nanorod, the volume of an oxide island can be expressed as

$$V = hwl/2 \tag{2}$$

where h is the height of the island, w is island width, l is island height.

Then

$$l = 2V/hw \tag{3}$$

The perimeter P is given by

$$P = 2w + 2l \tag{4}$$

Assuming w and l are constants during the growth of oxide nanorod, by inserting equation (3) into (4), P can be expressed as a function of V

$$P = 2w + 4V/hw \tag{5}$$

Dividing the volume of oxide island V by the geometrical volume occupied by O in NiO unit cell Ω_O, the total number of oxygen atoms in the oxide island is determined as

$$N_O = \frac{V}{\Omega_O} \tag{6}$$

By inserting equations (5) and (6) into equation (1), a differential equation can be obtained

$$\frac{dV}{dt} = (2w + 4V/hw)\Omega_O K_O J_O^s \tag{7}$$

V(t) is obtained by solving above equation

$$\ln\left(2w + \frac{4}{hw}V(t)\right) = \frac{4}{hw}\Omega_O K_O J_O^s t + C \tag{8}$$

Set the boundary condition to be t=t$_0$, V=V$_0$

$$C = \ln\left(2w + \frac{4}{hw}V_0\right) - \frac{4}{hw}\Omega_O K_O J_O^s t_0 \tag{9}$$

By inserting equation (9) into equation (8), the growth rate of oxide island can be determined as

$$\ln\left(2w + \frac{4}{hw}V(t)\right) = \frac{4}{hw}\Omega_O K_O J_O^s(t - t_0) + \ln\left(2w + \frac{4}{hw}V_0\right) \tag{10}$$

$$2w + \frac{4}{hw}V(t) = \left(2w + \frac{4}{hw}V_0\right)e^{\frac{4}{hw}\Omega_O K_O J_O^s(t-t_0)} \tag{11}$$

163

$$V(t) = \left(\frac{hw^2}{2} + V_0\right)e^{\frac{4}{hw}\Omega_0 K_0 J_0^s(t-t_0)} - \frac{hw^2}{2} \tag{12}$$

A.2   Ni BULK DIFFUSION LIMITED GROWTH RATE OF NiO

The growth rate of an individual NiO in terms of the attaching rate of Ni to this island can be given as

$$\frac{dN_{Ni}}{dt} = J_{Ni}^s * A \tag{13}$$

where N_{Ni} is the total number of Ni atoms in the oxide island, J_{Ni}^s is the flux of Ni towards the surface, A is the Ni capture zone, in which the Ni atoms diffused to the surface will be attached to an existing island instead of forming new islands.

$$J_{Ni}^s = \frac{C_0\sqrt{D}}{\sqrt{\pi t}} \tag{14}$$

where C_0 is the initial concentration of Ni, D is the diffusivity of Ni in Cu.

Inserting (14) into (13):

$$\frac{dN_{Ni}}{dt} = \frac{AC_0\sqrt{D}}{\sqrt{\pi t}} \tag{15}$$

Integrating (15):

$$N_{Ni}(t) = \frac{2AC_0\sqrt{D}}{\sqrt{\pi}}\left(\sqrt{t - t_0}\right) + N_{Ni}^0 \tag{16}$$

where V_0 is island volume at time t_0.

The temporal evolution of volume of an oxide island can be expressed in terms of the number of Ni atoms in this oxide:

164

$$V_{NiO}^{Ni\,limited} = \Omega_{Ni} * N_{Ni} \tag{17}$$

where Ω_{Ni} is the geometrical volume occupied by a Ni atom in a unit NiO cell.

Inserting (16) into (17):

$$V_{NiO}^{Ni\,limited} = \frac{2\Omega_{Ni}AC_0\sqrt{D}}{\sqrt{\pi}}\left(\sqrt{t - t_0}\right) + V_0 \tag{18}$$

BIBLIOGRAPHY

1. Wallwork, G.R., *The oxidation of alloys.* Reports on Progress in Physics, 1976. **39**(5): p. 401.

2. Lawless, K.R., *The oxidation of metals.* Reports on Progress in Physics, 1974. **37**(2): p. 231.

3. Stott, F.H., *The protective action of oxide scales in gaseous environments at high temperature.* Reports on Progress in Physics, 1987. **50**(7): p. 861.

4. Yagyu, K., et al., *Dissociative Adsorption of Oxygen on Clean Cu(001) Surface.* The Journal of Physical Chemistry C, 2009. **113**(14): p. 5541-5546.

5. Chua, F.M., Y. Kuk, and P.J. Silverman, *Oxygen chemisorption on Cu(110): An atomic view by scanning tunneling microscopy.* Phys. Rev. Lett., 1989. **63**(4): p. 386.

6. Benndorf, C., et al., *Chemisorption and initial oxidation of Ni(110): AES, ELS and work function measurements.* Surface Science, 1980. **92**(2-3): p. 636-666.

7. Demuth, J.E., D.W. Jepsen, and P.M. Marcus, *Chemisorption Bonding of c(2×2) Chalcogen Overlayers on Ni(001).* Physical Review Letters, 1973. **31**(8): p. 540-542.

8. Coulman, D.J., et al., *Novel mechanism for the formation of chemisorption phases: The (2 x 1)O-Cu(110) ``added row'' reconstruction.* Phys. Rev. Lett., 1990. **64**(15): p. 1761.

9. Feidenhans'l, R., et al., *Oxygen chemisorption on Cu(110): A model for the c(6 x 2) structure.* Phys. Rev. Lett., 1990. **65**(16): p. 2027.

10. Jensen, F., et al., *Surface reconstruction of Cu(110) induced by oxygen chemisorption.* Phys. Rev. B: Condens. Matter, 1990. **41**(14): p. 10233.

11. Yang, J.C. and G. Zhou, *In situ ultra-high vacuum transmission electron microscopy studies of the transient oxidation stage of Cu and Cu alloy thin films.* Micron, 2012. **43**(11): p. 1195-1210.

12. Chattopadhyay, B. and G.C. Wood, *The Transient Oxidation of Fe-Cr and Ni-Cr Alloys.* Journal of The Electrochemical Society, 1970. **117**(9): p. 1163-1171.

13. Kear, B.H., et al., *On the transient oxidation of a Ni-15Cr-6Al alloy.* Oxidation of Metals, 1971. **3**(6): p. 557-569.

14. Wagner, C., *Contributions to the Theory of Surface Colouring of Metals.* Z. Phys. Chem., 1933. **21**: p. 25-41.

15. Wagner, C., *Theoretical Analysis of the Diffusion Processes Determining the Oxidation Rate of Alloys.* Journal of The Electrochemical Society, 1952. **99**(10): p. 369-380.

16. Wagner, C., *Formation of Composite Scales Consisting of Oxides of Different Metals.* Journal of The Electrochemical Society, 1956. **103**(11): p. 627-633.

17. Wagner, C., *Oxidation of Alloys Involving Noble Metals.* Journal of The Electrochemical Society, 1956. **103**(10): p. 571.

18. Tammann, G., Z. Anorg. Allgem. Chem., 1920. **III**: p. 78.

19. Pilling, N.B. and R.E. Bedworth, *Oxidation of Copper-Nickel Alloys at High Temperatures.* Industrial & Engineering Chemistry, 1925. **17**(4): p. 372-376.

20. Pilling, N.B. and R.E. Bedworth, J. Inst. Metals, 1926. **63**: p. 21.

21. Wagner, C. and K. Grunewld, Z. physik. Chem. B, 1938. **40**: p. 455.

22. Wood, G., *High-temperature oxidation of alloys.* Oxidation of Metals, 1970. **2**(1): p. 11-57.

23. Lahtonen, K., et al., *Oxygen adsorption-induced nanostructures and island formation on Cu{100}: Bridging the gap between the formation of surface confined oxygen chemisorption layer and oxide formation.* Journal of Chemical Physics, 2008. **129**(12): p. 124703.

24. Oed, W., et al., *Adsorbate-induced relaxation and reconstruction of c(2 × 2)O/Ni(100): A reinvestigation by leed structure analysis.* Surface Science, 1989. **224**(1–3): p. 179-194.

25. Holloway, P.H. and J.B. Hudson, *Kinetics of the reaction of oxygen with clean nickel single crystal surfaces: I. Ni(100) surface.* Surf. Sci., 1974. **43**(1): p. 123-140.

26. Holloway, P.H. and J.B. Hudson, *Kinetics of the reaction of oxygen with clean nickel single crystal surfaces: II. Ni(111) surface.* Surf. Sci., 1974. **43**(1): p. 141-149.

27. Orr, W.H., *Oxide Nucleation and Growth.* 1962, Cornell University: Ithaca, N.Y.

28. Zhou, G., L. Wang, and J.C. Yang, *Effects of surface topology on the formation of oxide islands on Cu surfaces.* J. Appl. Phys., 2005. **97**(6): p. 063509.

29.   Zhou, G., et al., *Nanoscale duplex oxide growth during early stages of oxidation of Cu-Ni(100).* Phys. Rev. B: Condens. Matter, 2009. **80**(13): p. 134106.

30.   Zhou, G.W., et al., *Composition effects on the early-stage oxidation kinetics of (001) Cu–Au alloys.* J. Appl. Phys., 2007. **101**(3): p. 033521-N.PAG.

31.   Luo, L., et al., *Dependence of degree of orientation of copper oxide nuclei on oxygen pressure during initial stages of copper oxidation.* Phys. Rev. B: Condens. Matter, 2011. **83**(15): p. 155418.

32.   Kang, Y., et al., *Transient Oxidation of Cu-5at.%Ni(001): Temperature Dependent Sequential Oxide Formation.* Oxidation of Metals, 2013. **79**(3-4): p. 303-311.

33.   Ellingham, H.J.T., *Transactions and Communications: Reducibility of Oxides and Sulphides in Metallurgical Process.* Journal of the Society of Chemical Industry, 1944. **63**(5): p. 125-133.

34.   Wagner, C. and K. Grunewald, *Theory of the tarnishing process. III.* Z. physik. Chem., 1938. **B40**: p. 455-75.

35.   Boreskov, G.K., Discuss. Faraday Soc., 1966. **41**: p. 263.

36.   Kofstad, P., *High Temperature Oxidation of Metals*. 1966, New York: John Wiley.

37.   Evans, U.R., *The Corrosion and Oxidation of Metals*. 1960, London: Edwin Arnold.

38.   Hauffe, K., *Oxidation of Metals*. 1965, New York: Plenum Press.

39.   McNaught, A.D. and A. Wilkinson, *Compendium of Chemical Terminology*. 2nd ed. Iupac Chemical Nomenclature Series. 1997: Blackwell Science Inc.

40.   Chemistry, I.U.o.P.a.A., *Quantities, Units and Symbols in Physical Chemistry*. 2nd ed. 1993, Oxford: Blackwell Science.

41.   Wagner, C., *Internal oxidation of Cu-Pd and Cu-Pt alloys.* Corrosion Science, 1968. **8**(12): p. 889-893.

42.   Rapp, R.A., *Kinetics, Microstructures and Mechanism of Internal Oxidation - Its Effect and Prevention in High Temperature Alloy Oxidation.* Corrosion, 1965. **21**(12): p. 382-401.

43.   Gesmundo, F. and F. Viani, *Transition from internal to external oxidation for binary alloys in the presence of an outer scale.* Oxidation of Metals, 1986. **25**(5-6): p. 269-282.

44.   Maak, F. and C. Wagner, Werkstoffe und Korrosion, 1961. **12**: p. 273.

45.   Rapp, R.A., *The transition from internal to external oxidation and the formation of interruption bands in silver-indium alloys.* Acta Metallurgica, 1961. **9**(8): p. 730-741.

46.   Czerski, L., S. Mrowec, and T. Werber, Archiw. Hutn., 1957. **2**: p. 183.

47.   Lichter, B.D. and C. Wagner, *The Attack of Copper‐Gold, Silver‐Gold, Nickel‐Copper, and Silver‐Copper Alloys by Sulfur at Elevated Temperatures.* Journal of The Electrochemical Society, 1960. **107**(3): p. 168-180.

48.   Price, L. and G. Thomas, J. Inst. Metals, 1938. **63**: p. 21.

49.   Czerski, L., S. Mrowec, and T. Werber, Archiw. Hutn., 1959. **4**: p. 245.

50.   Dunn, J., J. Inst. Metals, 1931. **46**: p. 25.

51.   Wagner, C., Z. Elektrochem, 1959. **63**: p. 772.

52.   Boehm, G. and M. Kahlweit, *Internal oxidation of metallic alloys.* Acta Metall., 1964. **12**(5): p. 641-8.

53.   Gesmundo, F. and Y. Niu, *The Internal Oxidation of Ternary Alloys I: The Single Oxidation of the Most-Reactive Component Under Low Oxidant Pressures.* Oxidation of Metals, 2003. **60**(5-6): p. 347-370.

54.   Culver, R.V. and F.C. Tompkins, *Advances in Catalysis.* Vol. XI. 1959, New York: Academic Press.

55.   Hayward, D.O., *Chemisorption and Reactions on Metallic Films.* 1971, New York: Academic Press.

56.   Jensen, F., et al., *Dynamics of oxygen-induced reconstruction of Cu(100) studied by scanning tunneling microscopy.* Phys. Rev. B: Condens. Matter, 1990. **42**(14): p. 9206.

57.   Mitchell, D.F. and K.R. Lawless, J. Paint Tech, 1966. **38**: p. 575.

58.   May, J.W. and L.H. Germer, *Incipient oxidation of (110) nickel.* Surface Science, 1968. **11**(3): p. 443-464.

59.   Benard, J., *L' Oxydation des Metaux.* Vol. 1. 1962, Paris: Gauthier-Villiars.

60.   Zhou, G., *Nucleation thermodynamics of oxide during metal oxidation.* Appl. Phys. Lett., 2009. **94**(20): p. 201905-3.

61.   Liu, X.Y., *A new kinetic model for three-dimensional heterogeneous nucleation.* The Journal of Chemical Physics, 1999. **111**(4): p. 1628-1635.

62.   McLean, M. and E.D. Hondros, *Interfacial energies and chemical compound formation.* Journal of Materials Science, 1973. **8**(3): p. 349-351.

63.   Hondros, E.D., *The effect of adsorbed oxygen on the surface energy of B.C.C. iron.* Acta Metallurgica, 1968. **16**(11): p. 1377-1380.

64.   Zhou, G.Y., Judith C., *Initial oxidation kinetics of Cu(100), (110), and (111) thin films investigated by in situ ultra-high-vacuum transmission electron microscopy.* J. Mater. Res., 2005. **20**(7): p. 1684-1694.

65.   Cabrera, N., *Semiconductor Surface Physics.* 1957, Philadelphia: University of Pennsylvania Press.

66.   Phillips, V.A., *Role of Defects in Evaporated Silver Films on the Nucleation of Sulfide ``Patches'&apos.* Journal of Applied Physics, 1962. **33**(2): p. 712-717.

67.   Zhou, G., *Nucleation-induced kinetic hindrance to the oxide formation during the initial oxidation of metals.* Phys. Rev. B: Condens. Matter, 2010. **81**(19): p. 195440.

68.   Zhou, G. and J.C. Yang, *Formation of Quasi-One-Dimensional Cu2O Structures by in situ Oxidation of Cu(100).* Phys. Rev. Lett., 2002. **89**(10): p. 106101.

69.   Zhou, G. and J.C. Yang, *Temperature effect on the Cu2O oxide morphology created by oxidation of Cu(0 0 1) as investigated by in situ UHV TEM.* Appl. Surf. Sci., 2003. **210**(3-4): p. 165-170.

70.   Yang, J.C., et al., *The Homogeneous Nucleation Mechanism of Cu2O on Cu(001).* Scripta Materialia, 1998. **38**(8): p. 1237-1242.

71.   Yang, J.C., et al., *The homogeneous nucleation mechanism of Cu$_2$O on Cu(001).* Scr. Mater., 1998. **38**(8): p. 1237-1242.

72.   Zhou, G.W., et al., *Cu$_2$O Island Shape Transition during Cu-Au Alloy Oxidation.* Phys. Rev. Lett., 2006. **96**(22): p. 226108.

73.   Luo, L., et al., *Comparative study of the alloying effect on the initial oxidation of Cu-Au(100) and Cu-Pt(100).* Appl. Phys. Lett., 2014. **104**(12): p. 121601/1-121601/5.

74.   Luo, L., et al., *Effect of gold composition on the orientations of oxide nuclei during the early stage oxidation of Cu-Au alloys.* J. Appl. Phys., 2012. **111**(8): p. 083533/1-083533/9.

75.   Hindam, H.M. and W.W. Smeltzer, *Growth and Microstructure of α‐Al2 O 3 on Ni‐Al Alloys: Internal Precipitation and Transition to External Scale.* Journal of The Electrochemical Society, 1980. **127**(7): p. 1622-1630.

76.   Chattopadhyay, B. and G.C. Wood, *The Transient Oxidation of Fe‑Cr and Ni‑Cr Alloys.* Journal of The Electrochemical Society, 1970. **117**(9): p. 1163-1171.

77.   Stott, F.H., P.K.N. Bartlett, and G.C. Wood, *Laser surface treatment and its influence on the development of healing Cr2O3 scales on nickel-chromium alloys.* Oxidation of Metals, 1987. **27**(1-2): p. 37-55.

78.   Tatlock, G.J., R.W. Devenish, and J.S. Punni. *Structural studies of internal oxides in nickel aluminum alloys.* 1991. Inst. Met.

79.   Hagel, W.C., *The Oxidation off Iron, Nickel and Cobalt-Base Alloys Containing Aluminum.* Corrosion, 1965. **21**(10): p. 316-326.

80.   Brumm, M.W. and H.J. Grabke, *The oxidation behaviour of NiAl-I. Phase transformations in the alumina scale during oxidation of NiAl and NiAl-Cr alloys.* Corrosion Science, 1992. **33**(11): p. 1677-1690.

81.   Chattopadhyay, B. and G.C. Wood, *The transient oxidation of alloys.* Oxidation of Metals, 1970. **2**(4): p. 373-399.

82.   Doychak, J., J.L. Smialek, and T.E. Mitchell, *Transient oxidation of Single-Crystal β-NiAl.* Metallurgical Transactions A, 1989. **20**(3): p. 499-518.

83.   Levin, I. and D. Brandon, *Metastable Alumina Polymorphs: Crystal Structures and Transition Sequences.* Journal of the American Ceramic Society, 1998. **81**(8): p. 1995-2012.

84.   Rybicki, G. and J. Smialek, *Effect of theθ-α-Al2O3 transformation on the oxidation behavior ofβ-NiAl + Zr.* Oxidation of Metals, 1989. **31**(3-4): p. 275-304.

85.   Clarke, D.R., *Epitaxial Phase Transformations in Aluminum Oxide.* physica status solidi (a), 1998. **166**(1): p. 183-196.

86.   Stott, F.H., G.C. Wood, and J. Stringer, *The influence of alloying elements on the development and maintenance of protective scales.* Oxidation of Metals, 1995. **44**(1-2): p. 113-145.

87.   Giggins, C.S. and F. Pettit, *The Effect of Alloy Grain-Size and Surface Deformation on the Selective Oxidation of Chromium in Ni-Cr Alloys at Temperatures of 900C and 1100C.* Trans. AIME., 1969. **245**: p. 2509.

88.   Stott, F.H., P.K.N. Bartlett, and G.C. Wood, *The influence of laser surface treatment on the high temperature oxidation of Cr2O3-forming alloys.* Materials Science and Engineering, 1987. **88**(0): p. 163-169.

89.   Bartlett, P.K.N. 1985, University of Manchester.

90. Giggins, C.S. and F.S. Pettit, *Oxidation of Ni-Cr-Al Alloys Between 1000° and 1200°C.* Journal of The Electrochemical Society, 1971. **118**(11): p. 1782.

91. Heinonen, M.H., et al., *Initial Oxidation of Fe–Al and Fe–Cr–Al Alloys: Cr as an Alumina Booster.* Oxidation of Metals, 2011. **76**(3-4): p. 331-346.

92. Yi, H.C., et al., *Oxidation of γ-Ni−Al−Si alloys at 1073 K.* Oxidation of Metals, 1995. **43**(1-2): p. 115-139.

93. Wagner, C., *Passivity and inhibition during the oxidation of metals at elevated temperatures.* Corrosion Science, 1965. **5**(11): p. 751-764.

94. Jackson, P.R.S. and G.R. Wallwork, *High temperature oxidation of iron-manganese-aluminum based alloys.* Oxidation of Metals, 1984. **21**(3-4): p. 135-170.

95. Tomaszewicz, P. and G.R. Wallwork, *The Oxidation of Fe-Al Alloys Containing Chromium, Nickel, or Manganese.* Corrosion, 1984. **40**(4): p. 152-157.

96. Götlind, H., et al., *The Effect of Water Vapor on the Initial Stages of Oxidation of the FeCrAl Alloy Kanthal AF at 900 °C.* Oxidation of Metals, 2007. **67**(5-6): p. 251-266.

97. Kitajima, Y., et al., *Rapid Formation of α-Al2O3 Scale on an Fe–Al Alloy by Pure-Metal Coatings at 900 °C.* Oxidation of Metals, 2010. **73**(3-4): p. 375-388.

98. Kitajima, Y., et al., *Acceleration of Metastable to Alpha Transformation of Al2O3 Scale on Fe–Al Alloy by Pure-Metal Coatings at 900 °C.* Oxidation of Metals, 2011. **75**(1-2): p. 41-56.

99. Shaaban, A., S. Hayashi, and K. Azumi, *Effects of Nano Metal Coatings on Growth Kinetics of α-Al2O3 Formed on Ni-50Al Alloy.* Oxidation of Metals, 2014. **82**(1-2): p. 85-97.

100. Airiskallio, E., et al., *High temperature oxidation of Fe–Al and Fe–Cr–Al alloys: The role of Cr as a chemically active element.* Corrosion Science, 2010. **52**(10): p. 3394-3404.

101. Airiskallio, E., et al., *Third element effect in the surface zone of Fe-Cr-Al alloys.* Physical Review B, 2010. **81**(3): p. 033105.

102. Cabrera, N. and N.F. Mott, *Theory of the oxidation of metals.* Reports on Progress in Physics, 1949. **12**(1): p. 163.

103. Wagner, C. and K.-E. Zimens, *Die Oxydationsgeschwindigkeit von Nickel bei kleinen Zusätzen von Chrom und Mangan. Beitrag zur Theorie des Anlaufvorganges.* Acta Chem. Scand., 1947. **1**: p. 547.

104. Wagner, C., in *Seminar on Atom Movements Amer. Soc. Metals.* 1951: Cleveland. p. 153.

105.   Yang, J.C., et al., *In-Situ UHV Tem Investigations of the Initial Oxidation Stage of Copper Thin Films.* MRS Bull., 1997. **481**: p. 557.

106.   Yang, J.C., et al., *Self-limiting oxidation of copper.* Applied Physics Letters, 1998. **73**(19): p. 2841-2843.

107.   Yang, J.C., D. Evan, and L. Tropia, *From nucleation to coalescence of Cu2O islands during in situ oxidation of Cu(001).* Applied Physics Letters, 2002. **81**(2): p. 241-243.

108.   McDonald, M.L., J.M. Gibson, and F.C. Unterwald, *Design of an ultrahigh-vacuum specimen environment for high-resolution transmission electron microscopy.* Review of Scientific Instruments, 1989. **60**(4): p. 700-707.

109.   Wagner, C.D. and G.E. Muilenberg, *Handbook of x-ray photoelectron spectroscopy: a reference book of standard data for use in x-ray photoelectron spectroscopy.* 1979: Perkin-Elmer Corp., Physical Electronics Division.

110.   Poulston, S., et al., *Surface Oxidation and Reduction of CuO and Cu2O Studied Using XPS and XAES.* Surf. Interface Anal., 1996. **24**(12): p. 811-820.

111.   Paul E, L., *X-ray induced photoelectron and auger spectra of Cu, CuO, Cu2O, and Cu2S thin films.* J. Electron. Spectrosc. Relat. Phenom., 1974. **4**(3): p. 213-218.

112.   Huang, W. and Y.A. Chang, *Thermodynamic properties of the Ni–Al–Cr system.* Intermetallics, 1999. **7**(8): p. 863-874.

113.   Raghavan, V., *Al-Mn-Ni (Aluminum-Manganese-Nickel).* Journal of Phase Equilibria and Diffusion, 2006. **27**(5): p. 493-496.

114.   Rhines, F.H., Trans. AIME., 1940. **137**: p. 246.

115.   Rauch, E.F. and M. Veron, *Coupled microstructural observations and local texture measurements with an automated crystallographic orientation mapping tool attached to a tem.* Materialwissenschaft und Werkstofftechnik, 2005. **36**(10): p. 552-556.

116.   Rauch, E.F. and L. Dupuy, *Rapid spot diffraction patterns identification through template matching.* Archives of Metallurgy and Materials, 2005. **50**(1): p. 87-99.

117.   Liu, X., et al., *Interfacial orientation and misorientation relationships in nanolamellar Cu/Nb composites using transmission-electron-microscope-based orientation and phase mapping.* Acta Materialia, 2014. **64**(0): p. 333-344.

118.   Bastow, B.D., G.C. Wood, and D.P. Whittle, *Morphologies of uniform adherent scales on binary alloys.* Oxidation of Metals, 1981. **16**(1-2): p. 1-28.

119.   Gesmundo, F. and B. Gleeson, *Oxidation of multicomponent two-phase alloys.* Oxidation of Metals, 1995. **44**(1-2): p. 211-237.

120.   Lide, D.R., ed. *CRC Handbook of Chemistry and Physics*. 2006, Taylor & Francis: Boca Raton, Florida.

121.   Oishi, T., S. Tagawa, and S. Tanegashima, *Activity Measurements of Copper in Solid Copper-Nickel Alloys using Copper-Beta-Alumina.* Materials Transactions, 2003. **44**: p. 1120.

122.   Rapp, R.A. and F. Maak, *Thermodynamic properties of solid copper-nickel alloys.* Acta Metallurgica, 1962. **10**(1): p. 63-69.

123.   Lippmann, S., et al., *Modelling temperature and concentration dependent solid/liquid interfacial energies.* Philosophical Magazine, 2016. **96**(1): p. 1-14.

124.   Yang, J.C. and M. Yeadon, *Oxygen surface diffusion in three-dimensional Cu_2O growth on Cu(001) thin films.* Appl. Phys. Lett., 1997. **70**(26): p. 3522.

125.   Van Dijk, T. and E.J. Mittemeijer, *The effect of interdiffusion on moiré patterns of thin bimetallic films.* Thin Solid Films, 1977. **41**(2): p. 173-178.

126.   Eberhart, M.E., M.M. Donovan, and R.A. Outlaw, *Ab initio calculations of oxygen diffusivity in group-IB transition metals.* Physical Review B, 1992. **46**(19): p. 12744-12747.

127.   Albert, E., R. Kirchheim, and H. Dietz, *Diffusitivity of oxygen in copper.* Scripta Metallurgica, 1981. **15**(6): p. 673-677.

128.   Sjövall, P. and P. Uvdal, *Oxygen sticking on Pd(111): double precursors, corrugation and substrate temperature effects.* Chemical Physics Letters, 1998. **282**(5–6): p. 355-360.

129.   Giggins, C.S. and F. Pettit, *Oxidation of Ni-Cr Alloys Between 800C and 1200C.* Trans. AIME., 1969. **245**: p. 2495.

130.   Zhao, W., *STEAM EFFECTS ON OXIDATION BEHAVIOR OF ALUMINA-SCALE FORMING NICKEL-BASED ALLOYS AND A KINETICS ANALYSIS OF COMPLEX SCALE EVOLUTION DURING ISOTHERMAL OXIDATION*, in *MSE*. 2012, University of Pittsburgh: Pittsburgh.

131.   Zhao, W. to be published.

132.   Yang, Y. and P. Zhang, *Activated O2 dissociation and formation of oxide islands on Be(0001): An atomistic model for metal oxidation.* Phys. Rev. B: Condens. Matter, 2010. **82**(7): p. 073406.

133. Stott, F.H., et al., *The transport of oxygen to the advancing internal oxide front during internal oxidation of nickel-base alloys at high temperature.* Solid State Ionics, 1984. **12**(0): p. 365-374.

134. Meijering, J.L., *Internal oxidation in alloys.* Advances in Materials Research, 1971. **5**: p. 1.

135. Schumann, E. and M. Rühle, *Microstructural observations on the oxidation of γ ′ -Ni3Al at high oxygen partial pressure.* Acta Metallurgica et Materialia, 1994. **42**(4): p. 1481-1487.

136. File, P.D., International Centre for Diffraction Data, 1991. **Card No. 10-425**.

137. Schumann, E., et al., *Microstructural observations on the oxidation of γ ′ -Ni3Al at low oxygen partial pressure.* Acta Metallurgica et Materialia, 1992. **40**(6): p. 1311-1319.

138. Lutterotti, L. and P. Scardi, *Simultaneous structure and size-strain refinement by Rietveld method.* Journal of Applied Crystallography, 1900. **23**: p. 246.

139. Sawada, H., *Residual electron density study of chromium sesquioxide by crystal structure and scattering factor refinement Note: harmonic scattering factor refinement.* Materials Research Bulletin, 1994. **29**: p. 239.

140. Essene, E.J. and D.R. Peacor, *Crystal chemistry and petrology of coexisting galaxite and jacobsite and other spinel solution and solvi.* American Mineralogist, 1983. **68**(3-4): p. 449.

141. Lippens, B.C. and J.H. De Boer, *Study of phase transformations during calcination of aluminum hydroxides by selected area electron diffraction.* Acta Crystallographica, 1964. **17**(10): p. 1312-1321.

142. Steiner, C.J.P., D.P.H. Hasselman, and R.M. Spriggs, *Kinetics of the Gamma-to-Alpha Alumina Phase Transformation.* Journal of the American Ceramic Society, 1971. **54**(8): p. 412-413.

143. Morrissey, K.J., et al., *Growth of α-Al2O3 Within a Transition Alumina Matrix.* Journal of the American Ceramic Society, 1984. **67**(5): p. c88-c90.

144. Simpson, T.W., et al., *Kinetics of the Amorphous → γ → α Transformations in Aluminum Oxide: Effect of Crystallographic Orientation.* Journal of the American Ceramic Society, 1998. **81**(1): p. 61-66.

145. Kumagai, M. and G.L. Messing, *Controlled Transformation and Sintering of a Boehmite Sol-Gel by α-Alumina Seeding.* Journal of the American Ceramic Society, 1985. **68**(9): p. 500-505.

146.   McArdle, J.L., et al., *Solid-Phase Epitaxy of Boehmite-Derived α-Alumina on Hematite Seed Crystals.* Journal of the American Ceramic Society, 1989. **72**(5): p. 864-867.

147.   Zhang, Z., L. Li, and J.C. Yang, *γ-Al2O3 thin film formation via oxidation of β-NiAl(110).* Acta Materialia, 2011. **59**(15): p. 5905-5916.

148.   Wanke, S.E. and P.C. Flynn, *The Sintering of Supported Metal Catalysts.* Catalysis Reviews, 1975. **12**(1): p. 93-135.

149.   Zhang, W., J.R. Smith, and A.G. Evans, *The connection between ab initio calculations and interface adhesion measurements on metal/oxide systems: Ni/Al2O3 and Cu/Al2O3.* Acta Materialia, 2002. **50**(15): p. 3803-3816.

150.   Meltzman, H., D. Mordehai, and W.D. Kaplan, *Solid–solid interface reconstruction at equilibrated Ni–Al2O3 interfaces.* Acta Materialia, 2012. **60**(11): p. 4359-4369.

151.   Borchers, C. and R. Bormann, *Determination of low-temperature interfacial energies from a pair interaction model.* Acta Materialia, 2005. **53**(13): p. 3695-3701.

152.   Bobeth, M., et al., *Out-diffusion of the noble component during the initial stage of the oxidation of γ′-Ni3Al.* Acta Metallurgica et Materialia, 1992. **40**(10): p. 2669-2676.

153.   Donlon, W.T., T.E. Mitchell, and A.H. Heuer, *Precipitation in non-stoichiometric spinel.* Journal of Materials Science. **17**(5): p. 1389-1397.

154.   Tsirelson, V.G., et al., *Ruby structure peculiarities derived from X-ray diffraction data localization of chromium atoms and electron deformation density.* physica status solidi (a), 1985. **87**(2): p. 425-433.

155.   Newnham E, E. and D.E. Haan Y. M, *Refinement of the a Al2O3, Ti2O3, V2O3 and Cr2O3 structures*, in *Zeitschrift für Kristallographie - Crystalline Materials*. 1962. p. 235.

156.   Jung, I.-H., et al., *Thermodynamic evaluation and optimization of the MnO-Al2O3 and MnO-Al2O3-SiO2 systems and applications to inclusion engineering.* Metallurgical and Materials Transactions B, 2004. **35**(2): p. 259-268.

157.   Golikov, Y.V., et al., *Phase diagrams of the Mn   Al   O system.* Journal of Physics and Chemistry of Solids, 1995. **56**(5): p. 767-775.

158.   Martínez-Villafañe, A., et al., *Enhanced Oxygen Diffusion Along Internal Oxide–Metal Matrix Interfaces in Ni–Al Alloys During Internal Oxidation.* Oxidation of Metals, 2002. **57**(3-4): p. 267-279.

159.   Whittle, D.P., et al., *Enhanced diffusion of oxygen during internal oxidation of nickel-base alloys.* Philosophical Magazine A, 1982. **46**(6): p. 931-949.

160. Glöersen, P.G., *Ion−beam etching.* Journal of Vacuum Science & Technology, 1975. **12**(1): p. 28-35.

161. Speck, P., D.J. Young, and J. Zhang, *Metal Dusting of Nickel–Aluminium Alloys.* Oxidation of Metals, 2009. **73**(1): p. 255-274.

162. Venezia, A.M. and C.M. Loxton, *Low pressure oxidation of Ni3Al alloys at elevated temperatures as studied by x-ray photoelectron spectroscopy and Auger spectroscopy.* Surface Science, 1988. **194**(1): p. 136-148.

163. Hayashi, S. to be published.

164. Kofstad, P., *High temperature corrosion.* 1988, New York: Elsevier Applied Science ; Sole distributor in the USA and Canada, Elsevier Science Pub. Co.

165. Guan, S.W. and W.W. Smeltzer, *Oxygen solubility and a criterion for the transition from internal to external oxidation of ternary alloys.* Oxidation of Metals, 1994. **42**(5-6): p. 375-391.

166. Nesbitt, J.A., *Predicting Minimum Al Concentrations for Protective Scale Formation on Ni‐Base Alloys: I. Isothermal Oxidation.* Journal of The Electrochemical Society, 1989. **136**(5): p. 1511-1517.

167. Nesbitts, J.A. and R.W. Heckel, *Interdiffusion in Ni-rich, Ni-Cr-Al alloys at 1100 and 1200 °C: Part II. Diffusion coefficients and predicted concentration profiles.* Metallurgical Transactions A, 1987. **18**(12): p. 2075-2086.

168. Hayashi, S. and B. Gleeson, *Early-Stage Oxidation Behavior of Pt-Modified γ'-Ni$_3$Al-Based Alloys with and without Hf Addition.* Oxidation of Metals, 2009. **71**(1): p. 5-19.

169. Pettit, F.S., *Oxidation Mechanisms for Nickel-Aluminum Alloys at Temperatures Between 900°C and 1300°C.* Trans. AIME., 1967. **239**: p. 1296-1305.

170. Čermák, J., *Diffusion of 51Cr Along High-Diffusivity Paths in Ni-Fe Alloys.* physica status solidi (a), 1990. **119**(2): p. 443-453.

171. de Reca, N.W. and C.A. Pampillo, *Grain boundary diffusivity via bulk diffusion measurements during grain growth.* Scripta Metallurgica, 1975. **9**(12): p. 1355-1361.

172. Čermák, J. and Z. Čochnář, *Self-diffusion of 63Ni along dislocations.* Materials Science and Engineering: A, 1994. **174**(1): p. 9-13.

173. Divinski, S.V., G. Reglitz, and G. Wilde, *Grain boundary self-diffusion in polycrystalline nickel of different purity levels.* Acta Materialia, 2010. **58**(2): p. 386-395.

174. Stechauner, G. and E. Kozeschnik, *Self-Diffusion in Grain Boundaries and Dislocation Pipes in Al, Fe, and Ni and Application to AlN Precipitation in Steel.* Journal of Materials Engineering and Performance, 2014. **23**(5): p. 1576-1579.

175. Houston, J.T. and K. Farrell, *Recrystallization of nickel-270.* Metallography, 1969. **2**(2): p. 239-246.

176. Dudova, N., A. Belyakov, and R. Kaibyshev, *Recrystallization behavior of a Ni–20%Cr alloy subjected to severe plastic deformation.* Materials Science and Engineering: A, 2012. **543**: p. 164-172.

177. Zhang, C., et al., *The Kinetics of Metadynamic Recrystallization in a Ni-Cr-Mo-Based Superalloy Hastelloy C-276.* Journal of Materials Engineering and Performance, 2016. **25**(2): p. 545-552.

178. Moulin, P., A.M. Huntz, and P. Lacombe, *Influence du carbone sur la diffusion du chrome et du nickel en volume et dans les joints de grains de l'alliage Ni-Cr 80/20.* Acta Metallurgica, 1979. **27**(9): p. 1431-1443.

179. Čermák, J., J. Růžičková, and A. Pokorná, *Grain-boundary diffusion of chromium in Ni3Al intermetallic modified by Fe, Cr and Zr.* Intermetallics, 1998. **6**(5): p. 437-443.

180. Cermak, J., et al., *Short-circuit diffusion in Ni   Al alloys.* Intermetallics, 1998. **6**(1): p. 21-28.

181. Zhao, W., et al., *Quantitative Approach for Determining the Critical Volume Fraction for the Transition from Internal to External Oxidation.* Oxidation of Metals, 2015. **83**(3-4): p. 187-201.

182. Park, J.-W. and C. Altstetter, *The diffusion and solubility of oxygen in solid nickel.* Metallurgical Transactions A, 1987. **18**(1): p. 43-50.

183. Campbell, F.C., *Elements of Metallurgy and Engineering Alloys.* 2008, Materials Park, OH, USA: ASM International.

184. Markworth, A.J., *On the kinetics of anisothermal oxidation.* Metallurgical Transactions A. **8**(12): p. 2014-2015.